



Centro Brasileiro de  
Pesquisas Físicas

David Quispe Aruquipa

# **Scalar and Gravitational Green Functions on Curved Spacetimes: Applications to Radiation Reaction and Quantum Communication**

Função de Green Escalar e Gravitacional em Espaço-tempo Curvo: Aplicações  
no Back-reaction e Comunicação Quântica

Rio de Janeiro, RJ, Brazil

2023

David Quispe Aruquipa

**Scalar and Gravitational Green Functions on Curved  
Spacetimes: Applications to Radiation Reaction and  
Quantum Communication**

Função de Green Escalar e Gravitacional em Espaço-tempo Curvo: Aplicações  
no Back-reaction e Comunicação Quântica

Dissertation presented to the Brazilian Center for  
Research in Physics in partial fulfilment of the  
requirements to obtain the degree of Doctor in  
Physics.

Dissertação apresentada ao Centro Brasileiro de  
Pesquisas Físicas como parte dos requisitos para  
obtenção do título de Doutor em Física.

Centro Brasileiro de

Pesquisas Físicas

Supervisor: Prof. Dr. Marc Casals Casanellas

ESTE EXEMPLAR CORRESPONDE À VERSÃO  
FINAL DA DISSERTAÇÃO DEFENDIDA PELO  
ALUNO DAVID QUISPE ARUQUIPA E ORI-  
ENTADA PELO PROF. DR. MARC CASALS  
CASANELLAS.

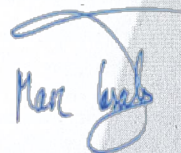
Rio de Janeiro, RJ, Brazil

2023

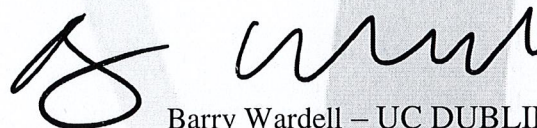
“SCALAR AND GRAVITATIONAL GREEN FUNCTIONS IN CURVED  
SPACETIME: APPLICATIONS TO RADIATION REACTION AND  
QUANTUM COMMUNICATION”

**DAVID QUISPE ARQUIPA**

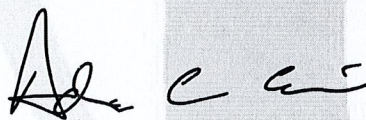
Tese de Doutorado em Física apresentada no  
Centro Brasileiro de Pesquisas Físicas do  
Ministério da Ciência Tecnologia e Inovação.  
Fazendo parte da banca examinadora os seguintes  
professores:



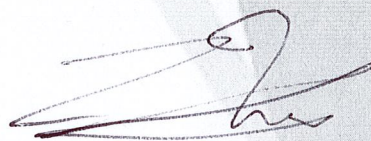
Marc Casals- Orientador/CBPF



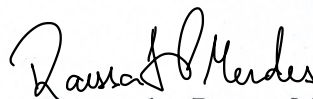
Barry Wardell – UC DUBLIN



Adrian Ottewill - UC DUBLIN



Alexandre Le Tiec – OBSERVATOIRE DE PARIS



Raissa Fernandes Pessoa Mendes - CBPF

Rio de Janeiro, 10 de maio de 2023.

# Acknowledgements

I would first like to thank my thesis supervisor Prof. Dr. Marc Casals Casanellas for guiding me and helping me to conclude this project. Next, I would like to thank the collaborators who also provided valuable contributions to this project: Robert H. Jonsson, Achim Kempf and Eduardo Martín-Martínez.

I must express my very profound gratitude to my mother for providing me with unfailing support and continuous encouragement throughout my years of study. This accomplishment would not have been possible without you. Thank you.

Finally, I would like to thank Coordenação de Aperfeiçoamento de Pessoal de Nível Superior (CAPES) and Fundação de Amparo à Pesquisa do Estado do Rio de Janeiro (FAPERJ) for the financial support.



# Abstract

The direct detection of gravitational waves by the Laser Interferometer Gravitational-Wave Observatory (LIGO) [1] marks the start of the era of gravitational wave astronomy, with important consequences for astrophysics and, potentially, for cosmology and theoretical physics. In the detection above, the source of gravitational waves was a binary system consisting of two black holes with tens of solar masses.

The main interest of this project focuses on a different regime, that of extreme mass-ratio inspirals (EMRIs). An example of such binary systems is a stellar-mass compact object (e.g. a neutron star or a black hole) orbiting around a massive black hole. In fact, there is a planned mission by the European Space Agency called the Laser Interferometer Space Antenna (LISA) [2], which aims at detecting gravitational waves emitted by EMRIs. EMRIs can be modelled within Einstein's theory of General Relativity by expanding the field equations in the mass-ratio  $\mu = m/M \ll 1$ , where  $M$  is the mass of the massive black hole and  $m$  is the mass of the small object. In order to provide accurate description of the motion of these binary systems, it is necessary to not treat the smaller compact object as a test mass (zeroth order in  $\mu$ ) but rather to take into account its own gravitational field to at least  $\mathcal{O}(\mu)$ . That is, the so-called gravitational *self-force* [3, 4, 5]. The self-force must then be incorporated into the equation of motion for the smaller body in order to find its evolution.

There exists a method for calculating the self-force which offers a particularly interesting physical insight. This method is via the Green function of the field equations. In this thesis, we will develop methods for calculating the Green function for scalar, electromagnetic, and gravitational perturbation fields of Schwarzschild spacetime. We will also use the Plebański-Hacyan spacetime as a toy model to explore additional techniques we could apply to Schwarzschild spacetime.

The Green function is a powerful tool and its applications go beyond the calculation of the self-force. For instance, we also explore the quantum communication between two observers near a Schwarzschild black hole. It turns out that The manifestation of spacetime curvature in quantum communication occurs through the retarded Green function of the Klein-Gordon equation.

**Key-words:** General Relativity. Black holes, Gravitational Waves, Quantum Communication.

# Resumo

A detecção direta de ondas gravitacionais pelo *Laser Interferometer Gravitational-Wave Observatory* (LIGO) [1] marca o início da era da astronomia de ondas gravitacionais, com importantes consequências na astrofísica, e potencialmente, para a cosmologia e a física teórica. Na detecção do LIGO, a fonte das ondas gravitacionais foi um sistema binário de dois buracos negros de dezenas de massas solares.

O principal interesse deste projeto é focado em um regime diferente, o dos *Extreme Mass-Ratio Inspirals* (EMRIs). Um exemplo de tais sistemas é um objeto compacto de massa estelar  $m$  (uma estrela de nêutrons ou um buraco negro) orbitando ao redor de um buraco negro massivo de massa  $M$ . De fato, há uma missão planejada pela Agência Espacial Europeia (ESA) [2], que pretende detectar ondas gravitacionais emitidas pelos EMRIs. Os EMRIs podem ser modelados expandindo as equações de campo do Einstein na relação de massas  $\mu = m/M \ll 1$ , sendo  $M$  a massa do buraco negro massivo e  $m$  a massa do objeto menor. Para fornecer uma descrição precisa do movimento desses sistemas binários, o objeto menor não pode ser tratado como uma partícula teste (ordem zero em  $\mu$ ), o campo gravitacional criado por ele deve ser levado em conta. Ou seja, o chamado *self-force* gravitacional [3, 4, 5]. Assim, a *self-force* deve ser considerada para encontrar a evolução do objeto menor.

Existe um método para calcular a auto-força que oferece uma visão física particularmente interessante. Esse método é baseado na função de Green. Nesta tese, desenvolveremos métodos para calcular a função de Green para campos de perturbação escalar e gravitacional de espaços-tempos de Schwarzschild. Também usaremos o espaço-tempo Plebański-Hacyan como um modelo de brinquedo para explorar técnicas adicionais que podemos estender e aplicar ao espaço-tempo Schwarzschild.

A função Green é uma ferramenta poderosa e suas aplicações vão além do cálculo da *self-force*. Por exemplo, também exploramos a comunicação quântica entre dois observadores perto de um buraco negro de Schwarzschild. Acontece que a curvatura do espaço-tempo se manifesta na comunicação quântica por meio da função de Green retardada da equação de Klein-Gordon.

**Palavras-chaves:** Relatividade Geral, Buracos negros, Ondas Gravitacionais, Comunicação quântica.

# List of Figures

Figure 1 – The method of matched expansion for a particle in curved spacetime. The blue section of the particle’s worldline denotes the QL region of $x$ , the particle’s current position. A point $x'$ is in the distant past of $x$ when it lies on the orange section of the particle’s worldline. . . . .	30
Figure 2 – Grid distribution on the $(v, u)$ -plane. . . . .	59
Figure 3 – Numerical precision for the method (implemented in the BHPT) which calculates the renormalised angular momentum $\nu$ . For this test, we fixed the precision of $\omega$ to 36 and calculated $\nu$ for different values of $\omega$ and (integer) values of $\ell$ (blue dots). We observe that the precision in $\nu$ drops as $\omega$ and $\ell$ increases. In the area where the precision is zero, the method was not able to calculate $\nu$ . . . . .	65
Figure 4 – In blue we plot ${}_0G_{\text{ret}}$ (as a function of $\Delta t$ ) obtained via CID, in red its non-direct part ${}_0G_{\text{ret}}^{\text{nd}}$ obtained using (2.91) and in orange we plot $-V_0$ . In this scenario $x$ and $x'$ are static: with zero angular separation and located at $r = r' = 6M$ away from the black hole. . . . .	72
Figure 5 – $\ell$ -modes of ${}_2G_{\text{ret}}$ (orange line, according to Eq. (2.29)) and the $\ell$ -modes of the direct part (blue line, according to Eq. (2.13)) for $r = r' = 6M$ . . .	73
Figure 6 – Comparison between ${}_2G_{\text{ret}}$ (Black curve) and its non-direct part ${}_2G_{\text{ret}}^{\text{nd}}$ along a timelike circular geodesic at $r = r' = 6M$ , for two different methods for $G_{\ell}^{\text{dir}}$ . The first method (Gray-dashed curve) relies in a numerical method for calculating $\Delta_{2\text{d}}^{1/2}$ and the second one (Blue curve) makes use of a small coordinate expansion described in [6]. The red curve is the biscalar $-V_2$ . The subplot shows the continuation of the main plot where we can see that there is indeed a matching region between ${}_2G_{\text{ret}}$ (black; the lump about $\Delta t \approx 27.7M$ is due to the first secondary null ray) and $V_2$ (red-dashed). . . . .	74

Figure 7 – Left: Absolute value of ${}_2G_{\text{ret}}$ excluding the $\ell = 0, 1$ modes, and along a timelike circular geodesic at $r = r' = 6M$ . Right: Absolute value of the radial derivative of the left result. The vertical red-dashed line in the left plot marks the end of the maximal normal neighbourhood, in this scenario it is near $\Delta t \approx 27.7M$ . The blue-dashed curves are the absolute values of $-V_2 - \frac{1}{r^2} \sum_{\ell=0}^1 (2\ell + 1) {}_2G_\ell P_\ell(\cos(\sqrt{M/r^3}\Delta t))$ (left plot) and its radial derivative (right plot). . . . .	75
Figure 8 – Comparison between ${}_2\tilde{G}_{\omega\ell}$ and $g_{\omega\ell}^{(-2)}$ for $\ell = 2$ and $r = r' = 6M$ . In the top plot we observe that the real parts have no similarities in the large- $\omega$ regime. For the imaginary parts, despite having the same decay in the large- $\omega$ regime, the additional oscillations in $g_{\omega\ell}^{(-2)}$ is a feature that could bring numerical difficulties in the Fourier integral. . . . .	78
Figure 9 – Grid distribution for a finite difference scheme for solving a two-dimensional PDE where $u$ and $v$ denote the independent variables and $2h$ is the stepsize. . . . .	86
Figure 10 – Quantities as functions of $\eta = \Delta t$ in $\mathbb{M}_2 \times \mathbb{S}^2$ with $\zeta = 1/4$ , $\Delta y = y - y' = 0$ and $\gamma = \pi/2$ . Top plot: Retarded Green function as an $\ell$ -mode sum (blue) and $V$ using the fourth order CID scheme (dashed red), a small coordinate-separation expansion (green) and approximated by $\nu_0 + \nu_1 \sigma_{\text{PH}}$ (dashed gray). Bottom plot: Relative error between the third order and fourth order schemes for calculating $V$ with $h = 0.00261799$ . . . . .	96
Figure 11 – GTE order $k$ for the third and fourth order CID schemes for $\gamma = 1.56$ (top) and $\gamma = 0$ (bottom). The expected values for the order $k$ are close to the theoretical values (namely, $k = 1$ for the third order scheme and $k = 2$ for the fourth order one, drawn as horizontal black continuous lines). . . . .	98

Figure 12	–Plot of $V$ for all pairs of points in normal neighbourhoods with $\zeta = 1/4$ . The $u = 2\pi$ and $v = 2\pi$ lines correspond to the end of the normal neighbourhood where the (leading) singularity of $G_{\text{ret}}^{\text{PH}}$ , and so of $V$ , is of type PV ( $1/\sigma_{\text{PH}}$ ) (when away from caustics). The red line is along the static worldline considered in Fig. 10. . . . .	100
Figure 13	–Top: Plot of $V$ as a function of $\eta$ for different values of $\zeta$ and for the same scenario (and stepsize) as in Fig. 10. Bottom: 3D plot of $V$ as a function of $u$ and $v$ for $\zeta = 1$ . . . . .	101
Figure 14	–Leading order signal strength between Alice, spatially fixed at radius $r_A = 6M$ and Bob, spatially fixed at varying radii $r_B$ and angular separation $\gamma$ from Alice. The frequency of Alice’s detector is $\Omega_A = 1/M$ . The plot labels Bob’s position by $x_B = r_B \cos \gamma$ and $y_B = r_B \sin \gamma$ . The detectors couple to the field through sharp switching functions for $0 \leq \tau_A \leq M$ and $0 \leq \tau_B \leq 15M$ , respectively. The top of the plots is capped close to Alice’s position because the direct contribution diverges at exactly that point. The plot covers the radial coordinate position of Bob down to $r_B = 2.26M$ . The plot only covers positions up to a certain angular separation between Alice and Bob because the numerical evaluation of the signal strength is infeasible beyond this region. . . . .	119

Figure 15 – Direct contributions  $|C_2^d| + |D_2^d|$  to the signal strength in the scenario of Fig. 14b: The detectors are static: Alice is placed at a fixed radial coordinate  $r_A = 6M$ , whereas Bob’s radial coordinate  $r_B$  and angular separation  $\gamma$  vary, as labelled by  $x_B = r_B \cos \gamma$  and  $y_B = r_B \sin \gamma$ . The detector gaps are  $\Omega_A = 1/M$  and  $\Omega_B = 1/(2M)$ , and Alice couples to the field for her proper time interval  $0 \leq \tau_A \leq M$ . A red dot in Fig. 15b indicates Alice’s position, and the plot shows the direct null geodesic emanating from there to the green dot, as one example for Bob’s location. Note that the direct contribution is not defined at the exact angular separation  $\gamma = \pi$ ; the plot shows a numerical interpolation. . . . . 120

Figure 16 – The non-direct contribution  $|C_2^{\text{nd}}|$  and  $|D_2^{\text{nd}}|$  as a function of  $B_1$  for static detectors at  $r_A = 6M$  and  $r_B \approx 3.01M$  and  $\gamma = \pi/4$ , with  $\Omega_A = \Omega_B = 1/M$ . The switching on/off proper times are  $A_1 = 0$ ,  $A_2 = M$  and  $B_2 = B_1 + \tilde{\tau}_B(A_2)$ , with  $\tilde{\tau}_B(A_2) \approx 0.71M$ . Note that the corresponding direct contribution at  $B_1 = 0$  would be  $|C_2^d| \approx 0.0121551$  and  $|D_2^d| \approx 0.0107647$  which then drops down to zero as soon as  $B_1 > \tilde{\tau}_B(A_2)$ . . . . . 122

Figure 17 – Non-direct contributions  $|C_2^{\text{nd}}| + |D_2^{\text{nd}}|$  for static detectors as a function of Bob’s location for  $A_1 = B_1 = 0$ ,  $A_2 = M$ ,  $\Omega_A = 1/M$  and with further parameters as specified, comparing two different values of  $B_2$  and  $\Omega_A$ . A red dot indicates Alice’s location at  $r_A = 6M$ . Figs. 17a and 17b show the non-direct contribution to the total signal strength of Fig. 14. . . . . 124



Figure 18 – Non-direct contribution  $|C_2^{\text{nd}}| + |D_2^{\text{nd}}|$  for  $A_1 = B_1 = 0$ ,  $A_2 = M$ ,  $\Omega_A = 1/M$ ,  $B_2 = 15M$  and  $\Omega_B = 1/(2M)$ . A red dot indicates Alice’s location. This is a contourplot version of Fig. 17b. The dashed lines indicate how far the secondary null rays emitted by Alice have propagated at the time when Bob switches off his detector: the green line, with smaller angular separation  $\gamma$ , shows the earliest secondary null rays from Alice, and the white line, with larger  $\gamma$ , shows the last secondary null rays from Alice. . . . . 126

Figure 19 – Comparison of the integrand in  $C_2^{\text{nd}}$  in Eq. (4.44) for two different positions of Bob in the scenario of Fig. 17b: The top/bottom plots correspond to positions of Bob located at the top/bottom of the step-like feature due to tertiary light rays in Fig. 17b. Both positions have angular separation  $\gamma = 69\pi/100$  from Alice, but with different radial coordinates. The orange and green curves correspond to, respectively, the real and imaginary parts of the integrand (times  $M$ ) in Eq. (4.44). The solid blue and dashed red curves correspond to the GF  $M^2_0 G_{\text{ret}}/4\pi$  (which is a factor in that integrand) in, respectively, the DP and QL regions (extended to slightly negative values of  $w/M$  for ease of visualization). The horizontal axes contain the integration variable  $w$  in Eq. (4.44) divided by  $M$ . (Recall that the switching parameters are  $A_1 = B_1 = 0$ ,  $A_2 = M$ ,  $B_2 = 15M$ ,  $\Omega_A = 1/M$  and  $\Omega_B = 1/(2M)$ .) . . . 128

Figure 20 –Scenario where Alice follows a radially-infalling timelike geodesic starting from rest at  $r = 6M$ , and Bob is static at  $r = 6M$  (which corresponds to  $r_* = 6M + 2M \ln 4$ ). Alice’s worldline  $t = t(r_*(r_A))$  is given by the red line, Bob’s  $t = t(r_*(r_B))$  by the blue vertical line. The shaded regions indicate various coupling intervals during which Alice couples her detector to the field. The black-dashed lines represent the first radially-outgoing null geodesics emanating from Alice for each interval, the grey-dashed lines represent the last ones. All intervals last for the same amount of Alice’s proper time  $\Delta\tau_A = M/4$ . Time windows starting later on Alice’s worldline, i.e., closer to the horizon, extend over larger intervals of coordinate time (as well as of tortoise radial coordinate  $r_*$ ). . . . . 129

Figure 21 –Plots of  $|C_2|+|D_2|$  in the radial-infall scenario as a function of the radial coordinate  $r_A$  (when Alice switches on her detector) and detectors’ frequency  $\Omega = \Omega_A = \Omega_B$ . Independently of the value of  $r_A$ , Alice switches off her detector after a fixed amount  $\Delta\tau_A = M/4$  of her proper time. Top: 3D plot (the red line corresponds to the case where  $\Omega = 1/M$ ). Bottom: 2D plot as a function of  $r_A$  for a sample of values of  $\Omega$  (so these curves are just cross-sections of the 3D plot at the top). . . . . 131

Figure 22 –Plots of direct  $|C_2^d|$  and non-direct  $|C_2^{nd}|$  contributions to  $C_2$  in the radial-infall scenario as functions of  $r_A$  (when Alice switches on her detector) and detectors’ frequency  $\Omega$ . Top: 3D plot where the blue and orange surfaces respectively correspond to  $|C_2^d|$  and  $|C_2^{nd}|$ . Bottom: 2D plot as a function of  $r_A$  for a sample of values of  $\Omega$  (so these curves are just cross-sections of the 3D plot at the top). . . . . 132

Figure 23	– Absolute values of the real (left) and imaginary (right) parts of ${}_{-2}\tilde{G}_{\omega,2}^T$ . In this case $r = r' = 6M$ . The black solid line is obtained by applying the Chandrasekhar transformation on ${}_2\tilde{G}_{\omega,2}$ (see Eq. (5.29)) whereas the red dots are obtained using the numerical method available in the BHPT. . . . .	140
Figure 24	– Fourier modes ${}_{-2}\tilde{G}_{\omega\ell}^T$ , for $\ell = 2$ (left) and $\ell = 20$ (right), alongside their corresponding large- $\omega$ asymptotic expansions (dashed curves) from (5.36).	142
Figure 25	– Teukolsky $\ell$ -mode ${}_{-2}G_\ell^T$ (for $r = r' = 6M$ and $\ell = 2$ ) calculated using the two integrals appearing in Eq. (5.38). Due to the different numerical tweaks we introduced during the Fourier integral, we observe a discrepancy in the results depending on which integral we use in Eq. (5.38). . . . .	143
Figure 26	– Comparison of ${}_{-2}G_2^T(r, r, t - t')$ (with $r = 6M$ ) calculated according to (5.34) (blue), the quasi-normal mode $\ell = 2, n = 0$ estimated using [7] (black-dashed) and the late time decay $\Delta t^{-(2\ell+3)}$ (orange-dashed). . . . .	144
Figure 27	– Full retarded Teukolsky Green function ( ${}_{-2}G_{\text{ret}}^T$ ) for two different scenarios, the $\ell$ -sum was capped at $\ell = 100$ and we used $\ell_{\text{cut}} = 8$ for the static case and $\ell_{\text{cut}} = 12$ for the circular case. . . . .	146
Figure 28	– Comparison between ${}_{-2}\mathcal{C}_R(r, \Delta t){}_{-2}\mathcal{C}_R(r', \Delta t){}_2G_\ell$ , ${}_{-2}\mathcal{C}_R(r, \Delta t){}_{-2}\mathcal{C}_R(r', \Delta t)G_\ell^{\text{dir}}$ and $S(\Delta t){}_{-2}\mathcal{C}_R(r, \Delta t){}_{-2}\mathcal{C}_R(r', \Delta t)G_\ell^{\text{dir}}$ for $\ell = 2$ (top) and $\ell = 25$ (bottom). . . . .	151

Figure 29 – Logarithmic plot comparing the direct signal strength  $|C_2^d| + |D_2^d|$  for radially separated static detectors in Schwarzschild and in Minkowski spacetime. In Schwarzschild spacetime Alice is located at  $r_A = 6M$ , her detector gap is  $\Omega_A = 10/M$  and she couples to the field for a proper time duration of  $A_2 - A_1 = 3M$ . Bob’s radial coordinate is  $r_B$ . He couples to the field in such a way that he receives all of Alice’s direct null geodesics. The resulting signal strengths in Schwarzschild spacetime are shown for Bob using an identical detector with  $\Omega_B = 10/M$  (green), and a resonant detector with  $\Omega_B = \nu\Omega_A$  (yellow). In Minkowski spacetime (blue), Alice and Bob use identical detectors ( $\Omega_A = \Omega_B = 10/M$ ) which are placed so that their static distance in Minkowski spacetime  $d(r_A, r_B)$  is the same as in the Schwarzschild scenario (see Eq. (D.6)). . 183

Figure 30 – The figure compares various measures of distance between two radially separated static observers, Alice (sender) at  $r_A = 6M$  and Bob at varying  $r_B$ , in Schwarzschild spacetime. The plot shows half of the signal return time for Alice (blue, dashed) and Bob (yellow, dashed), i.e., the time it takes for a signal to propagate from Alice to Bob measured in terms of the respective proper times of Alice and Bob, and the static distance (green, solid) in Eq. (D.6). The plot also shows the “mimicking distance” (red, solid), i.e., the distance in Minkowski spacetime at which two identical detectors ( $\Omega_B = \Omega_A$ ) achieve the same direct signal strength as the two detectors in Schwarzschild spacetime at  $r_A$  and  $r_B$  when they are resonantly-tuned ( $\Omega_B = \nu\Omega_A$ ). (The return times and the mimicking distance diverge, as  $r_B \rightarrow 2M$ , whereas the static distance remains finite, see (D.7).) . . . . . 185

Figure 31 – Contribution to the leading order signal strength from a  $\text{PV}\left(\frac{1}{\sigma}\right)$ -distribution, as resulting from Eq. (F.4), with  $\nu = \sqrt{(1 - 2/6)/(1 - 2/3.01)} \approx 1.40954$ ,  $A_1 = 0$  and  $A_2 = M$ . The horizontal axes show  $B'_1 := B_1 - \frac{w_2 - A_2 + 2A_1}{\nu}$  which is the switch-on time  $B_1$  of Bob shifted so that, for  $B'_1 < 0$ , Alice and Bob are not connected by the singularity of the  $\text{PV}\left(\frac{1}{\sigma}\right)$ -distribution while coupling to the field. This corresponds to Bob switching off his detector before any secondary null geodesics emanating from Alice arrive at his location. The graphs are symmetric about the point  $B'_1 = \frac{A_2 - A_1}{\nu}$ . This corresponds to the switching-on and switching-off of sender and receiver being exactly connected by secondary null geodesics. The parameters in Fig. 31a match those in Fig. 16, thus the curve with equal frequencies ( $\Omega_A = \Omega_B$ ) here reproduces the features due to secondary null geodesics seen there. . . . . 190

Figure 32 – Contribution to the leading order signal strength from  $\text{PV}\left(\frac{1}{\sigma}\right)$ -distribution, as resulting from Eq. (F.7), with  $\nu = \sqrt{(1 - 2/6)/(1 - 2/3.01)} \approx 1.40954$ ,  $A_1 = 0$  and  $s_2 = 5M$ . (For this cumulative signal strength we always have  $B_1 = A_1/\nu = 0$ .) Alice’s first light ray, emanating at  $A_1 = 0$ , is connected by the  $\text{PV}\left(\frac{1}{\sigma}\right)$ -singularity to the point on Bob’s worldline with proper time  $\tau_B = (w_2 + A_1)/\nu \approx 3.55M$ . Alice’s last light ray, emanating at her proper time  $A_2$ , is connected to Bob’s worldline at his proper time  $\tau_B = (w_2 + A_2)/\nu$  which is different for the two figures. The curve in Fig. 32a with  $\Omega_B = \Omega_A/2$  reproduces the features discussed in Figs. 18 and 17. In all three figures the oscillations in all curves decay as  $B_2 \rightarrow \infty$  and asymptote to constant values. (Note for non-colour print: The curve in Figs. 32b and 32c asymptote in the same order as they appear in the legend.) . . . . . 194

# Contents

<b>1</b>	<b>Field perturbations of curved spacetime</b>	<b>22</b>
1.1	General relativity	22
1.2	Particles In Curved Spacetime	23
1.3	Scalar Green function in curved spacetime	24
1.3.0.1	Singular and regular Green functions	24
1.4	Motion of a scalar charge in curved spacetime	25
1.5	Motion of a point mass in curved spacetime	27
1.6	Method of matched expansions for the tail integral	30
1.7	Black hole spacetimes	32
1.7.1	Schwarzschild spacetime	32
1.7.2	Kerr spacetime	34
1.8	Gravitational perturbations of Schwarzschild spacetime	35
1.8.1	Even and odd parity field perturbations	36
1.8.2	Gauge transformation for $h_{\mu\nu}^{(\ell m)}$	36
1.8.3	Odd-parity perturbations in the Regge-Wheeler gauge	37
1.8.4	Even-parity perturbations	40
1.8.5	Teukolsky formalism and the Teukolsky equation	41
1.8.6	Metric reconstruction in the radiation gauge	45
<b>2</b>	<b>Calculation of the Regge-Wheeler Green function</b>	<b>48</b>
2.1	Retarded Green function in the QL region	49
2.1.1	Calculation of $\Delta^{1/2}(r, r')$	51
2.1.2	Van Vleck determinant and $\sigma^\mu{}_\nu$ along radial null geodesics	53
2.1.3	Calculation of $V_s$	55
2.2	Retarded Green function in the DP region	56
2.2.1	The RWE as a Characteristic Initial Value problem	57
2.2.2	The radial Regge-Wheeler equation	63



2.2.3	Convergence of Fourier integral of ${}_s\tilde{G}_{\omega l}$ and its radial derivative . . .	68
2.3	Results for the retarded GF of the Regge-Wheeler equation. . . . .	70
2.3.1	Spin-0 case . . . . .	71
2.3.2	Spin-2 case . . . . .	73
2.3.3	Regularisation process in the frequency domain . . . . .	75
<b>3</b>	<b>Hadamard Tail from Initial Data on the Light Cone in Plebański-Hacyan</b>	
	<b>spacetime . . . . .</b>	<b>80</b>
3.1	Hadamard biscalars in PH spacetime . . . . .	82
3.2	The wave equation as a characteristic initial value problem . . . . .	85
3.2.1	Numerical scheme . . . . .	86
3.2.2	CID scheme setup . . . . .	87
3.2.2.1	Third order CID scheme . . . . .	88
3.2.2.2	Fourth order CID scheme . . . . .	90
3.2.3	Results for $V$ . . . . .	95
3.3	Going beyond PH spacetime . . . . .	102
<b>4</b>	<b>Quantum communication near a black hole . . . . .</b>	<b>103</b>
4.1	Signaling with Unruh-DeWitt detectors . . . . .	104
4.1.1	Quantum channel between detectors . . . . .	104
4.1.2	Leading order signal strength . . . . .	107
4.1.3	In what sense are the leading order signals classical or quantum? . .	109
4.1.4	Symmetry of signaling terms between time-mirrored scenarios . . .	112
4.2	Signaling in Schwarzschild spacetime . . . . .	113
4.2.1	Direct and non-direct contributions to the signal strength . . . . .	114
4.2.2	Signaling between two static observers . . . . .	117
4.2.3	Shifting Bob's coupling . . . . .	121
4.2.4	Long time-like coupling of Bob . . . . .	124
4.2.5	Signaling between static and radial-infalling observers . . . . .	129
<b>5</b>	<b>The Teukolsky Green function . . . . .</b>	<b>133</b>

5.1	Hadamard construction of ${}_sG_{\text{ret}}^T$ . . . . .	134
5.2	Mode decomposition for ${}_sG_{\text{ret}}^T$ . . . . .	137
5.2.1	Convergence of the Fourier integral of ${}_{-2}\tilde{G}_{\omega\ell}^T$ . . . . .	141
5.2.2	Full Teukolsky Green function . . . . .	145
5.2.3	Chandrasekhar operator in the time domain and regularisation . . . . .	147
<b>6</b>	<b>Conclusions</b> . . . . .	<b>153</b>
	<b>Bibliography</b> . . . . .	<b>159</b>
	<b>Appendix</b> . . . . .	<b>174</b>
<b>APPENDIX A</b>	<b>Asymptotic coefficients <math>a_n^{\text{in}}</math> and <math>a_n^{\text{in}}</math> for <math>{}_s\tilde{X}_{\omega\ell}^{\text{in}}</math> and <math>{}_s\tilde{X}_{\omega\ell}^{\text{up}}</math></b> . . . . .	<b>175</b>
<b>APPENDIX B</b>	<b>Going beyond a fourth order CID scheme for calculating <math>V</math> in PH spacetime</b> . . . . .	<b>177</b>
<b>APPENDIX C</b>	<b>Derivation of time-mirror symmetry</b> . . . . .	<b>179</b>
<b>APPENDIX D</b>	<b>Contribution to the leading order signal strength from <math>C_2^{\text{d}}</math> and <math>D_2^{\text{d}}</math></b> . . . . .	<b>181</b>
<b>APPENDIX E</b>	<b>Change of integration variable in tail contribution for static detectors</b> . . . . .	<b>187</b>
<b>APPENDIX F</b>	<b>Signal contribution from principal value distribution</b> . . . . .	<b>189</b>

# Outline

Since Einstein published his theory of General Relativity in 1915, the understanding of gravity changed drastically. One of the predictions of General Relativity are gravitational waves: “ripples” in spacetime. The existence of gravitational waves was confirmed in 2015 by LIGO’s detection [1]. In that case, the gravitational waves were emitted by a binary black hole inspiral. The evolution of such binary systems is mathematically difficult because of the non-linearity of the Einstein field equations. The source for LIGO’s detection was a binary system of two stellar-mass black holes, the model to describe this system was obtained with a mix of numerical and analytic methods. A different regime of interest is the extreme mass-ratio inspiral (EMRI), where one of the objects is a supermassive black hole and the other a small compact object.

In the case of EMRIs, linearizing the Einstein field equations provides a good description to leading-order in the extreme mass-ratio  $m/M$ , where  $m$  is the mass of the smaller object and  $M$  that of the larger object (in astrophysical settings, EMRIs typically have mass ratios of the order  $10^{-5}$  to  $10^{-7}$ ). Away from the worldline of the smaller object, we can then write the metric of this binary system as  $\mathbf{g}_{\mu\nu} = g_{\mu\nu} + h_{\mu\nu}$  where  $g_{\mu\nu}$  is the metric of the massive black hole and  $h_{\mu\nu} = \mathcal{O}(m)$  of the smaller black hole. Because  $m/M$  is very small, at leading order the massive black hole can be considered at rest, and so we focus our attention on the evolution of the smaller black hole.

The perturbation  $h_{\mu\nu}$  describes (far away from the source) gravitational waves (GW) emitted by the system. One can take the viewpoint that such emission backreacts on the smaller object, thus deviating it from a geodesic of  $g_{\mu\nu}$ . However,  $h_{\mu\nu}$  formally diverges on the worldline of  $m$  and so it must be appropriately regularized there. The regularized metric perturbation, when differentiated, gives rise to the gravitational self-force  $F_\mu$  [3].

The evolution of the orbit of a smaller object when including the self-force (SF) has

been accomplished in some specific cases. For instance, in [8] the evolution of a small mass inspiralling into a massive, spherically-symmetric (Schwarzschild) black hole was obtained by using the approximation of the so-called ‘geodesic self-force’. In its turn, [9] obtained a self-consistent (i.e., exact, not approximated) orbital evolution for a scalar charge near a Schwarzschild black hole. In Refs. [10, 4, 5, 11] one can find different reviews about the fundamental theory and current progress made for calculating the self-force.

We note that the scalar self-force is often used as a simple model for the gravitational self-force [12, 13, 14, 15, 16, 17]. On a different scenario, it has been shown that spacetime’s curvature plays an important role in quantum signaling [18, 19]. Specifically, the scalar retarded Green function is intricately connected to the signal strength of a communication channel. We thus also examine this setting and investigate the physical implications of quantum communication in curved spacetime.

This thesis is organised in the following way. In Chapter 1 we first review fundamental concepts about Green functions in curved spacetime. Next, we give a short introduction about the motion of a scalar charge and point particle in curved spacetime and its relation with the retarded Green function. In the last sections, we introduce the Schwarzschild and Kerr spacetimes and provide the framework we use to describe field perturbations of Schwarzschild spacetime.

In Chapter 2 we calculate the retarded Green function of the Regge-Wheeler equation for spins 0 and 2. This was accomplished by splitting the spacetime in two regions: quasi-local and distant-past. In the quasi-local region we calculated the main Hadamard biscalars to construct the direct and non-direct part of the retarded Green function. In the distant past region we provided two methods for calculating the retarded Green function, both were based on a mode decomposition approach. We then calculated the modes in the time domain (using characteristic initial data) and in the frequency domain (via factorized Green function method). In Appendix A we provide the coefficients of the large- $\omega$  (the Fourier frequency) asymptotics for solutions to the Regge-Wheeler equation detailed in Chapter 2.

In Chapter 3 we provide a numerical scheme for computing the Hadamard tail  $V(x, x')$  in Plebański-Hacyan spacetime from initial data on the light cone. This toy model for black hole spacetimes allowed us to understand how to set up a characteristic initial value problem in four dimensions. Although the symmetries of the spacetime simplified the field equation for  $V(x, x')$ , we found a coordinate singularity connected to the angular separation between  $x$  and  $x'$ . We found out that this coordinate singularity has an impact on the order of the global truncation error of the numerical scheme. After handling this coordinate singularity, we obtained a scheme (with third and fourth orders in the local truncation error) to compute  $V(x, x')$  (for any pair of points where it is defined) for the coupling constant  $\xi = 0, 1/8, 1/4, 1/2$ . Since Schwarzschild and Plebański-Hacyan spacetimes share the same spherical symmetry, the Hadamard tail in Schwarzschild spacetime should have the same coordinate singularity we found in the field equation for  $V(x, x')$ . In Appendix B we provide a brief prescription for how one can expand the scheme we developed for calculating  $V(x, x')$ . We expect that the calculations in Plebański-Hacyan spacetime to be useful for calculating the Hadamard tail in Schwarzschild spacetime. With my supervisor Marc Casals, we submitted a paper with these new results and recently was accepted for publication [20].

In Chapter 4 we move to a different setting and explore quantum communication in curved spacetime. In this setting two observers attempt to communicate via a quantum scalar field near a black hole. It turned out that the leading order in the signal strength (a measure for the probability of successfully transmit information through the quantum channel) is mainly determined by the scalar retarded Green function. The effects of the spacetime curvature is then manifested on the quantum communication via the scalar retarded Green function. We then obtained the leading order signal strength in two main scenarios: In the first one, the sender is fixed at a spatial point and we move the spatial position of the receiver to different static positions near the black hole; in the second scenario, the receiver is fixed at a spatial position while the sender follows a radial infall geodesic. In Appendices C–E–F, we include additional calculations that helped to understand and simplify our calculations of the leading order signal strength. These results

were published on a paper with my supervisor Marc Casals in collaboration with Robert Jonsson, Achim Kempf and Eduardo Martín-Martínez [19].

In Chapter 5 we calculate the retarded Teukolsky Green function for spin  $-2$ . These results rely on previous calculations already presented in Chapter 2. Once again, calculating the retarded Teukolsky Green function is not sufficient for self-force calculations, we should provide a regularisation procedure as well. We made partial progress on this by calculating the direct part of the Teukolsky Green function. Although this result was not fully completed, we hope that this can be a good starting point for future work in which the problems we found during our calculations can be addressed.

I also published a work unrelated to this thesis in collaboration with Ricardo Mosna and Paulo Pitelli [21]. In this paper, we explored an analogue model for the two-dimensional anti de-Sitter spacetime ( $\text{AdS}_2$ ) based on a radial fluid flow with a point source/sink at the origin. The wave propagation is then uniquely defined only when one imposes an extra boundary condition at the source/sink (which corresponds to the spatial infinity of  $\text{AdS}_2$ ). Once we smooth out the velocity profile at the source/sink, the extra boundary condition is no longer necessary. In its turn, this process led to a deformation of the  $\text{AdS}_2$  spacetime near its spatial infinity.

Throughout this Thesis, we use natural units  $G = c = \hbar = 1$  and follow the sign convention  $(-, +, +, +)$  for the metric. Tensorial indices are denoted by Greek letters and the spatial component of a vector, say  $u^\mu$ , is represented by the same symbol but with an arrow on top of it, e.g.,  $u^\mu = (u^0, \vec{u})$ . Tetrad indices are denoted by a Latin index in brackets, e.g.,  $\eta_{(a)(b)}$ .



# 1 Field perturbations of curved spacetime

In this Chapter we first start with a brief introduction to general relativity. Next, we review the fundamental concepts behind the motion and self-consistent evolution of a scalar charge in curved spacetime. We then move to the gravitational case and review the motion of a point particle in curved spacetime. In this thesis the preferred method for calculating the self-field is via Green function methods, we also give an introduction to Green functions and how to regularise them. In the last sections, we focus on a specific type of spacetime, the Schwarzschild spacetime. To conclude, we give a brief review of gravitational perturbations of Schwarzschild spacetime.

## 1.1 General relativity

It 1915, Albert Einstein came up with a new perspective for describing gravity. His idea is now embodied in the so-called Einstein's field equations [22, 23, 24]

$$R_{\mu\nu} - \frac{1}{2}Rg_{\mu\nu} = 8\pi T_{\mu\nu}, \quad (1.1)$$

where  $g_{\mu\nu}$  is the metric tensor,  $R_{\mu\nu} = R^\alpha_{\mu\alpha\nu}$  is the Ricci tensor (where  $R^\mu_{\nu\alpha\beta}$  is the Riemann tensor),  $R = R^\mu_{\mu}$  is the Ricci scalar and  $T_{\mu\nu}$  is the stress-energy tensor of the matter distribution.

In the absence of matter ( $T_{\mu\nu} = 0$ ), Eq. (1.1) reduces to

$$R_{\mu\nu} = 0, \quad (1.2)$$

and from this, the Weyl tensor  $C_{\mu\nu\alpha\beta}$  agrees with the Riemann tensor, i.e.,

$$\begin{aligned} C_{\mu\nu\alpha\beta} = & R_{\mu\nu\alpha\beta} + \frac{1}{n-2} (R_{\mu\beta}g_{\nu\alpha} - R_{\mu\alpha}g_{\nu\beta} + R_{\nu\alpha}g_{\mu\beta} - R_{\nu\beta}g_{\mu\alpha}) \\ & + \frac{R}{(n-1)(n-2)} (g_{\mu\alpha}g_{\nu\beta} - g_{\mu\beta}g_{\nu\alpha}) = R_{\mu\nu\alpha\beta}, \end{aligned} \quad (1.3)$$

where  $n$  is the spacetime dimension.

Some known vacuum solutions are the Minkowski spacetime

$$g_{\mu\nu} = \eta_{\mu\nu} = \text{diag}(-1, 1, 1, 1)$$

(in Cartesian coordinates) or the Schwarzschild spacetime (which we show later).

The motion of test particles and light are now given by the geodesic equation

$$\frac{du^\mu}{d\lambda} + \Gamma^\mu_{\alpha\beta} u^\alpha u^\beta = 0, \quad (1.4)$$

where  $u^\mu = \frac{dx^\mu}{d\lambda}$  is the 4-velocity,  $\lambda$  is an affine parameter and  $\Gamma^\mu_{\alpha\beta}$  are the Christoffel symbols. For non-test particles, their motion deviates from a geodesic motion due to the interaction of the particle with its self-field. We thus need to incorporate this interaction in the equations of motion.

## 1.2 Particles In Curved Spacetime

Since classical mechanics describing a physical system often reduces to solving a set of equations of motion, this idea is also maintained in general relativity. In the case of classical electromagnetism previous works from Lorentz, Abraham, Poincaré and Dirac attempted to describe the motion of a point electric charge. A generalization of Dirac's results to curved spacetimes was made by DeWitt and Brehme [25]. Later on, Gralla, Harte and Wald provided a rigorous derivation of the equation of motion [26, 27] without requiring any postulate or renormalization procedures. Back in 1997 Mino, Sasaki and Tanaka came up with one of the first attempts at describing the motion of a point mass in curved spacetime [28]. In the same year Quinn and Wald were able to obtain the same equations but with a different approach [29]. Later on Quinn generalised this axiomatic approach to use it for the calculation of the SF acting on a point scalar charge [30]. Since in this project we are interested in the method of Green function, we first provide key concepts about the scalar Green function in curved spacetime, these ideas are not limited to the scalar case, in fact, some key properties of the Green function are present in both, electromagnetic and gravitational fields.

### 1.3 Scalar Green function in curved spacetime

The field equation for a massless scalar field  $\Phi(x)$  in a background spacetime  $\mathcal{M}$  with metric  $g_{\mu\nu}$  satisfies the wave equation

$$(\square - \xi R)\Phi(x) = -4\pi\mu(x), \quad (1.5)$$

where  $\square = g^{\mu\nu}\nabla_\mu\nabla_\nu$ ,  $\xi$  is a coupling constant and  $\mu(x)$  is a prescribed source. We define a Green function  $G(x, x')$  to be a distribution such that  $\Phi(x)$  can be calculated via

$$\Phi(x) = \int_{\mathcal{M}} G(x, x')\mu(x')\sqrt{-g'}d^4x', \quad (1.6)$$

where the integral is evaluated over the entire  $\mathcal{M}$ . From this expression it is straightforward to show that the Green function  $G(x, x')$  also satisfies a wave equation with a Dirac delta distribution as a source, i.e.,

$$(\square - \xi R)G(x, x') = -4\pi\delta_4(x, x'), \quad (1.7)$$

where  $\delta_4(x, x')$  is the invariant Dirac delta distribution and is defined by

$$\delta_4(x, x') \equiv \frac{\delta_4(x - x')}{\sqrt{-g(x)}}. \quad (1.8)$$

The boundary conditions imposed on  $G(x, x')$  will determine the different types of Green functions one can obtain from Eq. (1.7). In particular, we are interested in the retarded Green function,  $G_{\text{ret}}(x, x')$ , which has causal boundary conditions, i.e., it is zero when  $x'$  does not lie on or inside the past light cone of  $x$ .

#### 1.3.0.1 Singular and regular Green functions

The retarded solution to the scalar wave equation is the one physically relevant because it delivers the proper outgoing-wave boundary conditions at infinity. Once the field's source is provided, the retarded field can be determined by using Eq. (1.6) with  $G(x, x')$  being replaced by the retarded GF  $G_{\text{ret}}(x, x')$ . For point-like sources the retarded field is singular on the worldline, this divergence has to be properly handled before formulating the equations of motion. To understand the origin of this divergence, it is convenient to decompose  $G_{\text{ret}}(x, x')$  into a *singular* Green function  $G_{\text{S}}(x, x')$  and a *regular* two-point

function  $G_R(x, x')$ , i.e.,  $G_R(x, x') = G_{\text{ret}}(x, x') - G_S(x, x')$ . This decomposition process imposes the following properties on the singular Green function [5]:

- $G_S(x, x')$  satisfies the inhomogeneous wave equation,
 
$$(\square - \xi R)G_S(x, x') = -4\pi\delta_4(x, x'),$$
- $G_S(x, x') = G_S(x', x)$ ,
- $G_S(x, x') = 0$  when  $x$  is in the chronological past or future of  $x'$  ( $I^\pm(x')$ ).

As a consequence of these properties, the regular two-point function has the following properties

- $G_R(x, x')$  satisfies the homogeneous wave equation, i.e.,  $(\square - \xi R)G_R(x, x') = 0$ ,
- $G_R(x, x') = G_{\text{ret}}(x, x')$  when  $x$  is in the chronological future of  $x'$  ( $I^+(x')$ ),
- $G_R(x, x') = 0$  when  $x$  is in the chronological past of  $x'$  ( $I^-(x')$ ).

The symmetry in the singular GF manifests its non-causality, any field constructed from it will contain ingoing and outgoing radiation in equal amounts. Thus, the total radiation will have no effect on the particle's motion.

## 1.4 Motion of a scalar charge in curved spacetime

The equation of motion of a point particle with scalar charge  $q$  can be derived using the Lagrangian formalism. The system consists of the point particle which is moving along a certain worldline  $\Gamma$  in a background spacetime  $\mathcal{M}$  with metric  $g_{\mu\nu}$ . In its turn, the scalar charge produces a scalar field  $\Phi(x)$  that will interact with the particle. Therefore, the action of the entire system is given by

$$S = S_{\text{field}} + S_{\text{particle}} + S_{\text{interaction}}, \quad (1.9)$$

where  $S_{\text{field}}$  is the action of the free scalar field  $\Phi(x)$ ,  $S_{\text{particle}}$  is the action of the free point particle, and  $S_{\text{interaction}}$  represents the interaction between the particle and the scalar field.

In general  $S$  is a functional of the field  $\Phi$ , the particle's position  $z$  and the spacetime metric  $g_{\mu\nu}$ . To obtain the equations of motion for the particle and for the field, we impose the total action  $S$  to be stationary with respect to the corresponding variations,  $\delta\Phi$  for the field equation, and  $\delta z$  for the particle's equation of motion. This leads to the following equations of motion

$$(\square - \xi R)\Phi(x) = -4\pi q \int_{\Gamma} \delta_4(x, z(\tau)) d\tau, \quad (1.10)$$

$$m(\tau) \frac{Du^\mu}{d\tau} = q(g^{\mu\nu} + u^\mu u^\nu) \nabla_\nu \Phi(z(\tau)), \quad (1.11)$$

$$\frac{dm(\tau)}{d\tau} = -qu^\mu \nabla_\mu \Phi(z(\tau)), \quad (1.12)$$

where  $\tau$  is an affine parameter,  $z(\tau)$  is the particle's worldline,  $u^\mu = \frac{dz^\mu}{d\tau}$ ,  $D/d\tau = u^\mu \nabla_\mu$ . It can be seen that the mass of the particle  $m(\tau)$  is not necessarily constant. This fact implies that the particle can radiate monopole waves. By using the regular two-point function  $G_R(x, x')$ , we construct the regular field  $\Phi_R(x)$ , this field reads to the following gradient

$$\nabla_\mu \Phi_R(x) = -\frac{1}{12}(1 - 6\xi)qRu_\mu + q(g_{\mu\nu} + u_\mu u_\nu) \left( \frac{1}{3}\dot{a}^\nu + \frac{1}{6}R^\nu{}_\lambda u^\lambda \right) + \Phi_\mu^{\text{tail}}(x), \quad (1.13)$$

$$\Phi_\mu^{\text{tail}}(x) = q \int_{-\infty}^{\tau^-} \nabla_\mu G_{\text{ret}}(x, z(\tau')) d\tau', \quad (1.14)$$

where  $a^\mu$  is the covariant four-acceleration, an overdot indicates differentiation with respect to  $\tau$  and  $R_{\mu\nu}$  is the Ricci curvature. We denote the integral in Eq. (1.14) by tail integral. Note that this integral has to be evaluated along the particle's entire past. The equations of motion for the particle are then given by [5]

$$m(\tau)a^\mu = f_{\text{ext}}^\mu + q^2(\delta_\nu^\mu + u^\mu u_\nu) \left[ \frac{1}{3m} \frac{Df_{\text{ext}}^\nu}{d\tau} + \frac{1}{6}R^\nu{}_\lambda u^\lambda + \int_{-\infty}^{\tau^-} \nabla^\nu G_{\text{ret}}(z(\tau), z(\tau')) d\tau' \right], \quad (1.15)$$

$$\frac{dm(\tau)}{d\tau} = -\frac{1}{12}(1 - 6\xi)q^2R - q^2u^\mu \int_{-\infty}^{\tau^-} \nabla_\mu G_{\text{ret}}(z(\tau), z(\tau')) d\tau', \quad (1.16)$$

where  $f_{\text{ext}}^\mu$  is an external force. In order to solve these equations we first need to evaluate the tail integral and before that, we have to calculate the retarded GF. Therefore, the self-consistent evolution for the scalar charge can be reduced to the calculation of  $G_{\text{ret}}(x, x')$ , the scalar retarded GF.

## 1.5 Motion of a point mass in curved spacetime

In order to derive the equations of motion for a massive particle in curved spacetime, we now have to calculate the gravitational field produced by this particle. A standard procedure to simplify the problem constrains the particle's mass  $m$  to be small so that its gravitational field can be treated as a perturbation on a background metric. In this way, the exact metric of the perturbed spacetime will be the sum of a *background* (independent of  $m$ ) part  $g_{\mu\nu}$  and a *perturbation* part  $h_{\mu\nu}$ . To perform this decomposition we write the perturbed spacetime metric in the following way

$$\mathfrak{g}_{\mu\nu} = g_{\mu\nu} + h_{\mu\nu}, \quad (1.17)$$

where we are establishing a **sans-serif** font to denote tensors related to the perturbed spacetime and regular symbols for tensors related to the background spacetime. Additionally we will denote by  $;\mu$  the covariant derivative with respect to the background metric  $g_{\mu\nu}$  and  $\nabla_\mu$  for the covariant derivative with respect to the perturbed metric  $\mathfrak{g}_{\mu\nu}$ . The exact Einstein tensor is then given by

$$\mathbf{G}^{\mu\nu} = G^{\mu\nu}[g] + \delta G^{\mu\nu}[g, h] + \Delta G^{\mu\nu}[g, h], \quad (1.18)$$

where  $G^{\mu\nu}$  denotes the Einstein tensor of the background spacetime and we assume that it vanishes,  $\delta G^{\mu\nu}[g, h]$  contains the linearized Einstein operator

$$\delta G^{\mu\nu} \equiv \frac{1}{2} \left( g^{\alpha\beta} \gamma^{\mu\nu}{}_{;\alpha\beta} + 2R_{\alpha}{}^{\mu}{}_{\beta}{}^{\nu} \gamma^{\alpha\beta} \right) + \frac{1}{2} \left( \gamma^{\mu\alpha}{}_{;\alpha}{}^{\nu} + \gamma^{\nu\alpha}{}_{;\alpha}{}^{\mu} - g^{\mu\nu} \gamma^{\alpha\beta}{}_{;\alpha\beta} \right), \quad (1.19)$$

where  $\gamma^{\mu\nu}$  is the trace-reversed metric perturbation

$$\gamma^{\mu\nu} \equiv h^{\mu\nu} - \frac{1}{2} g^{\mu\nu} g_{\alpha\beta} h^{\alpha\beta}.$$

The last term in the right hand side of Eq. (1.18) is simply the remaining non-linear terms. After re-writing  $\mathbf{G}^{\mu\nu}$  in a more convenient way, the exact Einstein field equations may be written as

$$\delta G^{\mu\nu} = 8\pi \left( \mathbf{T}^{\mu\nu} - \frac{1}{8\pi} \Delta G^{\mu\nu} \right) \equiv 8\pi T_{\text{eff}}^{\mu\nu}, \quad (1.20)$$

where  $\mathbf{T}^{\mu\nu}$  is the energy-momentum tensor of the perturbed spacetime. This equation provides the exact content of the Einstein field equation and it is written in such a



way that the left-hand side only contains linear terms in the metric perturbation. Thus, obtaining the field equation for  $\gamma^{\mu\nu}$  reduces to solving Eq. (1.20) with an effective source  $T_{\text{eff}}^{\mu\nu}$ . However, this equation is neither hyperbolic nor elliptic and that makes it difficult to properly obtain the retarded solutions for  $\gamma^{\mu\nu}$ . By choosing an appropriate gauge condition we are able to transform Eq. (1.20) into a hyperbolic equation. This gauge turns out to be the *Lorenz gauge condition*, i.e.,

$$\gamma^{\mu\nu}{}_{;\nu} = 0. \quad (1.21)$$

With this constraint the field equations reduce to

$$\square\gamma^{\mu\nu} + 2R_{\alpha}{}^{\mu}{}_{\beta}{}^{\nu}\gamma^{\alpha\beta} = 16\pi T_{\text{eff}}^{\mu\nu}, \quad (1.22)$$

and a retarded solution to this equation may be written in terms of the so-called retarded Green function

$$\gamma^{\mu\nu} = 4 \int_{\mathcal{M}} G_{\text{ret}}{}^{\mu\nu}{}_{\mu'\nu'}(x, x') T_{\text{eff}}^{\mu'\nu'}(x') \sqrt{-g'} d^4x', \quad (1.23)$$

where  $G_{\text{ret}}{}^{\mu\nu}{}_{\mu'\nu'}(x, x')$  is the retarded gravitational GF [5] of Eq. (1.22) and the integral covers the entire spacetime  $\mathcal{M}$ .

In order to integrate Eq. (1.22) we follow a standard technique based on the perturbative nature of  $m$  and  $h_{\mu\nu}$ . We consider  $m$  as an expansion parameter<sup>1</sup> and solve the field equation iteratively. In the first iteration we fix the particle's worldline  $\Gamma$  and set  $h_0^{\mu\nu}$  (the zero-order of  $h_{\mu\nu}$ ) to zero in  $T_{\text{eff}}^{\mu\nu}$ . The result from this step returns the first-order approximation  $h_1^{\mu\nu}[\Gamma] = \mathcal{O}(m)$ . During the next iteration  $h_1^{\mu\nu}$  is included in  $T_{\text{eff}}^{\mu\nu}$  so that Eq. (1.22) now returns the second-order approximation  $h_2^{\mu\nu}[\Gamma] = \mathcal{O}(m, m^2)$ . We repeat this iterative procedure until we obtain an accurate approximation to  $h_{\mu\nu}$ . Now that a prescription for solving the field equation is established, we formulate the equation of motion for the point particle. Given the action for a point particle moving along a worldline  $\Gamma$  with tangent vector  $\dot{z}^\mu = dz^\mu/d\lambda$  (where  $\lambda$  is an arbitrary parameter)

$$S_{\text{particle}} = -m \int_{\Gamma} \sqrt{-\mathbf{g}_{\mu\nu} \dot{z}^\nu \dot{z}^\mu} d\lambda, \quad (1.24)$$

<sup>1</sup>This assumption should be taken carefully. By expansion in  $m$  we are trying to indicate that from a perturbative point of view, linear terms in  $m$  are considered first order corrections to  $h_{\mu\nu}$ . Consequently, the background metric  $g_{\mu\nu}$  is kept fixed in the following calculations.

we are able to derive the equation of motion:

$$\frac{D\dot{z}^\alpha}{d\lambda} = \frac{1}{\sqrt{-\mathbf{g}_{\mu\nu}\dot{z}^\mu\dot{z}^\nu}} \left( \frac{d}{d\lambda} \sqrt{-\mathbf{g}_{\mu\nu}\dot{z}^\mu\dot{z}^\nu} \right) \dot{z}^\alpha, \quad (1.25)$$

where  $\frac{D}{d\lambda} = \dot{z}^\mu \nabla_\mu$ . In the background spacetime this equation of motion can be easily re-written considering Eq. (1.48) and

$$C^\alpha{}_{\beta\gamma} \equiv \Gamma^\alpha_{\beta\gamma} - \Gamma^\alpha_{\beta\gamma}, \quad (1.26)$$

the exact difference between the perturbed metric connection  $\Gamma^\alpha_{\beta\gamma}$ , and the background metric connection  $\Gamma^\alpha_{\beta\gamma}$ . The equation of motion in the background spacetime is then given by

$$\frac{Du^\alpha}{d\tau} = -C^\alpha_{\mu\nu} u^\mu u^\nu + \frac{1}{\sqrt{1 - h_{\mu\nu} u^\mu u^\nu}} \left( \frac{d}{d\tau} \sqrt{1 - h_{\mu\nu} u^\mu u^\nu} \right) u^\alpha, \quad (1.27)$$

where we replaced  $\lambda$  by the particle's proper time  $\tau$  and  $u^\alpha = dz^\alpha/d\tau$  is the four-velocity in the background spacetime.

As detailed above, the approach we are taking to calculate  $h_{\mu\nu}$  is an iterative procedure. For this purpose the equation of motion expressed as in Eq. (1.27) is not useful and we have to re-write it having in mind the perturbative nature of the particle. On the first iteration, the equation of motion is given by [5]

$$\frac{Du^\mu}{d\tau} = -\frac{1}{2} (g^{\mu\nu} + u^\mu u^\nu) (2h_{\nu\lambda;\rho} - h_{\lambda\rho;\nu}) u^\lambda u^\rho + \mathcal{O}(m^2). \quad (1.28)$$

Similar to the scalar case, we regularise the metric perturbation  $h_{\mu\nu}$  before solving the equation of motion. Following the same approach as in the scalar case, the regular metric perturbation  $h_{\mu\nu}^R$  leads to the regular  $h_{\mu\nu;\lambda}$

$$h_{\mu\nu;\lambda}^R = -4m \left( u_{(\mu} R_{\nu)\rho\lambda\xi} + R_{\mu\rho\nu\xi} u_\lambda \right) u^\rho u^\xi + h_{\mu\nu;\lambda}^{\text{tail}}, \quad (1.29)$$

$$h_{\mu\nu;\lambda}^{\text{tail}} = 4m \int_{-\infty}^{\tau^-} \nabla_\lambda \left( G^{\text{ret}}{}_{\mu\nu\mu'\nu'} - \frac{1}{2} g_{\mu\nu} g^{\alpha\beta} G^{\text{ret}}{}_{\alpha\beta\mu'\nu'} \right) (z(\tau), z(\tau')) u^{\mu'} u^{\nu'} d\tau', \quad (1.30)$$

where  $G^{\text{ret}}{}_{\mu\nu\mu'\nu'}$  is the retarded GF of Eq. (1.22). In this gravitational case we denote the integral in Eq. (1.30) by tail integral.

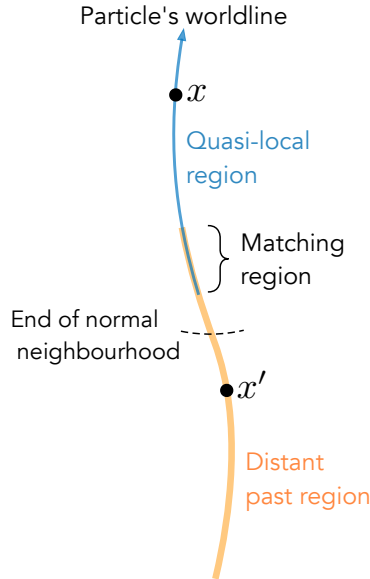


Figure 1 – The method of matched expansion for a particle in curved spacetime. The blue section of the particle’s worldline denotes the QL region of  $x$ , the particle’s current position. A point  $x'$  is in the distant past of  $x$  when it lies on the orange section of the particle’s worldline.

## 1.6 Method of matched expansions for the tail integral

Anderson and Wiseman [31] proposed the so-called method of matched expansions for evaluating the tail integral in Eq. (1.14)<sup>2</sup>. This method essentially consists of splitting the integral in two regions. The first region corresponds to points  $x$  and  $x' = z(\tau')$  that are “close” and it is called the quasi-local (QL) region. The second region corresponds to points  $x$  and  $x' = z(\tau')$  that are not “close” and it is called distant past (DP). For instance, for  $G_{\text{ret}}$  the tail integral is

$$\int_{-\infty}^{\tau^-} \nabla_{\mu} G_{\text{ret}}(x, z(\tau')) d\tau' = \underbrace{\int_{-\infty}^{\tau_m} \nabla_{\mu} G_{\text{ret}}(x, z(\tau')) d\tau'}_{\text{DP region}} + \underbrace{\int_{\tau_m}^{\tau^-} \nabla_{\mu} G_{\text{ret}}(x, z(\tau')) d\tau'}_{\text{QL region}}, \quad (1.31)$$

where  $\tau_m < \tau^-$  is the matching (proper) time such that  $z(\tau_m) \in \text{DP} \cap \text{QL}$ . Therefore, in order for this method to work, we need to ensure that there is an overlap between the QL and the DP regions.

In Fig. 1 we illustrate these two regions. In each region we provide two different approaches for calculating  $G_{\text{ret}}(x, x')$ . The retarded GF is evaluated using different expansions in these two regions and one would expect to have a matching region where both expansions agree to sufficient accuracy.

<sup>2</sup>This method was originally derived for the spin-0 case but it can also be applied to general spin.

In order to provide a suitable expansion in each region, in [31] Anderson and Wiseman used the Hadamard form of  $G_{\text{ret}}(x, x')$  [32, 33, 5] to calculate the tail integral in the QL region. In fact, the QL region is a subregion of a more general region called normal neighbourhood. A normal neighbourhood of  $x$ ,  $\mathcal{N}(x)$ , is a region containing  $x$  such that every  $x'$  in that region is connected to  $x$  by a unique geodesic which lies within the region.

Given a field point  $x$  and a base point  $x' \in \mathcal{N}(x)$ , the Hadamard form of  ${}_sG_{\text{ret}}(x, x')$  is given by

$$G_{\text{ret}}(x, x') = \mathcal{U}(x, x')\delta(\sigma)\theta_+(x, x') - \mathcal{V}(x, x')\theta(-\sigma)\theta_+(x, x'), \quad (1.32)$$

where  $\delta(\sigma)$  is the Dirac delta distribution,  $\mathcal{U}(x, x')$  and  $\mathcal{V}(x, x')$  are two regular biscalars<sup>3</sup>,  $\theta_+(x, x')$  is a Heaviside-like distribution and equals 1 if  $x$  lies in the future of  $x'$  and equals 0 elsewhere, the biscalar  $\sigma = \sigma(x, x')$  is Synge's world function and is equal to half of the squared distance along the geodesic<sup>4</sup> connecting  $x$  and  $x'$ , i.e.,

$$\sigma(x, x') = \frac{1}{2}(\tau_1 - \tau_0) \int_{\tau_0}^{\tau_1} g_{\mu\nu}(z(\tau))t^\mu t^\nu d\tau, \quad (1.33)$$

where  $t^\mu = t^\mu(\tau) = \frac{dz^\mu(\tau)}{d\tau}$  is a vector tangent to the geodesic  $z(\tau)$ , and  $\tau_0$  ( $\tau_1$ ) is the proper time where  $z(\tau_0) = x'$  ( $z(\tau_1) = x$ ).

We usually refer to  $\mathcal{U}(x, x')\delta(\sigma)\theta_+(x, x')$  as the direct-part of  $G_{\text{ret}}(x, x')$  and  $G_{\text{ret}}(x, x') - \mathcal{U}(x, x')\delta(\sigma)\theta_+(x, x')$  as the non-direct part. In this way, we can set  $G_{\text{ret}}(x, x') = -\mathcal{V}(x, x')$  in the QL region and rewrite the second integral in the right hand side of Eq. (1.31) as [31]

$$\int_{\tau_m}^{\tau^-} \nabla_\mu G_{\text{ret}}(x, z(\tau')) d\tau' = - \int_{\tau_m}^{\tau} \nabla_\mu \mathcal{V}(x, z(\tau')) d\tau'. \quad (1.34)$$

The upper limit in the integral can be changed to  $\tau$  since  $\mathcal{V}(x, x')$  is regular at coincidence.

In the DP region the Hadamard form is no longer valid and we require a different expansion for  $G_{\text{ret}}(x, x')$ . For instance, in spacetimes with spherical and axial symmetry we can perform a decomposition in spin-weighted spherical harmonics. We develop further this decomposition in following chapters.

<sup>3</sup>A biscalar is a function that depends on two spacetime points,  $x$  and  $x'$ .

<sup>4</sup>This geodesic must be unique in order for  $\sigma$  to be defined.

## 1.7 Black hole spacetimes

Astrophysical observations suggest that most astrophysical systems (e.g., binary systems) might involve compact objects with axial symmetry. In scenarios where the angular momentum of the compact object is negligible, we can consider the system to have spherical symmetry. Having this in mind, we focus our attention on two well-known black hole spacetimes: Schwarzschild and Kerr spacetime.

### 1.7.1 Schwarzschild spacetime

The Schwarzschild spacetime (a vacuum solution to Einstein's field equations) is a black hole spacetime with spherical symmetry. Its line element in the standard Schwarzschild coordinates  $(t, r, \theta, \phi)$ <sup>5</sup> is given by

$$ds^2 = g_{\mu\nu} dx^\mu dx^\nu = -f dt^2 + f^{-1} dr^2 + r^2 (d\theta^2 + \sin^2 \theta d\phi^2), \quad (1.35)$$

where  $f = f(r) = 1 - 2M/r$  and  $M$  is the mass of the black hole and  $g_{\mu\nu}$  denotes the Schwarzschild metric. We should emphasize that we will not explore how field perturbations behave inside the event horizon. We are mostly interested in a region outside the black hole's event horizon. Therefore, the metric defined via Eq. (1.35) is sufficient for further calculations. Additionally, for analyses requiring calculations near the event horizon, it is worth introducing the tortoise coordinate

$$r_* = r + 2M \ln \left( \frac{r}{M} - 2 \right), \quad (1.36)$$

which ranges from  $-\infty$  to  $\infty$ .

From a geometrical point of view, the Schwarzschild metric admits the conformal transformation

$$d\hat{s}^2 = r^{-2} ds^2 = -\frac{f}{r^2} (dt^2 - dr_*^2) + d\theta^2 + \sin^2 \theta d\phi^2, \quad (1.37)$$

where we used Eq. (1.36) to obtain  $dr = f dr_*$ . The conformal metric defined via the line element  $d\hat{s}$  in Eq. (1.37) is a product of the 2-sphere  $\mathbb{S}^2$  with a spacetime  $\mathcal{M}_2$ . The line

<sup>5</sup>The range for each coordinate is  $t \in (-\infty, \infty)$ ,  $r \in (2M, \infty)$ ,  $\theta \in [0, \pi]$  and  $\phi \in [0, 2\pi)$ .

element in  $\mathcal{M}_2$  (denoted by  $d\hat{s}_2$ ) in the  $(t, r_*)$  coordinates is given by

$$d\hat{s}_2^2 = -\frac{f}{r^2}(dt^2 - dr_*^2). \quad (1.38)$$

As we shall see in Chapter 2, this conformal transformation becomes useful since the resulting spacetime (with geometry  $\mathcal{M}_2 \times \mathbb{S}^2$ ) allows us to obtain fundamental quantities in Schwarzschild spacetime from quantities defined in  $\mathcal{M}_2$  and  $\mathbb{S}^2$ .

In order to calculate the geodesics in Schwarzschild spacetime, there are different approaches one can follow. The most common one is based on the Lagrangian formalism. In this formalism geodesics in Schwarzschild spacetime are derived from the Lagrangian [34]

$$\mathcal{L} = \frac{1}{2}g_{\mu\nu} \frac{dx^\mu}{ds} \frac{dx^\nu}{ds}, \quad (1.39)$$

where  $s$  is an affine parameter (usually the geodesic's proper time),  $\mathcal{L}$  equals to 0 for null geodesics and 1 for timelike geodesics. We then take this Lagrangian and insert into Lagrange's equations

$$\frac{d}{ds} \left( \frac{\partial \mathcal{L}}{\partial \dot{x}^\mu} \right) = \frac{\partial \mathcal{L}}{\partial x^\mu}, \quad (1.40)$$

where the overdot indicates differentiation with respect to  $s$ . From this equations we immediately find that

$$\frac{d}{ds} (ft) = 0, \quad \frac{d}{ds} (r^2 \sin^2 \theta \dot{\phi}) = 0, \quad (1.41)$$

which lead to the two constants of motion  $E$  (particle's energy) and  $L$  (Particle's angular momentum). Furthermore, the spherical symmetry allows us to set  $\theta = \frac{\pi}{2}$  and  $\dot{\theta} = 0$  without losing generality. Having this in mind the geodesic equations are then given by

$$\dot{t} = \frac{E}{f}, \quad (1.42)$$

$$\dot{r}^2 = E^2 - f(r) \left( \kappa + \frac{L^2}{r^2} \right), \quad (1.43)$$

$$\dot{\phi} = \frac{L}{r^2}, \quad (1.44)$$

where

$$\kappa = \begin{cases} 0, & \text{for null geodesics,} \\ 1, & \text{for timelike geodesics} \end{cases}.$$

In particular, Eq. (1.43) puts in evidence the existence of circular geodesics. In this case the equation for  $r$  reduces to  $\dot{r} = 0$  and we find the condition

$$E^2 = f(r_{\text{circ}}) \left( \kappa + \frac{L^2}{r_{\text{circ}}^2} \right),$$

where  $r_{\text{circ}}$  is the orbit radius.

For null geodesics ( $\kappa = 0$ ), we find the unstable circular orbit at  $r = 3M$ . On the other hand, for timelike geodesics, depending on the energy and angular momentum, we have not only circular but also eccentric geodesics. It can also be shown that the innermost circular orbit (ISCO) for timelike geodesics is  $r = r_{\text{ISCO}} = 6M$ .

## 1.7.2 Kerr spacetime

The Kerr spacetime describes a rotating black hole which is known for having axial symmetry. In Boyer-Lindquist coordinates, the Kerr geometry can be described via the line element

$$\begin{aligned} ds^2 = & - \left( 1 - \frac{2Mr}{\Sigma} \right) dt^2 - \frac{4aMr \sin^2 \theta}{\Sigma} dt d\theta + \frac{\Sigma}{\Delta_K} dr^2 + \Sigma d\theta^2 \\ & + \left( \Delta_K + \frac{2Mr(r^2 + a^2)}{\Sigma} \right) \sin^2 \theta d\phi^2, \end{aligned} \quad (1.45)$$

where  $M$  is the mass of the black hole,  $a$  is the angular momentum per unit mass and

$$\Sigma = r^2 + a^2 \cos^2 \theta, \quad (1.46)$$

$$\Delta_K = r(r - 2M) + a^2. \quad (1.47)$$

It can be shown that Schwarzschild spacetime is a particular case of Kerr spacetime where  $a = 0$ . Unlike Schwarzschild spacetime where geodesics can always be constrained to a plane with fixed  $\theta$ , in Kerr spacetime this is no longer the case. In fact, in addition to the two constants of motion ( $E$  and  $L$ ), we find a third one usually referred to as the Carter constant [35].

## 1.8 Gravitational perturbations of Schwarzschild spacetime

In the literature we find a handful of formalisms for describing field perturbations. Regge and Wheeler [36] came up with the first approach for obtaining the equation of motion for a gravitational perturbation in a background spacetime. Later on, works from Vishveshwara [37] and Zerilli [38] also brought fundamental results for understanding gravitational perturbations. In this Section we provide a review about the field equations governing gravitational perturbations of Schwarzschild spacetime.

In order to derive the field equations for a gravitational perturbation in Schwarzschild spacetime, we follow a standard procedure consisting of decomposing the perturbed metric  $\mathfrak{g}_{\mu\nu}$  as

$$\mathfrak{g}_{\mu\nu} = g_{\mu\nu} + h_{\mu\nu}, \quad (1.48)$$

where  $g_{\mu\nu}$  is the (background) Schwarzschild metric and  $h_{\mu\nu}$  is the metric perturbation. Inserting  $\mathfrak{g}_{\mu\nu}$  back into the vacuum Einstein's field equation yields

$$R_{\mu\nu} + \delta R_{\mu\nu} = 0, \quad (1.49)$$

where we grouped all the first order terms involving  $h_{\mu\nu}$  in  $\delta R_{\mu\nu}$  and  $R_{\mu\nu}$  is the Schwarzschild Ricci tensor. Since  $R_{\mu\nu} = 0$  for Schwarzschild spacetime, the field perturbation equations is simply

$$\delta R_{\mu\nu} = 0. \quad (1.50)$$

More specifically, we follow [39] to obtain (here the selection of a gauge has not been made yet)

$$\delta R_{\mu\nu} = -\delta\Gamma_{\mu\nu}{}^{\beta}{}_{;\beta} + \delta\Gamma_{\mu\beta}{}^{\beta}{}_{;\nu}, \quad (1.51)$$

$$\delta\Gamma_{\mu\nu}{}^{\rho} = \frac{1}{2}g^{\rho\alpha}(h_{\mu\alpha;\nu} + h_{\nu\alpha;\mu} - h_{\mu\nu;\alpha}), \quad (1.52)$$

where the the semicolons denote covariant differentiation with respect to the background metric. The boundary conditions for  $h_{\mu\nu}$  are typically placed at infinity and at the event horizon. These conditions are chosen such that solutions to Eq. (1.50) are physical. More specifically, the boundary conditions we impose are outgoing waves at infinity and ingoing waves at the event horizon.



### 1.8.1 Even and odd parity field perturbations

In order to simplify the field equations for the metric perturbation, we propose a mode decomposition, i.e.,

$$h_{\mu\nu}(t, r, \theta, \phi) = \sum_{\ell=0}^{\infty} \sum_{m=-\ell}^{\ell} h_{\mu\nu}^{(\ell m)}(t, r, \theta, \phi), \quad (1.53)$$

where  $h_{\mu\nu}^{(\ell m)}(t, r, \theta, \phi)$  are functions characterized by parities  $(-1)^{\ell+1}$  (odd) and  $(-1)^{\ell}$  (even), and they take the form [36]

$$h_{\mu\nu}^{(\ell m)} = \begin{pmatrix} 0 & 0 & -h_0 \frac{1}{\sin \theta} \partial_{\phi} & h_0 \sin \theta \partial_{\theta} \\ 0 & 0 & -h_1 \frac{1}{\sin \theta} \partial_{\phi} & h_1 \sin \theta \partial_{\theta} \\ \text{sym} & \text{sym} & h_2 \left( \frac{1}{\sin \theta} \partial_{\theta} \partial_{\phi} - \frac{\cos \theta}{\sin^2 \theta} \partial_{\phi} \right) & \frac{1}{2} h_2 \left( \frac{1}{\sin \theta} \partial_{\phi}^2 + \cos \theta \partial_{\theta} - \sin \theta \partial_{\theta}^2 \right) \\ \text{sym} & \text{sym} & \text{sym} & -h_2 (\sin \theta \partial_{\theta} \partial_{\phi} - \cos \theta \partial_{\phi}) \end{pmatrix} Y_{\ell m}, \quad (1.54)$$

(where  $Y_{\ell m}$  are the spherical harmonics) for odd-parity and

$$h_{\mu\nu}^{(\ell m)} = \begin{pmatrix} f H_0 & H_1 & h_0 \partial_{\theta} & h_0 \partial_{\phi} \\ \text{sym} & \frac{H_2}{f} & h_1 \partial_{\theta} & h_1 \partial_{\phi} \\ \text{sym} & \text{sym} & r^2 (K + G \partial_{\theta}^2) & r^2 G \left( \partial_{\theta} \partial_{\phi} - \frac{\cos \theta}{\sin \theta} \partial_{\phi} \right) \\ \text{sym} & \text{sym} & \text{sym} & r^2 \left( K \sin^2 \theta + G (\partial_{\phi}^2 + \sin \theta \cos \theta \partial_{\theta}) \right) \end{pmatrix} Y_{\ell m}, \quad (1.55)$$

for even-parity. Here the ‘‘sym’’ text refers to a component of  $h_{\mu\nu}^{(\ell m)}$  that is calculated using the symmetry  $h_{\mu\nu}^{(\ell m)} = h_{\nu\mu}^{(\ell m)}$  and the functions  $h_0, h_1, h_2, H_0, H_1, H_2, K$  and  $G$  are functions of  $t$  and  $r$  to be determined.

### 1.8.2 Gauge transformation for $h_{\mu\nu}^{(\ell m)}$

Although the modes of the metric perturbation given in Eqs. (1.55)–(1.54) simplify the field equations to some extent, there are still six functions to calculate. We reduce these functions by introducing a gauge transformation

$$h_{\mu\nu}^{(\ell m)} \rightarrow h_{\mu\nu}^{(\ell m)} + \xi_{\mu;\nu} + \xi_{\nu;\mu}, \quad (1.56)$$

where  $\xi^{\mu}$  is a gauge vector. By choosing appropriate values for  $\xi^{\mu}$ , we are able to cancel some of the components in  $h_{\mu\nu}^{(\ell m)}$ .

### 1.8.3 Odd-parity perturbations in the Regge-Wheeler gauge

For odd-parity perturbations, the gauge vector takes the form [36]

$$\xi^\mu = \Lambda(t, r) \left( 0, 0, \epsilon^{\theta A} \partial_A Y_{\ell m}, \epsilon^{\phi A} \partial_A Y_{\ell m} \right), \quad (1.57)$$

where  $A = \theta, \phi$ ,  $\epsilon^{\mu\nu}$  is the Levi-Civita symbol, and  $\Lambda(t, r)$  is an arbitrary function chosen such that it annuls the  $h_2$  factor in Eq. (1.54)<sup>6</sup>.

By applying a gauge transformation on  $h_{\mu\nu}^{(\ell m)}$  with the gauge vector given in Eq. (1.57), the modes for odd-parity perturbations reduce to

$$h_{\mu\nu}^{(\ell m)} = \begin{pmatrix} 0 & 0 & -h_0 \frac{1}{\sin\theta} \partial_\phi & h_0 \sin\theta \partial_\theta \\ 0 & 0 & -h_1 \frac{1}{\sin\theta} \partial_\phi & h_1 \sin\theta \partial_\theta \\ \text{sym} & \text{sym} & 0 & 0 \\ \text{sym} & \text{sym} & 0 & 0 \end{pmatrix} Y_{\ell m}. \quad (1.58)$$

This gauge transformation is often referred to as the Regge-Wheeler gauge which was first introduced in [36].

Without loss of generality we can perform a rotation on  $h_{\mu\nu}^{(\ell m)}$  due to the spherical symmetry of the spacetime. Particularly, so that  $h_{\mu\nu}$  has no  $\phi$ -dependence and there is no contribution from  $m \neq 0$  modes:

$$h_{\mu\nu} = \sum_{\ell=0}^{\infty} h_{\mu\nu}^{(\ell)}, \quad (1.59)$$

where (redefining  $h_0$  and  $h_1$  so as to absorb an  $\ell$ -dependent constant factor coming from  $Y_{\ell m}$ )

$$h_{\mu\nu}^{(\ell)} = \begin{pmatrix} 0 & 0 & 0 & h_0(t, r) \\ 0 & 0 & 0 & h_1(t, r) \\ 0 & 0 & 0 & 0 \\ h_0(t, r) & h_1(t, r) & 0 & 0 \end{pmatrix} \times \sin\theta \partial_\theta P_\ell(\cos\theta). \quad (1.60)$$

An important consequence arises when we work with  $h_{\mu\nu}^{(\ell)}$  instead of  $h_{\mu\nu}^{(\ell m)}$ . After performing the rotation, we immediately note that  $h_{\mu\nu}^{(0)} = 0$ . Therefore, this mode (responsible for producing changes in the mass  $M$  of the black hole) cannot be computed from  $h_{\mu\nu}^{(\ell)}$ .

<sup>6</sup>For even-parity perturbations, we could also provide another gauge vector to annul some components in Eq. (1.55).

We should also treat the  $\ell = 1$  case separately. When inserting Eq. (1.60) back into Eq. (1.50), we find only two non-vanishing Ricci tensor components,  $\delta R_{r\phi}$  and  $\delta R_{t\phi}$ . These two components yield

$$\delta R_{r\phi} = \partial_t \left[ \partial_t h_1 - r^2 \partial_r \left( \frac{h_0}{r^2} \right) \right], \quad (1.61)$$

$$\delta R_{t\phi} = r^2 \partial_r^2 h_0 - 2h_0 - \partial_r (r^2 \partial_t h_1). \quad (1.62)$$

When imposing  $\delta R_{r\phi} = 0$  and  $\delta R_{t\phi} = 0$  in the above equations, substituting Eq. (1.61) in Eq. (1.62) shows that  $\delta R_{t\phi}$  vanishes identically. Thus, we end up with a single partial differential equation for two unknown variables,  $h_0$  and  $h_1$ . Consequently, similar to the  $\ell = 0$  mode, the  $\ell = 1$  mode cannot be calculated in the Regge-Wheeler gauge.

For  $\ell \geq 2$ , we find the differential equations

$$\partial_t h_0 = f \partial_r (f h_1), \quad \text{from: } \delta R_{\theta\phi}, \quad (1.63)$$

$$-\partial_t^2 h_1 + \partial_r \partial_t h_0 - \frac{2}{r} \partial_t h_0 = \frac{\ell(\ell+1) - 2}{r^2} f h_1, \quad \text{from: } \delta R_{r\phi}, \quad (1.64)$$

$$-\partial_r^2 h_0 + \partial_r \partial_t h_1 + \frac{2}{r} \partial_t h_1 = -\frac{r\ell(\ell+1) - 4M}{r^3 f} h_0, \quad \text{from: } \delta R_{t\phi}, \quad (1.65)$$

where the last equation is a direct consequence from the first two. By combining Eqs. (1.63)–(1.64) and defining

$$Q(t, r) \equiv \frac{r}{f} h_1(t, r), \quad (1.66)$$

we obtain the so-called Regge-Wheeler equation in (1+1)-dimensions

$$\left[ -\partial_t^2 + f \partial_r f \partial_r - f \left( \frac{\ell(\ell+1)}{r^2} - \frac{6M}{r^3} \right) \right] Q(t, r) = 0. \quad (1.67)$$

By decomposing  $Q(t, r)$  in its Fourier modes  $\tilde{Q}(r)$ :

$$Q(t, r) = \frac{1}{2\pi} \int_{-\infty}^{\infty} \tilde{Q}(r) e^{-i\omega t} d\omega, \quad (1.68)$$

we obtain the radial Regge-Wheeler equation for gravitational perturbations [36]

$$\left[ f \frac{d}{dr} f \frac{d}{dr} + \omega^2 - f \left( \frac{\ell(\ell+1)}{r^2} - \frac{6M}{r^3} \right) \right] \tilde{Q}(r) = 0, \quad (1.69)$$

which was first derived by Regge and Wheeler back in 1957.

Once  $Q$  is determined, calculating  $h_1$  is immediate from Eq. (1.66). For  $h_0$ , however, we require to solve an additional differential equation which involves  $h_1$  (see Eqs. (1.63) or (1.65)). A more convenient approach for calculating  $h_0$  from  $h_1$  is through their relation in the frequency domain. Specifically, given the Fourier modes  $\tilde{h}_0$  and  $\tilde{h}_1$  of  $h_0$  and  $h_1$ , respectively, the counterpart of Eq. (1.63) in the frequency domain is [36]

$$\tilde{h}_0 = i \frac{f}{\omega} \partial_r (f \tilde{h}_1), \quad (1.70)$$

where  $\omega$  is the frequency and

$$\tilde{h}_a = \int_{-\infty}^{\infty} h_a(t, r) e^{i\omega t} dt, \quad \text{for } a = \{0, 1\}. \quad (1.71)$$

In this way, once  $h_0$  and  $h_1$  are known, reconstructing the metric perturbation, excluding the  $\ell = 0, 1$  modes, is direct. On the other hand, the first modes  $h_{\mu\nu}^{(0,0)}$  and  $h_{\mu\nu}^{(1,m)}$  need to be calculated separately.

Although this approach for calculating  $h_{\mu\nu}$  was first introduced by Regge-Wheeler in [36], in subsequent works, it has been shown that the radial Regge-Wheeler equation can also describe scalar and electromagnetic perturbations. Let  ${}_s\chi$  be a spin- $s$  field describing scalar ( $s = 0$ ), electromagnetic ( $s = 1$ ), and gravitational ( $s = 2$ ) perturbations produced by a source  ${}_sS$ . This field satisfies the partial differential equation [40]

$$\left( \square + s^2 \frac{2M}{r^3} \right) {}_s\chi(t, r, \theta, \phi) = {}_sS(t, r, \theta, \phi). \quad (1.72)$$

It can be shown that when writing  ${}_s\chi$  and  ${}_sS$  as a mode decomposition

$$\begin{aligned} {}_s\chi(t, r, \theta, \phi) &= \sum_{\ell=0}^{\infty} \sum_{m=-\ell}^{\ell} \frac{{}_sX_{\ell m}(t, r)}{r} Y_{\ell m}(\theta, \phi), \\ {}_sS(t, r, \theta, \phi) &= \sum_{\ell=0}^{\infty} \sum_{m=-\ell}^{\ell} \frac{{}_sS_{\ell m}(t, r)}{r} Y_{\ell m}(\theta, \phi), \end{aligned} \quad (1.73)$$

the modes  ${}_sX_{\ell m}(t, r)$  satisfy the differential equation

$$\left[ \frac{\partial^2}{\partial r_*^2} - \frac{\partial^2}{\partial t^2} - f \left( \frac{\ell(\ell+1)}{r^2} + \frac{2M(1-s^2)}{r^3} \right) \right] {}_sX_{\ell m}(t, r) = {}_sS_{\ell m}(t, r). \quad (1.74)$$

where  $\frac{d}{dr_*} = f \frac{d}{dr}$  (which is derived from Eq. (1.36)). In this way, we find that the above equation reduces to Eq. (1.67) for  $s = 2$  implying that  ${}_2X_{\ell m} = Q$  and  ${}_sS_{\ell m} = 0$ .

In a similar manner, Eq. (1.69) is generalised to

$$\left[ \frac{d^2}{dr_*^2} + \omega^2 - f \left( \frac{\ell(\ell+1)}{r^2} + \frac{2M(1-s^2)}{r^3} \right) \right] {}_s\tilde{\chi}_{\omega\ell}(r) = {}_s\tilde{S}_{\omega\ell}, \quad (1.75)$$

where  ${}_s\tilde{\chi}_{\omega\ell}(r)$  and  ${}_s\tilde{S}_{\omega\ell}$  are the Fourier modes of the  $\ell$ -modes of  ${}_s\chi$  and  ${}_sS$ , respectively.

In this way, perturbations of Schwarzschild spacetime can be described by a spin- $s$  field  ${}_s\chi$ . The source  ${}_sS$  is constructed from the actual physical perturbation source. For instance, for scalar perturbations ( $s = 0$ ) produced by a scalar charge, the source  ${}_0S$  is given by (see Eqs. (1.10))

$${}_0S(x) = -4\pi q \int_{\Gamma} \delta_4(x, z(\tau)) d\tau.$$

### 1.8.4 Even-parity perturbations

The gauge vector  $\xi^\mu$  for even parity perturbations is [36]

$$\xi^\mu = \left( M_0(t, r) Y_{\ell m}, M_1(t, r) Y_{\ell m}, M_2(t, r) \partial_\theta Y_{\ell m}, M_2(t, r) \frac{1}{\sin^2 \theta} \partial_\theta Y_{\ell m} \right), \quad (1.76)$$

where  $M_0$ ,  $M_1$ , and  $M_2$  are chosen such that we annul the  $h_0$ ,  $h_1$  and  $G$  functions in Eq. (1.55), i.e.,

$$h_{\mu\nu}^{(\ell m)} = \begin{pmatrix} fH_0 & H_1 & 0 & 0 \\ H_1 & \frac{H_2}{f} & 0 & 0 \\ 0 & 0 & r^2K & 0 \\ 0 & 0 & 0 & r^2K \sin^2 \theta \end{pmatrix} \times Y_{\ell m}. \quad (1.77)$$

Once again, we perform a similar rotation as we did for odd-parity perturbations and obtain

$$h_{\mu\nu}^{(\ell)} = \begin{pmatrix} fH_0 & H_1 & 0 & 0 \\ H_1 & \frac{H_2}{f} & 0 & 0 \\ 0 & 0 & r^2K & 0 \\ 0 & 0 & 0 & r^2K \sin^2 \theta \end{pmatrix} \times P_\ell(\cos \theta). \quad (1.78)$$

We then insert this expression into Eq. (1.50) to obtain the corresponding equations for  $H_0$ ,  $H_1$ ,  $H_2$  and  $K$ . Zerilli in [38] provided a detailed procedure for deriving another

master function  $Z(t, r)$ <sup>7</sup> (similar to  $Q(t, r)$ ) from which one can reconstruct even-parity perturbations. This equation is commonly known as the (homogeneous) Zerilli equation [38] in (1+1)-dimensions

$$\left[ -\partial_t^2 + f\partial_r f\partial_r - f \frac{2\lambda^2(\lambda+1)r^3 + 6\lambda^2 Mr^2 + 18\lambda M^2 r + 18M^3}{r^3(\lambda r + 3M)^2} \right] Z = 0, \quad (1.79)$$

where  $\lambda = \frac{1}{2}(\ell - 1)(\ell + 2)$ . We will not develop further even-parity perturbations in this thesis. Calculating the even-perturbations are necessary if one requires to calculate the metric perturbation in the Regge-Wheeler-Zerilli gauge. However, As we detail in the next section, solutions to the spin-2 Regge-Wheeler equation can be used to obtain the full radiative part of the metric perturbation.

### 1.8.5 Teukolsky formalism and the Teukolsky equation

After Regge and Wheeler introduced their prescription for describing gravitational perturbations [36], years later Teukolsky came up with another formalism for describing scalar, gravitational, electromagnetic, and neutrino-field perturbations of a rotating black hole[41].

The Teukolsky formalism (named after Saul A. Teukolsky) is based on the Newman-Penrose formalism [42]. In this formalism we start defining a null tetrad

$$e_{(a)}{}^\mu = \{l^\mu, n^\mu, m^\mu, m^{\mu*}\}.$$

We then project all tensors onto these tetrad. As a result, we end up with a full set of equations relating  $e_{(a)}{}^\mu$ , the spin coefficients  $\gamma_{(a)(b)(c)}$ <sup>8</sup>, the Weyl tensor  $C_{\mu\nu\alpha\beta}$ , the Ricci tensor, and the scalar curvature.

In particular, for gravitational perturbations, we look at the so-called Weyl-Newman-Penrose scalars (or Weyl-NP scalars). More specifically, these scalars are the projected

<sup>7</sup>The original derivation was done in the frequency domain. However, its generalization in the time domain is direct.

<sup>8</sup>These coefficients are defined via  $\gamma_{(c)(a)(b)} = e_{(c)}{}^\mu e_{(b)}{}^\nu \nabla_\nu e_{(a)\mu}$ .

component of the Weyl tensor. They are given by [43]

$$\psi_0 = C_{\mu\nu\alpha\beta} l^\mu m^\nu l^\alpha m^\beta, \quad (1.80)$$

$$\psi_1 = C_{\mu\nu\alpha\beta} l^\mu n^\nu l^\alpha m^\beta, \quad (1.81)$$

$$\psi_2 = C_{\mu\nu\alpha\beta} l^\mu m^\nu m^{\alpha*} n^\beta, \quad (1.82)$$

$$\psi_3 = C_{\mu\nu\alpha\beta} l^\mu n^\nu m^{\alpha*} n^\beta, \quad (1.83)$$

$$\psi_4 = C_{\mu\nu\alpha\beta} n^\mu m^{\nu*} n^\alpha m^{\beta*}, \quad (1.84)$$

These five complex-valued scalars encode the 10 out of the 20 components of the Riemann tensor<sup>9</sup>. In the Teukolsky formalism,  $e_{(a)}^\mu$  are the so-called Kinnersley tetrad. For Schwarzschild spacetime, they are given by

$$e_{(1)}^\mu = l^\mu = (f^{-1}, 1, 0, 0), \quad (1.85)$$

$$e_{(2)}^\mu = n^\mu = \left(\frac{1}{2}, -\frac{1}{2}f, 0, 0\right), \quad (1.86)$$

$$e_{(3)}^\mu = m^\mu = \left(0, 0, \frac{1}{\sqrt{2}r}, \frac{i \csc \theta}{\sqrt{2}r}\right), \quad (1.87)$$

$$e_{(4)}^\mu = m^{\mu*} = \left(0, 0, \frac{1}{\sqrt{2}r}, -\frac{i \csc \theta}{\sqrt{2}r}\right). \quad (1.88)$$

With this tetrad choice, the only non-vanishing Weyl-NP scalar is  $\psi_2 = -M/r^3$ .

For gravitational perturbations, the scalars of interest are  $\psi_0$  and  $\psi_4$  since a perturbation of these scalars returns the radiative components of the metric perturbation. More specifically, we decompose the scalars  $\psi_0$  and  $\psi_4$  into a background part (identified by an  $A$  superscript) and a perturbation part (identified by a  $B$  superscript), i.e.,

$$\psi_0 = \psi_0^A + \psi_0^B, \quad \psi_4 = \psi_4^A + \psi_4^B. \quad (1.89)$$

Since  $\psi_0^A = \psi_4^A = 0$  for Schwarzschild spacetime, we can drop the labels in  $\psi_0^B$  and  $\psi_4^B$  and use  $\psi_0$  and  $\psi_4$  as the actual (gravitational) field perturbations of the black hole. Teukolsky found out that the equations satisfied by  $\psi_0$  and  $\psi_4$  can be decoupled and derived from a single *master* function. This master function turned out to be a spin- $s$  field which, unlike

<sup>9</sup>The remaining 10 components (contained in the Ricci tensor) do not play a significant role in the following calculations. Moreover, we pay more attention to  $\psi_0$  and  $\psi_4$  since they are the ones containing information about the radiative part of the metric perturbation.

the spin of  ${}_s\chi$  in Eq. (1.72), it can take negative and fractional values as well [41], i.e.,  $s = 0, \pm\frac{1}{2}, \pm 1, \pm 2$ . Let  ${}_s\Psi$  be this master function. In particular, we have [41]

$${}_0\Psi = {}_0\chi, \quad (1.90)$$

$${}_2\Psi = \psi_0, \quad (1.91)$$

$${}_{-2}\Psi = r^4\psi_4, \quad (1.92)$$

and for the remaining cases  $s = \pm 1$  and  $s = \pm\frac{1}{2}$ ,  ${}_s\Psi$  describes electromagnetic and neutrino perturbations, respectively. In the following and onward we keep  $s$  unfixed despite our expressions not being mainly focused on these last two types of perturbation. We will give the corresponding values to  $s$  when explicit values are required.

The derivation of the field equation for  ${}_s\Psi$  is not trivial. It requires to calculate the spin coefficients and also use the Ricci and Bianchi identities. After putting all these quantities together, the field equation for  ${}_s\Psi$  is given by [44]

$$\left[ \square + \frac{2s}{r^2} \left( \frac{3M-r}{f} \partial_t + (r-M) \partial_r + i \frac{\cos\theta}{\sin^2\theta} \partial_\phi + \frac{1-s \cot^2\theta}{2} \right) \right] {}_s\Psi(x, x') = -4\pi {}_s\mathcal{T}(x, x'), \quad (1.93)$$

where  ${}_s\mathcal{T}(x, x')$  is the perturbation source<sup>10</sup>.

Despite field perturbations being reduced to one single partial differential equation, the non-trivial angular dependence of  ${}_s\Psi$  in Eq. (1.93) brings an additional difficulty. However, Chandrasekhar found that for  $s \leq 0$ , solutions to Eq. (1.93) are related with homogeneous solutions to Eq. (1.72) via [34]

$${}_s\Psi = \tilde{\partial}^{|s|} {}_s\mathcal{C}(t, r) {}_s\chi, \quad (1.94)$$

where  ${}_s\chi$  is a homogeneous solution to Eq. (1.72),  ${}_s\mathcal{C}(t, r)$  is given by

$${}_s\mathcal{C}(t, r) = (rf)^{|s|} \left( \frac{\partial}{\partial r} - f^{-1} \frac{\partial}{\partial t} \right)^{|s|} r^{|s|-1}, \quad (1.95)$$

and

$$\tilde{\partial} = - \left( \partial_\theta + \frac{i}{\sin\theta} \partial_\phi - s \cot\theta \right) \quad (1.96)$$

<sup>10</sup>An explicit calculation of  ${}_s\mathcal{T}(x, x')$  from the stress-energy tensor can be found in [41].



is the spin raising operator. Similarly, the spin lowering operator is

$$\bar{\delta} = - \left( \partial_\theta - \frac{i}{\sin \theta} \partial_\phi + s \cot \theta \right), \quad (1.97)$$

and when applied on spin-weighted spherical harmonics  ${}_s Y_{\ell m}(\theta, \phi)$ , they yield

$$\bar{\delta}({}_s Y_{\ell m}) = + \sqrt{\ell(\ell+1) - s(s+1)} {}_{s+1} Y_{\ell m}, \quad (1.98)$$

$$\delta({}_s Y_{\ell m}) = - \sqrt{\ell(\ell+1) - s(s-1)} {}_{s-1} Y_{\ell m}. \quad (1.99)$$

Once again, the symmetries of Schwarzschild spacetime (manifested in Eq. (1.93)) allow us to decompose  ${}_s \Psi$  as

$${}_s \Psi = \sum_{\ell=|s|}^{\infty} \sum_{m=-\ell}^{\ell} \int_{-\infty}^{\infty} {}_s \tilde{R}_{\omega\ell}(r) {}_s Y_{\ell m}(\theta, \phi) e^{-i\omega t} d\omega, \quad (1.100)$$

where the radial function  ${}_s \tilde{R}_{\omega\ell}(r)$  satisfies the radial Teukolsky equation [41]<sup>11</sup>, i.e.,

$$\left[ r^2 f(r) \frac{d^2}{dr^2} + 2(r-M)(s+1) \frac{d}{dr} + 4i\omega sr + s(s+1) - \ell(\ell+1) + \frac{r^2 \omega^2 - 2i\omega s(r-M)}{f(r)} \right] {}_s \tilde{R}_{\omega\ell}(r) = r^2 {}_s \tilde{T}_{\omega\ell}(r), \quad (1.101)$$

where the source Fourier modes  ${}_s \tilde{T}_{\omega\ell}$  can be obtained by decomposing  ${}_s T$  in the same way as  ${}_s \Psi$

$${}_s T = \sum_{\ell=|s|}^{\infty} \sum_{m=-\ell}^{\ell} \int_{-\infty}^{\infty} {}_s \tilde{T}_{\omega\ell}(r) {}_s Y_{\ell m}(\theta, \phi) e^{-i\omega t} d\omega. \quad (1.102)$$

In case the radial function  ${}_s \tilde{R}_{\omega\ell}$  is a homogeneous solution to the radial Teukolsky equation, we are able to find the counterpart of Eq. (1.94) in the frequency domain. In particular, for  $s = -2$  this transformation takes the form

$${}_{-2} \tilde{R}_{\omega\ell}(r) = {}_{-2} \tilde{\mathcal{C}}(r, \omega) {}_2 \tilde{\chi}_{\omega\ell}, \quad (1.103)$$

where  ${}_{-2} \tilde{\mathcal{C}}(r, \omega)$  is given by [34]

$${}_{-2} \tilde{\mathcal{C}}(r, \omega) = (rf)^2 \left( \frac{d}{dr} + i \frac{\omega}{f} \right)^2 r. \quad (1.104)$$

<sup>11</sup>This equation was first derived in Kerr spacetime by Teukolsky.

### 1.8.6 Metric reconstruction in the radiation gauge

There are two radiation gauges and they are identified according to the condition they impose on the metric  $h_{\mu\nu}$ , i.e.,

$$\begin{cases} h_{\mu\nu}l^\nu = 0, & \text{Ingoing radiation gauge (IRG),} \\ h_{\mu\nu}n^\nu = 0, & \text{Outgoing radiation gauge (ORG).} \end{cases} \quad (1.105)$$

In both cases the metric is traceless, i.e.,  $h_\mu{}^\mu = 0$ .

Unlike the calculation of the metric perturbation in the Regge-Wheeler gauge, obtaining the metric perturbation in the radiation gauge (from the Weyl-NP scalars  $\psi_0$  and  $\psi_4$ ) is not trivial. Based on a previous work from Cohen and Kegeles [45], Chrzanowski provided the first prescription for reconstructing the metric perturbation in the radiation gauge [46]. Later on, Wald [47] showed that the prescription in Ref. [46] did not lead to a real metric perturbation. In a later work, Cohen and Kegeles [48] based on the results of Chrzanowski and Wald, they established the standard procedure we now have for reconstructing the metric perturbation in the radiation gauge. This procedure starts with the following considerations (from now and onward, the spin  $s$  can only take the values of  $\pm 2$ )

- The metric perturbation  $h_{\mu\nu}$  satisfies the field equation

$$\hat{\mathcal{E}}[h_{\mu\nu}] = T_{\mu\nu},$$

where  $\hat{\mathcal{E}}[h_{\mu\nu}]$  is the linearized Einstein tensor (e.g.  $\delta R_{\mu\nu}$  for vacuum solutions).

- There exists an operator  $\hat{\mathcal{T}}_s$  which allows us to transform  $h_{\mu\nu}$  into a Weyl-NP scalar

$$\hat{\mathcal{T}}_s[h_{\mu\nu}] = \psi_{0/4}. \quad (1.106)$$

- In the Teukolsky formalism,  ${}_s\Psi$  describes gravitational perturbations of Schwarzschild spacetime, this satisfies

$$\hat{\mathcal{O}}_s[{}_s\Psi] = {}_s\mathcal{T} = \hat{\mathcal{S}}_s[T_{\mu\nu}], \quad (1.107)$$

where  $\hat{\mathcal{S}}_s$  is certain second order differential operator which allows us to construct the Teukolsky source  ${}_s\mathcal{T}$  from  $T_{\mu\nu}$  [46].

According to Wald [47], given a homogeneous solution  $\Psi$  to the Teukolsky equation, if this satisfies

$$\hat{\mathcal{O}}_s^\dagger[\Psi] = 0 \quad (1.108)$$

(where the  $\hat{\mathcal{O}}_s^\dagger$  is the adjoint of  $\hat{\mathcal{O}}_s$ ), then a metric reconstructed from this solution (namely  $h_{\mu\nu}^{\text{rec}}$ ) is a vacuum solution of the Einstein's field equation. This reconstructed metric is then given by

$$h_{\mu\nu}^{\text{rec}} = 4\Re\left(\hat{\mathcal{S}}_s^\dagger[\Psi]_{\mu\nu}\right). \quad (1.109)$$

Furthermore, we should also impose that

$$\hat{\mathcal{T}}_s[h_{\mu\nu}^{\text{rec}}] = \hat{\mathcal{T}}_s\hat{\mathcal{S}}_s^\dagger\Psi_{\text{IRG/ORG}} = \psi_{0/4}, \quad (1.110)$$

where the IRG (ORG) label on  $\Psi$  indicates that the associated metric perturbation  $h_{\mu\nu}^{\text{rec}}$  is in the ingoing (outgoing) radiation gauge. Therefore, the first step for calculating the radiative components of the metric perturbation consists of finding  $\Psi$  (usually referred to as *Hertz potential*) such that it satisfies Eq. (1.108) and Eq. (1.109). Once this field is known, we reconstruct the metric perturbation following Chrzanowski's procedure.

Nakano and Sasaki [44] came up with a different approach for reconstructing the *tail* integral of the metric perturbation, a key component for obtaining the regular part of the metric perturbation. This approach consisted of calculating the non-direct part of the retarded Green function  ${}_{-2}G_{\text{ret}}^T(x, x')$  of Eq. (1.93) for  $s = -2$ . Next, they constructed the regular part of  $r^4\psi_4$  (a homogeneous solution to Eq. (1.93)) integrating the non-direct part of  ${}_{-2}G_{\text{ret}}^T(x, x')$  against a prescribed source (see [44]). Once the regular part of  $r^4\psi_4$  is determined, Nakano and Sasaki applied Chrzanowski's procedure to reconstruct the metric perturbation.

The method for calculating the non-direct part of  $G_{\text{ret}}^T(x, x')$  in [44] consisted of applying the Chandrasekhar transformation on the non-direct part of the retarded Regge-Wheeler Green function (namely  ${}_sG_{\text{ret}}^{\text{nd}}$ ). However, as we show in a following chapter, ap-

plying differential operators on  ${}_sG_{\text{ret}}^{\text{nd}}$  induces undesired distributions. Thus, it is necessary to modify the original metric reconstruction procedure proposed by Chrzanowski so that these additional distributions are properly removed.

In principle, Nakano and Sasaki applied this metric reconstruction procedure in the IRG and obtained the tail integral for the metric perturbation (to first post-Newtonian order) using the regular part of  $\psi_4$ . This last step in [44] is quite unclear since Chrzanowski's procedure requires a Hertz potential to reconstruct the metric perturbation. The regular part of  $\psi_4$  does not seem to comply with this requirement of being a Hertz potential. In a following chapter we aim to see in detail the prescription in [44].

## 2 Calculation of the Regge-Wheeler Green function

In this chapter we cover the main methods and techniques we are using to understand field perturbations in a background spacetime. In particular, the background spacetime we are interested in is the Schwarzschild spacetime.

As discussed in Chapter 1, solving the equation of motion in curved spacetime is not trivial. The field produced by the particle cannot be ignored since it produces a back reaction effect on the particle itself. This effect is commonly incorporated into the particle's equation of motion as a SF and, as a result, the particle does not follow a geodesic motion in the background spacetime. The first step towards the calculation of the SF involves calculating the retarded Green function of the Regge-Wheeler equation (see Eq. (1.72)). However, this is not the only alternative since the SF is a gauge-dependent quantity. Thus, when solving the Regge-Wheeler equation we are constraining ourselves to the Regge-Wheeler gauge which, as pointed out in Chapter 1, has some downsides during the regularisation process [49, 50].

Throughout this chapter and on-wards, we will use the acronym RWE to refer to the Regge-Wheeler equation given in Eq. (1.72) (i.e., it includes the three types of field perturbations). If necessary, we may add in front of “RWE” when we require to focus on a specific field perturbation. Unless the opposite is specified, we will use the term “retarded GF” to refer to the retarded Green function of the RWE.

For field perturbations in Schwarzschild spacetime, we first calculate the retarded GF for the RWE. In a following Chapter, we make use of these results to calculate the Teukolsky Green function.

Let  ${}_sG_{\text{ret}}(x, x')$  be the retarded GF of the RWE. Hence,  ${}_sG_{\text{ret}}(x, x')$  satisfies Eq. (1.72)

with  ${}_sS$  being a covariant Dirac-delta distribution, i.e.,

$$\left(\square + s^2 \frac{2M}{r^3}\right) {}_sG_{\text{ret}}(x, x') = -\delta_4(x, x') = -\frac{4\pi}{rr'} \delta(t - t') \delta(r - r') \delta(\Omega_2 - \Omega'_2), \quad (2.1)$$

where  $\Omega_2$  is the solid angle of the 2-sphere. This GF is characterized for having support only on and inside the future light cone of  $x'$ .

Our approach for solving Eq. (2.1) is based on the method of matched expansions detailed in Sec. 1.6, i.e., We calculate  ${}_sG_{\text{ret}}$  in the QL and DP regions.

For the QL region, the Hadamard form of  ${}_sG_{\text{ret}}(x, x')$  is given by

$${}_sG_{\text{ret}}(x, x') = U(x, x') \delta(\sigma) \theta(t - t') - V_s(x, x') \theta(-\sigma) \theta(t - t'), \quad (2.2)$$

where  $U(x, x')$  and  $V_s(x, x')$  are two regular biscalars to be determined.

From Eq. (2.2) we observe that  ${}_sG_{\text{ret}}(x, x')$  diverges on the light cone. In fact, it has been observed [51, 52, 53, 54, 55, 56] that the retarded GF diverges when  $x'$  and  $x$  are connected by a null geodesic (even beyond normal neighbourhoods) displaying the following *global* fourfold (leading) singularity structure<sup>1</sup>:  $\delta(\sigma) \rightarrow \text{PV}(1/\sigma) \rightarrow -\delta(\sigma) \rightarrow -\text{PV}(1/\sigma) \rightarrow \delta(\sigma) \dots$ , where PV denotes the principal value distribution.

## 2.1 Retarded Green function in the QL region

For simplicity, in Eq. (2.2) we will drop the arguments in  ${}_sG_{\text{ret}}$ ,  $U$ ,  $V_s$  and in any other related biscalars. The first term in the right hand side of Eq. (2.2) (which involves  $U$ ) is the direct part of  ${}_sG_{\text{ret}}$  and the second term (which involves  $V_s$ ) is the non-direct part of  ${}_sG_{\text{ret}}$ .

By substituting Eq. (2.2) back in Eq. (2.1) and after some algebra<sup>2</sup> the biscalars

<sup>1</sup>Here,  $\sigma$  refers to a well-defined extension of the world function outside normal neighbourhoods [53, 6]. We also note that this structure does not hold at caustics [53] and that the subleading order (in Schwarzschild and outside caustics) is given in [53].

<sup>2</sup>We will see this in more detail in Chapter 5.

$U$  and  $V_s$  satisfy the following equations

$$\begin{aligned}
U &= \Delta^{1/2}, \\
\left(\square + s^2 \frac{M}{r^3}\right) V_s &= 0, \\
\sigma^\alpha \nabla_\alpha \hat{V}_s + \frac{1}{2} (\sigma^\alpha{}_\alpha - 2) \hat{V}_s &= \frac{1}{2} \square U|_{\sigma=0}, \\
[V_s] \equiv V_s|_{x=x'} &= -\frac{M}{r^3} s^2,
\end{aligned} \tag{2.3}$$

where  $x = (t, r, \theta, \phi)$ ,  $x' = (t', r', \theta', \phi')$ , Greek indices on  $\sigma$  indicate covariant differentiation with respect to  $x$  (or  $x'$  if the index has an apostrophe),  $\hat{V}_s \equiv V_s|_{\sigma=0}$ , and  $\Delta$  is the van Vleck determinant given by

$$\Delta(x, x') = -\frac{\det[-\sigma_{\alpha\beta'}]}{\sqrt{-g(x)}\sqrt{-g(x')}},$$

with  $g(x)$  ( $g(x')$ ) being the determinant of the metric evaluated at  $x$  ( $x'$ ). Note that in (2.3) we introduced the bracket notation  $[V_s]$  to indicate that the quantity in brackets ( $V_s$  in this case) is evaluated at coincidence  $x = x'$ . Throughout the thesis, we will use this square-bracket notation for other quantities to indicate that they are evaluated at coincidence.

It is worth noting that in (2.3), the transport equation for  $\hat{V}_s$  together with  $[V_s] = -\frac{M}{r^3} s^2$  determines  $V_s$  on the light cone. We then use  $\hat{V}_s$  as initial data to solve the wave equation for  $V_s$ . This kind of initial data is usually referred to as Characteristic Initial Data (CID) and  $V_s$  satisfies a characteristic Initial Value Problem (or characteristic IVP for short).

By using the Hadamard form for solving Eq. (2.1), for the non-direct part we no longer have to worry about the distributional source and instead we have to solve a homogeneous equation for  $V_s$ . Therefore, if  $x'$  lies within a normal neighbourhood of  $x$ , to obtain the retarded GF it is sufficient to solve Eqs. (2.3) instead of directly solving Eq. (2.1). Outside  $\mathcal{N}(x)$  the GF equation becomes a homogeneous equation since the distributional source has support only at coincidence, i.e.,  $x' = x$ .

### 2.1.1 Calculation of $\Delta^{1/2}(r, r')$

From Eq. (2.2) it is straightforward to see that the term involving  $U$  only has support on the light cone. There exist different approaches to calculate the van Vleck determinant. Particularly, the method we adopt here is based on solving a set of transport equations along the geodesic joining  $x$  and  $x'$ . This approach was first explored by Avramidi [57], later on Ottewill and Wardell used it to derive the corresponding transport equation for  $\Delta^{1/2}$  [58]

$$\frac{d\Delta^{1/2}}{d\tau} = -\frac{1}{2\tau} Q^\mu{}_\mu \Delta^{1/2}, \quad (2.4)$$

$$\frac{dQ^\mu{}_\nu}{d\tau} = u^\alpha \left( Q^\mu{}_\beta \Gamma^\beta{}_{\alpha\nu} - \Gamma^\mu{}_{\alpha\beta} Q^\beta{}_\nu \right) - \frac{1}{\tau} (Q^\mu{}_\alpha Q^\alpha{}_\nu + Q^\mu{}_\nu) - \tau R^\mu{}_{\alpha\nu\beta} u^\alpha u^\beta, \quad (2.5)$$

where  $R^\alpha{}_{\beta\mu\nu}$  is the Riemann tensor,  $\Gamma^\alpha{}_{\mu\nu}$  are the Christoffel symbols,  $\tau$  is an affine parameter,  $u^\mu = \frac{dx^\mu}{d\tau}$  is a vector tangent to the geodesic joining  $x$  and  $x'$  and the quantity  $Q^\mu{}_\nu$  is related to Synge's world function via

$$Q^\mu{}_\nu = \delta^\mu{}_\nu - \sigma^\mu{}_\nu. \quad (2.6)$$

The initial conditions to solve Eqs. (2.4)–(2.5) are, respectively,

$$\Delta^{1/2}|_{x=x'} = 1 \text{ and } Q^\mu{}_\nu|_{x=x'} = 0.$$

A second approach we consider for calculating the direct part of Eq. (2.2) is described in [6]. This approach uses the conformal transformation given in Eq. (1.37) to express  $U\delta(\sigma)\theta(\Delta t)$  in terms of quantities defined in  $\mathcal{M}_2$  and  $\mathbb{S}^2$ . There is a property relating the GF's from two spacetimes with conformally related metrics [33, 59]. For Schwarzschild and  $\mathcal{M}_2 \times \mathbb{S}^2$ , we have [33, 59]

$${}_s G_{\text{ret}}(x, x') = \frac{1}{r r'} {}_s \hat{G}_{\text{ret}}(x, x'), \quad (2.7)$$

where  ${}_s \hat{G}_{\text{ret}}$  is the corresponding retarded GF in  $\mathcal{M}_2 \times \mathbb{S}^2$  spacetime.

Eq. (2.7) shows that the direct parts of  ${}_s G_{\text{ret}}$  and  ${}_s \hat{G}_{\text{ret}}$  are related via [6]

$$\Delta^{1/2}(r, r', \Delta t, \gamma) \delta(\sigma) \theta(\Delta t) = \frac{1}{r r'} \hat{\Delta}^{1/2}(r, r', \Delta t, \gamma) \delta(\hat{\sigma}) \theta(\Delta t), \quad (2.8)$$



with  $\gamma$  being the angular separation between  $x$  and  $x'$  and is defined via

$$\cos \gamma \equiv \cos \theta \cos \theta' + \sin \theta \sin \theta' \cos(\varphi - \varphi'), \quad (2.9)$$

$\Delta t = t - t'$ ,  $\hat{\Delta}^{1/2}$  and  $\hat{\sigma}$  being, respectively, the van Vleck determinant and Synge's world function in  $\mathcal{M}_2 \times \mathbb{S}^2$ . In terms of  $\gamma$  and  $\eta$ , the proper time in  $\mathcal{M}_2$ ,  $\hat{\sigma}$  is given by [6]

$$\hat{\sigma} = -\frac{1}{2}\eta^2 + \frac{1}{2}\gamma^2. \quad (2.10)$$

Since  $\mathcal{M}_2 \times \mathbb{S}^2$  is a direct product,  $\hat{\Delta}^{1/2}$  can be factorized as [55]

$$\hat{\Delta}^{1/2}(r, r', \Delta t, \gamma) = \Delta_{2d}^{1/2}(r, r', \Delta t) \cdot \Delta_{\mathbb{S}^2}^{1/2}(\gamma), \quad (2.11)$$

where  $\Delta_{2d}$  ( $\Delta_{\mathbb{S}^2} = \frac{\gamma}{\sin \gamma}$ ) is the van Vleck determinant in  $\mathcal{M}_2$  ( $\mathbb{S}^2$ ).

The direct part of  ${}_sG_{\text{ret}}$  can be decomposed as

$$U(x, x')\delta(\sigma)\theta_+(x, x') = \Delta^{1/2}(r, r'; \Delta t)\delta(\sigma)\theta(\Delta t) = \frac{1}{rr'} \sum_{\ell=0}^{\infty} (2\ell + 1)G_{\ell}^{\text{dir}} P_{\ell}(\cos \gamma), \quad (2.12)$$

where  $\gamma$  is the angle between  $x$  and  $x'$  and  $G_{\ell}^{\text{dir}} = G_{\ell}^{\text{dir}}(r, r'; \Delta t)$  are the  $\ell$ -modes of the direct part. By using Eqs. (2.8)–(2.11) we find that  $G_{\ell}^{\text{dir}}$  is given by [6]

$$\begin{aligned} G_{\ell}^{\text{dir}} &= \frac{\theta(\Delta t)}{2} \int_{-1}^1 \Delta_{2d}^{1/2}(r, r', \Delta t) \frac{\gamma}{\sin \gamma} \delta(\hat{\sigma}) d(\cos \gamma) \\ &= \frac{\theta(\Delta t)}{2} \theta(\pi - \eta) \Delta_{2d}^{1/2} P_{\ell}(\cos \eta) \sqrt{\frac{\sin \eta}{\eta}}. \end{aligned} \quad (2.13)$$

We consider two methods to calculate  $G_{\ell}^{\text{dir}}$ . The first method relies on solving Eq. (2.4) in (1+1)-dimensions to compute  $\Delta_{2d}^{1/2}$  in  $\mathcal{M}_2$ . The second method consists of a (small distance) coordinate expansion for  $\Delta_{2d}^{1/2}$  and Synge's world function  $\sigma_{2d}$  in  $\mathcal{M}_2$ . In Ref. [6], the authors develop this method and provide accurate values for  $\Delta_{2d}^{1/2} = \Delta_{2d}^{1/2}(r, r'; \Delta t)$  and  $\eta = \eta(r, r'; \Delta t)$ . When putting all these results back in Eq. 2.13, they found that

$$\begin{aligned} G_{\ell}^{\text{dir}} &= \frac{1}{2} + \frac{(2M + r\ell(\ell + 1))}{8fr^3} \Delta r^2 - \frac{f(2M + r\ell(\ell + 1))}{8r^3} \Delta t^2 \\ &\quad + \frac{(12M^2 - Mr(3\ell(\ell + 1) + 11) + r^2(3\ell(\ell + 1) + 2))}{24r^5 f^2} \Delta r^3 \\ &\quad + \frac{3Mr(3\ell(\ell + 1) + 5) - r^2(3\ell(\ell + 1) + 2) - 24M^2}{24r^5} \Delta r \Delta t^2 + \mathcal{O}(\delta x^4), \end{aligned} \quad (2.14)$$

where  $\Delta x = x - x'$  with  $x = (t, r)$ .

### 2.1.2 Van Vleck determinant and $\sigma^\mu{}_\nu$ along radial null geodesics

Although the transport equations for the components of  $Q^\mu{}_\nu$  are coupled and difficult to solve, there is a particular scenario where we are able to calculate them analytically. This case corresponds to radial null geodesics where, in the Penrose limit<sup>3</sup> the Schwarzschild spacetime is flat. This limit implies  $\Delta(x, x') = 1$  and suggests that Eqs. (2.4)–(2.5) could be simplified in this particular case. In the following we explore this possibility.

We start with the 4-velocity for a radial null geodesic with energy  $E$ :

$$u^\mu = (\dot{t}, \dot{r}, \dot{\theta}, \dot{\phi}) = E(f^{-1}, \epsilon, 0, 0) \equiv Et^\mu, \quad (2.15)$$

where an overdot indicates differentiation with respect to an affine parameter  $\lambda$ , and  $\epsilon$  is equal to  $+1$  and  $-1$  for ingoing and outgoing geodesics, respectively. Since for radial null geodesics  $\dot{r}$  is constant, we can use  $r$  as an affine parameter.

The transport equations (2.4)–(2.5) are then given by

$$(r - r') \frac{d\Delta^{1/2}}{dr} = -\frac{1}{2} Q^\alpha{}_\alpha \Delta^{1/2}, \quad (2.16)$$

$$(r - r') \frac{dQ^\mu{}_\nu}{dr} = \epsilon(r - r') \left( Q^\mu{}_\alpha \Gamma^\alpha{}_{\nu\beta} t^\beta - Q^\alpha{}_\nu \Gamma^\mu{}_{\alpha\beta} t^\beta \right) - Q^\mu{}_\alpha Q^\alpha{}_\nu - Q^\mu{}_\nu - (r - r')^2 R^\mu{}_{\alpha\nu\beta} t^\alpha t^\beta. \quad (2.17)$$

The symmetry  $\sigma_{\alpha\beta} = \sigma_{\beta\alpha}$  implies

$$Q^r{}_t = -f^2 Q^t{}_r, \quad (2.18)$$

and since we are only interested in radial null geodesics, it follows that

$$Q^A{}_B(x, x') = 0, \quad (2.19)$$

for any  $A, B \in \{\theta, \phi\}$ .

---

<sup>3</sup>The Penrose limit establishes that any spacetime reduces to a plane wave spacetime near a null geodesic. A plane wave spacetime is characterized by the metric  $ds^2 = h(u, x, y)du^2 + 2dudv + dx^2 + dy^2$  where  $(u, v, x, y)$  are Brinkmann coordinates, and  $h(u, x, y)$  is a known function.

When putting Eq. (2.19) back into Eq. (2.17) for the non-zero components  $Q^t_t$ ,  $Q^r_r$  and  $Q^t_r = -f^{-2}Q^r_t$ , we obtain

$$(r - r') \frac{dQ^t_t}{dr} = -\frac{2M(r - r')^2}{r^3 f} - Q^t_t - (Q^t_t)^2 + (fQ^t_r)^2 + \frac{\epsilon 2M(r - r')}{r^2} Q^t_r, \quad (2.20)$$

$$(r - r') \frac{dQ^r_r}{dr} = \frac{2M(r - r')^2}{r^3 f} - Q^r_r - (Q^r_r)^2 + (fQ^t_r)^2 - \frac{\epsilon 2M(r - r')}{r^2} Q^t_r, \quad (2.21)$$

$$(r - r') \frac{dQ^t_r}{dr} = \frac{\epsilon 2M(r - r')^2}{r^3 f^2} - Q^t_r - Q^t_r(Q^t_t + Q^r_r) - \frac{M(r - r')}{r^2 f^2} (2fQ^t_r - \epsilon Q^t_t + \epsilon Q^r_r). \quad (2.22)$$

And, from  $\Delta(x, x') = 1$  together with Eq. (2.17) and Eq. (2.19) we can conclude that

$$Q^\alpha_\alpha = Q^t_t + Q^r_r = 0 \implies Q^r_r = -Q^t_t. \quad (2.23)$$

Adding Eqs. (2.20)–(2.21) and using  $Q^\alpha_\alpha = 0 = \text{const}$  together with Eq. (2.18) and Eq. (2.23), we obtain

$$(r - r') \frac{dQ^\alpha_\alpha}{dr} = -2(Q^t_t)^2 + 2(fQ^t_r)^2 = 0 \implies Q^t_t = \pm fQ^t_r. \quad (2.24)$$

When inserting Eqs. (2.23)–(2.24) back into the transport equations (2.20) and (2.21) we note that, in order for these equations to be consistent, the  $+/-$  sign in Eq. (2.24) must be chosen so that it corresponds to ingoing/outgoing geodesics respectively (i.e., so that it is equal to “ $-\epsilon$ ”). The resulting first-order, linear ordinary differential equation for  $Q^t_t$  is:

$$(r - r') \frac{dQ^t_t}{dr} = -\frac{2M(r - r')^2}{r^3 f} - \frac{r^2 - 2Mr'}{r^2 f} Q^t_t, \quad (2.25)$$

and in order to integrate it we use Eqs. (2.23)–(2.24) and Eq. (2.18) to obtain

$$Q^t_t = -Q^r_r = \frac{M}{f} \left( \frac{3r - r'}{r^2} - \frac{2 \ln \left( \frac{r}{r'} \right)}{r - r'} \right), \quad (2.26)$$

$$Q^t_r = -\frac{Q^r_t}{f^2} = \pm \frac{Q^t_t}{f} = \pm \frac{M}{f^2} \left( \frac{3r - r'}{r^2} - \frac{2 \ln \left( \frac{r}{r'} \right)}{r - r'} \right),$$

where the  $+/-$  sign corresponds to ingoing/outgoing geodesics respectively.

In this way, Eqs. (2.19) and (2.26) provide the analytical expressions we were looking for. Once  $Q^\mu_\nu$  is determined, the expressions for  $\sigma^\mu_\nu$  are immediate. We have analytically (and numerically) verified that these expressions for  $Q^\alpha_\beta$  are indeed a solution of the system (2.5), and thus that  $\Delta(x, x') = 1$  along radial null geodesics in Schwarzschild.

### 2.1.3 Calculation of $V_s$

The remaining equation in (2.3) involving the biscalar  $V_s$  may also be solved via transport equations by writing  $V_s$  as an expansion in increasing powers of  $\sigma$

$$V_s = \sum_{k=0}^{\infty} {}_s\nu_k \sigma^k, \quad (2.27)$$

where the coefficients  ${}_s\nu_k$  satisfy certain transport equations [58]. This approach, however, is not recommended because the transport equations for  ${}_s\nu_k$  becomes increasingly difficult to solve as  $k$  increases. Instead, the approach we follow is based on an expansion in powers of the coordinate separation (between  $x$  and  $x'$ ) rather than an expansion in  $\sigma$ . By considering the symmetries of Schwarzschild spacetime,  $V_s$  may be written as [60]

$$V_s = V_s(x, x') = \sum_{i,j,k=0}^{\infty} {}_s v_{ijk}(r) (t - t')^{2i} (1 - \cos \gamma)^j (r - r')^k, \quad (2.28)$$

where  ${}_s v_{ijk}$  are some coefficients to be determined. Since the expansion in Eq. (2.28) can be seen as a power series in the separation of the points, it is not guaranteed to converge for all points  $x$  and  $x'$  even inside a normal neighbourhood [60]. Casals, Dolan, Ottewill and Wardell [60] adopted the Hadamard-WKB method proposed in [61] and developed a prescription for calculating  ${}_0 v_{ijk}$ <sup>4</sup>. In order to calculate  $V_s$ , we took the prescription detailed in [60] and generalised it to any given spin  $s$ . This generalisation consisted of taking Eq. (2.10) of Ref. [60] and adding the term  $-s^2 \frac{M}{r^3}$  to the potential. Below we list some of the  ${}_s v_{i,j,k}$  coefficients:

---

<sup>4</sup>The code for calculating these coefficients can be found in [62].

$$\begin{aligned}
{}_s v_{0,0,0} &= -\frac{Ms^2}{r^3}, \\
{}_s v_{1,0,0} &= -\frac{Ms^2 f}{4r^6} [M(s^2 - 4) + r], \\
{}_s v_{1,1,0} &= \frac{M^2 f}{1680r^7} [2M(70s^6 - 665s^4 + 784s^2 + 81) + 9r(35s^4 - 56s^2 - 9)], \\
{}_s v_{1,1,1} &= \frac{M^2}{1680r^9} [-16M^2(70s^6 - 665s^4 + 784s^2 + 81) \\
&\quad + 14Mr(7(5s^4 - 70s^2 + 92)s^2 + 81) + 27r^2(35s^4 - 56s^2 - 9)] \\
{}_s v_{2,0,0} &= -\frac{Mf}{1344r^{10}} [4M^3(9 - 14s^2(s^4 - 20s^2 + 70)) + 4M^2r(7s^2(s^4 - 30s^2 + 131) - 9) \\
&\quad + Mr^2(147s^4 - 1036s^2 + 9) + 84r^3s^2] \\
{}_s v_{2,1,0} &= -\frac{M^2 f}{4032r^{11}} [6M^3(-2438s^2 + 7(s^4 - 34s^2 + 272)s^4 - 405) \\
&\quad + M^2r(-21s^8 + 1078s^6 - 10808s^4 + 15088s^2 + 2853) \\
&\quad - 9Mr^2(21s^6 - 343s^4 + 543s^2 + 119) + 18r^3(-14s^4 + 27s^2 + 7)] \\
{}_s v_{2,2,0} &= \frac{M^2 f}{887040r^{12}} [66M^4(14s^{10} - 735s^8 + 10752s^6 - 41990s^4 + 16974s^2 - 13365) \\
&\quad - 22M^3r(21s^{10} - 1610s^8 + 28728s^6 - 117690s^4 + 21161s^2 - 61560) \\
&\quad - 15M^2r^2(23276s^2 + 77(5(s^2 - 28)s^2 + 587)s^4 + 51050) \\
&\quad + 3Mr^3(-3465s^6 + 8250s^4 + 67551s^2 + 62794) + 150r^4(33s^2(s^2 - 5) - 113)].
\end{aligned}$$

We note that for  $i = j = k = 0$ ,  ${}_s v_{0,0,0} = [V_s]$  as expected.

## 2.2 Retarded Green function in the DP region

In the DP region the retarded GF is simply given by the homogeneous solution to Eq. (2.1). Once again, the symmetries of Schwarzschild spacetime allows us to perform a mode sum decomposition to  ${}_s G_{\text{ret}}(r, r', \Delta t, \gamma)$ , i.e.,

$${}_s G_{\text{ret}}(r, r', \Delta t, \gamma) = \frac{1}{r r'} \sum_{\ell=0}^{\infty} (2\ell + 1) {}_s G_{\ell}(r, r'; \Delta t) P_{\ell}(\cos \gamma), \quad (2.29)$$

where  ${}_s G_{\ell}$  are the  $\ell$ -modes of  ${}_s G_{\text{ret}}$ .

When substituting Eq. (2.29) back into Eq. (2.1), it can be seen that the  $\ell$ -modes

${}_sG_\ell$  satisfy a (1+1)-dimensional partial differential equation <sup>5</sup>

$$\left[ \frac{\partial^2}{\partial r_*^2} - \frac{\partial^2}{\partial t^2} - \frac{f(r)}{r^2} \left( \ell(\ell+1) + \frac{2M(1-s^2)}{r} \right) \right] {}_sG_\ell = -\delta(\Delta t)\delta(r_* - r'_*). \quad (2.30)$$

The boundary conditions for these modes are chosen according to the boundary condition of the retarded GF  ${}_sG_{\text{ret}}$ . In practice the sum in Eq. (2.29) must be truncated at a certain value of  $\ell$ . One problem with discarding the higher  $\ell$ -modes in Eq. (2.29) produce spurious oscillations in  ${}_sG_{\text{ret}}$ . The authors in [56] smoothed out these oscillations by introducing a factor  $\exp[-\ell^2/(2\ell_{\text{cut}})^2]$  in the mode sum, where  $\ell_{\text{cut}}$  is a cutoff value for the  $\ell$ -modes. A second problem with truncating Eq. (2.29) manifests at coincidence. The mode sum approaches the singularity in  ${}_sG_{\text{ret}}$  at  $x = x'$  as a Gaussian distribution that narrows as more  $\ell$ -modes are included in the sum. The DP region is the region where the truncated sum in Eq. (2.29) is accurate enough. The method of matched expansions allows us to solve this problem near coincidence by matching  $V_s$  with the calculation of  ${}_sG_{\text{ret}}$  via Eq. (2.29).

### 2.2.1 The RWE as a Characteristic Initial Value problem

When solving the equation of motion of a physical system the initial data is commonly placed on a surface where the time coordinate is constant. However, the  $\ell$ -modes  ${}_sG_\ell$  in Eq. (2.29) do not have their initial data along a surface with  $t = \text{constant}$ . In fact, the initial data to solve Eq. (2.30) is placed on the light cone of  $x'$ . Mark, Zimmerman, Du and Chen in [63] came up with a finite difference method to solve the  $s = 0$  case of Eq. (2.30) to order  $h^2$ , where  $2h$  is the stepsize<sup>6</sup> of the grid. Here we apply a similar scheme but to order  $h^4$  instead of  $h^2$ . We begin by rewriting Eq. (2.30) in terms of the null coordinates  $u$  and  $v$ :

$$u = t - r_*, \quad v = t + r_*. \quad (2.31)$$

<sup>5</sup>In order to obtain this equation we should also consider expressing the  $\delta(\Omega - \Omega')$  distribution (in the right-hand side of Eq. (2.1)) as a mode sum, i.e.,

$$\delta(\Omega - \Omega') = \sum_{\ell=0}^{\infty} \frac{2\ell+1}{4\pi} P_\ell(\cos \gamma).$$

<sup>6</sup>This stepsize is kept fixed throughout the calculations so that the grid is uniform.

From the Hadamard form in (1+1)-dimensions,  ${}_sG_\ell$  can be written as

$${}_sG_\ell(v, u) = {}_s g_\ell(v, u) \theta(u - u') \theta(v - v'), \quad (2.32)$$

where for simplicity we omitted the  $u'$  and  $v'$  arguments in  ${}_sG_\ell$ . In  $(t, r_*)$  coordinates, the product distribution  $\theta(u - u') \theta(v - v')$  can be rewritten as  $\theta(\Delta t - r_* + r'_*) \theta(\Delta t + r_* - r'_*)$ . From this product we note that  $\Delta t = r_* - r'_*$  and  $\Delta t = r'_* - r_*$  are the equations for a light cone centered at  $(t', r'_*)$  in  $\mathcal{M}_2$ . Therefore, the product  $\theta(\Delta t - r_* + r'_*) \theta(\Delta t + r_* - r'_*)$  implies that  ${}_sG_\ell$  is zero outside the future light cone of the point  $(t', r'_*)$ . This implies [53]

$$\theta(u - u') \theta(v - v') = \theta(-\sigma_{\mathcal{M}_2}) \theta(\Delta t), \quad (2.33)$$

where  $\sigma_{\mathcal{M}_2}$  is Synge's world function in  $\mathcal{M}_2$ .

It can be shown that the new modes  ${}_s g_\ell$  in Eq. (2.32) satisfy

$$\frac{\partial^2 {}_s g_\ell}{\partial v \partial u} + \mathcal{Q}(r) {}_s g_\ell = 0, \quad (2.34)$$

$${}_s g_\ell(v = v', u) = \frac{1}{2}, \quad (2.35)$$

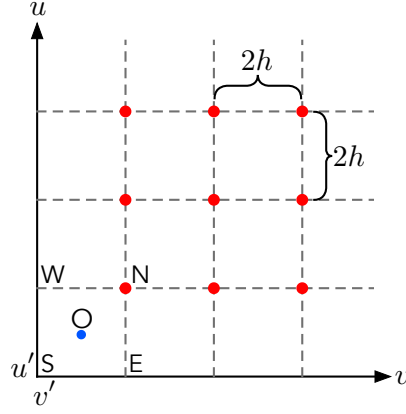
$${}_s g_\ell(v, u = u') = \frac{1}{2},$$

where

$$\mathcal{Q}_s(r) \equiv \frac{1}{4} \left( 1 - \frac{2M}{r} \right) \left( \frac{\ell(\ell+1)}{r^2} + \frac{2M(1-s^2)}{r^3} \right), \quad (2.36)$$

similarly to  ${}_sG_\ell$ ,  ${}_s g_\ell$  also depends on  $u'$  and  $v'$  but we will omit them since we are keeping them fixed. Ref. [63] solved this CID problem by using the scheme proposed in Lousto and Price [64]. The scheme we develop is based on the same approach taken in [63]. As we detail below, besides the initial data given in Eq. (2.35) we also use first order derivatives as additional data to provide a higher order scheme than the one in [63]. This CID problem can be solved by constructing an equally-spaced grid in the  $(v, u)$ -plane. Let  $2h$  be the stepsize between the nodes of the grid along either the  $u$ -direction or the  $v$ -direction. In Fig. 2 we show the grid arrangement in the  $(v, u)$ -plane.

The value of  ${}_sG_\ell(v, u)$  at each node is then calculated by integrating Eq. (2.34) over each square formed by four nodes (e.g.,  $S$ ,  $E$ ,  $N$  and  $W$  in Fig. (2)) of the grid. For

Figure 2 – Grid distribution on the  $(v, u)$ -plane.

instance, in Fig. 2 the integration of Eq. (2.34) over the square  $SENW$  yields

$$\int_{SENW} \frac{\partial^2 {}_s g_\ell}{\partial v \partial u} dv du + \int_{SENW} \mathcal{Q}_s(r) {}_s g_\ell dv du = 0. \quad (2.37)$$

The first integral in the above equation is exact and trivially performed:

$$\int_{SENW} \frac{\partial^2 {}_s g_\ell}{\partial v \partial u} du dv = {}_s g_\ell^N - {}_s g_\ell^E - {}_s g_\ell^W + {}_s g_\ell^S, \quad (2.38)$$

where  ${}_s g_\ell^K$  denotes the value of  ${}_s g_\ell$  at the point  $K = S, E, W$  or  $N$ .

In order to perform the second integral, we make some approximations. Taking into account that the stepsize between nodes is small (i.e.,  $h \ll M$ ), the integrand  $\mathcal{Q}_s \cdot {}_s g_\ell$  of the second term in Eq. (2.37) can be expanded about the point in the middle of the  $SENW$  square,  $O \equiv (v_0, u_0)$  (see Fig. 2). Expanding  $\mathcal{Q}_s \cdot {}_s g_\ell$ , as well as  ${}_s g_\ell$ , which we shall need later, as Taylor series and then truncating them at a desired order, we obtain

$$\mathcal{Q}_s(r) {}_s g_\ell(v, u) = \sum_{\substack{0 \leq m, n \leq 3 \\ m+n \leq 3}} \frac{1}{m! n!} \left( \frac{\partial^{m+n}}{\partial v^m \partial u^n} (\mathcal{Q}_s \cdot {}_s g_\ell) \right)_O (v - v_0)^m (u - u_0)^n + \mathcal{O}(h^4), \quad (2.39)$$

$${}_s g_\ell(v, u) = \sum_{\substack{0 \leq m, n \leq 3 \\ m+n \leq 3}} \frac{1}{m! n!} \left( \frac{\partial^{m+n}}{\partial v^m \partial u^n} {}_s g_\ell \right)_O (v - v_0)^m (u - u_0)^n + \mathcal{O}(h^4). \quad (2.40)$$

Thus the second integral in Eq. (2.37) is given to  $\mathcal{O}(h^6)$  by

$$\int_{SENW} \mathcal{Q}_s(r) {}_s g_\ell(v, u) dv du = 4(\mathcal{Q}_s \cdot {}_s g_\ell)_O h^2 + \frac{2}{3} \left[ \frac{\partial^2}{\partial v^2} (\mathcal{Q}_s \cdot {}_s g_\ell) + \frac{\partial^2}{\partial u^2} (\mathcal{Q}_s \cdot {}_s g_\ell) \right]_O h^4 + \mathcal{O}(h^6). \quad (2.41)$$



However, with the initial data given in Eq. (2.35), it is not possible to reach up to order  $\mathcal{O}(h^6)$ . To achieve this order, additional information should be given along  $u = u'$  as well as along  $v = v'$ . Specifically, Eq. (2.35) readily yields the longitudinal derivatives along these characteristic lines (which are zero), but we also require the transversal derivatives.

$$\begin{aligned} \int \frac{\partial}{\partial v} \left( \frac{\partial_s g_\ell}{\partial u} \right)_{u'} dv &= \left( \frac{\partial_s g_\ell}{\partial u} \right)_{u'} = - \left( \int \mathcal{Q}_s(r) {}_s g_\ell(v, u) dv \right)_{u'} \\ &= -\frac{1}{2} \left( \int \mathcal{Q}_s(r) dv \right)_{u'} + p(u'), \\ \int \frac{\partial}{\partial u} \left( \frac{\partial_s g_\ell}{\partial v} \right)_{v'} du &= \left( \frac{\partial_s g_\ell}{\partial v} \right)_{v'} = - \left( \int \mathcal{Q}_s(r) {}_s g_\ell(v, u) du \right)_{v'} \\ &= -\frac{1}{2} \left( \int \mathcal{Q}_s(r) du \right)_{v'} + q(v'), \end{aligned} \quad (2.42)$$

for some functions  $p(u')$  and  $q(v')$ , where we have used Eq. (2.35). We use the notation of  $u'$  as a subscript in the brackets to indicate evaluation at  $u = u'$ ; similarly for  $v'$  to indicate  $v = v'$  and for  $v', u'$  below to indicate both  $v = v'$  and  $u = u'$ .

From the Hadamard series for  ${}_s g_\ell(v, u)$ :

$${}_s g_\ell(v, u) = \sum_{n=0}^{\infty} q_n \sigma_2^n,$$

where  $\sigma_2$  is the Synge's world function in 2-dimensional flat spacetime and  $q_n$  are coefficients to be determined. By using Eq. (2.35), it is trivial to show that, at coincidence,

$$\left( \frac{\partial_s g_\ell}{\partial v} \right)_{v', u'} = \left( \frac{\partial_s g_\ell}{\partial u} \right)_{v', u'} = 0, \quad (2.43)$$

and use it to calculate  $p(u')$  and  $q(v')$ . Thus the integrals in Eq. (2.42) reduce to

$$\begin{aligned} \left( \frac{\partial_s g_\ell}{\partial u} \right)_{u'} &= \left( \frac{1}{2} \int \mathcal{Q}_s(r) dv \right)_{v', u'} - \frac{1}{2} \left( \int \mathcal{Q}_s(r) dv \right)_{u'} \\ &= -\frac{1}{4} \left( \frac{\ell(\ell+1)}{r} + \frac{M(1-s^2)}{r^2} \right)_{v', u'} + \frac{1}{4} \left( \frac{\ell(\ell+1)}{r} + \frac{M(1-s^2)}{r^2} \right)_{u'}, \\ \left( \frac{\partial_s g_\ell}{\partial v} \right)_{v'} &= \left( \frac{1}{2} \int \mathcal{Q}_s(r) du \right)_{v', u'} - \frac{1}{2} \left( \int \mathcal{Q}_s(r) du \right)_{v'} \\ &= \frac{1}{4} \left( \frac{\ell(\ell+1)}{r} + \frac{M(1-s^2)}{r^2} \right)_{v', u'} - \frac{1}{4} \left( \frac{\ell(\ell+1)}{r} + \frac{M(1-s^2)}{r^2} \right)_{u'}. \end{aligned} \quad (2.44)$$

These two equations are used to evaluate the derivatives of  ${}_s g_\ell$  at the points  $E$ ,  $W$  and  $S$  (later on we apply a similar reasoning to calculate the derivatives at the point  $N$ ).

Now, we construct a system of 12 equations by evaluating the Taylor series for  ${}_s g_\ell$  and its derivatives at the points  $E$ ,  $W$ ,  $N$ ,  $S$ . The 12 unknowns of this system are the 10 coefficients of the Taylor series in Eq. (2.40), which are evaluated at  $O$ , together with the two first-order derivatives of  ${}_s g_\ell$  evaluated at the point  $N$ . Once the system is solved, the coefficients of the Taylor series turn out to be

$$4{}_s g_\ell^O = 2{}_s g_\ell^E + 2{}_s g_\ell^W + h \left( \frac{\partial {}_s g_\ell}{\partial u} - \frac{\partial {}_s g_\ell}{\partial v} \right)_E - h \left( \frac{\partial {}_s g_\ell}{\partial u} - \frac{\partial {}_s g_\ell}{\partial v} \right)_W + \mathcal{O}(h^4), \quad (2.45)$$

$$8h \left( \frac{\partial {}_s g_\ell}{\partial u} \right)_O = -5{}_s g_\ell^S - {}_s g_\ell^E + 5{}_s g_\ell^W + {}_s g_\ell^N - 2h \left( \frac{\partial {}_s g_\ell}{\partial u} + \frac{\partial {}_s g_\ell}{\partial v} \right)_S - 2h \left( \frac{\partial {}_s g_\ell}{\partial u} - \frac{\partial {}_s g_\ell}{\partial v} \right)_W + \mathcal{O}(h^4), \quad (2.46)$$

$$8h \left( \frac{\partial {}_s g_\ell}{\partial v} \right)_O = -5{}_s g_\ell^S + 5{}_s g_\ell^E + {}_s g_\ell^W - {}_s g_\ell^N - 2h \left( \frac{\partial {}_s g_\ell}{\partial u} + \frac{\partial {}_s g_\ell}{\partial v} \right)_S + 2h \left( \frac{\partial {}_s g_\ell}{\partial u} - \frac{\partial {}_s g_\ell}{\partial v} \right)_E + \mathcal{O}(h^4), \quad (2.47)$$

$$4h^2 \left( \frac{\partial^2 {}_s g_\ell}{\partial u^2} \right)_O = {}_s g_\ell^S - {}_s g_\ell^E - {}_s g_\ell^W + {}_s g_\ell^N + 2h \left( \frac{\partial {}_s g_\ell}{\partial u} \right)_E - 2h \left( \frac{\partial {}_s g_\ell}{\partial u} \right)_W + \mathcal{O}(h^4), \quad (2.48)$$

$$4h^2 \left( \frac{\partial^2 {}_s g_\ell}{\partial v^2} \right)_O = {}_s g_\ell^S - {}_s g_\ell^E - {}_s g_\ell^W + {}_s g_\ell^N - 2h \left( \frac{\partial {}_s g_\ell}{\partial v} \right)_E + 2h \left( \frac{\partial {}_s g_\ell}{\partial v} \right)_W + \mathcal{O}(h^4), \quad (2.49)$$

$$4h^2 \left( \frac{\partial^2 {}_s g_\ell}{\partial v \partial u} \right)_O = {}_s g_\ell^N + {}_s g_\ell^S - {}_s g_\ell^E - {}_s g_\ell^W + \mathcal{O}(h^4), \quad (2.50)$$

$$\frac{2}{3} h^3 \left( \frac{\partial^3 {}_s g_\ell}{\partial v^3} \right)_O = {}_s g_\ell^S - {}_s g_\ell^E + h \left( \frac{\partial {}_s g_\ell}{\partial v} \right)_S + h \left( \frac{\partial {}_s g_\ell}{\partial v} \right)_E + \mathcal{O}(h^4), \quad (2.51)$$

$$\frac{2}{3} h^3 \left( \frac{\partial^3 {}_s g_\ell}{\partial u^3} \right)_O = {}_s g_\ell^S - {}_s g_\ell^W + h \left( \frac{\partial {}_s g_\ell}{\partial u} \right)_S + h \left( \frac{\partial {}_s g_\ell}{\partial u} \right)_W + \mathcal{O}(h^4), \quad (2.52)$$

$$4h^3 \left( \frac{\partial^3 {}_s g_\ell}{\partial v^2 \partial u} \right)_O = {}_s g_\ell^N + {}_s g_\ell^S - {}_s g_\ell^E - {}_s g_\ell^W + 2h \left( \frac{\partial {}_s g_\ell}{\partial v} \right)_S - 2h \left( \frac{\partial {}_s g_\ell}{\partial v} \right)_W + \mathcal{O}(h^4), \quad (2.53)$$

$$4h^3 \left( \frac{\partial^3 {}_s g_\ell}{\partial v \partial u^2} \right)_O = {}_s g_\ell^N + {}_s g_\ell^S - {}_s g_\ell^E - {}_s g_\ell^W + 2h \left( \frac{\partial {}_s g_\ell}{\partial u} \right)_S - 2h \left( \frac{\partial {}_s g_\ell}{\partial u} \right)_E + \mathcal{O}(h^4). \quad (2.54)$$

Inserting Eqs. (2.38), (2.41) and (2.45)–(2.49) into Eq. (2.37), we obtain

$$\begin{aligned}
(6 + 2\mathcal{Q}_s h^2)_O {}_s g_\ell^N &= \left[ 6 - 10Qh^2 - 2 \left( \frac{\partial^2 \mathcal{Q}_s}{\partial v^2} + \frac{\partial^2 \mathcal{Q}_s}{\partial u^2} \right) h^4 \right]_O ({}_s g_\ell^E + {}_s g_\ell^W) - (6 + 2Qh^2)_O {}_s g_\ell^S \\
&+ \left[ 4\mathcal{Q}_s + \left( \frac{\partial^2 \mathcal{Q}_s}{\partial v^2} + \frac{\partial^2 \mathcal{Q}_s}{\partial u^2} \right) h^2 \right]_O \left[ \left( \frac{\partial {}_s g_\ell}{\partial v} - \frac{\partial {}_s g_\ell}{\partial u} \right)_E - \left( \frac{\partial {}_s g_\ell}{\partial v} - \frac{\partial {}_s g_\ell}{\partial u} \right)_W \right] h^3 \\
&+ \left[ f(r) \frac{d\mathcal{Q}_s}{dr} \right]_O \left[ \left( \frac{\partial {}_s g_\ell}{\partial v} - \frac{\partial {}_s g_\ell}{\partial u} \right)_E + \left( \frac{\partial {}_s g_\ell}{\partial v} - \frac{\partial {}_s g_\ell}{\partial u} \right)_W \right] h^4 \\
&- 3 \left[ f(r) \frac{d\mathcal{Q}_s}{dr} \right]_O ({}_s g_\ell^E - {}_s g_\ell^W) h^3 + \mathcal{O}(h^6).
\end{aligned} \tag{2.55}$$

Since, from Eqs. (2.35) and (2.44), the values at the points  $E$ ,  $W$  and  $S$  of  ${}_s g_\ell$  and its derivatives are known, we are able to calculate, via Eq. (2.55), the value of  ${}_s g_\ell$  at the point  $N$ . Additionally, we need to calculate the first order derivatives of  ${}_s g_\ell$  at the point  $N$ . Those derivatives are easily obtained by integrating Eq. (2.34) once along  $u = u_0 + h$  and once along  $v = v_0 + h$ :

$$\begin{aligned}
\left( \frac{\partial {}_s g_\ell}{\partial v} \right)_N &= \left( \frac{\partial {}_s g_\ell}{\partial v} \right)_E + \left( \int_{u_0-h}^{u_0+h} \frac{\partial^2 {}_s g_\ell}{\partial v \partial u} du \right)_{v_0+h} = \left( \frac{\partial {}_s g_\ell}{\partial v} \right)_E - \left( \int_{u_0-h}^{u_0+h} \mathcal{Q}_s(r) {}_s g_\ell du \right)_{v_0+h}, \\
\left( \frac{\partial {}_s g_\ell}{\partial u} \right)_N &= \left( \frac{\partial {}_s g_\ell}{\partial u} \right)_W + \left( \int_{v_0-h}^{v_0+h} \frac{\partial^2 {}_s g_\ell}{\partial v \partial u} dv \right)_{u_0+h} = \left( \frac{\partial {}_s g_\ell}{\partial u} \right)_W - \left( \int_{v_0-h}^{v_0+h} \mathcal{Q}_s(r) {}_s g_\ell dv \right)_{u_0+h}.
\end{aligned} \tag{2.56}$$

We then use Eq. (2.39) and Eqs. (2.45)–(2.54) to calculate the above integrals to  $\mathcal{O}(h^4)$ . Once these derivatives are known, we can continue to apply this procedure consecutively throughout the whole grid in order to obtain  ${}_s g_\ell(v, u)$  at the various nodes. Note that this scheme is not restricted to the scalar case only, Eq. (2.55) and Eq. (2.56) are given in terms of  $\mathcal{Q}_s(r)$  and as can be seen in Eq. (2.36) and Eqs. (2.44), this method applies to  $s = 0, \pm 1, \pm 2$ . Thus, this CID method, can be used to solve Eq. (2.30) as long as its initial data is written as in Eq. (2.35).

O’Toole, Ottewill and Wardell in [65] came up with a new approach to implement a higher order method which consists in calculating the necessary derivatives of  ${}_0 g_\ell$  along the light cone to have a given order in  $h$ . While Eq. (2.55) and Eq. (2.56) require three previously evolved values to compute the next one, the approach in [65] requires more

than three values in order to have a higher order scheme. From Eq. (19) in [65] (which is the equivalent expression to Eq. (2.55)), we clearly observe this dependency on points outside the current square. By comparing these two expressions, the key difference is that in our case the value of  $g_\ell^N$  only depends on values at points  $E$ ,  $W$ , and  $S$ . However, instead of requiring data at more neighbouring points as in [65], we require the evaluation of first order derivatives at  $E$ ,  $W$ , and  $S$ .

## 2.2.2 The radial Regge-Wheeler equation

Given the  $\ell$ -mode decomposition for  ${}_sG_{\text{ret}}$  in Eq. (2.29), we go further and decompose  ${}_sG_\ell$  as

$${}_sG_\ell(r, r'; \Delta t) = \frac{1}{2\pi} \int_{-\infty}^{\infty} {}_s\tilde{G}_{\omega\ell}(r, r') e^{-i\omega\Delta t} d\omega, \quad (2.57)$$

where  ${}_s\tilde{G}_{\omega\ell}$  are the Fourier modes of  ${}_sG_\ell$ . Inserting this decomposition into Eq. (2.30) produces the (sourced) radial Regge-Wheeler equation for arbitrary spin:

$$\left[ \frac{d^2}{dr_*^2} + \omega^2 - f \left( \frac{\ell(\ell+1)}{r^2} + \frac{2M(1-s^2)}{r^3} \right) \right] {}_s\tilde{G}_{\omega\ell} = -\delta(r_* - r'_*). \quad (2.58)$$

Indeed, the above equation indicates that  ${}_s\tilde{G}_{\omega\ell}$  is a GF for Eq. (1.75). Instead of solving Eq. (2.58) directly, we apply the method of factorized Green functions and construct  ${}_s\tilde{G}_{\omega\ell}$  from two homogeneous solutions to Eq. (2.58), namely  ${}_s\tilde{X}_{\omega\ell}^{\text{in}}$  and  ${}_s\tilde{X}_{\omega\ell}^{\text{up}}$ . The asymptotic boundary conditions for these two solutions are

$${}_s\tilde{X}_{\omega\ell}^{\text{in}} \sim \begin{cases} {}_s\tilde{X}_{\omega\ell}^{\text{in,tra}} e^{-i\omega r_*}, & r_* \rightarrow -\infty, \\ {}_s\tilde{X}_{\omega\ell}^{\text{in,inc}} e^{-i\omega r_*} + {}_s\tilde{X}_{\omega\ell}^{\text{in,ref}} e^{i\omega r_*}, & r_* \rightarrow \infty \end{cases} \quad (2.59)$$

and

$${}_s\tilde{X}_{\omega\ell}^{\text{up}} \sim \begin{cases} {}_s\tilde{X}_{\omega\ell}^{\text{up,inc}} e^{i\omega r_*} + {}_s\tilde{X}_{\omega\ell}^{\text{up,ref}} e^{-i\omega r_*}, & r_* \rightarrow -\infty, \\ {}_s\tilde{X}_{\omega\ell}^{\text{up,tra}} e^{i\omega r_*}, & r_* \rightarrow \infty \end{cases}. \quad (2.60)$$

In this way,  ${}_s\tilde{G}_{\omega\ell}(r, r')$  is given by

$$\begin{aligned} {}_s\tilde{G}_{\omega\ell}(r, r') &= - \frac{{}_s\tilde{X}_{\omega\ell}^{\text{in}}(r_{<}) {}_s\tilde{X}_{\omega\ell}^{\text{up}}(r_{>})}{W({}_s\tilde{X}_{\omega\ell}^{\text{in}}, {}_s\tilde{X}_{\omega\ell}^{\text{up}})} \\ &= - \frac{{}_s\tilde{X}_{\omega\ell}^{\text{in}}(r') {}_s\tilde{X}_{\omega\ell}^{\text{up}}(r) \theta(r' - r) + {}_s\tilde{X}_{\omega\ell}^{\text{in}}(r) {}_s\tilde{X}_{\omega\ell}^{\text{up}}(r') \theta(r - r')}{W({}_s\tilde{X}_{\omega\ell}^{\text{in}}, {}_s\tilde{X}_{\omega\ell}^{\text{up}})} \end{aligned} \quad (2.61)$$

where  $r_< = \min(r, r')$ ,  $r_> = \max(r, r')$ ,  $W({}_s\tilde{X}_{\omega\ell}^{\text{in}}, {}_s\tilde{X}_{\omega\ell}^{\text{up}})$  is the Wronskian and is given by

$$W({}_s\tilde{X}_{\omega\ell}^{\text{in}}, {}_s\tilde{X}_{\omega\ell}^{\text{up}}) = {}_s\tilde{X}_{\omega\ell}^{\text{in}} \frac{d}{dr_*} {}_s\tilde{X}_{\omega\ell}^{\text{up}} - {}_s\tilde{X}_{\omega\ell}^{\text{up}} \frac{d}{dr_*} {}_s\tilde{X}_{\omega\ell}^{\text{in}}. \quad (2.62)$$

There are a handful of methods for computing  ${}_s\tilde{G}_{\omega\ell}$ . The so-called MST method (named after Mano, Suzuki, and Takasugi [66, 67, 68]) provides an expansion in terms of hypergeometric functions to calculate  ${}_s\tilde{X}_{\omega\ell}^{\text{in}}$  and  ${}_s\tilde{X}_{\omega\ell}^{\text{up}}$ . By providing the necessary boundary conditions, one can also implement a numerical method. Depending on the regime we are interested in, we should select the appropriate method for that specific regime. For instance, the MST method is very efficient in providing accurate solutions for  $M\omega$  small. When moving to the opposite regime (i.e., large  $M\omega$  and (or) large  $\ell$ ), a numerical method might be more practical. The downside of a numerical approach is in finding an accurate way to calculate the boundary conditions. For  ${}_2\tilde{X}_{\omega\ell}^{\text{up}}$ , the boundary conditions (obtained via an asymptotic expansion) need to be placed on an appropriate value of  $r_*$  since its accuracy varies with  $\omega$  and  $\ell$ . As we detail in the next sections, we adopt an analytical method (based on a series expansion) to calculate  ${}_2\tilde{X}_{\omega\ell}^{\text{in}}$  and a numerical method for  ${}_2\tilde{X}_{\omega\ell}^{\text{up}}$ .

There is a public software repository called “*Black Hole Perturbation Toolkit*”<sup>7</sup> (BHPT) where one can find very useful tools for self-force (SF) calculations. This repository collects many codes and results obtained by different contributors<sup>8</sup> and, particularly, there is a package called *Regge-Wheeler* where one can find an implementation of the MST method for  ${}_s\tilde{X}_{\omega\ell}^{\text{in}}$  and  ${}_s\tilde{X}_{\omega\ell}^{\text{up}}$  together with a numerical method.

We found a technical limitation in the MST method implemented in the BHPT. As  $\ell$  and/or  $M\omega$  increases, the method for calculating the renormalised angular momentum  $\nu$  loses significant precision (see Fig. 3). To diminish this issue, we could increase the working precision during the calculations. However, we observed that the accuracy for  $\nu$  did not increase linearly with the working precision. That is why we follow a different approach to compute  ${}_s\tilde{X}_{\omega\ell}^{\text{in}}$  and  ${}_s\tilde{X}_{\omega\ell}^{\text{up}}$ .

<sup>7</sup><https://bhptoolkit.org>.

<sup>8</sup><https://bhptoolkit.org/users.html>.

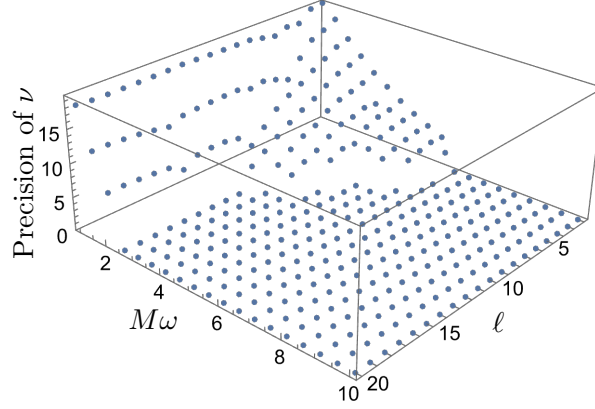


Figure 3 – Numerical precision for the method (implemented in the BHPT) which calculates the renormalised angular momentum  $\nu$ . For this test, we fixed the precision of  $\omega$  to 36 and calculated  $\nu$  for different values of  $\omega$  and (integer) values of  $\ell$  (blue dots). We observe that the precision in  $\nu$  drops as  $\omega$  and  $\ell$  increases. In the area where the precision is zero, the method was not able to calculate  $\nu$ .

### Calculation of ${}_s\tilde{X}_{\omega\ell}^{\text{in}}$

For  ${}_2\tilde{X}_{\omega\ell}^{\text{in}}$  we follow the prescription previously developed in [69]. We write  ${}_2\tilde{X}_{\omega\ell}^{\text{in}}$  in terms of a new function  $y(r, \omega)$

$${}_s\tilde{X}_{\omega\ell}^{\text{in}} = \left(\frac{r}{2M}\right)^{1+s} \left(\frac{r}{2M} - 1\right)^{-i2M\omega} y(r, \omega). \quad (2.63)$$

By inserting the above equation in Eq. (1.75), we find that  $y(r, \omega)$  satisfies the differential equation

$$r^2 f \frac{d^2 y(r, \omega)}{dr^2} + (B_1 + B_2 r) \frac{dy(r, \omega)}{dr} + (\omega^2 r^2 f - 2\eta\omega r f + B_3) y(r, \omega) = 0, \quad (2.64)$$

where

$$B_1 = -2M(2s + 1), \quad (2.65)$$

$$B_2 = 2(1 + s - i2M\omega), \quad (2.66)$$

$$B_3 = s(s + 1) - \ell(\ell + 1) - i2M(2s + 1)\omega + 8M^2\omega^2, \quad (2.67)$$

$$\eta = -2M\omega. \quad (2.68)$$

In [69] Leaver provides a detailed procedure for solving Eq. (2.64). In particular, he refers to a previous work of Jaffé [70] in which  $y(r, \omega)$  is solved by providing the following ansatz

$$y(r, \omega) = e^{i\omega r} \left(\frac{r}{2M}\right)^{-\frac{1}{2}B_2 - i\eta} u(f), \quad (2.69)$$

where  $u(f)$  satisfies the differential equation

$$f(1-f)^2 u''(f) + (c_1 + c_2 f + c_3 f^2) u'(f) + (c_4 + c_5 f) u(f) = 0, \quad (2.70)$$

with

$$\begin{aligned} c_1 &= B_2 + \frac{B_1}{2M}, \\ c_2 &= -2(c_1 + 1 + i(\eta - 2M\omega)), \\ c_3 &= c_1 + 2(1 + i\eta), \\ c_5 &= \left(\frac{1}{2}B_2 + i\eta\right) \left(\frac{1}{2}B_2 + i\eta + 1 + \frac{B_1}{2M}\right), \\ c_4 &= -c_5 - \frac{1}{2}B_2 \left(\frac{1}{2}B_2 - 1\right) + \eta(i - \eta) + i2M\omega c_1 + B_3. \end{aligned}$$

Lastly, Eq. (2.69) is solved via a series expansion about  $f = 0$ , i.e.,

$$u(f) = \sum_{n=0}^{\infty} a_n f^n, \quad (2.71)$$

where  $a_n$  are coefficients to be determined. By inserting the above series in Eq. (2.69), the coefficients  $a_n$  satisfy the following three-term recurrence relations

$$\alpha_0 a_1 + \beta_0 a_0 = 0, \quad (2.72)$$

$$\alpha_n a_{n+1} + \beta_n a_n + \gamma_n a_{n-1} = 0, \quad n > 0, \quad (2.73)$$

where

$$\alpha_n = (n+1) \left( n + B_2 + \frac{B_1}{2M} \right), \quad (2.74)$$

$$\beta_n = -2n^2 - 2 \left( B_2 + i(\eta - 2M\omega) + \frac{B_1}{2M} \right) n \quad (2.75)$$

$$- \left( \frac{1}{2}B_1 + i\eta \right) \left( B_2 + \frac{B_2}{2M} \right) + i\omega (B_1 + 2MB_2) + B_3, \quad (2.76)$$

$$\gamma_n = \left( n - 1 + \frac{1}{2}B_2 + i\eta \right) \left( n + \frac{1}{2}B_2 + i\eta + \frac{B_1}{2M} \right). \quad (2.77)$$

This approach for calculating  ${}_s\tilde{X}_{\omega\ell}^{\text{in}}$  turns out to be efficient for the different regimes in the frequency  $\omega$ . Moreover, the first order derivative for  ${}_s\tilde{X}_{\omega\ell}^{\text{in}}$  is immediate from Eqs. (2.63), (2.69) and (2.71).

## Calculation of ${}_s\tilde{X}_{\omega\ell}^{\text{up}}$

The method we choose for calculating  ${}_s\tilde{X}_{\omega\ell}^{\text{up}}$  relies in solving Eq. (1.75) numerically. By denoting  ${}_s\tilde{X}_{\omega\ell}^{\text{up}'}(r) \equiv \frac{d}{dr}{}_s\tilde{X}_{\omega\ell}^{\text{up}}(r) = y_2(r)$ , Eq. (1.75) can be rewritten as

$${}_s\tilde{X}_{\omega\ell}^{\text{up}'}(r) = y_2(r), \quad (2.78)$$

$$f \frac{d}{dr} (f y_2(r)) = \frac{f}{r^2} \left( \ell(\ell + 1) + \frac{2M(1 - s^2)}{r} \right) {}_s\tilde{X}_{\omega\ell}^{\text{up}}(r). \quad (2.79)$$

The boundary conditions we use to solve this system are constructed from the purely outgoing waves at  $r_* \rightarrow \infty$ . From a numerical point of view, we place this limit in a region known as the *wave zone*. Within this region, gravitational waves propagate freely, do not depend on their source composition, and obey the superposition principle. We then place the boundary conditions on a value  $R$  of the radial coordinate  $r$  within the wave zone<sup>9</sup>. We establish the boundary conditions as an asymptotic series

$${}_s\tilde{X}_{\omega\ell}^{\text{up}}(r) \sim e^{i\omega r_*} \sum_{n=0}^N \frac{b_n}{r^n}, \quad r \rightarrow \infty \quad (2.80)$$

$$y_2(r) = {}_s\tilde{X}_{\omega\ell}^{\text{up}'}(r) \sim e^{i\omega r_*} \sum_{n=0}^{N-1} \frac{b_n}{r^n} \left( \frac{i\omega}{f(r)} - \frac{n}{r} \right), \quad r \rightarrow \infty \quad (2.81)$$

where the coefficients  $b_n$  satisfy a recurrence relation<sup>10</sup>, and  $N$  is determined according to the required precision for the numerical scheme applied for solving Eqs. (2.78)–(2.79). More specifically, we determine  $N$  by inserting  ${}_s\tilde{X}_{\omega\ell}^{\text{up}}(R)$ ,  ${}_s\tilde{X}_{\omega\ell}^{\text{up}'}(R)$  and  ${}_s\tilde{X}_{\omega\ell}^{\text{up}''}(R)$  into Eq. (1.75) and imposing the left hand side to be  $\mathcal{O}(10^{-k})$  where  $k$  represents the *precision* of the numerical method. This indirect way of approximating the precision for  ${}_s\tilde{X}_{\omega\ell}^{\text{up}}(R)$  is not ideal but we observed it worked well in providing the minimum required precision for the boundary conditions.

In the BHPT toolkit, there is a working code that implements this procedure for determining the boundary conditions for  ${}_s\tilde{X}_{\omega\ell}^{\text{up}}$ . Then, the BHPT solves the radial RWE using the numerical integrator embedded in the *Mathematica* software package. In the results we show later on, we made use of this code to obtain  ${}_s\tilde{X}_{\omega\ell}^{\text{up}}$ .

<sup>9</sup>For a given a value of  $\omega$ ,  $R$  can be estimated via the condition  $\omega R \gg 1$ .

<sup>10</sup>This relation can be obtained by putting the asymptotic series back into the radial RWE and demanding each term in  $1/R^n$  to vanish.



### 2.2.3 Convergence of Fourier integral of ${}_s\tilde{G}_{\omega\ell}$ and its radial derivative

Since the Fourier integrals of  ${}_s\tilde{X}_{\omega\ell}^{\text{in}}$  and  ${}_s\tilde{X}_{\omega\ell}^{\text{up}}$  converge, it is not difficult to show that the Fourier integral of  ${}_s\tilde{G}_{\omega\ell}$  converges. When working with  ${}_s\tilde{G}_{\omega\ell}$ , in principle, it is not necessary to verify whether the Fourier integral of its radial derivative converges or not. However, for self-force calculations, these derivatives are eventually required. We thus go a step further and explore the radial derivative of  ${}_s\tilde{G}_{\omega\ell}$ .

A simple way to investigate the convergence of the Fourier integral of  ${}_s\tilde{G}_{\omega\ell}$  can be done by providing a large- $\omega$  asymptotic expansion for  ${}_s\tilde{X}_{\omega\ell}^{\text{in}}$  (and  ${}_s\tilde{X}_{\omega\ell}^{\text{up}}$ ). This expansion is given by [71]

$${}_s\tilde{X}_{\omega\ell}^{\text{in}}(r) = e^{-i\omega r^*} \left( 1 + \sum_{n=1}^{\infty} \frac{a_n^{\text{in}}(r)}{\omega^n} \right) + [\dots], \quad (2.82)$$

$${}_s\tilde{X}_{\omega\ell}^{\text{up}}(r) = e^{i\omega r^*} \left( 1 + \sum_{n=1}^{\infty} \frac{a_n^{\text{up}}(r)}{\omega^n} \right) + [\dots], \quad (2.83)$$

where [...] denotes terms with exponential decay, the coefficients  $a_n^{\text{in}}$  and  $a_n^{\text{up}}$  can be computed recursively by inserting Eqs. (2.82)–(2.83) back into Eq. (1.75) and starting with  $a_0^{\text{in}} = a_0^{\text{up}} = 1$ . In principle, in [71] these expansions were proposed for  $s = 0$ . However, here we provide a more general expression which is valid for any spin  $s$ . The coefficients  $a^{\text{in}}$  and  $a^{\text{up}}$  are then given by

$$a_n^{\text{in}}(r) = -\frac{i}{2}f(r)\frac{d}{dr}a_{n-1}^{\text{in}}(r) + \frac{i}{2}\int_{\infty}^r \left[ \frac{\Lambda}{\rho^2} + \frac{2M\hat{s}}{\rho^3} \right] a_{n-1}^{\text{in}}(\rho)d\rho, \quad (2.84)$$

$$a_n^{\text{up}}(r) = \frac{i}{2}f(r)\frac{d}{dr}a_{n-1}^{\text{up}}(r) - \frac{i}{2}\int_{\infty}^r \left[ \frac{\Lambda}{\rho^2} + \frac{2M\hat{s}}{\rho^3} \right] a_{n-1}^{\text{up}}(\rho)d\rho, \quad (2.85)$$

where  $\Lambda = \ell(\ell + 1)$  and  $\hat{s} = 1 - s^2$ . In Appendix A we wrote down these coefficients for  $n = 1, 2, 3, 4$ .

A direct substitution of Eqs. (2.82)–(2.85) in Eq. (2.61) and after taking the limit  $r \rightarrow r'$ , we find that

$$\begin{aligned} {}_s\tilde{G}_{\omega\ell}(r', r') &= \frac{i}{2\omega} + \frac{if(r')(2M\hat{s} + \Lambda r')}{4r'^3\omega^3} + \left[ \Lambda r'^2(f(r')(30M + (3\Lambda - 5)r') - r') \right. \\ &\quad \left. + 4Mr'\hat{s}(3f(r')(M\hat{s} + 8M + (\Lambda - 2)r') - M) \right] \frac{if(r')}{16r'^7\omega^5} + \mathcal{O}\left(\frac{1}{M^6\omega^6}\right), \end{aligned} \quad (2.86)$$

is independent from the direction the limit  $r \rightarrow r'$  is taken from. We also observe that the Fourier integral of Eq. (2.86) will converge except for  $\Delta t = 0$ . This is expected since  ${}_sG_\ell$  has the  $\theta(-\sigma_{\mathcal{M}_2})\theta(\Delta t)$  distributions in it (see p. 58). When looking at each term in the right hand side of Eq. (2.86), we notice that they are purely imaginary. This indicates that for  $r = r'$ ,  $\Re [{}_s\tilde{G}_{\omega\ell}]$  decays exponentially and  $\Im [{}_s\tilde{G}_{\omega\ell}]$  has a power-law decay in  $\omega$ .

For the first order derivatives of  ${}_s\tilde{G}_{\omega\ell}$ , the Heaviside distributions in Eq. (2.61) lead to a direction-dependent limit. In order to inspect this, once again, we take Eqs. (2.82)–(2.85) and insert them in Eq. (2.61). Next, we differentiate the result with respect to  $r$  (similar results arise for  $r'$ ) and take the limit  $r \rightarrow r'$  along both directions. This yields

$$\lim_{r \rightarrow r'^+} \frac{\partial}{\partial r} {}_s\tilde{G}_{\omega\ell}(r, r') = \frac{1}{2f(r')} + \frac{i(\Lambda r'(3M - r') + M\hat{s}(8M - 3r'))}{4r'^5\omega^3} + \mathcal{O}\left(\frac{1}{M^4\omega^4}\right) \quad (2.87)$$

$$\lim_{r \rightarrow r'^-} \frac{\partial}{\partial r} {}_s\tilde{G}_{\omega\ell}(r, r') = -\frac{1}{2f(r')} + \frac{i(\Lambda r'(3M - r') + M\hat{s}(8M - 3r'))}{4r'^5\omega^3} + \mathcal{O}\left(\frac{1}{M^4\omega^4}\right), \quad (2.88)$$

where  $r \rightarrow r'^+$  ( $r \rightarrow r'^-$ ) denotes the direction where  $r$  approaches  $r'$  from larger (smaller) values than  $r'$ . From these asymptotic expressions, we observe in more detail the direction-dependent term in each limit. Furthermore, these terms lead to a  $\pm\delta(\Delta t)$  divergence in the time domain. Due to the type of divergence arising from the direction-dependent terms in  $\lim_{r \rightarrow r'} \frac{\partial}{\partial r} {}_s\tilde{G}_{\omega\ell}(r, r')$ , the terms  $\pm\frac{1}{2f(r')}$  in the right hand side of Eqs. (2.87)–(2.88) are referred to as *quasi-direct* terms [44]. We deal with these quasi-direct terms by subtracting them from the Fourier integral (and add them separately if needed in further calculations). A practical way to remove them is by taking the average of Eqs. (2.87)–(2.88) [44], i.e.,

$$\lim_{r \rightarrow r'} \frac{\partial}{\partial r} {}_s\tilde{G}_{\omega\ell}(r, r') = \frac{1}{2} \lim_{r \rightarrow r'^+} \frac{\partial}{\partial r} {}_s\tilde{G}_{\omega\ell}(r, r') + \frac{1}{2} \lim_{r \rightarrow r'^-} \frac{\partial}{\partial r} {}_s\tilde{G}_{\omega\ell}(r, r'), \quad (2.89)$$

and similarly for  $\frac{\partial}{\partial r'} {}_s\tilde{G}_{\omega\ell}(r, r')$

$$\lim_{r \rightarrow r'} \frac{\partial}{\partial r'} {}_s\tilde{G}_{\omega\ell}(r, r') = \frac{1}{2} \lim_{r \rightarrow r'^+} \frac{\partial}{\partial r'} {}_s\tilde{G}_{\omega\ell}(r, r') + \frac{1}{2} \lim_{r \rightarrow r'^-} \frac{\partial}{\partial r'} {}_s\tilde{G}_{\omega\ell}(r, r'). \quad (2.90)$$

For self-force calculations, the above limits are fundamental to calculate the self-field (e.g., see Eq. (1.14)).

## 2.3 Results for the retarded GF of the Regge-Wheeler equation.

The key quantities to calculate the retarded GF of the RWE are: the Hadamard tail  $V_s$ , the van Vleck determinand  $\Delta^{1/2} = \frac{1}{r r'} \Delta_{2d}^{1/2} \cdot \Delta_{S^2}^{1/2}$  and the  $\ell$ -modes of  ${}_s G_{\text{ret}}$ . We focused on the scalar ( $s = 0$ ) and gravitational ( $s = 2$ ) cases.

In the results for the Hadamard tail  $V_s$ , we truncated the sum in Eq. (2.28) in the following way (see [60])

$$\sum_{i,j,k=0}^{\infty} \rightarrow \sum_{j=0}^{j_{\max}} \sum_{i=0}^{j_{\max}-j} \sum_{k=0}^{j_{\max}-j-i},$$

where we took  $j_{\max} = 21$ . This value for  $j_{\max}$  was determined by the computational power we had for calculating  ${}_s v_{i,j,k}$ .

For the van Vleck determinant, as mentioned earlier, we numerically solved the transport equation for  $\Delta_{2d}^{1/2}$  and also used the expansion provided in [6]. In the process of calculating  $\Delta_{2d}^{1/2}$  we also calculated  $\sigma_{\mathcal{M}_2}$  and  $\eta = \sqrt{-2\sigma_{\mathcal{M}_2}}$ ,

In the DP region, the  $\ell$ -modes of  ${}_s G_{\text{ret}}$  are calculated: via CID (described in Sec. 2.2.1) and via Fourier integral (described in Sec. 2.2.2). Since the result we are interested in is the non-direct part of  ${}_s G_{\text{ret}}$ , we use the method of matched expansions to obtain this it. We also follow another method previously introduced in [6]. This method consists of subtracting  $G_{\ell}^{\text{dir}}$  from  ${}_s G_{\ell}$  and use the result in the mode sum. Let  ${}_s G_{\text{ret}}^{\text{nd}}$  be the non-direct part of  ${}_s G_{\text{ret}}$ , we can construct it via the following mode sum

$${}_s G_{\text{ret}}^{\text{nd}} = \frac{1}{r r'} \sum_{\ell=0}^{\infty} (2\ell + 1) ({}_s G_{\ell} - G_{\ell}^{\text{dir}}) P_{\ell}(\cos \gamma). \quad (2.91)$$

While the purpose of subtracting  $G_{\ell}^{\text{dir}}$  from  ${}_s G_{\ell}$  is to remove the Gaussian distribution located at  $\sigma = 0$  (at  $\Delta t = 0$  in the static case), this process ideally works when we include *all* the  $\ell$ -modes the mode sum of Eq. (2.91). In practice, the mode sum has to be capped at a finite value  $\ell = \ell_{\max}$ . As a result, the high  $\ell$ -modes excluded during the truncation bring back the spurious oscillations (to a lesser extent for  $\eta < \pi$  due to the subtraction of  $G_{\ell}^{\text{dir}}$ ) that were present in Eq. (2.29). Therefore, once again we require to include the smoothing factor  $\exp[-\ell^2/(2\ell_{\text{cut}})^2]$  (previously mentioned in Sec. 2.2) in Eq. (2.91) to smear such oscillations.

In the frequency domain, when we compute the Fourier modes  ${}_s\tilde{G}_{\omega\ell}$ , we make use of the property  ${}_s\tilde{G}_{-\omega\ell}^* = {}_s\tilde{G}_{\omega\ell}$  (which is a direct consequence of  ${}_sG_\ell \in \mathbb{R}$ ) to reduce the integral in Eq. (2.57) to

$${}_sG_\ell(r, r', \Delta t) = \frac{2}{2\pi} \int_0^\infty \Re [{}_s\tilde{G}_{\omega\ell}(r, r')] \cos(\omega\Delta t) d\omega + \frac{2}{2\pi} \int_0^\infty \Im [{}_s\tilde{G}_{\omega\ell}(r, r')] \sin(\omega\Delta t) d\omega. \quad (2.92)$$

Moreover, by considering that  ${}_sG_{\text{ret}}$  is zero when  $\Delta t < 0$ , it is straightforward to conclude that  ${}_sG_\ell = 0$  for  $\Delta t < 0$ . Thus, for some  $T > 0$  we can write

$$\begin{aligned} {}_sG_\ell(r, r', -T) &= \frac{1}{\pi} \int_0^\infty \Re [{}_s\tilde{G}_{\omega\ell}(r, r')] \cos(\omega T) d\omega - \\ &\quad \frac{1}{\pi} \int_0^\infty \Im [{}_s\tilde{G}_{\omega\ell}(r, r')] \sin(\omega T) d\omega = 0, \quad \text{for } T > 0, \end{aligned} \quad (2.93)$$

which immediately implies

$$\int_0^\infty \Re [{}_sG_\ell(r, r')] \cos(\omega\Delta t) d\omega = \int_0^\infty \Im [{}_sG_\ell(r, r')] \sin(\omega\Delta t) d\omega, \quad \text{for } \Delta t > 0. \quad (2.94)$$

Having this in mind,  ${}_sG_\ell(r, r', \Delta t)$  could be calculated from either the real or the imaginary part of  ${}_s\tilde{G}_{\omega\ell}(r, r')$ , i.e.,

$$\begin{aligned} {}_sG_\ell(r, r', \Delta t) &= \frac{2}{\pi} \theta(\Delta t) \int_0^\infty \Im [{}_s\tilde{G}_{\omega\ell}(r, r')] \sin(\omega\Delta t) d\omega \\ &= \frac{2}{\pi} \theta(\Delta t) \int_0^\infty \Re [{}_s\tilde{G}_{\omega\ell}(r, r')] \cos(\omega\Delta t) d\omega. \end{aligned} \quad (2.95)$$

From the asymptotic analysis discussed in Sec. 2.2.3, we can conclude that in Eq. (2.95) the integrand containing  $\Re [{}_s\tilde{G}_{\omega\ell}]$  decays exponentially when  $r = r'$ . Therefore, from a numerical point of view, it is more convenient to use the second integral in Eq. (2.95) to calculate  ${}_sG_\ell(r = r', r'; \Delta t)$ .

### 2.3.1 Spin-0 case

For the spin-0 case, in the DP region, we applied the CID scheme to compute the scalar retarded GF. The stepsize for the scheme was  $2h = 2\frac{5}{12} \times 10^{-2}$ , we truncated the mode sum at  $\ell_{\text{max}} = 100$  and included the smoothing factor with  $\ell_{\text{cut}} = \ell_{\text{max}}/5$ . This result

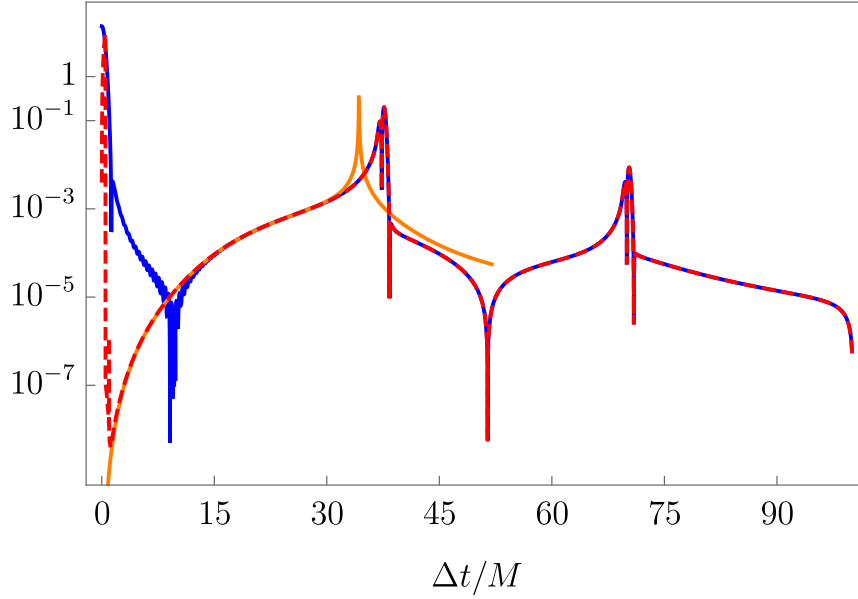


Figure 4 – In blue we plot  ${}_0G_{\text{ret}}$  (as a function of  $\Delta t$ ) obtained via CID, in red its non-direct part  ${}_0G_{\text{ret}}^{\text{nd}}$  obtained using (2.91) and in orange we plot  $-V_0$ . In this scenario  $x$  and  $x'$  are static: with zero angular separation and located at  $r = r' = 6M$  away from the black hole.

corresponds to the blue curve in Fig. 4. In order to obtain the non-direct part of  ${}_0G_{\text{ret}}$  (which we denoted by  ${}_0G_{\text{ret}}^{\text{nd}}$ ), we match the biscalar  $-V_0$  with  ${}_0G_{\text{ret}}$  (the minus sign in front of  $V_0$  is a consequence of Eq. (2.2)). For the scenario in Fig. 4, we can see that the biscalar  $-V_0$  (orange curve) and  ${}_0G_{\text{ret}}$  from the DP do have a region where both converge to the same values. Therefore, it is possible to perform a matching procedure between them to obtain  ${}_0G_{\text{ret}}^{\text{nd}}$ . The second alternative for calculating  ${}_0G_{\text{ret}}^{\text{nd}}$  (i.e., via the mode sum in Eq. (2.91)) corresponds to the red-dashed curve in Fig. 4 where the  $\ell$ -modes of the direct part (i.e.,  $G_{\ell}^{\text{dir}}$ ) were calculated by solving numerically the corresponding transport equations for  $\Delta_{2d}^{1/2}$ .

Although the resulting  ${}_0G_{\text{ret}}^{\text{nd}}$  improved significantly when compared with  ${}_0G_{\text{ret}}$ , the values near coincidence were not computed correctly. The reason for this is that the numerical method for calculating  $\Delta_{2d}^{1/2}$  was not accurate enough for  $\Delta t$  small. Particularly, we were not able to obtain sufficiently accurate values for  $\eta$  near coincidence. However, one can still perform a matching between this non-direct part and  $V_0$  to correct the problem near coincidence.

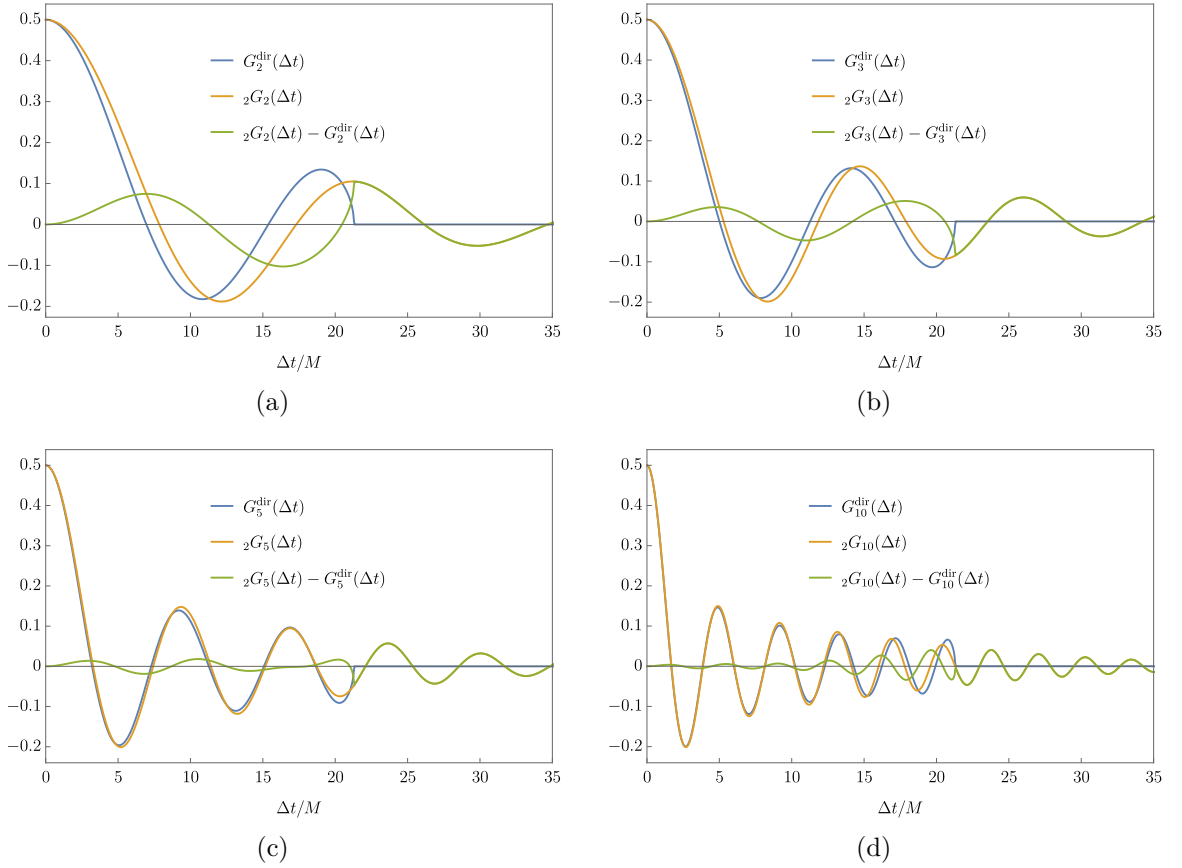


Figure 5 –  $\ell$ -modes of  ${}_2G_{\text{ret}}$  (orange line, according to Eq. (2.29)) and the  $\ell$ -modes of the direct part (blue line, according to Eq. (2.13)) for  $r = r' = 6M$ .

### 2.3.2 Spin-2 case

In Fig. 5 we plot the different  $\ell$ -modes in Eq. (2.91) (with  $s = 2$ ) as functions of  $\Delta t$  and for the same scenario as in Fig. 6. The  $\ell$ -modes of the direct part (blue curve) were calculated via Eq. (2.13) using a coordinate expansion for  $\Delta_{2d}^{1/2}$  and  $\eta$  [6] in the same way as [6]. Besides calculating  ${}_2G_\ell$  (blue curve) via CID, we also obtained them from their frequency modes  ${}_2\tilde{G}_{\omega\ell}$ . We computed  ${}_2\tilde{G}_{\omega\ell}$  via Eq. (2.61). For the In solution  ${}_2\tilde{X}_{\omega\ell}^{\text{in}}$ , we apply the prescription detailed in Sec. 2.2.2. On the other hand, the Up solution  ${}_s\tilde{X}_{\omega\ell}^{\text{up}}$  is obtained using the numerical method available in the BHPT (we briefly discussed this method in Sec. 2.2.2 as well).

Similar to the spin-0 case, we also applied the same methods (and parameters) to compute  ${}_2G_{\text{ret}}$  in both regions, QL and DP. In Fig. 6 we plot  ${}_2G_{\text{ret}}$  (and other related quantities) along a timelike circular geodesic at  $r = r' = 6M$ . The black curve corresponds

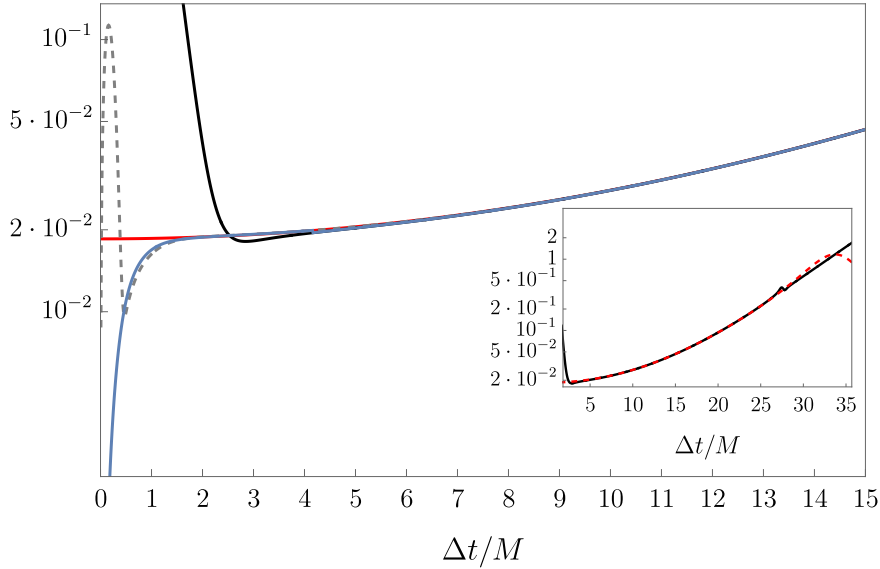


Figure 6 – Comparison between  ${}_2G_{\text{ret}}$  (Black curve) and its non-direct part  ${}_2G_{\text{ret}}^{\text{nd}}$  along a timelike circular geodesic at  $r = r' = 6M$ , for two different methods for  $G_{\ell}^{\text{dir}}$ . The first method (Gray-dashed curve) relies in a numerical method for calculating  $\Delta_{2\text{d}}^{1/2}$  and the second one (Blue curve) makes use of a small coordinate expansion described in [6]. The red curve is the biscalar  $-V_2$ . The subplot shows the continuation of the main plot where we can see that there is indeed a matching region between  ${}_2G_{\text{ret}}$  (black; the lump about  $\Delta t \approx 27.7M$  is due to the first secondary null ray) and  $V_2$  (red-dashed).

to  ${}_2G_{\text{ret}}$ , the red curve is  $-V_2$  calculated using Eq. (2.28) (with the corresponding truncation in the sum), and the blue and gray-dashed curves correspond to the non-direct part of  ${}_2G_{\text{ret}}$ . The gray-dashed curve was calculated in the same way as the red-dashed curve in Fig. 4. For this reason, it also presents the same issue at small  $\Delta t$  as in the spin-0 case. On the other hand, the blue curve is  ${}_2G_{\text{ret}}^{\text{nd}}$  calculated using a small coordinate expansion (prescribed in [6]) for  $\Delta_{2\text{d}}^{1/2}$ . When we compare these two results for the non-direct part with  $V_2$ , we find a good agreement for  $\Delta t > 2M$ . A key difference between the spin-0 and spin-2 cases is in the value of  $V_s$  at coincidence. While  $V_0|_{x=x'}$  is zero, the value of  $V_2|_{x=x'}$  is  $-4M/r^3$ . From the Hadamard form, it is straightforward to show that near coincidence the non-direct part is not simply  $V_2$  but  $V_2(x, x')\theta(-\sigma)\theta(x, x')$ . Since the mode sum was truncated at a finite value of  $\ell$ , this resulted in an imperfect representation of the  $\theta(-\sigma)\theta(x, x')$  factor near coincidence. It is likely that this imperfect representation of the Heaviside factor is responsible for the non-direct part of  ${}_2G_{\text{ret}}$  (blue and gray-dashed curves in Fig. 6) going to zero instead of  $-4M/r^3$ . Near coincidence, we expect that as  $\ell_{\text{cut}} \rightarrow \infty$  the non-direct part tends to  $V_2$ .

In Fig. 7 we plot  ${}_2G_{\text{ret}}$  (and its radial derivative) along a timelike circular geodesic

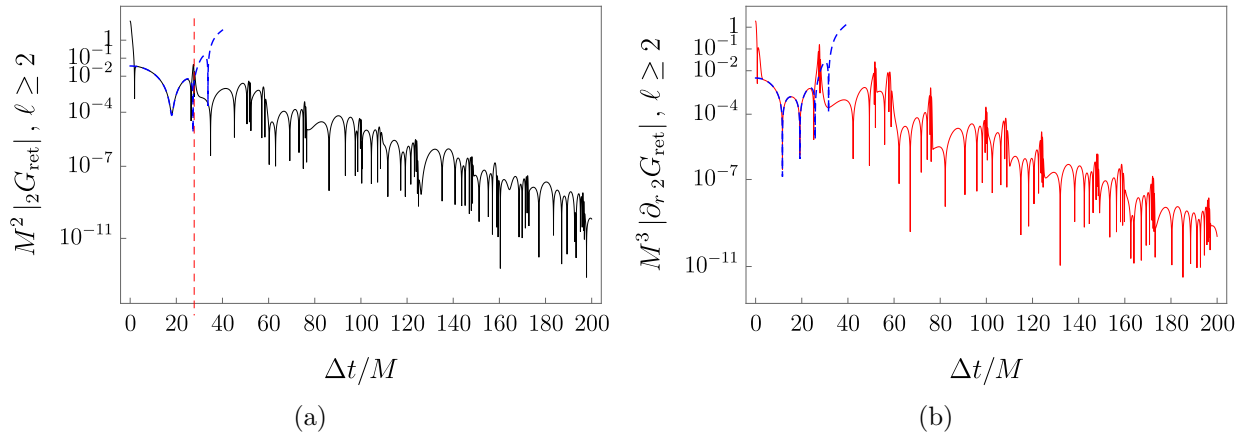


Figure 7 – Left: Absolute value of  ${}_2G_{\text{ret}}$  excluding the  $\ell = 0, 1$  modes, and along a timelike circular geodesic at  $r = r' = 6M$ . Right: Absolute value of the radial derivative of the left result. The vertical red-dashed line in the left plot marks the end of the maximal normal neighbourhood, in this scenario it is near  $\Delta t \approx 27.7M$ . The blue-dashed curves are the absolute values of  $-V_2 - \frac{1}{r^2} \sum_{\ell=0}^1 (2\ell + 1) {}_2G_\ell P_\ell(\cos(\sqrt{M/r^3} \Delta t))$  (left plot) and its radial derivative (right plot).

at  $r = r' = 6M$  without including the contributions from the  $\ell = 0, 1$  modes since they have no physical meaning<sup>11</sup>. The dashed-blue curves corresponds to  $V_2$  (left) and its radial derivative (right), also excluding the corresponding contributions from the first two  $\ell$ -modes.

When we compared the  $\ell$ -modes computed via CID with the ones constructed via integration of  ${}_2\tilde{G}_{\omega\ell}$ , we found a minimum of nine digits of agreement between both methods at early times ( $\Delta t < 10M$ ), and a minimum of seven digits at late times ( $\Delta t \approx 100M$ ). As  $\ell$  increases this minimum agreement drops to six digits at early times and five digits at late times. Since the frequency domain method is expected to be more accurate at late times, we presume that the accumulated error in the CID scheme is responsible for this drop.

### 2.3.3 Regularisation process in the frequency domain

Although the regularisation process via Eq. (2.91) provided significant improvements in the scalar case, in the spin-2 case the Heaviside distribution present in  ${}_sG_{\text{ret}}^{\text{md}}$  made the mode sum to approach  $V_2$  in an inadequate way. As an alternative to the

<sup>11</sup>As detailed in Sec. 1.8.3, the first two modes  $h_{\mu\nu}^{(0)}$  and  $h_{\mu\nu}^{(1)}$  cannot be obtained from the RWE. The  $\ell = 0, 1$  modes resulting from solving Eq. (2.30) are not associated to  $h_{\mu\nu}^{(\ell)}$ .



method of matched expansion for solving this issue, we explored a prescription previously introduced in [44]. Despite the method was applied on an approximation for  ${}_s\tilde{G}_{\omega\ell}$  to 1PN (post-Newtonian) order, the procedure should not depend on it. The prescription consists of taking the regularisation process to the frequency domain. In order to accomplish this, we require to calculate the Fourier modes of  $G_\ell^{\text{dir}}$ . This is still an open problem not completely figured out yet.

In [72] the authors came up with a new procedure to regularise the (spin-0) Feynman Green function<sup>12</sup>  $G_F(x, x')$  in Bertotti-Robinson spacetime. This method consists of providing an expansion in  $\delta$  (a small parameter that measures the geodesic distance between  $x$  and  $x'$ ) for the singular part of  $G_F(x, x')$

$$G_S(x, x') = \frac{G_S^{(-2)}(x, x')}{\delta^2} + \frac{G_S^{(-1)}(x, x')}{\delta} + G_S^{(0)}(x, x') + \dots \quad (2.96)$$

where  $G_S^{(n)}(x, x')$  are the coefficients of the expansion. Next, they perform an  $\ell$ -mode and Fourier decomposition of the coefficients  $G_S^{(n)}(x, x')$  (where  $n = -2, -1, 0, \dots$ ), i.e.,

$$G_S^{(n)}(x, x') = \frac{1}{rr'} \sum_{\ell=0}^{\infty} (2\ell + 1) \left[ \frac{1}{2\pi} \int_{-\infty}^{\infty} g_{\omega\ell}^{(n)}(r, r') e^{-i\omega\Delta t} d\omega \right] P_\ell(\cos \gamma), \quad (2.97)$$

where  $g_{\omega\ell}^{(n)}(r, r')$  are the Fourier modes of the  $\ell$ -modes of  $G_S^{(n)}(x, x')$ . Once the modes  $g_{\omega\ell}^{(n)}$  are determined, one can reconstruct the first leading order terms in the expansion of Eq. (2.96) and proceed with the regularisation process.

Although the results in [72] are for Bertotti-Robinson spacetime, later on the authors were able to calculate the first three  $G_S^{(n)}(x, x')$  coefficients in Schwarzschild spacetime [73]. In particular, for  $n = -2$ , they found out that

$$g_{\omega\ell}^{(-2)}(r, r') = \frac{rr'}{2f} |\omega| j_\ell(\beta|\omega|\alpha_-) h_\ell^{(1)}(\beta|\omega|\alpha_+), \quad (2.98)$$

where  $j_\ell(\cdot)$  and  $h_\ell^{(1)}(\cdot)$  are, respectively, the spherical Bessel and Hankel (of first kind) functions,  $\beta = \frac{r}{\sqrt{f}}$ ,  $\alpha_\pm = \left(\alpha \pm \sqrt{\alpha^2 - 1}\right)^{1/2}$  and  $\alpha = 1 + \frac{(r-r')^2}{2r^2f}$ . The Fourier integral of  $g_{\omega\ell}^{(-2)}$  leads to the following  $\ell$ -mode

$$G_\ell^{(-2)}(r, r'; \Delta t) = \frac{1}{2\pi} \int_{-\infty}^{\infty} g_{\omega\ell}^{(-2)} e^{-i\omega\Delta t} d\omega \quad (2.99)$$

$$= \frac{1}{2} \frac{r'}{r} P_\ell \left( \alpha - \frac{\Delta t^2}{2\beta^2} \right) \theta \left( 1 - \alpha + \frac{\Delta t^2}{2\beta^2} \right) \theta \left( 1 + \alpha - \frac{\Delta t^2}{2\beta^2} \right), \quad (2.100)$$

<sup>12</sup>The Feynman Green function satisfies the wave equation  $\square G_F(x, x') = -\delta_4(x, x')$

which is connected to the  $\ell$ -modes of the Feynman Green function.

These partial results are the closest expression that could lead to a potential regularisation process in the frequency domain. Although  $G_S(x, x')$  is not the direct part of  ${}_2G_{\text{ret}}$ , it is well known [25, 59] that  ${}_sG_{\text{ret}}$  is proportional to the real part of the Feynman Green function. Thus, it would not be surprising to find a relation between  $g_{\omega\ell}^{(n)}$  and the actual Fourier modes of  $G_\ell^{\text{dir}}$ . In fact, the authors in [72] recently proved that after the change  $|\omega| \rightarrow \omega$  in Eq. (2.98),  $g_{\omega\ell}^{(-2)}$  is indeed the leading order coefficient needed to construct the Fourier modes of  $G_\ell^{\text{dir}}$  [73]

In Fig. 8 we compare the real (top) and the imaginary (bottom) parts of  ${}_2\tilde{G}_{\omega\ell}$  and  $g_{\omega\ell}^{(-2)}$  for  $\ell = 2$  and  $r = r' = 6M$ . For the real part, we observe that  $\Re[{}_2\tilde{G}_{\omega\ell}]$  and  $\Re[g_{\omega\ell}^{(-2)}]$  do not have the same decay as  $\omega$  increases. To understand in detail the difference between  ${}_s\tilde{G}_{\omega\ell}$  and  $g_{\omega\ell}^{(-2)}$ , we examine the large- $\omega$  asymptotic for  $g_{\omega\ell}^{(-2)}$  (after taking  $|\omega| \rightarrow \omega$  and  $r = r'$ )

$$g_{\omega\ell}^{(-2)} = \frac{r^2}{4f\beta^2\omega} \left(1 - e^{i(2\beta\omega - \ell\pi)}\right) + \mathcal{O}\left(\frac{1}{M^2\omega^2}\right).$$

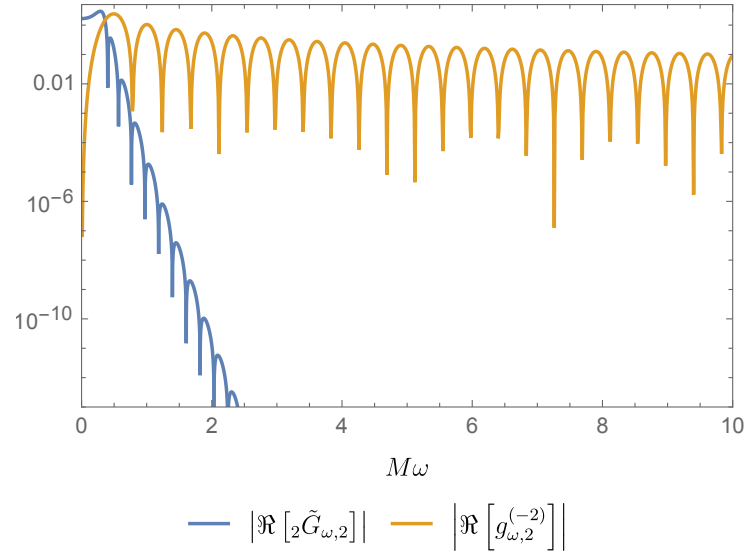
From the leading order in the above asymptotic expansion, we observe that for  $r = r'$ , the frequency in the oscillations seen in Fig. 8 is equal to  $2\beta$  for both, real and imaginary parts. The apparent double frequency in the oscillation of  $|\Im[g_{\omega\ell}^{(-2)}]|$  is merely The oscillation frequency in Fig. 8b is duplicated (i.e., equal to  $4\beta$ ) due to the absolute value introduced for the log-plot. The origin of the oscillations appearing in  $g_{\omega\ell}^{(-2)}$  is connected to the fact that  $G_\ell^{(-2)}(r, r'; \Delta t)$  has a compact support. More precisely, by using Eq. (2.99) and the convolution theorem, we can rewrite  $g_{\omega\ell}^{(-2)}$  as

$$\begin{aligned} g_{\omega\ell}^{(-2)} &= h_{\omega\ell}^{(-2)} * \int_{-\infty}^{\infty} \theta\left(1 - \alpha + \frac{\Delta t^2}{2\beta^2}\right) \theta\left(1 + \alpha - \frac{\Delta t^2}{2\beta^2}\right) d\Delta t \\ &= h_{\omega\ell}^{(-2)} * \frac{2 \sin\left(\sqrt{2(1+\alpha)}\beta\omega\right)}{\omega}, \end{aligned} \quad (2.101)$$

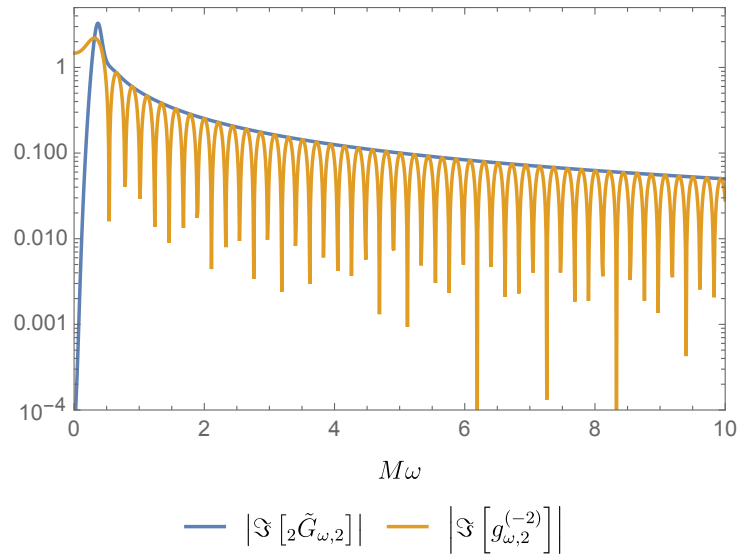
where the  $*$  symbol denotes convolution with respect to  $\omega$ , and

$$h_{\omega\ell}^{(-2)} = \frac{1}{2} \frac{r'}{r} \int_{-\infty}^{\infty} P_\ell\left(\alpha - \frac{\Delta t^2}{2\beta^2}\right) d\Delta t.$$

Eq. (2.101) suggests that for  $r = r'$  ( $\alpha = 1$ ) the oscillations in  $g_{\omega\ell}^{(-2)}$  are indirectly linked to the Heaviside distributions present in  $G_\ell^{(-2)}$ . Conversely, the absence of the  $\theta(1 + \alpha - \frac{\Delta t^2}{2\beta^2})$



(a)



(b)

Figure 8 – Comparison between  ${}_2\tilde{G}_{\omega\ell}$  and  $g_{\omega\ell}^{(-2)}$  for  $\ell = 2$  and  $r = r' = 6M$ . In the top plot we observe that the real parts have no similarities in the large- $\omega$  regime. For the imaginary parts, despite having the same decay in the large- $\omega$  regime, the additional oscillations in  $g_{\omega\ell}^{(-2)}$  is a feature that could bring numerical difficulties in the Fourier integral.

distribution in  ${}_sG_\ell$  makes the distinction between  $g_{\omega\ell}^{(-2)}$  and  ${}_s\tilde{G}_{\omega\ell}$  more evident in the large- $\omega$  regime. This analysis has not been proven rigorously.

From a numerical point of view, these results will not help regularising  ${}_2G_{\text{ret}}$  since subtracting  $g_{\omega\ell}^{(-2)}$  from  ${}_2\tilde{G}_{\omega\ell}$  does not bring any numerical advantage in the  $\omega$ -integral, specially in the real part where the exponential decay of  $\Re[{}_2\tilde{G}_{\omega\ell}]$  turns into a power law decay if we subtract  $\Re[g_{\omega\ell}^{(-2)}]$  from it.

Before concluding this chapter, let us summarize the results we obtained so far. We introduced different tools and methods for computing the retarded GF for the RWE. As we pointed out in Chapter 1, calculating  ${}_sG_{\text{ret}}$  is the first step towards the calculation of the self-force, the next step is to regularise it. To accomplish this task we proposed a handful of methods which consisted in calculating the Hadamard tail  $V_s$  and perform a matching between  ${}_sG_{\text{ret}}$  (obtained via Eq. (2.29)) and  $V_s$ . We also obtained the non-direct part of  ${}_sG_{\text{ret}}$  by subtracting (mode by mode) the direct part (2.12) from (2.29). For  $s = 2$  this subtraction procedure improved significantly the results and only failed in a small interval near  $\Delta t = 0$ .

In situations where there is no overlap between the QL and the DP region, we can extend one of the regions and try to produce an overlap region. This can be accomplished by either providing a more accurate expression for  $V_s$  or improving the mode sum for  ${}_sG_{\text{ret}}$ . Finding more accurate approaches for calculating  $V_s$  is not an easy task. In the next chapter we give a prescription for how to obtain the Hadamard tail via CID in a (toy model) spacetime which shares some symmetries of Schwarzschild spacetime. This toy model establishes the initial techniques and manifests the difficulties we may have to deal with when we move to Schwarzschild spacetime to solve a 4-dimensional CID for  $V_s$  (the Hadamard tail of  ${}_sG_{\text{ret}}$ ).

As a physical application for the results we shown in this chapter, in Chapter 4 we will discuss how the quantum communication near a Schwarzschild black hole is affected by spacetime's curvature via the (scalar) retarded GF.

### 3 Hadamard Tail from Initial Data on the Light Cone in Plebański-Hacyan spacetime

*Note: This Chapter is based on [20].*

Calculating the Hadamard tail is not an easy task. In Chapter 2 we relied on a small coordinate expansion to have an approximation for  $V_s$  near the coincidence. For the method of matched expansions, this approximation for  $V_s$  could be enough for performing a matching with  ${}_sG_{\text{ret}}$  within a region of interest. However, for other applications (see Chapter 4) we may be interested in regions where a small coordinate expansion is not accurate enough and a matching process is not numerically possible. We may improve the accuracy by adding additional terms in the expansion; however, this approach may rapidly increase computational costs. Therefore, we look for a more accurate and efficient alternative for calculating  $V_s$  than a small coordinate expansion. In this Chapter we provide a numerical scheme that allow us to calculate the Hadamard tail in Plebański-Hacyan spacetime (PH).

The PH spacetime shares the same spherical symmetry we find in Schwarzschild spacetime. This allows us to use the PH spacetime as a toy model to explore some key features about the non-direct part of the retarded Green function. The PH spacetime is a four-dimensional manifold composed by a direct product of a 2-sphere  $\mathbb{S}^2$  and a two-dimensional Minkowski spacetime  $\mathbb{M}_2$ . Its line element in  $(t, y, \theta, \varphi)$  coordinates is given by [74]

$$ds^2 = -dt^2 + dy^2 + d\theta^2 + \sin^2\theta d\varphi^2 = -dt^2 + dy^2 + d\Omega_2^2, \quad (3.1)$$

where we made the units choice that the radius of the 2-sphere is equal to one. The coordinates  $(t, y) \in \mathbb{R}^2$  are global inertial coordinates in  $\mathbb{M}_2$ , and  $(\theta, \varphi)$  are the standard angular coordinates in  $\mathbb{S}^2$ . From the line element in Eq. (3.1), it is straightforward to find that the Ricci scalar for PH spacetime is  $R = 2$ .

We now focus on spin-zero field perturbations. Scalar perturbations satisfy the wave equation, i.e., their retarded Green function satisfies

$$\left(\square_{\text{PH}} - m^2 - \xi R\right) G_{\text{ret}}^{\text{PH}}(x, x') = -4\pi\delta_4(x, x'), \quad (3.2)$$

where  $\square_{\text{PH}}$  is the d'Alembertian operator in  $\mathbb{M}_2 \times \mathbb{S}^2$  (i.e., PH spacetime),  $m$  is the mass of the field,  $\xi$  is a coupling constant and  $x$  and  $x'$  are the field and base spacetime points, respectively.

Within a normal neighbourhood, the Hadamard form for the retarded Green function is given by

$$G_{\text{ret}}^{\text{PH}} = [U_{\text{PH}}(x, x')\delta(\sigma_{\text{PH}}) - V(x, x')\theta(-\sigma_{\text{PH}})]\theta_+(x, x'), \quad (3.3)$$

where  $U_{\text{PH}}$  and  $V$  are two smooth biscalars, and  $\sigma_{\text{PH}}$  is Synge's world function in PH spacetime. We prefer not to add a PH label on the Hadamard tail  $V$  for the sake of the notation we introduce later on. The Hadamard tail  $V$  satisfies the homogeneous wave equation

$$\left(\square_{\text{PH}} - m^2 - \xi R\right) V = 0, \quad (3.4)$$

and it has the following constraint on the light cone [55]

$$\hat{V}_\alpha \sigma_{\text{PH}}^\alpha + \frac{1}{2}(\sigma_{\text{PH}}^\alpha{}_\alpha - 2)\hat{V} = \frac{1}{2}\left(\square_{\text{PH}} - m^2 - \xi R\right) U_{\text{PH}}|_{\sigma_{\text{PH}}=0}, \quad (3.5)$$

where  $\hat{V} \equiv V|_{\sigma_{\text{PH}}=0}$ . The initial condition to solve the above transport equation is the value of  $V$  at coincidence (i.e.,  $x' = x$ ):

$$\hat{V}(x, x) = \frac{1}{12}(1 - 6\xi)R(x) - \frac{1}{2}m^2 = \frac{1}{6}(1 - 6\xi) - \frac{1}{2}m^2, \quad (3.6)$$

which is a direct consequence of  $V$  being a smooth function at coincidence. Thus, the constraint in Eq. (3.5) (together with the initial condition (3.6)) show that  $V$  satisfies a characteristic initial value problem. Having this in mind, a good starting point towards the calculation of  $V$  within a normal neighbourhood is to express  $V$  in terms of the asymptotic series:

$$V(x, x') = \sum_{n=0}^{\infty} \nu_n(x, x')\sigma_{\text{PH}}^n, \quad (3.7)$$

where the coefficients  $\nu_n(x, x')$  satisfy certain recurrence relations in the form of transport equations [25, 75]. In [76] there is a detailed procedure to calculate the  $\nu_n$  coefficients from a series of transport equations. As the coefficient order  $n$  increases, the transport equation for  $\nu_n$  becomes difficult to solve analytically. Another issue to consider while using this approach is related to the convergence of Eq. (3.7). Although this series converges uniformly in normal neighbourhoods [25, 33], its convergence in the maximal normal neighbourhood is not actually guaranteed. A more suitable approach for calculating  $V$  is to expand it in a small *coordinate* distance between  $x$  and  $x'$ . As we detail in the next sections, the approach we follow for calculating  $V$  is by providing a CID scheme where the initial data is obtained from the  $\nu_n$  coefficients.

### 3.1 Hadamard biscalars in PH spacetime

Before going further, it is worth reviewing some of PH spacetime symmetries and see how they are reflected on quantities like the van Vleck determinant  $\Delta_{\text{PH}}$ . Since PH is a product of two manifolds, the van Vleck determinant can be expressed as a product of the van Vleck determinants in  $\mathbb{M}_2$  and  $\mathbb{S}^2$  [55]:

$$\Delta_{\text{PH}}(x, x') = \Delta_{\mathbb{M}_2} \cdot \Delta_{\mathbb{S}^2}, \quad (3.8)$$

where  $\Delta_{\text{PH}} = 1$  is the van Vleck determinant in  $\mathbb{M}_2$  and  $\Delta_{\mathbb{S}^2} = \frac{\gamma}{\sin \gamma}$  is the van Vleck determinant in  $\mathbb{S}^2$ .

Another key quantity is Synge's world function. In this case, the world function  $\sigma_{\text{PH}}$  is simply given by the sum of the world functions  $\sigma_{\mathbb{M}_2}$  and  $\sigma_{\mathbb{S}^2}$  in  $\mathbb{M}_2$  and  $\mathbb{S}^2$ , respectively. That is [55]

$$\sigma_{\text{PH}} = \sigma_{\mathbb{M}_2} + \sigma_{\mathbb{S}^2}. \quad (3.9)$$

Furthermore, these world functions are given by

$$\sigma_{\mathbb{M}_2} = -\frac{1}{2}\eta^2 \equiv -\frac{1}{2}(t - t')^2 + \frac{1}{2}(y - y')^2 \quad (3.10)$$

and

$$\sigma_{\mathbb{S}^2} = \frac{\gamma^2}{2}, \quad (3.11)$$

where  $\gamma$  is given by (2.9).

Consequently, for  $\sigma_{\text{PH}}$  we have

$$\sigma_{\text{PH}}(x, x') = -\frac{1}{2}\eta^2 + \frac{1}{2}\gamma^2 = -\frac{1}{2}(t - t')^2 + \frac{1}{2}(y - y')^2 + \frac{1}{2}\gamma^2, \quad (3.12)$$

where we identify  $\eta$  as the geodesic distance in  $\mathbb{M}_2$  and  $\gamma \in [0, \pi]$  (the angle between  $x$  and  $x'$ ) is the geodesic *separation* in  $\mathbb{S}^2$ . Within a normal neighbourhood of  $\mathbb{S}^2$ ,  $\gamma$  is also a geodesic distance. Null geodesics (for which  $\sigma_{\text{PH}} = 0$  in a normal neighbourhood) focus at the first caustic points:  $\eta = \gamma = \pi$ . After crossing the first caustic, the envelope of null geodesics emanating from a base point  $x'$  forms the (future) boundary of the maximal normal neighbourhood of the base point; this boundary is given by  $\eta = 2\pi - \gamma \in [\pi, 2\pi]$  (see the left panel of Fig.1 in [55]). Since  $V(x, x')$  is only defined in normal neighbourhoods, this will also be part of the boundary of the grid in our numerical scheme. The other part is given by the null hypersurface corresponding to the envelope of future-directed *direct* null geodesics (the characteristic surface where the initial data is placed on and also excludes the non-causal part of the maximal normal neighbourhood), i.e., by  $\eta = \gamma \in [0, \pi)$  (so that it is  $\sigma_{\text{PH}} = 0$  with  $\eta \geq 0$ ). That is, the future boundary  $\eta = 2\pi - \gamma \in [\pi, 2\pi]$  of the maximal normal neighbourhood of an arbitrary base point together with the boundary  $\eta = \gamma \in [0, \pi)$  of the causal future of the base point form the boundary of our numerical grid.

In  $(t, y, \theta, \varphi)$  coordinates, the d'Alembertian  $\square_{\text{PH}}$  takes the standard form

$$\begin{aligned} \square_{\text{PH}} &= \square_{\mathbb{M}_2} + \square_{\mathbb{S}^2}, \\ \square_{\mathbb{M}_2} &= -\frac{\partial^2}{\partial t^2} + \frac{\partial^2}{\partial y^2}, \\ \square_{\mathbb{S}^2} &= \frac{1}{\sin \theta} \frac{\partial}{\partial \theta} \sin \theta \frac{\partial}{\partial \theta} + \frac{1}{\sin^2 \theta} \frac{\partial^2}{\partial \varphi^2}. \end{aligned} \quad (3.13)$$

Furthermore, the symmetries of  $\mathbb{M}_2$  and  $\mathbb{S}^2$  manifolds allow us to reduce the  $\square_{\mathbb{M}_2}$  and  $\square_{\mathbb{S}^2}$  operators to *ordinary* differential operators. Given the geodesic distances  $\eta$  and  $\gamma$ , we find that

$$\square_{\mathbb{M}_2} = -\frac{\partial^2}{\partial \eta^2} - \frac{1}{\eta} \frac{\partial}{\partial \eta} \quad (3.14)$$



and

$$\square_{\mathbb{S}^2} = \frac{\partial^2}{\partial \gamma^2} + \cot \gamma \frac{\partial}{\partial \gamma} = \frac{1}{\sin \gamma} \frac{\partial}{\partial \gamma} \left( \sin \gamma \frac{\partial}{\partial \gamma} \right). \quad (3.15)$$

With this, the wave equation (3.4) becomes

$$\left( \frac{\partial^2}{\partial \gamma^2} + \cot \gamma \frac{\partial}{\partial \gamma} - \frac{\partial^2}{\partial \eta^2} - \frac{1}{\eta} \frac{\partial}{\partial \eta} - \zeta \right) V = 0, \quad (3.16)$$

where  $\zeta \equiv m^2 + \xi R = m^2 + 2\xi$ . As we shall see in the following, this reduction in the d'Alembert operator simplifies the calculation of  $V$ .

Despite the PH spacetime being highly symmetric, out of  $U_{\text{PH}}$  and  $V$ , only  $U_{\text{PH}} = \Delta_{\text{PH}}^{1/2}$  can be calculated analytically. In this theses we propose a numerical method for solving  $V$ . In [55], it was found that  $V = V(\eta, \gamma)$  and  $\nu_n = \nu_n(\gamma)$ ,  $\forall n \geq 0$ . It was also found that in PH spacetime

$$\hat{V} = \nu_0(\gamma) = \frac{1}{8} U_{\text{PH}}(\gamma) \left( 1 - 4\zeta + \frac{1}{\gamma^2} - \frac{\cot \gamma}{\gamma} \right). \quad (3.17)$$

The higher coefficients  $\nu_n$ ,  $n > 0$ , are obtainable from  $\nu_{n-1}$  via the recurrence relation [55]

$$\frac{d}{d\gamma} \left( \gamma^{k+1} \tilde{\nu}_k \right) = -\frac{1}{2k} \frac{\gamma^{k-1/2}}{\sqrt{\sin \gamma}} \left\{ \frac{d}{d\gamma} \left[ \sin \gamma \frac{d}{d\gamma} \left( \sqrt{\frac{\gamma}{\sin \gamma}} \tilde{\nu}_{k-1} \right) \right] - \zeta \sin \gamma \sqrt{\frac{\gamma}{\sin \gamma}} \tilde{\nu}_{k-1} \right\}, \quad (3.18)$$

where  $\nu_n = U_{\text{PH}} \tilde{\nu}_n$ , and the integration constant is determined by imposing regularity at coincidence. For instance, setting  $n = 1$  and solving Eq. (3.18) for  $\tilde{\nu}_1$ , we find that  $\nu_1 = U_{\text{PH}} \tilde{\nu}_1$  is given by

$$\nu_1 = \frac{U_{\text{PH}}}{128\gamma^4} \left[ 15 - \gamma^2 \left( 1 + \gamma^2(1 - 4\zeta)^2 - 8\zeta \right) - 2\gamma \left( 3 - \gamma^2(1 - 4\zeta) \right) \cot \gamma - 9\gamma^2 \csc^2 \gamma \right], \quad (3.19)$$

As mentioned earlier, a more suitable method for obtaining  $V$  is by solving a characteristic initial value problem using  $\hat{V} = \nu_0$  as CID. From the  $\nu_0$  coefficient, we note that  $\hat{V}$  is regular for  $\gamma \in [0, \pi)$  but it diverges as  $\gamma \rightarrow \pi$ . More precisely,  $V$  diverges like  $(\pi - \gamma)^{-3/2}$  at the antipodal points  $\gamma = \pi$ . However, as previously detailed, these points lie outside of the maximal normal neighbourhood. As we will show in the next section, the  $\nu_n$  coefficients in Eq. (3.7) are a key component for establishing the CID data on the light cone. The symmetries present in PH spacetime will allow us to develop

a two dimensional CID scheme for computing  $V$ . More specifically, we are interested in providing a numerical scheme which will evolve initial data placed on the light cone, i.e., on  $\sigma_{\text{PH}} = -\frac{1}{2}\eta^2 + \frac{1}{2}\gamma^2 = 0$ . In order to establish this CID, we use Eqs. (3.7), (3.17) and (3.19). Additionally, we note that  $\eta$  and  $\gamma$  are not suitable variables for the CID problem, we should provide more appropriate ones.

## 3.2 The wave equation as a characteristic initial value problem

We start by introducing the variables

$$u \equiv \eta - \gamma, \quad v \equiv \eta + \gamma, \quad (3.20)$$

which are naturally more suitable for establishing a characteristic initial value problem, since  $\sigma_{\text{PH}} = -\frac{1}{2}uv$ . The d'Alembertian operator in PH spacetime is then given by

$$\square_{\text{PH}} = -4 \frac{\partial^2}{\partial u \partial v} - Q \frac{\partial}{\partial v} - S \frac{\partial}{\partial u}, \quad (3.21)$$

where

$$Q \equiv \frac{2}{v+u} - \cot \frac{v-u}{2},$$

$$S \equiv \frac{2}{v+u} + \cot \frac{v-u}{2}.$$

We now rewrite the wave equation in terms of  $u$  and  $v$

$$\left( 4 \frac{\partial^2}{\partial u \partial v} + Q \frac{\partial}{\partial v} + S \frac{\partial}{\partial u} + \zeta \right) V(x, x') = 0. \quad (3.22)$$

We note the appearance of *first-order* derivatives with respect to  $u$  and  $v$ , arising from the first-order derivatives with respect to  $\eta$  and  $\gamma$  in Eq. (3.16). We also see that the domains for  $u$  and  $v$  are constrained by the range of  $\gamma \in [0, \pi]$  and the region where  $V$  is defined. Later on, we detail the implication of these constraints.

After we rewrote the wave equation in terms of  $u$  and  $v$ , we also need to rewrite the initial data on the light cone in terms of  $u$  and  $v$ . On the  $u$ - $v$  plane in Fig. 9, the light cone of  $x'$  starts at  $u = v = 0$  (which corresponds to the coincidence  $x = x'$ ) and extends

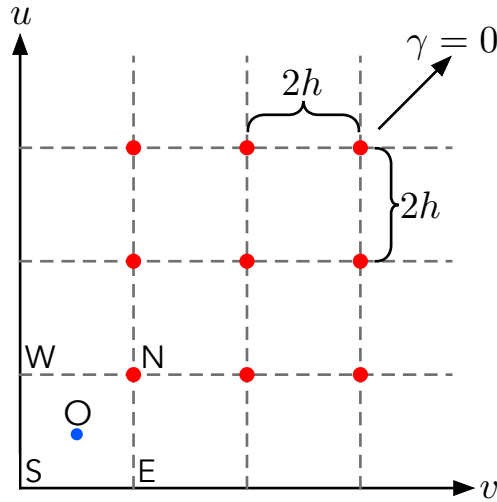


Figure 9 – Grid distribution for a finite difference scheme for solving a two-dimensional PDE where  $u$  and  $v$  denote the independent variables and  $2h$  is the stepsize.

along the  $u = 0$  and  $v = 0$  lines. Therefore, the initial data  $\hat{V}$  expressed in terms of  $u$  and  $v$  is given by

$$\begin{aligned} V|_{u=0} &= \nu_0 \left( \frac{v}{2} \right), \\ V|_{v=0} &= \nu_0 \left( -\frac{u}{2} \right), \end{aligned} \tag{3.23}$$

where  $\nu_0 = \nu_0(\gamma)$  is given in Eq. (3.17).

In this way, the wave equation (3.22) together with the CID (3.23) establish our characteristic initial value problem. In the following, we detail the numerical method to solve it.

### 3.2.1 Numerical scheme

CID schemes in  $1 + 1$ -dimensions are widely known in the literature. In previous works, however, the PDE did not contain first order derivatives as Eq. (3.22) does. More precisely, these CID schemes focus on calculating the  $\ell$ -modes of the retarded Green functions in Schwarzschild spacetime (see Eq. (C2) in [19] for instance). In Refs. [63, 65] we find two approaches for solving a CID problem. In [65], the authors provide an order  $h^6$  scheme which, in principle, can be generalised to arbitrary order. Despite our numerical scheme sharing the same principles as Refs. [63, 65], the first order derivative with respect to  $\gamma$  in Eq. (3.22) introduces a coordinate singularity at  $\gamma = 0$  that requires an addi-

tional analysis. Since  $V = V(\eta, \gamma)$  in PH spacetime, the PDE we are solving is also two dimensional as in Refs. [63, 65] but its domain now becomes the maximal normal neighbourhood. On its turn, this domain constrains the independent variables to the intervals  $u \in [0, 2\pi)$  and  $v \in [0, u]$  (directly related to the range  $\gamma \in [0, \pi)$  inside the maximal normal neighbourhood).

In order for us to compare our CID problem with Refs. [63, 65] and the CID problem in Schwarzschild spacetime in general, without losing generality, we will place the two PH spacetime points  $x$  and  $x'$  on the equator, i.e.,  $x$  and  $x'$  have  $\theta = \theta' = \frac{\pi}{2}$  and  $\varphi' = 0$ , and, as a consequence, we have that  $\gamma \equiv \varphi \in (-\pi, \pi)$  denotes the azimuthal angle of  $x$  (instead of the angular separation). With this change in the range of  $\gamma$ , the variables  $u$  and  $v$  continue to be defined as in (3.20) but now with  $\gamma \in (-\pi, +\pi)$  being an azimuthal angle. The region of interest for calculating  $V(x, x')$  (i.e., the causal part of the maximal normal neighbourhood) is now bounded by  $\eta = 2\pi - \gamma$  together with  $\eta = \gamma$  if  $\gamma \in [0, \pi]$ , and by  $\eta = 2\pi + \gamma$  together with  $\eta = -\gamma$  if  $\gamma \in [-\pi, 0]$  after extending the range of  $\gamma$ . In their turn, the new range for the CID variables changed from  $v \in [0, 2\pi]$  and  $u \in [0, v]$  to  $v, u \in [0, 2\pi)$ .

Now we describe our CID scheme. In the following, we adopt the convention that, unless otherwise explicitly specified, the “order” of a scheme will refer to the local truncation error (LTE); thus, in particular, a “third (fourth) order scheme” will refer to a numerical scheme with LTE of order three (four). We first start with a third order CID scheme. As an introduction to the prescription and for analysing its key distinctions from the previous CID schemes given in Refs. [63, 65], the third order scheme is the simplest scheme we can start with. We then extend the scheme to the next order, a fourth order scheme. In Appendix B we provide the basics for extending the method to a fifth (and even sixth) order scheme.

### 3.2.2 CID scheme setup

The setup for solving the wave equation (3.22) (with (3.23) as CID) requires to construct a uniform grid of points on the  $u - v$  plane (see Fig. 9). The spacing between

points is  $2h$ . Once we establish the grid, we proceed to integrate Eq. (3.22) over each square on the grid. Let  $SENW$  be an arbitrary square in the grid in Fig. 9. Assuming that  $V$  is given at the  $E$ ,  $W$  and  $S$  points,  $V$  at  $N$  is the value we seek for. We have

$$4 \int_{SENW} \frac{\partial^2 V}{\partial v \partial u} dv du + \int_{SENW} Q \frac{\partial V}{\partial v} dv du + \int_{SENW} S \frac{\partial V}{\partial u} dv du + \zeta \int_{SENW} V dv du = 0. \quad (3.24)$$

In order to simplify our notation, from now on a subindex  $N$ ,  $E$ ,  $W$ ,  $S$  or  $O$  in a quantity indicates that the quantity is evaluated at the corresponding point on the grid. The first integral in the left hand side of Eq. (3.24) is immediate, i.e.,

$$\int_{SENW} \frac{\partial^2 V}{\partial v \partial u} dv du = V_N - V_E - V_W + V_S. \quad (3.25)$$

For the remaining three integrals, we Taylor expand the integrands about the central point  $O = (v_O, u_O)$  in the square. Given a function  $F(u, v)$  analytic on  $O$ , its Taylor expansion is given by

$$F(v, u) = \sum_{\substack{0 \leq m, n \leq K \\ m+n \leq K}} \frac{1}{m! n!} \left( \frac{\partial^{m+n} F}{\partial v^m \partial u^n} \right)_O (v - v_O)^m (u - u_O)^n + \mathcal{O}(h^{K+1}), \quad (3.26)$$

where  $K$  determines the order in the expansion. We then use the above expansion (replacing  $F$  with the corresponding integrands) to calculate the last three integrands in Eq. (3.24) to the desired order. This order will determine the order in the scheme.

### 3.2.2.1 Third order CID scheme

Using Eq. (3.26) to order  $h^2$ , the last three integrals in the left hand side of Eq. (3.24) are given by

$$\int_{SENW} Q \frac{\partial V}{\partial v} dv du = 4h^2 Q_O \left( \frac{\partial V}{\partial v} \right)_O + \mathcal{O}(h^4), \quad (3.27)$$

$$\int_{SENW} S \frac{\partial V}{\partial u} dv du = 4h^2 S_O \left( \frac{\partial V}{\partial u} \right)_O + \mathcal{O}(h^4), \quad (3.28)$$

$$\int_{SENW} V dv du = 4h^2 V_O + \mathcal{O}(h^4), \quad (3.29)$$

where, once again, the  $O$  subindex indicates that the corresponding quantity is evaluated at the point  $O$ . Considering the first two leading orders in the Taylor expansion should

(in principle) return the integrals to order  $h^3$ . However, it is straightforward to show that the contribution to the integrals from the next-to-leading order in the Taylor expansion vanishes.

The Taylor coefficients in the right hand side of Eqs. (3.27)–(3.29) are obtained in the following way. We evaluate the Taylor expansion for  $V$  and its first order derivatives at the points  $E$ ,  $W$  and  $S$  to order  $h$ . We thus have a system of three equations to solve for  $V_O$ ,  $\left(\frac{\partial V}{\partial u}\right)_O$  and  $\left(\frac{\partial V}{\partial v}\right)_O$ . We thus find that

$$V_O = \frac{V_E + V_W}{2} + \mathcal{O}(h^2), \quad (3.30)$$

$$\left(\frac{\partial V}{\partial u}\right)_O = \frac{V_W - V_S}{2h} + \mathcal{O}(h), \quad (3.31)$$

$$\left(\frac{\partial V}{\partial v}\right)_O = \frac{V_E - V_S}{2h} + \mathcal{O}(h). \quad (3.32)$$

Therefore, we put the integrals (3.25) and (3.27)–(3.29) together with Eqs. (3.30)–(3.32) back into Eq. (3.24) and solve for  $V_N$ . This yields

$$V_N = -V_S - \left( \frac{V_E + V_W - 2V_S}{u_O + v_O} - \frac{1}{2}(V_E - V_W) \cot \frac{v_O - u_O}{2} \right) h + \left( 1 - \frac{\zeta}{2} h^2 \right) (V_E + V_W) + \mathcal{O}(h^3), \quad (3.33)$$

for  $u_O \neq v_O$ . When comparing the above expression for  $V_N$  with its counterpart (the multipolar modes of the RGF in Schwarzschild spacetime) in Refs. [63, 65], we immediately note the additional term of order  $h$  in Eq. (3.33). This is directly connected to the two *first* order derivatives in Eq. (3.16), a term absent in [63, 65]. In fact, the order in the right hand side of Eqs. (3.31)–(3.32) is the reason for Eq. (3.33) being *third* order, instead of being fourth order as in [63, 65].

Another crucial difference arises from the coordinate singularity in Eq. (3.16), i.e., along  $\gamma = 0$  (or  $u_O = v_O$ ). As can be seen in Eq. (3.33), the cot function is not well-defined for  $u_O = v_O$ . We should look at that term in more detail before calculating  $V_N$  for this particular case. By applying the spherical symmetry of  $\mathbb{M}_2 \times \mathbb{S}^2$ , it follows that  $V(\eta, \gamma) = V(\eta, -\gamma)$ , and this yields the symmetry  $V_E = V_W$  for all squares centered at  $O$  with  $u_O = v_O$ . Thus, the proper way to evaluate the term involving the cot function in

Eq. (3.33) is by taking the limit  $\gamma_O \equiv \frac{v_O - u_O}{2} \rightarrow 0$

$$[(V_E - V_W) \cot \gamma_0]_{\gamma_0=0} = \lim_{\gamma_0 \rightarrow 0} \frac{V_E - V_W}{\tan(\gamma_0)} = \mathcal{O}(h), \quad (3.34)$$

where, in order to take the limit, we applied L'Hôpital's rule and expressed  $V_E$  and  $V_W$  as small  $\gamma$ -expansions. Consequently, for squares with  $u_O = v_O$ ,  $V_N$  is given by

$$V_N = -V_S - h \left( \frac{V_E - V_S}{v_O} \right) + (2 - \zeta h^2) V_E + \mathcal{O}(h^3), \quad \text{for } \gamma_O = 0, \quad (3.35)$$

where, once again, we applied the  $V_E = V_W$  symmetry.

We can now establish the scheme as follows We start by splitting the grid in Fig. (9) into two triangles, we use the  $u = v$  diagonal (i.e.,  $\gamma = 0$ ) to do so. With no particular preference, we apply the scheme to points along the diagonal and *bottom* triangle, and as can be seen in Eq. (3.35), along the diagonal (i.e.,  $u_O = v_O$ )  $V_N$  only depends on  $V_E$  and  $V_S$ . This suggests that, for the choice of bottom triangle, and after applying the symmetries along  $\gamma = 0$ , the initial data is simply given by  $V|_{u=0}$ . Points located on the top triangle are easily obtained using the  $V(\eta, \gamma) = V(\eta, -\gamma)$  symmetry. In case we apply the scheme to points along the diagonal and top triangle, the initial data would be given by  $V|_{v=0}$ . Therefore, the spherical symmetry reduces the amount of data to calculate by almost half regardless of which triangle we decide to evolve.

To conclude, our third order CID scheme consists of calculating  $V_N$  at each point along  $\gamma = 0$  using Eq. (3.35), and for points in the bottom triangle, we use Eq. (3.33). We then evolve the field  $V$  for increasing values of  $u$  by using (3.33) until we reach  $\gamma_O = 0$ ; finally, at  $\gamma_O = 0$ , we switch to using (3.35). In the next subsection we develop a scheme of one higher order.

### 3.2.2.2 Fourth order CID scheme

The starting point for establishing a fourth order CID scheme is to have the integrals in Eq. (3.24) to order  $h^4$ . In fact, this is already the case in Eqs. (3.27)–(3.29). However, we note that the order in the Taylor coefficients given in Eqs. (3.31)–(3.32) lowered the order in the integrals and, consequently, led to a third order scheme. Therefore,

in order to obtain a fourth order CID scheme, the next higher order in Eqs. (3.31)–(3.32) has to be calculated. Including these next higher order terms is connected with higher (than in the third order scheme) Taylor coefficients in Eq. (3.26), i.e., we require to calculate additional Taylor coefficients in Eq. (3.26) (with  $F = V$ ). Furthermore, as we show later on, the expression for  $V_N$  to  $\mathcal{O}(h^4)$  along  $\gamma = 0$  does depend on second order derivatives of  $V$  at the point  $O$ . More precisely, the fourth order CID scheme requires the calculation of seven additional Taylor coefficients in addition to higher order versions of Eqs. (3.31)–(3.32). In order to calculate these Taylor coefficients, we construct a system of 12 equations in the following way. We take Eq. (3.26) (with  $F = V$ ) up to order  $h^3$  (inclusive) and its first order derivatives at the points  $N$ ,  $E$ ,  $W$  and  $S$ . Ten of these equations, when solved, give the required Taylor coefficients, i.e., the values of  $V$  and its first, second and third order derivatives at the point  $O$ . As we see later on, these Taylor coefficients are expressed in terms of  $V$  and its first order derivatives at the points  $E$ ,  $W$ ,  $N$  and  $S$ . Despite calculating ten Taylor coefficients, for the fourth order CID scheme, only five of them are required. Specifically, the expressions

$$8h \left( \frac{\partial V}{\partial u} \right)_O = -5V_S - V_E + 5V_W + V_N - 2h \left( \frac{\partial V}{\partial u} + \frac{\partial V}{\partial v} \right)_S - 2h \left( \frac{\partial V}{\partial u} - \frac{\partial V}{\partial v} \right)_W + \mathcal{O}(h^4), \quad (3.36)$$

$$8h \left( \frac{\partial V}{\partial v} \right)_O = -5V_S + 5V_E + V_W - V_N - 2h \left( \frac{\partial V}{\partial u} + \frac{\partial V}{\partial v} \right)_S + 2h \left( \frac{\partial V}{\partial u} - \frac{\partial V}{\partial v} \right)_E + \mathcal{O}(h^4), \quad (3.37)$$

$$4h^2 \left( \frac{\partial^2 V}{\partial u^2} \right)_O = V_S - V_E - V_W + V_N + 2h \left( \frac{\partial V}{\partial u} \right)_E - 2h \left( \frac{\partial V}{\partial u} \right)_W + \mathcal{O}(h^4), \quad (3.38)$$

$$4h^2 \left( \frac{\partial^2 V}{\partial v^2} \right)_O = V_S - V_E - V_W + V_N - 2h \left( \frac{\partial V}{\partial v} \right)_E + 2h \left( \frac{\partial V}{\partial v} \right)_W + \mathcal{O}(h^4), \quad (3.39)$$

$$4h^2 \left( \frac{\partial^2 V}{\partial v \partial u} \right)_O = V_N + V_S - V_E - V_W + \mathcal{O}(h^4), \quad (3.40)$$



are directly used in the fourth order scheme. The expressions for the five remaining Taylor coefficients are

$$4V_O = 2V_E + 2V_W + h \left( \frac{\partial V}{\partial u} - \frac{\partial V}{\partial v} \right)_E - h \left( \frac{\partial V}{\partial u} - \frac{\partial V}{\partial v} \right)_W + \mathcal{O}(h^4), \quad (3.41)$$

$$\frac{2}{3}h^3 \left( \frac{\partial^3 V}{\partial v^3} \right)_O = V_S - V_E + h \left( \frac{\partial V}{\partial v} \right)_S + h \left( \frac{\partial V}{\partial v} \right)_E + \mathcal{O}(h^4), \quad (3.42)$$

$$\frac{2}{3}h^3 \left( \frac{\partial^3 V}{\partial u^3} \right)_O = V_S - V_W + h \left( \frac{\partial V}{\partial u} \right)_S + h \left( \frac{\partial V}{\partial u} \right)_W + \mathcal{O}(h^4), \quad (3.43)$$

$$4h^3 \left( \frac{\partial^3 V}{\partial v^2 \partial u} \right)_O = V_N + V_S - V_E - V_W + 2h \left( \frac{\partial V}{\partial v} \right)_S - 2h \left( \frac{\partial V}{\partial v} \right)_W + \mathcal{O}(h^4), \quad (3.44)$$

$$4h^3 \left( \frac{\partial^3 V}{\partial v \partial u^2} \right)_O = V_N + V_S - V_E - V_W + 2h \left( \frac{\partial V}{\partial u} \right)_S - 2h \left( \frac{\partial V}{\partial u} \right)_E + \mathcal{O}(h^4). \quad (3.45)$$

The remaining two equations out of the total twelve mentioned previously are used for calculating the first order derivatives of  $V$  at the point  $N$ , i.e.,

$$\begin{aligned} \left( \frac{\partial V}{\partial u} \right)_N &= \frac{V_S - V_E - V_W + V_N}{h} - \left( \frac{\partial V}{\partial u} \right)_E + \left( \frac{\partial V}{\partial u} \right)_W + \left( \frac{\partial V}{\partial u} \right)_S + \mathcal{O}(h^3), \\ \left( \frac{\partial V}{\partial v} \right)_N &= \frac{V_S - V_E - V_W + V_N}{h} + \left( \frac{\partial V}{\partial v} \right)_E - \left( \frac{\partial V}{\partial v} \right)_W + \left( \frac{\partial V}{\partial v} \right)_S + \mathcal{O}(h^3). \end{aligned} \quad (3.46)$$

These derivatives have no immediate usage when calculating  $V_N$ . However, they will be required at the next step when we move rightwards in the  $u - v$  plane. In this next step, the previous point labeled with  $N$  now becomes the point  $W$ . Ideally, with the expressions for the additional Taylor coefficients and the first order derivatives of  $V$  at the point  $N$ , we have the necessary expressions to establish a fourth order CID scheme. However, we note the following. While  $V_O$  in Eq. (3.30) is order  $h^2$ , the new expressions in Eqs. (3.36)–(3.37) for the first order derivatives are to order  $h^3$ . From a numerical point of view, we found that the numerical results are more accurate when we use the following expressions<sup>1</sup> (which are the same order as Eq. (3.30)) instead of Eqs. (3.36)–(3.37)

$$4h \left( \frac{\partial V}{\partial u} \right)_O = V_W - V_E - V_S + V_N + \mathcal{O}(h^3), \quad (3.47)$$

$$4h \left( \frac{\partial V}{\partial v} \right)_O = V_E - V_W - V_S + V_N + \mathcal{O}(h^3). \quad (3.48)$$

<sup>1</sup>For obtaining Eqs. (3.47)–(3.48) we constructed a system of 4 equations –other than the system of 12 equations mentioned above– by using Eq. (3.26) evaluated at the  $E$ ,  $W$ ,  $N$  and  $S$  points. We then solved this system for  $V_O$ ,  $\left( \frac{\partial^2 V}{\partial u \partial v} \right)_O$ ,  $\left( \frac{\partial V}{\partial u} \right)_O$ , and  $\left( \frac{\partial V}{\partial v} \right)_O$ , and Eqs. (3.47)–(3.48) are the expressions for the two latter quantities.

With this, we have all the necessary expressions to obtain  $V_N$  to order  $h^4$ , but only for squares with  $u_O \neq v_O$  (i.e.,  $\gamma_O \neq 0$ , we treat the  $u_O = v_O$  case separately below). Thus, we put Eqs. (3.25), (3.30), (3.47)–(3.48) and (3.27)–(3.29) back into Eq. (3.24) and solve for  $V_N$  to obtain

$$\begin{aligned} V_N = & V_E + V_W - V_S - \left( \frac{V_E + V_W - 2V_S}{u_O + v_O} - \frac{1}{2}(V_E - V_W) \cot \frac{v_O - u_O}{2} \right) h \\ & + \left( \frac{(2 - (u_O + v_O)^2 \zeta)(V_E + V_W) - 4V_S}{2(u_O + v_O)^2} - \frac{V_E - V_W}{2(u_O + v_O)} \cot \frac{v_O - u_O}{2} \right) \left( h^2 - \frac{h^3}{u_O + v_O} \right) \\ & + \mathcal{O}(h^4), \quad \gamma_O \neq 0. \end{aligned} \quad (3.49)$$

Now, similar to the third order scheme, the terms involving the cot function in Eq. (3.49) should be evaluated separately for  $u_O = v_O$  (i.e.,  $\gamma_O = 0$ ). Taking the limit  $\gamma_O \rightarrow 0$  is no longer an option since the leading term in Eq. (3.34) cannot be ignored in a fourth order scheme. Instead, we go one step back and rewrite the second and third integrals in Eq. (3.24) as

$$\begin{aligned} \int_{SE\text{NW}} \left( Q \frac{\partial V}{\partial v} + S \frac{\partial V}{\partial u} \right) du dv &= \frac{8h^2}{u_O + v_O} \left( \frac{\partial V}{\partial v} + \frac{\partial V}{\partial u} \right)_O \\ &\quad - 4h^2 \cot \frac{v_O - u_O}{2} \left( \frac{\partial V}{\partial v} - \frac{\partial V}{\partial u} \right)_O + \mathcal{O}(h^4) \\ &= \frac{8h^2}{u_O + v_O} \left( \frac{\partial V}{\partial v} + \frac{\partial V}{\partial u} \right)_O - 4h^2 \cot \gamma_O \left( \frac{\partial V}{\partial \gamma} \right)_O + \mathcal{O}(h^4), \end{aligned} \quad (3.50)$$

where, in order to take the desired limit  $\gamma_O \rightarrow 0$ , we have expressed the second term in the right hand side of Eq. (3.50) in terms of  $\gamma$  instead of  $u$  and  $v$ . For the first term, the limit  $\gamma_O \rightarrow 0$  simply reduces to setting  $u_O = v_O$  and  $\left( \frac{\partial V}{\partial u} \right)_O = \left( \frac{\partial V}{\partial v} \right)_O$ , as a consequence of the symmetries of  $\mathbb{M}_2 \times \mathbb{S}^2$ . For the second terms, we apply L'Hôpital's rule<sup>2</sup> to calculate the limit  $\gamma_O \rightarrow 0$ . This reads

$$\lim_{\gamma_O \rightarrow 0} \int_{SE\text{NW}} \left( Q \frac{\partial V}{\partial v} + S \frac{\partial V}{\partial u} \right) dv du = \frac{8h^2}{v_O} \left( \frac{\partial V}{\partial v} \right)_O - 4h^2 \left( \frac{\partial^2 V}{\partial \gamma^2} \right)_O + \mathcal{O}(h^4), \quad (3.51)$$

for  $\gamma_O = 0$ . Once we performed the limit, we write the above expression back in terms of  $u$  and  $v$ . The second order derivative with respect to  $\gamma$  can be written as

$$\left( \frac{\partial^2 V}{\partial \gamma^2} \right)_O = \left( \frac{\partial^2 V}{\partial u^2} \right)_O - 2 \left( \frac{\partial^2 V}{\partial u \partial v} \right)_O + \left( \frac{\partial^2 V}{\partial v^2} \right)_O. \quad (3.52)$$

<sup>2</sup>The  $V(\eta, \gamma) = V(\eta, -\gamma)$  symmetry implies  $\left( \frac{\partial V}{\partial \gamma} \right)_{\gamma=0} = 0$ , which prompts us to use L'Hôpital's rule.

Despite these second order derivatives are only required along  $\gamma = 0$ , we have to propagate them from the CID, i.e., we eventually need them away from  $\gamma = 0$  as well. The limit given in Eq. (3.51) is the last expression needed for the  $u_O = v_O$  case.

The first and fourth integrals in Eq. (3.24) are the same as in the third order scheme, i.e., they are given by Eqs. (3.25) and (3.29), respectively. The second and third integrals are now calculated using Eq. (3.51) together with the Taylor coefficients calculated via Eqs. (3.38)–(3.40) and (3.48). Putting all the integrals together in Eq. (3.24) and isolating  $V_N$  yields

$$V_N = 2V_E - V_S + \left[ \left( \frac{\partial V}{\partial v} - \frac{\partial V}{\partial u} \right)_E + \frac{V_S - V_E}{v_O} \right] h + \frac{1}{2v_O} \left[ \frac{V_S - (1 - 2\zeta v_O^2)V_E}{v_O} + \left( \frac{\partial V}{\partial v} - \frac{\partial V}{\partial u} \right)_E \right] \cdot \left( h^2 + \frac{h^3}{2v_O} \right) + \mathcal{O}(h^4), \quad \gamma_O = 0. \quad (3.53)$$

We used the symmetry  $V_E = V_W$  together with  $\left( \frac{\partial V}{\partial u} \right)_W = \left( \frac{\partial V}{\partial v} \right)_E$  and  $\left( \frac{\partial V}{\partial v} \right)_W = \left( \frac{\partial V}{\partial u} \right)_E$  to express the above expression in terms of data on the  $E$  and  $S$  points. These additional symmetries are easily derived from  $V(\eta, \gamma) = V(\eta, -\gamma)$  and, consequently, we can still reduce the amount of data we calculate as in the third order scheme.

As can be seen in Eqs. (3.49) and (3.53), our fourth order CID scheme requires calculating data on the light cone other than the data for  $\hat{V}$ . Specifically, we now require the first order derivatives of  $V$  on the light cone. In order to provide these data, we simply differentiate Eq. (3.7) once with respect to  $u$  and once with respect to  $v$ . We then evaluate these derivatives at  $\sigma_{\text{PH}} = \frac{1}{2}uv = 0$ . In this way, these derivatives are expressed in terms of the Hadamard coefficients  $\nu_0$  and  $\nu_1$ , i.e.,

$$\left. \frac{\partial V}{\partial u} \right|_{u=0} = -\frac{1}{2}\nu_0' \left( \frac{v}{2} \right) - \frac{v}{2}\nu_1 \left( \frac{v}{2} \right), \quad (3.54)$$

$$\left. \frac{\partial V}{\partial u} \right|_{v=0} = -\frac{1}{2}\nu_0' \left( -\frac{u}{2} \right), \quad (3.55)$$

$$\left. \frac{\partial V}{\partial v} \right|_{u=0} = \frac{1}{2}\nu_0' \left( \frac{v}{2} \right), \quad (3.56)$$

$$\left. \frac{\partial V}{\partial v} \right|_{v=0} = \frac{1}{2}\nu_0' \left( -\frac{u}{2} \right) - \frac{u}{2}\nu_1 \left( -\frac{u}{2} \right), \quad (3.57)$$

where the primes indicate differentiation with respect to  $\gamma$ . Since we are solving a characteristic initial value problem for  $V$ , the derivatives in Eqs. (3.54)–(3.57) should be obtainable from the value of  $V$  on the light cone (i.e.,  $\hat{V}$ ). In fact, in PH spacetime, we find that  $\hat{V} = \nu_0$  and  $\nu_1$  are uniquely obtainable from  $\nu_0$  together with the regularity condition for  $\nu_1$  at coincidence (see Eq. (24) in [53]; moreover, the Hadamard coefficients  $\nu_n$  with  $n > 0$  can be calculated from previous coefficients  $\nu_{n-1}$  in an arbitrary spacetime [64, 63, 65]).

Therefore, we can illustrate the fourth order CID scheme in the following way. We start with the same grid we constructed in the third order scheme (see Fig 9) and place the initial data (now including the first order derivatives of  $V$ ) along  $u = 0$  if we want to evolve points on and below the  $\gamma = 0$  line<sup>3</sup>. Next, we apply Eq. (3.49) to calculate  $V_N$  for squares not centered along  $\gamma = 0$ , and Eq. (3.53) for squares centered along  $\gamma = 0$ . Unlike the third order scheme, we now need to calculate both first order derivatives at the point  $N$  using Eq. (3.46) and for all  $\gamma$ . The additional analysis required along  $\gamma = 0$  does not appear in [64, 63, 65] again, as pointed out in the previous scheme, the PDE in those cases does not have a singular point like  $\gamma = 0$  in  $\mathbb{M}_2 \times \mathbb{S}^2$ .

Given two working prescriptions for calculating  $V$  to different orders (namely, third and fourth order schemes), we used the *Mathematica* software package to implement these two schemes. We present and analyse these results in the following section.

### 3.2.3 Results for $V$

We start by comparing  $V(x, x')$  with  $G_{\text{ret}}^{\text{PH}}(x, x')$ . In the top plot of Fig 10 we explore a static scenario where  $y = y'$  and  $\gamma = \pi/2$  for  $\zeta = \frac{1}{4}$ . In the plot we have:  $V$  calculated using the fourth order CID scheme with  $h = 0.00261799$  (red-dashed curve); The retarded Green function  $G_{\text{ret}}^{\text{PH}}$  calculated via an  $\ell$ -mode decomposition (with the sum capped at  $\ell = 800$ ) given in Eq. (134) in<sup>4</sup> [55] (blue curve); The basic approximation  $\nu_0 + \nu_1\sigma_{\text{PH}}$  to  $V$  (gray-dashed curve);  $V$  calculated using a small coordinate distance expansion (see

<sup>3</sup>For the opposite choice of evolving points on and *above* the  $\gamma = 0$  line, the initial data is instead placed along  $v = 0$ .

<sup>4</sup>We note that in [55] the last expression in Eq. (134) there is a missing factor  $\theta(-\sigma_{\mathbb{M}_2})$ .

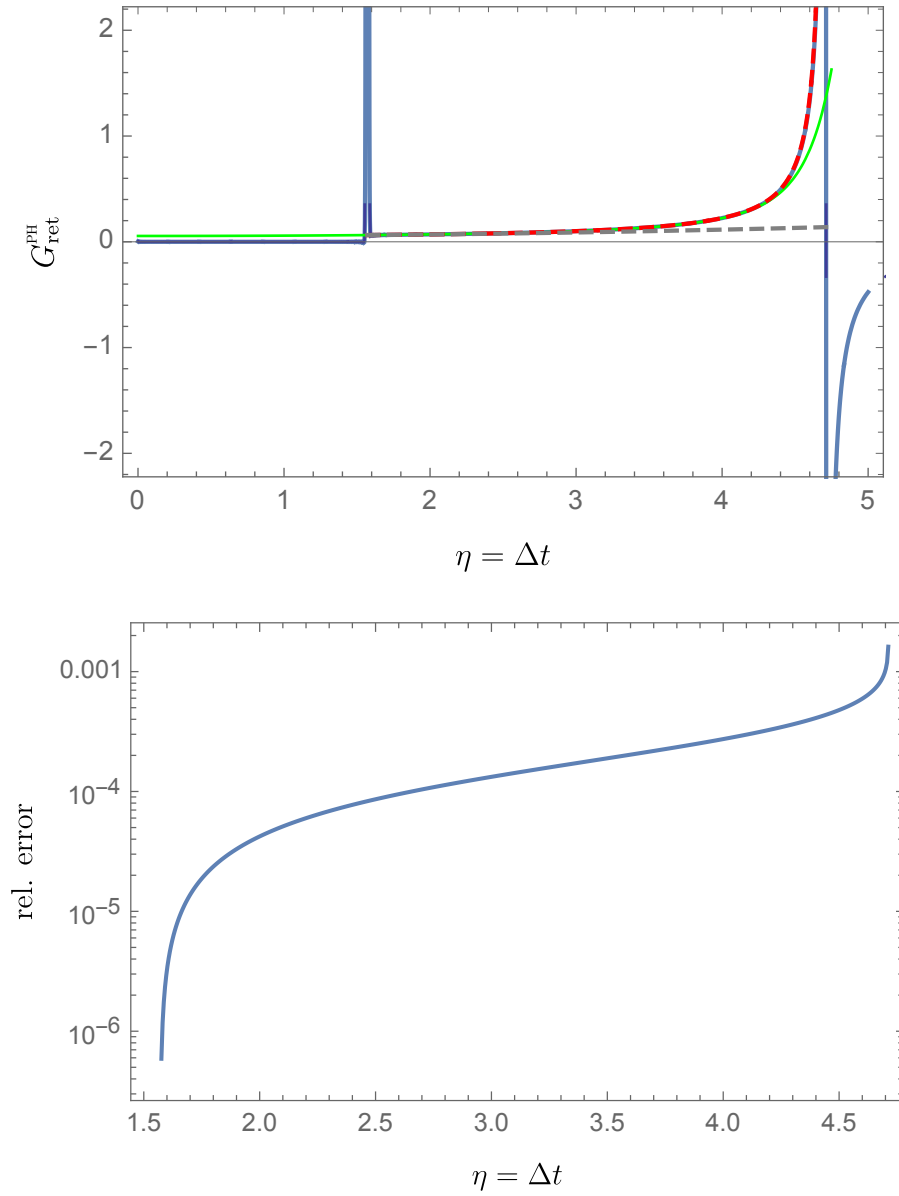


Figure 10 – Quantities as functions of  $\eta = \Delta t$  in  $\mathbb{M}_2 \times \mathbb{S}^2$  with  $\zeta = 1/4$ ,  $\Delta y = y - y' = 0$  and  $\gamma = \pi/2$ . Top plot: Retarded Green function as an  $\ell$ -mode sum (blue) and  $V$  using the fourth order CID scheme (dashed red), a small coordinate-separation expansion (green) and approximated by  $\nu_0 + \nu_1 \sigma_{\text{PH}}$  (dashed gray). Bottom plot: Relative error between the third order and fourth order schemes for calculating  $V$  with  $h = 0.00261799$ .

Ref. [60]) (green curve). As anticipated by the Hadamard form for  $G_{\text{ret}}^{\text{PH}}$ , there is a  $\delta(\sigma_{\text{PH}})$  divergence (at  $\eta = \pi/2$ ) related to the direct null geodesics. This divergence also signals the start of causal separation between  $x$  and  $x'$ . After this divergence, we observe the expected agreement between  $V$  and  $G_{\text{ret}}^{\text{PH}}$  all the way until  $\eta = \frac{3\pi}{2}$  where we encounter the next divergence. This time, this is of type [55] which agrees with  $G_{\text{ret}}^{\text{PH}}$  in the plot.

In the bottom plot of Fig. 10, we show the relative error between the two CID schemes, third order and fourth order, for the same stepsize  $2h = 2 \times 0.00261799$ . The local truncation errors are  $\mathcal{O}(h^3)$  and  $\mathcal{O}(h^4)$  and we observe that the relative error between the two schemes is at least order  $10^{-4}$ , which is consistent with the local truncation error. Let us see in detail this value for the relative error. Let  $e_3$  and  $e_4$  be the *global* truncation errors (GTEs) for the schemes with *local* truncation errors  $\mathcal{O}(h^3)$  and  $\mathcal{O}(h^4)$ , respectively. These errors for the  $n$ -th evolved point in the grid are given by  $e_3 = \mathcal{O}(n(2h)^3)$  and  $e_4 = \mathcal{O}(n(2h)^4)$ . For a fixed point close to the end of the normal we have  $n = \mathcal{O}((2h)^{-2})$  evaluations<sup>5</sup> carried out, this gives GTEs  $e_3 = \mathcal{O}(2h)$  and  $e_4 = \mathcal{O}((2h)^2)$ . Therefore, for the case in Fig. 10, we have  $e_3 = \mathcal{O}(10^{-3})$  and  $e_4 = \mathcal{O}(10^{-5})$ , which could be considered as relative errors due to  $V$  being  $\mathcal{O}(1)$  near the end of the normal neighbourhood<sup>6</sup>. In this way, the GTE  $e_3 = \mathcal{O}(10^{-3})$  does agree nicely with the relative error between the two schemes shown in the bottom plot of Fig. 10. On its own, this relative error provides a basic idea about the improvement the fourth order scheme brings over the third order one. Preferably, we should look at the GTE. If we provide three expressions for  $V$  calculated using the same CID scheme but with different stepsizes ( $2h$ ,  $4h$  and  $8h$  in our case, with corresponding solutions denoted by  $V_{(2h)}$ ,  $V_{(4h)}$  and  $V_{(8h)}$ ), we can show that [77]

$$\frac{V_{(2h)} - V_{(4h)}}{V_{(4h)} - V_{(8h)}} = \frac{(2h)^k - (4h)^k}{(4h)^k - (8h)^k} + \mathcal{O}(h) = \frac{1}{2^k} + \mathcal{O}(h), \quad (3.58)$$

where  $k$  denotes the order of the GTE associated to the CID scheme. As justified above, we expect  $k = 1$  for a third order CID scheme and  $k = 2$  for a fourth order one.

<sup>5</sup>More accurately, it should be  $n = \mathcal{O}((2h)^{-2}/2)$ , where the extra factor  $1/2$  arises due to the fact that the grid, which in principle would be a square as per Fig. 9, really becomes a triangle because of application of the symmetries mentioned around Eq. (3.35). But  $n = \mathcal{O}((2h)^{-2})$  is fine as an order of magnitude.

<sup>6</sup> $V$  is  $\mathcal{O}(1)$  only up to  $\eta \lesssim 4.5$ . For  $\eta \gtrsim 4.5$ ,  $V$  is no longer  $\mathcal{O}(1)$  and absolute errors cannot be considered as relative errors.

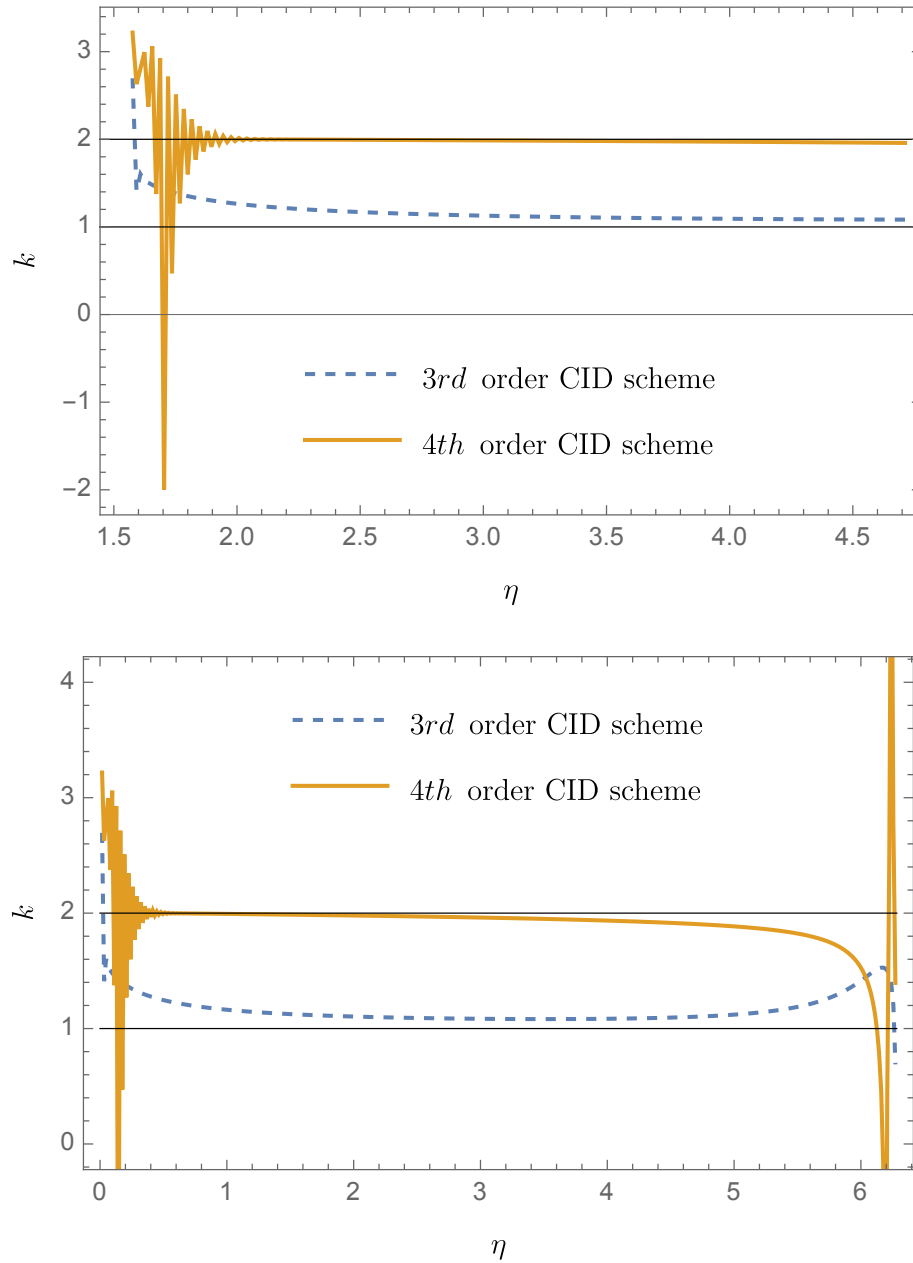


Figure 11 – GTE order  $k$  for the third and fourth order CID schemes for  $\gamma = 1.56$  (top) and  $\gamma = 0$  (bottom). The expected values for the order  $k$  are close to the theoretical values (namely,  $k = 1$  for the third order scheme and  $k = 2$  for the fourth order one, drawn as horizontal black continuous lines).

In Fig. 11 we plot the GTE order  $k$  (calculated using Eq. (3.58)) as a function of  $\eta$  for two different angular separations:  $\gamma = 1.56$  in the top plot and  $\gamma = 0$  in the bottom one. In these plots, we observe a good consistency between the numerically-calculated value of  $k$  and the theoretically-given value of  $k$  (i.e.,  $k = 1$  and  $k = 2$  for the third and fourth order schemes, respectively). We find some oscillations in both plots about the expected value of  $k$ . This is merely due to the fact that Eq. (3.58) is an approximated expression for calculating  $k$ . Furthermore, in the bottom plot of Fig. 11 there are additional oscillations near the end of the normal neighbourhood. This is unsurprising since the plot is for  $\gamma = 0$  and its end is at  $\eta = 2\pi - \gamma = 2\pi$ , i.e., a caustic point<sup>7</sup>, and it is expected to have an enhancement in the singularity of  $G_{\text{ret}}^{\text{PH}}$  at caustics [55] (similar to Schwarzschild spacetime [53]).

Although  $V$  for the scenario in Fig. 10 has been calculated before [55], in the following we present new results for which a CID scheme is more efficient than other known methods in the literature (e.g. a small coordinate expansion or Hadamard series).

In Fig. 12, we plot  $V$  obtained with the fourth order CID scheme for  $\zeta = \frac{1}{4}$  for any  $x'$  and  $x$  (with  $x$  lying inside the causal part of the maximal normal neighbourhood of  $x'$ ). The red line corresponds to the case previously discussed in Fig. 10, i.e.,  $y = y'$  and  $\gamma = \frac{\pi}{2}$ . Reproducing the result in Fig. 12 without using a CID scheme might require supplementary calculations. For instance, we could follow the method of matched expansions and calculate  $V$  in a quasi-local region via a small distance expansion. Next we apply the method of matched expansions (for this we require to calculate  $G_{\text{ret}}^{\text{PH}}$  in the DP region).

Besides calculating  $V$  for a single value of  $\zeta = \frac{1}{4}$ , we also examine some other values for  $\zeta$  to observe the influence of  $\xi$  on  $V$ . In the top plot of Fig. 13 we show  $V$  calculated using the third order scheme, for  $\zeta = 0, \frac{1}{4}, \frac{1}{3}, \frac{1}{2}, 1$  for the same scenario as in Fig. 10. We should emphasise that since the stress-energy tensor imposes additional constraints on the coupling constant  $\xi$ , the results for  $V$  where  $\zeta > \frac{1}{3}$  correspond to a field with non-zero mass [78]. As can be seen in the plot, the magnitude of  $V$  decreases as  $\zeta$  increases. In the

<sup>7</sup>Caustics are at  $\eta = \gamma = m\pi$ , for  $m \in \mathbb{Z}$ .



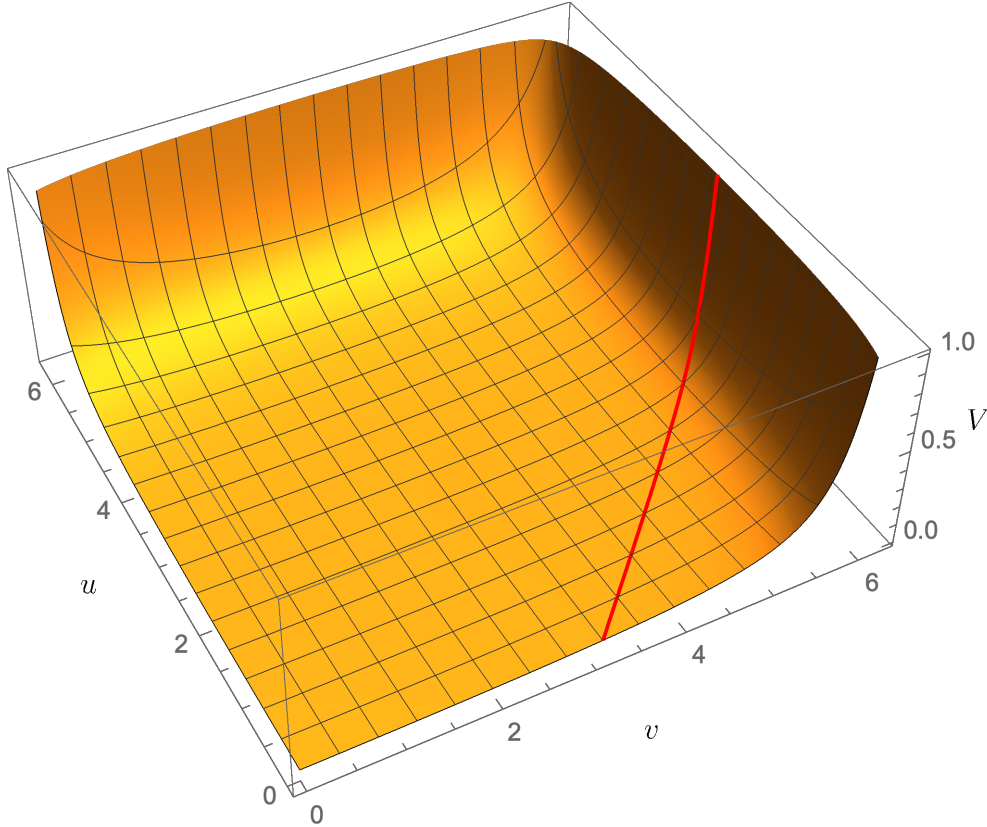


Figure 12 – Plot of  $V$  for all pairs of points in normal neighbourhoods with  $\zeta = 1/4$ . The  $u = 2\pi$  and  $v = 2\pi$  lines correspond to the end of the normal neighbourhood where the (leading) singularity of  $G_{\text{ret}}^{\text{PH}}$ , and so of  $V$ , is of type PV ( $1/\sigma_{\text{PH}}$ ) (when away from caustics). The red line is along the static worldline considered in Fig. 10.

bottom plot, we plot  $V$  for all pairs of spacetime points (as long as they lie in normal neighbourhoods, so that  $V$  is defined), but now for  $\zeta = 1$ . Different from the  $\zeta = \frac{1}{4}$  case, there is a more marked change in the form of  $V$  near  $\gamma = \pm\pi$ . We also calculated  $V$  for the other values of  $\zeta$  we show in the top plot of Fig. 13 but the differences were not significant compared to the  $\zeta = \frac{1}{4}$  case.

To conclude, we presented and implemented a new method for calculating the Hadamard tail biscalar  $V$  for wave propagation in PH spacetime. This method is based on integrating the homogeneous wave equation using Characteristic Initial Data placed along the light cone. The CID scheme provided an efficient way to obtain  $V$  at *all* spacetime points where it is defined, for different values of  $\zeta = m^2 + 2\xi$ . Being able to calculate  $V$  (and the retarded Green function) at *all* pairs of points is practical, specially, for a potential application to the self-consistent evolution of a particle via self-force.

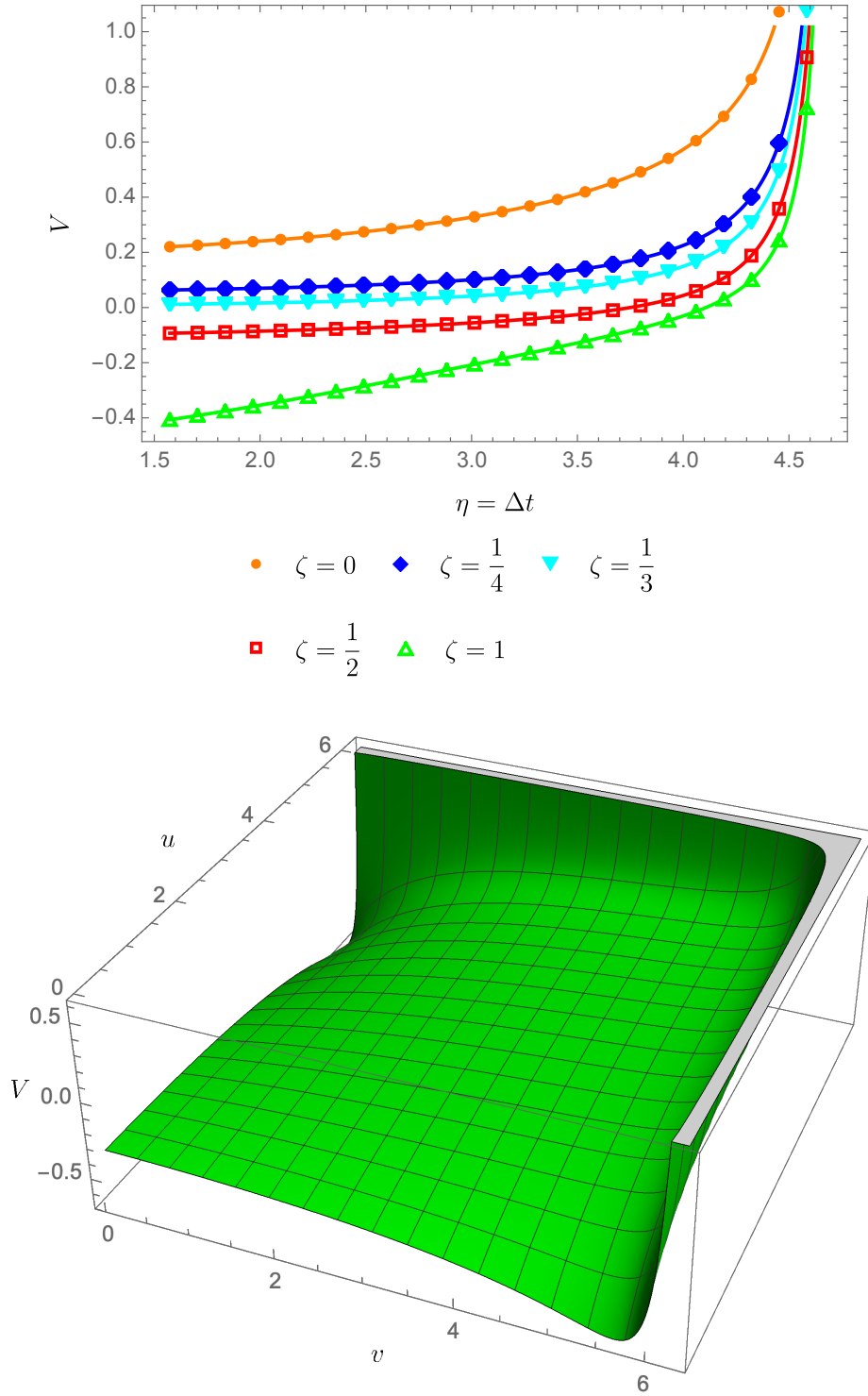


Figure 13 – Top: Plot of  $V$  as a function of  $\eta$  for different values of  $\zeta$  and for the same scenario (and stepsize) as in Fig. 10. Bottom: 3D plot of  $V$  as a function of  $u$  and  $v$  for  $\zeta = 1$ .

All these results were included and presented in a paper already published in [20].

### 3.3 Going beyond PH spacetime

Calculating the Hadamard tail  $V$  in  $\mathbb{M}_2 \times \mathbb{S}^2$  is particularly easier than in black hole spacetimes: First, although setting up the Characteristic Initial Data  $\hat{V}$  has some difficulties, it can be calculated analytically and, second, the wave equation turns into a *two-dimensional* PDE. In Schwarzschild spacetime, for the Hadamard tail  $V_s$  defined via Eq. (2.2), one can numerically solve the transport equation for  $\hat{V}_s = V_s|_{\sigma=0}$  (as it is done in [76]) and establish the required CID on the light cone. The wave equation in Schwarzschild spacetime is only reduced to a *three-dimensional* PDE instead of a two-dimensional one as in PH spacetime. In fact, for scalar perturbations, the Hadamard tail  $V_0(x, x')$  satisfies the wave equation

$$\left( -\frac{\partial^2}{\partial t^2} + \frac{\partial^2}{\partial r_*^2} + \frac{2f}{r} \frac{\partial}{\partial r_*} + \frac{f}{r^2} \square_{\mathbb{S}^2} \right) V_0(t - t', r, r', \gamma) = 0, \quad (3.59)$$

where  $r_*$  is the usual tortoise coordinate (see Eq. (1.36)). By providing the corresponding CID calculated in [76], we could formulate a three-dimensional CID scheme for Eq. (3.59). However, as can be seen in Fig. 4 in [76] the light cone (i.e., the characteristic initial surface) is not a trivial surface to start the propagation from, i.e., establishing an equally spaced grid in the same way as in Fig. 9 might be difficult to figure out. We attempted to implement this CID scheme, but these additional difficulties did not allow us to go further.

## 4 Quantum communication near a black hole

*Note: This Chapter (and the related Appendixes) consists of adapted parts of [19].*

As discussed in previous chapters, the applications of the retarded GF ( ${}_0G_{\text{ret}}$  in particular) is not limited to self-force calculations. The Klein-Gordon equation (i.e., the wave equation for a scalar field) plays an important role in quantum field theory. As we detail in this chapter, the retarded GF of the Klein-Gordon equation in curved spacetime determines key aspects in the quantum communication between two observers near a Schwarzschild black hole.

For two observers to share information between them, they require a communication device for each one and a channel to transmit the information. We use particle detectors as communication devices and a massless quantum scalar field plays the role of the communication channel. We denote as Alice the observer who wants to transmit some information to the receiver that we call Bob.

Generally speaking, in curved spacetimes particle detectors allow one to better understand the notion of measurement in quantum field theory [79, 80] and have proven a powerful tool to define the elusive notion of particle in quantum field theory [81]. For example, particle detectors have been used in a number of curved spacetimes scenarios to characterize the particle content of different vacuum states. The applications of particle detectors range from cosmology [82] to black hole scenarios such as Schwarzschild and Schwarzschild-AdS spacetimes (e.g., see [83, 84]). They have also been used to study the entanglement structure of quantum field theory vacua both in flat spacetimes [85, 86, 87], cosmological backgrounds [88, 89] as well as in other simple curved scenarios such as the Anti-deSitter spacetimes [90, 91] or in the presence of BTZ black holes [92].

## 4.1 Signaling with Unruh-DeWitt detectors

To model the communication devices of Alice and Bob, we use the Unruh-DeWitt particle detector model [93, 94]. This model allows us to understand key features of light-matter interaction when angular momentum exchange plays a negligible role in the detector's dynamics [95]. Each particle detector can be viewed as modeling an atom moving along a given worldline. In particular, we choose a two-level (quantum) particle detector with Hamiltonian

$$\hat{H}_D^{\tau_D} = \frac{\Omega_D}{2} (|e_D\rangle \langle e_D| - |g_D\rangle \langle g_D|), \quad (4.1)$$

where  $D = A, B$  labels, respectively, Alice's and Bob's detector, the (orthogonal) states  $|e_D\rangle$  and  $|g_D\rangle$  represent, respectively, the excited and ground states of an atom,  $\Omega_D \geq 0$  is simply the energy gap between the two states. We use the superindex  $\tau_D$  in  $H_D^{\tau_D}$  to remark that this Hamiltonian generates translations with respect to the detector's proper time  $\tau_D$ . The quantum field chosen as the communication channel is a massless Klein-Gordon field which we denote with  $\hat{\phi}(x)$ . Therefore, transmitting information from Alice to Bob turns the interaction between both detectors with the scalar field. In the interaction picture, this interaction between the scalar field and one detector is given by the Hamiltonian

$$\hat{H}_{\text{int},D}^{\tau_D} = \lambda_D \eta_D(\tau_D) \hat{\phi}(x_D(\tau_D)) \otimes (|e_D\rangle \langle g_D| e^{i\Omega_D \tau_D} + |g_D\rangle \langle e_D| e^{-i\Omega_D \tau_D}), \quad (4.2)$$

where  $x_D(\tau_D)$  denotes the detector's worldline,  $\lambda_D$  is a coupling constant that measures the strength coupling between the detector  $D$  and the field. The function  $\eta(\tau_D)$  is a switching function that determines when the detector couples to the field. We assume a weak interaction between detector and field so that perturbation theory applies.

### 4.1.1 Quantum channel between detectors

When Alice, the sender, wants to send a message to Bob, the receiver, she first prepares her detector and encodes the message in the initial state (for instance, she could use two different states for encoding bit values '0' and '1'). With the switching function, she controls the coupling time of her detector to the field. On the other hand, Bob prepares

his detector at some fixed state, say the ground state  $|g_D\rangle$  (the same results can be achieved for any other initial state [96]). By coupling his detector to the field, this interacts with Alice's signal that has propagated through the field. After some time, both Alice and Bob switch off their detectors. It turns out that the final state of Bob's detector depends on Alice's signal. This means that Bob might be able to decode Alice's message by measuring the final state of his detector.

In this scenario composed by two detectors interacting via a scalar field, the total Hilbert space of the system  $\mathcal{H} = \mathcal{H}_A \otimes \mathcal{H}_F \otimes \mathcal{H}_B$  is the tensor product of Alice's and Bob's detector Hilbert spaces,  $\mathcal{H}_A$  and  $\mathcal{H}_B$  respectively, and the Hilbert space of the field,  $\mathcal{H}_F$ . Therefore, the total interaction Hamiltonian for the system is given by

$$\hat{H}_{\text{int}}^t(t) = \hat{H}_{\text{int,A}}^t(t) \otimes \hat{\mathbb{I}}_B + \hat{\mathbb{I}}_A \otimes \hat{H}_{\text{int,B}}^t(t). \quad (4.3)$$

Notice that the Hamiltonians  $\hat{H}_{\text{int,A}}^t$  and  $\hat{H}_{\text{int,B}}^t$  generate translations with respect to a global time parameter  $t$ . While the Hamiltonian in Eq. (4.1) generates translations with respect to the proper time of detector D, in Eq. (4.3) we are adding up two Hamiltonians corresponding to detectors with different proper times. Thus we require to perform a proper transformation. As shown in [95], the relationship between a detector-field Hamiltonian generating translations with respect to proper time  $\tau_D$  and one generating translations with respect to a different time parameter is, in general, complicated. However, as shown in [95], for pointlike detectors the relationship simplifies: In the pointlike case, given the Hamiltonian  $H_{\text{int,D}}^{\tau_D}$  generating translations with respect to a time parameter  $\tau_D$  (e.g., detector's proper time), the Hamiltonian  $\hat{H}_{\text{int,D}}^t(t)$  generating translations with respect to a different time parameter  $t$  is given by

$$\hat{H}_{\text{int,D}}^t(t) = \frac{d\tau_D}{dt} \hat{H}_{\text{int,D}}^{\tau_D}[\tau_D(t)]. \quad (4.4)$$

The initial state of the total system denoted by  $\rho_0$  can be constructed from the states of the detectors (denoted by  $\rho_A$  for Alice and  $\rho_B$  for Bob) and the scalar field state  $\rho_\phi$ , i.e.,

$$\rho_0 = \rho_A \otimes \rho_\phi \otimes \rho_B = \rho_A \otimes \rho_\phi \otimes |g_B\rangle \langle g_B|, \quad (4.5)$$

where, without losing generality, we fixed the initial state of Bob's detector to the ground state  $|g_B\rangle$ . In the interaction picture,  $\rho_0$  evolves once Alice's and Bob's detectors couple

to the field. Particularly, Bob's detector final state is given by

$$\rho = \hat{U} \rho_0 \hat{U}^\dagger, \quad (4.6)$$

where  $\hat{U}$  is the unitary operator that governs the evolution of the system. The final state of Bob's detector is obtained by taking the partial trace over the field and Alice's detector of the total final state of detectors

$$\rho_B = \text{Tr}_{A,\phi}(\rho). \quad (4.7)$$

As mentioned earlier, we treat the time evolution of the detectors perturbatively. For this approach to work we need field states for which the Wightman function<sup>1</sup> is regular enough for a perturbative approach to time evolution to work. In particular, we assume that the field starts out in a state which we assume to be Hadamard<sup>2</sup>, at least in the region of spacetime where Alice and Bob's worldlines are within the support of their switching functions. This assumption ensures that the detector transition probabilities we calculate below are well defined. Note that the assumption on the field state is still very general.

We then use a Dyson series to obtain a perturbative expansion for  $\hat{U}$

$$\hat{U} = \mathbb{I} - i \int_{-\infty}^{\infty} dt_1 \hat{H}_{\text{int}}^{t_1}(t_1) - \int_{-\infty}^{\infty} dt_1 \int_{-\infty}^{t_1} dt_2 \hat{H}_{\text{int}}^{t_1}(t_1) \hat{H}_{\text{int}}^{t_2}(t_2) + \dots \quad (4.8)$$

Notice that each Hamiltonian generates translation with respect to different time parameters. Thus, one needs to perform the proper transformations before evaluating the integrals in the above equation.

The dependence of Bob's final state  $\rho_B$  on Alice's initial state  $\rho_A$  is captured by the quantum channel map

$$\Xi : \rho_A \mapsto \rho_B, \quad (4.9)$$

that is, the completely positive and trace-preserving map which maps the density operator of Alice's initial state to the density operator of Bob's final state. The quantum channel between detectors was first studied in [98]. It has since been studied both in the perturbative regime [99, 96] as well as non-perturbatively [100, 101].

<sup>1</sup>The Wightman function is the correlation function  $G_+(x, x') = \langle \hat{\phi}(x) \hat{\phi}(x') \rangle$ .

<sup>2</sup>A Hadamard state is a state for which the singular part of its two-point function has the form  $\frac{\Delta^{1/2}}{\sigma} + V_0 \ln \sigma$  [97].

### 4.1.2 Leading order signal strength

Treating the interaction between field and detectors perturbatively and assuming, as above, that Bob's detector starts out in the state  $|g_B\rangle$ , and that the field's initial state is Hadamard and has vanishing one-point function (in the region where the detectors couple to the field), the perturbative expansion of Bob's final state is

$$\begin{aligned} \rho_B = & \left(1 - \lambda_B^2 P_2\right) |g_B\rangle \langle g_B| + \lambda_B^2 P_2 |e_B\rangle \langle e_B| + \lambda_A \lambda_B (\zeta C_2 + \zeta^* D_2^*) |e_B\rangle \langle g_B| \\ & + \lambda_A \lambda_B (\zeta^* C_2^* + \zeta D_2) |g_B\rangle \langle e_B| + \mathcal{O}(\lambda_D^4), \end{aligned} \quad (4.10)$$

where  $\zeta$ ,  $\theta$  and  $\beta$  are the (complex) coefficients of Alice's initial state

$$\rho_A = \theta |e_A\rangle \langle e_A| + \beta |g_A\rangle \langle g_A| + \zeta |e_A\rangle \langle g_A| + \zeta^* |g_A\rangle \langle e_A|, \quad (4.11)$$

the coefficients  $P_2$ ,  $C_2$  and  $D_2$  come from the Dyson series and partial trace [99], they are given by

$$P_2 = \int_{-\infty}^{\infty} dt_1 \frac{d\tau_B(t_1)}{dt_1} \int_{-\infty}^{\infty} dt_2 \frac{d\tau_B(t_2)}{dt_2} \eta_B(t_1) \eta_B(t_2) e^{i\Omega_B(\tau_B(t_1) - \tau_B(t_2))} \langle \hat{\phi}(x_B(t_2)) \hat{\phi}(x_B(t_1)) \rangle, \quad (4.12)$$

$$\begin{aligned} C_2 = & \int_{-\infty}^{\infty} dt_1 \frac{d\tau_B(t_1)}{dt_1} \int_{-\infty}^{t_1} dt_2 \frac{d\tau_A(t_2)}{dt_2} \eta_B(t_1) \eta_A(t_2) \times \\ & e^{i(\Omega_B \tau_B(t_1) - \Omega_A \tau_A(t_2))} [\hat{\phi}(x_A(t_2)), \hat{\phi}(x_B(t_1))], \end{aligned} \quad (4.13)$$

$$\begin{aligned} D_2 = & - \int_{-\infty}^{\infty} dt_1 \frac{d\tau_B(t_1)}{dt_1} \int_{-\infty}^{t_1} dt_2 \frac{d\tau_A(t_2)}{dt_2} \eta_B(t_1) \eta_A(t_2) \times \\ & e^{-i(\Omega_B \tau_B(t_1) + \Omega_A \tau_A(t_2))} [\hat{\phi}(x_A(t_2)), \hat{\phi}(x_B(t_1))], \end{aligned} \quad (4.14)$$

where  $\langle \hat{\phi}(x) \hat{\phi}(x') \rangle$  is the Wightman function and  $[\hat{\phi}(x), \hat{\phi}(x')]$  is the commutator of the field. Here we assume, that for the coordinate time used as integration variable,  $t_1 > t_2$  implies that  $(t_1, \vec{x})$  cannot lie in the past light-cone of  $(t_2, \vec{y})$  for arbitrary spatial coordinates  $\vec{x}, \vec{y}$ . The switching functions as functions of coordinate time are given by  $\eta_D(t) = \eta_D(\tau_D(t))$ .

For communication purposes we can ignore  $P_2$  because it is related to the probability of Bob's detector to become excited (i.e., it is independent of Alice's detector initial state). The remaining two coefficients  $C_2$  and  $D_2$  are directly connected to the impact of Alice's initial state on Bob's final state.



To understand the role of  $C_2$  and  $D_2$  in the quantum communication, consider the scenario where Alice wants to transmit (in a single attempt) a bit of information ('0' or '1') to Bob. Alice prepares her detector for an optimal communication and encodes the bit in the initial state. On the other end, Bob uses an optimal choice of measurement. The probability  $p$  for transmitting the bit correctly is then given by

$$p = \frac{1}{2} + \lambda_A \lambda_B (|C_2| + |D_2|) + \mathcal{O}(\lambda_D). \quad (4.15)$$

Thus, the leading order signal strength (the term in brackets) is only determined by the absolute values of  $C_2$  and  $D_2$ .

To simplify the calculation of the signal strength it is helpful to note that one obtains  $D_2$  from  $C_2$  by changing the overall sign of the term, and the sign of  $\Omega_B$ , i.e.,

$$D_2(\Omega_A, \Omega_B) = -C_2(\Omega_A, -\Omega_B). \quad (4.16)$$

For the switching functions  $\eta_A$  and  $\eta_B$  we use a smooth switching function, this ensures that the integrals in Eq. (4.12), (4.13) and (4.14) for  $P_2$ ,  $C_2$  converge. In particular, for non-smoothing functions  $P_2$  exhibits ultraviolet divergences (see, e.g., [102, 103, 104]). The signal terms  $C_2$  and  $D_2$  are less sensitive to this issue. For instance, in Minkowski spacetime, the integrals converge even for sharp switching functions of the form

$$\eta_B(\tau_D) = \eta_{[A_1, A_2]}(\tau_D) := \begin{cases} 1, & A_1 \leq \tau_D \leq A_2 \\ 0, & \text{otherwise} \end{cases}, \quad (4.17)$$

for some  $A_1, A_2 \in \mathbb{R}$  [96].

As can be seen in Eqs. (4.13)–(4.14), the commutator is the only term that involves the quantum field and, in fact, this can be expressed in terms of the (scalar) advanced and retarded GF [19]

$$[\hat{\phi}(x_1), \hat{\phi}(x_2)] = -\frac{i}{4\pi} ({}_0G_{\text{adv}}(x_1, x_2) - {}_0G_{\text{ret}}(x_1, x_2)) \hat{\mathbb{I}}, \quad (4.18)$$

where  $x_1$  and  $x_2$  are two spacetime points. Inserting this into Eq. (4.13) reads

$$C_2 = \frac{-i}{4\pi} \int_{-\infty}^{\infty} d\tau_B \eta_B(\tau_B) \int_{-\infty}^{\tau_A(t(\tau_B))} d\tau_A \eta_A(\tau_A) e^{i\Omega_B \tau_B} e^{-i\Omega_A \tau_A} {}_0G_{\text{ret}}(x_B(\tau_B), x_A(\tau_A)), \quad (4.19)$$

and from Eq. (4.16) we find a similar expression for  $D_2$ .

Therefore, Eq. (4.19) puts in evidence that quantum communication is affected by the spacetime structure. Furthermore, the leading order signal strength is related to the classical part of the field only and thus is independent of the state of the quantum field.

### 4.1.3 In what sense are the leading order signals classical or quantum?

Note that while the signalling between Alice and Bob is mediated through the field's retarded (i.e., classical) GF, this communication scenario would not be strictly possible in a classical scenario. The reason is that, in order to have a contribution to signalling that is of quadratic order in the coupling constants, i.e.,  $\mathcal{O}(\lambda_A \lambda_B)$ , in this protocol, we need the emitter antenna to have non-zero non-diagonal elements in the energy eigenbasis (see Eqs. (4.10)–(4.11)): the ability to prepare quantum superposition of observable states of the antenna (i.e.,  $\zeta \neq 0$ ) is crucial for this communication scenario to occur. If we did not consider quantum superpositions of antenna states, the leading order contribution to communication would happen at order  $\mathcal{O}(\lambda_D^4)$  and would consist of the emission of a real quantum by Alice's detector and the absorption of this real photon by Bob's, and this would be subleading to the protocol studied here.

However, this is a quirk derived from the fact that we are limiting ourselves to two-level antennas. We can prove that the protocol has indeed very little of quantum nature if we consider higher-dimensional detectors, for example, harmonic oscillators. We shall see that, in this case, even when there is no quantum superposition at the start, communication happens at order  $\mathcal{O}(\lambda_D^2)$ .

In order to see this, let us consider two Unruh-DeWitt detectors modelled as harmonic oscillators rather than two-level quantum systems (see, among many others, [105, 106, 107, 108, 109, 110, 111, 112]). The interaction Hamiltonian describing the detectors-field coupling in  $n + 1$  dimensions in flat spacetime for two detectors comoving with the field quantization frame  $(t, \vec{x})$  is

$$H_{\text{int}}^t = \sum_{D \in \{A, B\}} \lambda_D \eta_D(t) Q_D(t) \int_{\mathbb{R}^n} d^n \vec{x} F(\vec{x} - \vec{x}_D) \hat{\phi}(t, \vec{x}), \quad (4.20)$$

which is analogous to the Hamiltonian (4.2) substituting the monopole moment by the  $Q_D$  position quadrature of the harmonic oscillator. We recall that the index  $D \in \{A, B\}$  labels the detectors. We have generalized to spatially extended detectors with a smearing function  $F(\vec{x})$  (the special case of a pointlike detector is recovered when  $F(\vec{x}) = \delta(\vec{x})$ ).

The interaction picture position operators of the oscillators,  $Q_D(t)$ , are given in terms of ladder operators by

$$Q_D(t) = a_D^\dagger e^{i\Omega_D t} + a_D e^{-i\Omega_D t} \quad (4.21)$$

where  $\Omega_D$  is the energy gap between the energy levels of the D-th oscillator.

Let us assume that the two harmonic oscillator detectors and the field start at an arbitrary uncorrelated state:  $\rho_0 = \rho_A \otimes \rho_B \otimes \rho_\phi$ . After time evolution, the detectors-field system evolves to a state  $\rho_T = U \rho_0 U^\dagger$ , where  $U = \mathcal{T} \exp[-i \int dt H_I]$  where  $\mathcal{T}$  is the time ordering operator. The state of detector B after time evolution is obtained after tracing out detector A and the field from  $\rho_T$ . Expanding in Dyson series, we can write the post-interaction state of B as

$$\rho_{B,T} = \rho_B + \lambda_B \rho_{B,\text{noise}}^{(1)} + \lambda_B^2 \rho_{B,\text{noise}}^{(2)} + \lambda_A \lambda_B \rho_{B,\text{sig}}^{(2)} + \mathcal{O}(\lambda_D^3). \quad (4.22)$$

The two first corrections in Eq. (4.22) are local terms, independent of the initial state of the detector A, and even of whether the detector A couples to the field at all (and therefore constitute noise from the point of view of communication). The correction proportional to  $\lambda_A \lambda_B$  constitutes the leading order signalling term, and tells us about the impact that the initial state of detector A has on the final state of detector B.

Let us consider that the detectors' switching functions are compactly supported and that their supports do not overlap in time. Without loss of generality, let us also assume that the detector A is switched on before B. This means that

$$\text{supp}[\eta_A(t)] = [T_A^{\text{on}}, T_A^{\text{off}}], \quad \text{supp}[\eta_B(t)] = [T_B^{\text{on}}, T_B^{\text{off}}], \quad T_B^{\text{on}} > T_A^{\text{off}}. \quad (4.23)$$

Under this assumption [113], the leading order contribution to the time evolved state of detector B from the presence of detector A is equal to

$$\rho_{B,\text{sig}}^{(2)} = \iint_{\mathbb{R}^2} dt dt' \eta_A(t) \eta_B(t') \text{Tr} \left( Q_A(t) \rho_A \right) \mathcal{C}(t, t') \left[ Q_B(t'), \rho_B \right], \quad (4.24)$$

which is the analogue of Eq. (4.13) above, and where

$$\mathcal{C}(t, t') := \int_{\mathbb{R}^n} d^n \vec{x} \int_{\mathbb{R}^n} d^n \vec{x}' F(\vec{x} - \vec{x}_A) F(\vec{x}' - \vec{x}_B) \langle [\phi(t, \vec{x}), \phi(t', \vec{x}')] \rangle_{\rho_\phi} \quad (4.25)$$

is a purely imaginary function that corresponds to the pull-back of the commutator expectation value (The Pauli-Jordan functional) to the smeared trajectories of the detectors. Notice that this is independent of the field state since the commutator is a c-number. A full derivation of Eq. (4.24) can be found following step by step the analogous two-level system calculation that yields equation (15) in [113], with the substitution of the detectors' monopole moments  $m_D$  by the harmonic detectors'  $Q_D$  position operator:  $m_D \rightarrow Q_D$ .

We will now show that if A is initially in a coherent state (that can be produced and described classically) there will be a signal transmitted to B at leading order that can be read out just from the expectation value of its position operator  $Q_B$  (which is also classically accessible). Let us assume that A starts in a state  $\rho_A = |\alpha\rangle\langle\alpha|$  where  $a_A |\alpha\rangle = \alpha |\alpha\rangle$ , and that B starts in the ground state,  $\rho_B = |0\rangle\langle 0|$ . Then, since

$$\text{Tr}[Q_A |\alpha\rangle\langle\alpha|] = 2\Re(\alpha e^{-i\Omega_A t}), \quad (4.26)$$

and

$$[Q_B(t'), \rho_B] = e^{i\Omega_B t'} |1\rangle\langle 0| - e^{-i\Omega_B t'} |0\rangle\langle 1|, \quad (4.27)$$

the leading order signalling contribution becomes

$$\rho_{B,\text{sig}}^{(2)} = 2 \int_{-\infty}^{\infty} dt \int_{-\infty}^{\infty} dt' \eta_A(t) \eta_B(t') \Re(\alpha e^{-i\Omega_A t}) \mathcal{C}(t, t') [e^{i\Omega_B t'} |1\rangle\langle 0| - e^{-i\Omega_B t'} |0\rangle\langle 1|]. \quad (4.28)$$

We can now compute the signalling contribution from the presence of Alice to the expectation value of a quadrature  $Q'_B = a_B + a_B^\dagger$  of B. First, we decompose this expectation value into a noise (local) contribution and a signalling contribution as

$$\langle Q'_B \rangle_{\rho_{B,T}} = \underbrace{\lambda_B \text{Tr}[Q'_B \rho_{B,\text{noise}}^{(1)}]}_{\langle Q'_B \rangle_{\text{noise}}^{(1)}} + \underbrace{\lambda_B^2 \text{Tr}[Q'_B \rho_{B,\text{noise}}^{(2)}]}_{\langle Q'_B \rangle_{\text{noise}}^{(2)}} + \underbrace{\lambda_A \lambda_B \text{Tr}[Q'_B \rho_{B,\text{sig}}^{(2)}]}_{\langle Q'_B \rangle_{\text{sig}}^{(2)}} + \mathcal{O}(\lambda_D^3). \quad (4.29)$$

We now see that the expectation value of the  $Q'_B$  quadrature has a non-zero contribution from the presence of A that encodes information of: (a) whether A coupled to the field

or not, (b) the coherent amplitude of A and (c) A's spatial and temporal localization. Indeed, using the fact that  $\text{Tr}[Q'_B |0\rangle\langle 1|] = 1$ , we obtain that

$$\langle Q'_B \rangle_{\text{sig}}^{(2)} = 4i\lambda_A\lambda_B \int_{-\infty}^{\infty} dt \int_{-\infty}^{\infty} dt' \eta_A(t)\eta_B(t')\mathcal{C}(t,t') \sin(\Omega_B t') \Re(\alpha e^{-i\Omega_A t}), \quad (4.30)$$

which is, in general, non-vanishing. Therefore, we conclude that there is a leading order signal from a classical state of A (a coherent state), to a classical observable of B that is mediated through the (classical) radiation GF. In summary, we showed in this section that even in a scenario where no genuinely quantum features of the field or the antennas play a role we have that the leading order signalling is  $\mathcal{O}(\lambda_A\lambda_B)$ , as described in the previous Sec. 4.1.2, and identified in [18].

#### 4.1.4 Symmetry of signaling terms between time-mirrored scenarios

In curved spacetimes it is interesting to compare the signal strength from one region in spacetime to another to the signal strength in the reverse direction. For example, is it easier or harder to signal from a sender close to the black hole horizon to a more distant receiver than in a scenario where the sender is distant but the receiver is close to the horizon?

As we show in the following, the leading order signal strength in these two scenarios is identical if all other parameters except for the detector position are kept constant. This is because the leading order signal strength  $|C_2| + |D_2|$  is identical for pairs of signaling scenarios in static spacetimes which can be viewed as time-mirrored versions of each other.

By time-mirroring we mean the following procedure: Given one particular signaling scenario with worldlines  $x_D(t)$  and switching functions  $\eta_D(t)$ , the worldlines and switching functions of the time-mirrored scenario are obtained by inverting the sign of the argument, i.e., the worldlines become

$$x'_D(t) = x_D(-t). \quad (4.31)$$

for  $D = A, B$ , and the switching functions

$$\eta'_D(t) = \eta_D(-t). \quad (4.32)$$

The worldlines and switching functions can always be assumed to be defined on an interval  $t \in [-T, T]$ .

In the time-mirrored scenario, the roles of Alice and Bob are exchanged: We still assume the initial state of detectors and field to be a product state. However, now Bob acts as sender because he couples to the field first. Thus, Bob gets to encode a message for Alice into the initial state of his detector, and Alice will try to read out the message from the final partial state of her detector.

Note that the detector frequencies are not changed in the mirrored scenario. For example, Bob uses the same detector frequency  $\Omega_B$  in the mirrored scenario where he is the sender, as in the original scenario where he is the receiver.

As shown in Appendix C, the signal terms that result in the mirrored scenario relate to the original ones as

$$C'_2 = C_2, \quad D'_2 = -D_2^*. \quad (4.33)$$

In this way, the leading order signal strength  $|C'_2| + |D'_2| = |C_2| + |D_2|$  is the same for both scenarios. This property of the leading order signal strength was shown to hold in Minkowski spacetime before [96, 114]. However, because it only relies on the retarded Green function to fulfill

$${}_0G_{\text{ret}}(t, \vec{x}, t', \vec{x}') = {}_0G_{\text{ret}}(-t', \vec{x}', -t, \vec{x}), \quad (4.34)$$

it generalizes to all spacetimes with this property. This includes all static spacetimes and thus, in particular, also Schwarzschild spacetime.

## 4.2 Signaling in Schwarzschild spacetime

The spin-0 retarded GF due to its relation with the background metric, gives an insight into some of the main features of the spacetime. Particularly, there is a singularity structure present in  ${}_0G_{\text{ret}}$  that gives rise to some unique features in the leading order signal strength. As detailed in [53], this singularity structure is associated with field null wavefronts passing through a caustic point. More precisely, the number of times a null geodesic

joining  $x$  and  $x'$  has passed through a caustic point determines the singularity in  ${}_0G_{\text{ret}}$ . When a null geodesic passed through zero, one, and two caustic points, the singularities in  ${}_0G_{\text{ret}}$  are, respectively,  $\delta(\sigma)$ ,  $\text{PV}\left(\frac{1}{\sigma}\right)$ , and  $-\delta(\sigma)$ . Similarly, we refer to direct, secondary, and tertiary null rays to null geodesics that have passed through a caustic point, zero, one, and two times, respectively.

In order to perform the integrals in Eq. (4.19) (including the corresponding counterpart for  $D_2$ ) we require to find the relation between Alice and Bob proper times. We thus introduce a shift when defining Alice's proper time:

$$\tau_A(t) = v(r_A)(t + \Delta t_{A \rightarrow B}), \quad (4.35)$$

where  $v(r) = \sqrt{f(r)}$  and  $\Delta t_{A \rightarrow B}$  is the interval of coordinate time that it takes for a direct null geodesic to propagate from Alice at  $\vec{x}_A$  to Bob at  $\vec{x}_B$ . With this, we have that the direct null geodesic which reaches Bob at his proper time  $\tau_B$  emanates from Alice at her proper time

$$\tilde{\tau}_A(\tau_B) = \nu \tau_B, \quad \text{with } \nu \equiv \frac{v(r_A)}{v(r_B)}. \quad (4.36)$$

Similarly,  $\tilde{\tau}_B(\tau_A) = \tau_A/\nu$  is Bob's proper time at which the direct null geodesic which emanates from Alice at her proper time  $\tau_A$  reaches Bob. These two results are also a direct consequence of Schwarzschild spacetime being a static spacetime.

#### 4.2.1 Direct and non-direct contributions to the signal strength

Due to  ${}_0G_{\text{ret}}$  having support not only on the future light cone but also inside the light cone,  $C_2$  (and  $D_2$ ) could be seen as a quantity composed of two main contributions: A direct contribution term (coming from null rays on the light cone) and a non-direct contribution term (coming from rays inside the light cone). The direct contribution is easy to evaluate since it arises from the direct part of  ${}_0G_{\text{ret}}$  in Eq. (2.2). Let  $C_2^{\text{d}}$  denote the direct contribution, this is given by

$$\begin{aligned} C_2^{\text{d}} &\equiv \frac{-i}{4\pi} \int_{-\infty}^{\infty} d\tau_B \int_{-\infty}^{\tau_A(t(\tau_B))} d\tau_A \eta_B(\tau_B) \eta_A(\tau_A) e^{i(\Omega_B \tau_B - \Omega_A \tau_A)} U(x_B(\tau_B), x_A(\tau_A)) \delta(\sigma) \\ &= \frac{-i}{4\pi} \int_{-\infty}^{\infty} d\tau_B \eta_B(\tau_B) \eta_A(\tilde{\tau}_A(\tau_B)) e^{i(\Omega_B \tau_B - \Omega_A \tilde{\tau}_A(\tau_B))} \frac{U(x_B(\tau_B), x_A(\tilde{\tau}_A))}{|\Delta \lambda t_\alpha(\lambda_0) u_A^\alpha(\tilde{\tau}_A)|}. \end{aligned} \quad (4.37)$$

In the above we used  $\frac{dx_A}{d\tau_A}(\tau_A) = u_A^\mu(\tau_A)$ , and

$$\sigma_{\alpha'} = \frac{\partial}{\partial x^{\alpha'}} \sigma(x, x') = -\Delta\lambda(x, x') g_{\alpha'\beta'} t^{\beta'} \quad (4.38)$$

where  $\Delta\lambda(x, x') = \lambda_1 - \lambda_0 > 0$  is the difference in the affine parameter  $\lambda \in [\lambda_0, \lambda_1]$  along the unique null geodesic  $z(\lambda)$  such that  $x' = z(\lambda_0)$  and  $x = z(\lambda_1)$ , and  $t^\mu = \frac{dz^\mu}{d\lambda}$  is a tangent vector. These additional quantities allowed us to perform the integral over  $\tau_A$  by changing the argument in the Dirac-delta distribution from  $\sigma$  to  $\tau_A$ . The integral over  $\tau_B$  is performed numerically, we calculate  $U$  by solving (numerically) the transport equations detailed in Sec. 2.1.

We can derive some general properties of the direct contribution  $C_2^d$  from Eq. (4.37). For instance, we see directly that due to the factor  $\eta_B(\tau_B)\eta_A(\tilde{\tau}_A(\tau_B))$  in the integrand, the direct contribution vanishes unless Alice and Bob interact with the field at points that are connected by a direct null geodesic.

Furthermore, we see that  $|C_2^d|$  is maximal if  $\Omega_B\tau_B - \Omega_A\tilde{\tau}_A(\tau_B) = 0$ , i.e., if Alice's and Bob's detector frequencies are tuned such that they cancel the frequency shift arising between their worldlines due to motion and gravitation. To see this, first note that all factors in the integrand, apart from the complex exponential, are non-negative: The switching functions take values in  $\eta_D \in [0, 1]$ , the denominator is a non-negative real number, and  $U = \Delta^{1/2} > 0$ . Hence, in order to maximize  $|C_2^d|$ , Alice and Bob need to choose their detector frequencies in such a way that the exponential term oscillates as little as possible.

However, while this choice is optimal for  $|C_2^d|$ , it may not always be the optimal choice with respect to  $|C_2^d| + |D_2^d|$ . From Eq. (4.16), we see that the exponential factor in the integrand of  $D_2$  is always oscillatory, except for detectors with a vanishing energy gap. Generally, this means that a non-resonant choice of detector frequencies, while leading to a smaller value of  $|C_2^d|$ , may achieve a larger value of  $|C_2^d| + |D_2^d|$ . This applies in particular to scenarios where the length of the detector-field coupling is comparable to the detector's period.

For example, we can see this effect in the case of stationary detectors in a static



spacetime. Here,  $\tilde{\tau}_A(\tau_B) = \nu\tau_B + \tau_0$  is a linear function, so that equation Eq. (4.37) simplifies to

$$C_2^d = \frac{-i U(\vec{x}_B, \vec{x}_A)}{4\pi |\Delta\lambda t_\alpha(\lambda_0) u_A^\alpha(\tilde{\tau}_A)|} \int_{-\infty}^{\infty} d\tau_B \eta_B(\tau_B) \eta_A(\tilde{\tau}_A(\tau_B)) e^{i(\Omega_B - \nu\Omega_A)\tau_B}. \quad (4.39)$$

Here we used that due to the time-translational invariance we can rewrite

$$U(x_B(\tau_B), x_A(\tilde{\tau}_A)) = U(\vec{x}_B, \vec{x}_A),$$

and also  $t_\alpha(\lambda_0) u_A^\alpha(\tilde{\tau}_A)$  is constant and does not depend on  $\tilde{\tau}_A$ . If we assume that the switching functions are sharp switching functions  $\eta_A(\tau_A) = \eta_{[A_1, A_2]}(\tau_A)$  and  $\eta_B(\tau_B) = \eta_{[B_1, B_2]}(\tau_B)$ , as defined in Eq. (4.17), with switching times such that Bob receives all the direct null geodesics from Alice, i.e.,  $B_1 \leq A_1/\nu$  and  $B_2 \geq A_2/\nu$ , then

$$C_2^d = \frac{-i U(\vec{x}_B, \vec{x}_A)}{4\pi |\Delta\lambda t_\alpha(\lambda_0) u_A^\alpha(\tilde{\tau}_A)|} e^{i\frac{(\Omega_B - \nu\Omega_A)(A_1 + A_2)}{2\nu}} \frac{A_2 - A_1}{\nu} \text{sinc} \left[ \frac{(\Omega_B - \nu\Omega_A)(A_2 - A_1)}{2\nu} \right]. \quad (4.40)$$

For fixed switching times  $A_1$  and  $A_2$ , the sinc function explains why  $|C_2^d| + |D_2^d|$  is dominated by  $|C_2^d|$  in the regime of large detector frequencies and thus maximized when  $\Omega_B = \nu\Omega_A$ , where

$$\lim_{\Omega_B \rightarrow \nu\Omega_A} C_2^d = \frac{-i U(\vec{x}_B, \vec{x}_A)(A_2 - A_1)}{4\pi |\Delta\lambda t_\alpha(\lambda_0) u_A^\alpha(\tilde{\tau}_A)| \nu}. \quad (4.41)$$

Whereas for low detector frequencies choosing one or both of the frequencies to vanish, can lead to a larger  $|C_2^d| + |D_2^d|$  because the gain in  $|D_2^d|$  overcomes the loss in  $|C_2^d|$ .

In general it is not possible to avoid oscillations of the exponential term in all signaling scenarios. In fact it is possible that the oscillations limit the magnitude of  $C_2^d$  even if the detectors are allowed to interact with the field for arbitrary long times. This effect has been previously studied between accelerated detectors in Minkowski spacetime in [96, 114].

In addition to the direct contribution  $C_2^d$ , which often dominates the signal, the timelike support of  ${}_0G_{\text{ret}}$  gives rise to further contributions to the signal, which we call the *non-direct contribution*

$$C_2^{\text{nd}} = C_2 - C_2^d. \quad (4.42)$$

Thus, the leading order signal strength is given by

$$|C_2| + |D_2| = |C_2^{\text{nd}} + C_2^{\text{d}}| + |D_2^{\text{nd}} + D_2^{\text{d}}| \quad (4.43)$$

Since the specific properties of the non-direct part of  ${}_0G_{\text{ret}}$  depend decisively on the spacetime geometry, it is difficult to derive general properties for the non-direct signaling contributions.

Another challenge of the non-direct contribution is that it typically is more difficult to evaluate. However, in static spacetimes for detectors at rest at least the integral expression can be simplified: By a change of integration variables one can typically perform one of the two integrations analytically. In that way, only one numerical integration is left. For this, see Appendix E. Another method, which is particularly helpful when  ${}_0G_{\text{ret}}$  is expressed as a series, is developed in the following section.

## 4.2.2 Signaling between two static observers

In flat spacetime, the receiver typically switches on the detector when the unique (direct) null ray emanating from the sender's position arrives at the receiver's position. However, in curved spacetime the situation is different. There are timelike rays and non-direct null rays the receiver may be able to collect if the detector interacts with the field for long enough. The switching function for both Alice and Bob are sharp switching functions as given in Eq. (4.17).

The first setting we explore is when both the sender (Alice) and the receiver (Bob) are fixed in space, i.e.,  $\vec{x}_A$  and  $\vec{x}_B$  are constant. Let  $A_1$  be the proper time when Alice switches on her detector and  $A_2$  the switch-off proper time. Likewise, Bob switches on his detector at a proper time  $B_1$  immediately after the first signal emitted by Alice reaches his position. The total proper time interval Bob keeps his detector switched on is  $B_2 - B_1$ .

For this scenario,  $C_2$  is given by (see Appendix E for a detailed derivation)

$$C_2 = \int_{\max[\nu B_1 - A_2, 0]}^{\nu B_2 - A_1} dw \frac{e^{i\Omega_A w} \cdot {}_0G_{\text{ret}}(w/\nu(r_A) + \Delta t_{A \rightarrow B}, \vec{x}_B, \vec{x}_A)}{4\pi(\Omega_B - \nu\Omega_A)} \times \\ \left( e^{i(\Omega_B - \nu\Omega_A)\max[B_1, (w+A_1)/\nu]} - e^{i(\Omega_B - \nu\Omega_A)\min[B_2, (w+A_2)/\nu]} \right). \quad (4.44)$$

We can use the above expression together with Eq. (4.16) and obtain the corresponding expression for  $D_2$ .

In order to evaluate the integral in Eq. (4.44), we do it in two steps. The first step simply consists of calculating  $C_2^d$  using Eq. (4.37). In the second step we replace  ${}_0G_{\text{ret}}$  by its non-direct part and perform the integral. Thus,  $C_2$  is given by  $C_2 = C_2^d + C_2^{\text{nd}}$  where

$$C_2^{\text{nd}} = \int_{\max[\nu B_1 - A_2, 0]}^{\nu B_2 - A_1} dw \frac{e^{i\Omega_A w} \cdot {}_0G_{\text{ret}}^{\text{nd}}(w/v(r_A) + \Delta t_{A \rightarrow B}, \vec{x}_B, \vec{x}_A)}{4\pi(\Omega_B - \nu\Omega_A)} \times \\ \left( e^{i(\Omega_B - \nu\Omega_A)\max[B_1, (w+A_1)/\nu]} - e^{i(\Omega_B - \nu\Omega_A)\min[B_2, (w+A_2)/\nu]} \right). \quad (4.45)$$

Once again, a similar expression is derived for  $D_2 = D_2^d + D_2^{\text{nd}}$  by using Eq. (4.16).

In Fig. 14 we plot the leading order signal strength  $|C_2| + |D_2|$  for different static scenarios. Particularly, we maintain Alice's position fixed (at  $r_A = 6M$ ) and switched on for a fixed interval  $A_1 = 0 \leq \tau_A \leq M = A_2$ <sup>3</sup>. Bob is then located at different spatial positions so that we are able to map the leading order signal strength throughout a particular spatial region close to Alice's position. Similar to flat spacetime case, as Bob approaches Alice, the signal strength increases as expected. In fact, by looking at the expression for  $C_2^d$  in Eq. (4.37) (and the corresponding one for  $D_2^d$ ), it is straightforward to show that the signal strength diverges as the distance between Alice and Bob decreases. As Bob moves away from Alice, the average signal strength diminishes (in Appendix. D we provide an additional analysis regarding  $C_2^d$  and  $D_2^d$ ). Once the direct null rays were collected, Bob continues to receive signals from Alice. These remaining signals are part of the non-direct contribution. We found out that most of the features in Fig. 14 like the ripples (more significant in Fig. 14a) are connected to the non-direct contribution.

The leading order signal strength shown in Fig. 14 when split into the direct and non-direct contributions is largely dominated by the direct term. To evidence this fact, we simply compare the magnitudes of  $|C_2^d| + |D_2^d|$  and  $|C_2^{\text{nd}}| + |D_2^{\text{nd}}|$ . In Fig. 15 we plot the direct contribution  $|C_2^d| + |D_2^d|$  which puts in evidence not only that its magnitude is the same order as  $|C_2| + |D_2|$  but also shows that the ripples are connected to the non-direct contribution. These features are located around the region where Bob starts

<sup>3</sup> $\eta_A(\tau_A)$  in this case is a sharp switching function.

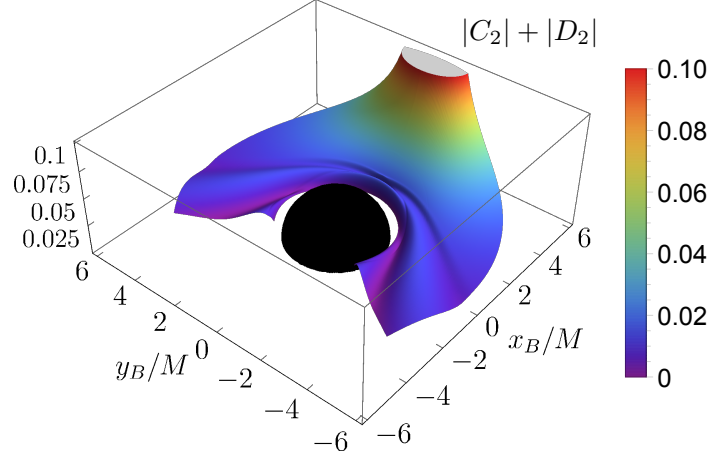
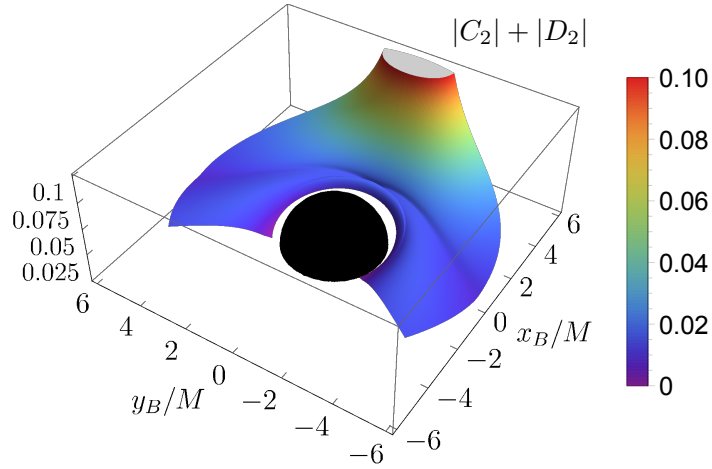
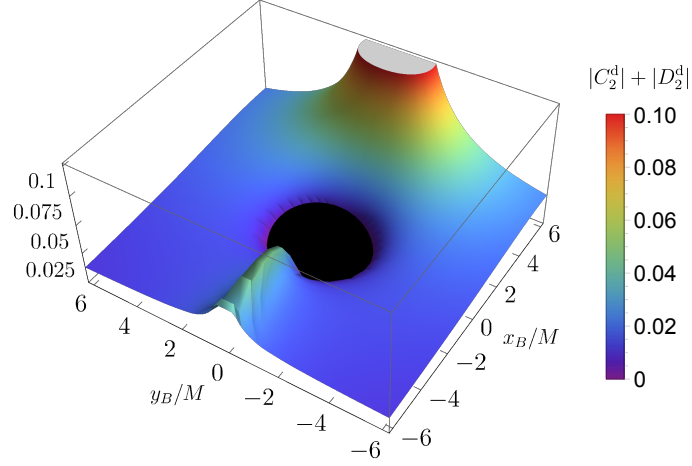
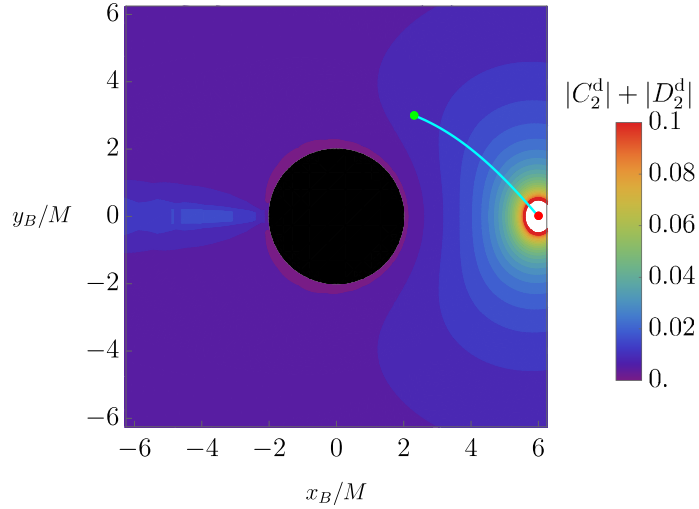
(a)  $\Omega_B = 1/M$ (b)  $\Omega_B = 1/(2M)$ 

Figure 14 – Leading order signal strength between Alice, spatially fixed at radius  $r_A = 6M$  and Bob, spatially fixed at varying radii  $r_B$  and angular separation  $\gamma$  from Alice. The frequency of Alice’s detector is  $\Omega_A = 1/M$ . The plot labels Bob’s position by  $x_B = r_B \cos \gamma$  and  $y_B = r_B \sin \gamma$ . The detectors couple to the field through sharp switching functions for  $0 \leq \tau_A \leq M$  and  $0 \leq \tau_B \leq 15M$ , respectively. The top of the plots is capped close to Alice’s position because the direct contribution diverges at exactly that point. The plot covers the radial coordinate position of Bob down to  $r_B = 2.26M$ . The plot only covers positions up to a certain angular separation between Alice and Bob because the numerical evaluation of the signal strength is infeasible beyond this region.



(a) Direct contribution to the signal strength of Fig. 14b.



(b) Contour plot version of Fig. 15a, also showing the direct null geodesic between the marked locations.

Figure 15 – Direct contributions  $|C_2^d| + |D_2^d|$  to the signal strength in the scenario of Fig. 14b: The detectors are static: Alice is placed at a fixed radial coordinate  $r_A = 6M$ , whereas Bob's radial coordinate  $r_B$  and angular separation  $\gamma$  vary, as labelled by  $x_B = r_B \cos \gamma$  and  $y_B = r_B \sin \gamma$ . The detector gaps are  $\Omega_A = 1/M$  and  $\Omega_B = 1/(2M)$ , and Alice couples to the field for her proper time interval  $0 \leq \tau_A \leq M$ . A red dot in Fig. 15b indicates Alice's position, and the plot shows the direct null geodesic emanating from there to the green dot, as one example for Bob's location. Note that the direct contribution is not defined at the exact angular separation  $\gamma = \pi$ ; the plot shows a numerical interpolation.

receiving contributions to the signal strength from null rays that go around the black hole, i.e., secondary null rays. As we shall see in the following, there will be additional features indicating the region where null rays that orbit the black hole once (tertiary null rays) start contributing to the signal strength. As seen in the leading order signal strength, collecting more null rays does not necessarily improve the signal strength. In the following subsections we discuss in more detail the contribution from these non-direct null rays.

### 4.2.3 Shifting Bob's coupling

As pointed out earlier, the non-direct contribution is smaller compared to the direct contribution in terms of magnitude. To investigate this in more detail, we study a signaling scenario where Bob couples to the field for a time interval whose length is synchronized to the duration of Alice's signal but the time when Bob switches on his detector is delayed more and more. In this way, as the switching time of Bob's detector becomes later, Bob's detector soon no more interacts with any of the direct null geodesics emanating from Alice's detector. Instead, e.g., for some late switching times, it interacts with the part of the signal that propagates along secondary and higher-orbiting null geodesics from Alice to him.

The resulting non-direct contribution is plotted in Fig. 16. Specifically, the plot shows the scenario where Alice is located at radial coordinate  $r_A = 6M$  and Bob at radial coordinate  $r_B \approx 3.01M$  with a total angular separation of  $\gamma = \pi/4$ . Both detectors have identical energy gaps  $\Omega_A = \Omega_B = 1/M$ . Alice switches on her detector over a proper time interval from  $A_1 = 0$  to  $A_2 = M$ . Since Bob is closer to the horizon than Alice is, the length of the signal is shorter in terms of his proper time, and is given by  $\tilde{\tau}_B(A_2) - \tilde{\tau}_B(A_1) = \tilde{\tau}_B(A_2) \approx 0.71M$ . While in Fig. 16 Bob always couples to the field for an interval of this duration,  $B_2 - B_1 = \tilde{\tau}_B(A_2)$ , we vary the point in time at which Bob switches on his detector, i.e., for a given switch-on proper time  $B_1$  we have  $B_2 = B_1 + \tilde{\tau}_B(A_2)$ .

This means that, for  $B_1 = 0$ , Bob switches on his detector when the first direct

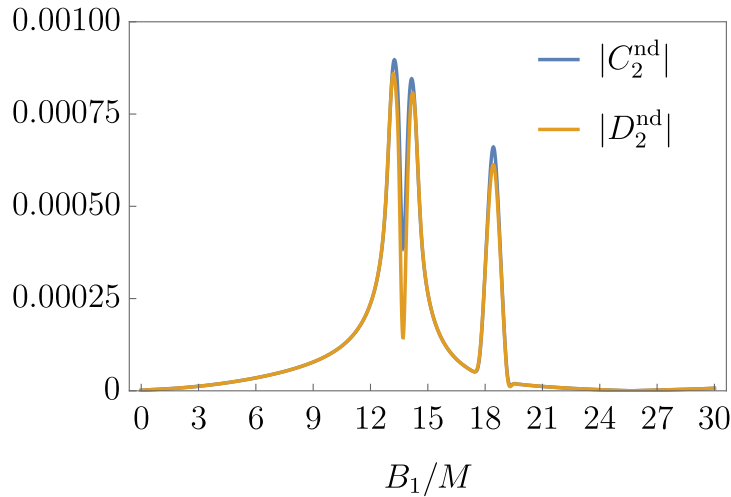


Figure 16 – The non-direct contribution  $|C_2^{\text{nd}}|$  and  $|D_2^{\text{nd}}|$  as a function of  $B_1$  for static detectors at  $r_A = 6M$  and  $r_B \approx 3.01M$  and  $\gamma = \pi/4$ , with  $\Omega_A = \Omega_B = 1/M$ . The switching on/off proper times are  $A_1 = 0$ ,  $A_2 = M$  and  $B_2 = B_1 + \tilde{\tau}_B(A_2)$ , with  $\tilde{\tau}_B(A_2) \approx 0.71M$ . Note that the corresponding direct contribution at  $B_1 = 0$  would be  $|C_2^{\text{d}}| \approx 0.0121551$  and  $|D_2^{\text{d}}| \approx 0.0107647$  which then drops down to zero as soon as  $B_1 > \tilde{\tau}_B(A_2)$ .

light signal from Alice (i.e., the one emanating at her proper time equal to  $A_1$ ) arrives at his location, and switches it off when the last direct light signal from Alice (i.e., the one emanating at her proper time equal to  $A_2$ ) arrives. In this case and for the given parameters, we have a direct contribution of magnitude  $|C_2^{\text{d}}| \approx 0.0121551$  and  $|D_2^{\text{d}}| \approx 0.0107647$ . For  $B_1 > 0$ , Bob switches on his detector *after* the first direct null geodesic has passed through his spatial location, hence the direct contribution decreases. Once  $B_1 > \tilde{\tau}_B(A_2)$ , Bob's detector does not interact with any direct null geodesics, and the direct contribution  $C_2^{\text{d}} = 0$  vanishes. However, we see that for later switching times, in the interval  $12M \leq B_1 \leq 20M$ , several spikes arise in the non-direct contribution which reach up to one fifth of the magnitude of the maximal direct contribution. These peaks are due to the part of the signal which propagates along secondary and tertiary null geodesics from Alice to Bob, and they arise due to the singular behaviour of the GF along null geodesics.

For example, a  $-\delta(\sigma)$ -singularity appears in the GF between points which are connected by a tertiary null geodesic, in similarity to points connected by direct primary geodesics [53]. Accordingly, we find a peak in the non-direct contribution when Bob's coupling interval is such that it exactly covers the arrival of all the tertiary null geodesics emanating from Alice. This is the case when Bob switches on exactly when the first of

the tertiary null geodesics arrives at his location at  $B_1 = B_{ter} \approx 18M$ .

Particularly interesting is the contribution from the secondary null geodesics: They cause the double peak structure in Fig. 16 centered around  $B_1 = B_{sec} \approx 14M$ , which is the proper time of Bob at which the first (i.e., emitted from Alice at  $\tau_A = A_1$ ) secondary null geodesic arrives at Bob's location. As discussed in Sec. 4.2.2, the GF diverges like a  $\text{PV}\left(\frac{1}{\sigma}\right)$ -distribution in the neighbourhood of points  $x$  which are connected to  $x'$  by secondary null geodesics. We can therefore qualitatively understand the properties of the part of the signal propagating along secondary null geodesics from the analytic solutions of Appendix F. There, we approximate the behaviour of the GF near the secondary null geodesic as  $\text{PV}\left(\frac{1}{\sigma}\right)$ , thus ignoring its regular coefficient: As discussed in Sec. 4.2.2, the GF diverges like a  $\text{PV}\left(\frac{1}{\sigma}\right)$ -distribution in the neighbourhood of points  $x$  which are connected to  $x'$  by secondary null geodesics. We can therefore qualitatively understand the properties of the part of the signal propagating along secondary null geodesics from the analytic solutions of Appendix F. There, we approximate the behaviour of the GF near the secondary null geodesic as  $\text{PV}\left(\frac{1}{\sigma}\right)$ , thus ignoring its regular coefficient: The most significant difference in comparison to the direct contribution (from  $\delta(\sigma)$ -distribution) is that the contributions from the secondary null geodesics have tails which extend beyond points that are connected by secondary null geodesics. That is, even if Bob switches off his detector (close to, but still) before the first secondary null geodesic arrives, or after the last one has passed by, there is still a contribution to the signal strength from the  $\text{PV}\left(\frac{1}{\sigma}\right)$ -distribution.

The results of Appendix F show that the signal features arising from secondary null geodesics are always roughly symmetric about Bob's switch-on time of  $B_1 = B_{sec}$ , i.e., when Bob's switching is aligned so that he exactly interacts with all secondary null geodesics emanating from Alice. For the parameters of Fig. 16 this point happens to be local minimum of the signal strength. For other parameters, in particular for longer interaction duration, richer features than the double-peak structure can arise, as seen in Fig. 31 of Appendix F. In particular, if the detectors are also resonant ( $\Omega_B = \nu\Omega_A$ ) then the signal strength exhibits a peak (with overlaid oscillatory features) around  $B_1 = B_{sec}$ .



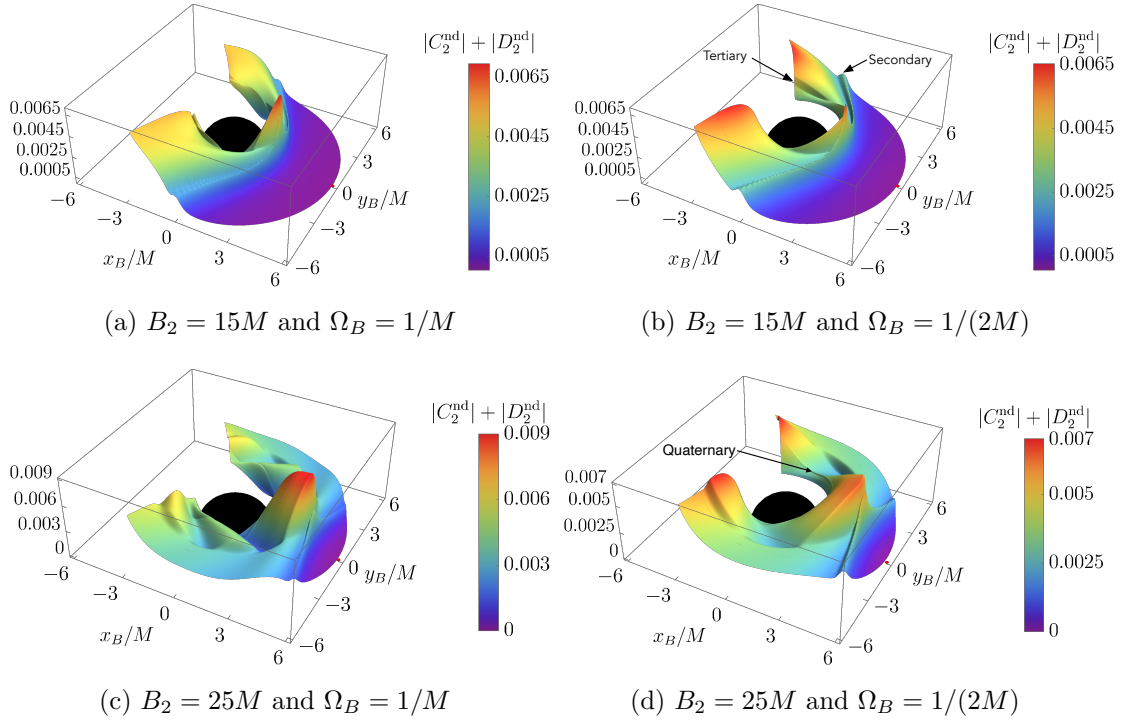


Figure 17 – Non-direct contributions  $|C_2^{\text{nd}}| + |D_2^{\text{nd}}|$  for static detectors as a function of Bob’s location for  $A_1 = B_1 = 0$ ,  $A_2 = M$ ,  $\Omega_A = 1/M$  and with further parameters as specified, comparing two different values of  $B_2$  and  $\Omega_A$ . A red dot indicates Alice’s location at  $r_A = 6M$ . Figs. 17a and 17b show the non-direct contribution to the total signal strength of Fig. 14.

#### 4.2.4 Long time-like coupling of Bob

The signaling scenario of Fig. 14 is slightly different from the scenario that we just considered in Fig. 16. Whereas in Fig. 16 the proper time window during which Bob couples to the field varies, while Bob remains at the same position, Fig. 14 compares the signal strength for different (static) positions of Bob, while his proper time window is fixed. At all the different positions, Bob switches on his detector at his proper time  $\tau_B = 0$  which is when the first primary null geodesic from Alice reaches him, which emanated from Alice at her proper time  $\tau_A = 0$ . Thus, depending on Bob’s spatial position, his switch-on happens at different coordinate times. At all positions, Bob is switched off after a fixed amount of his proper time has passed. Hence, Bob’s position determines to what extent his detector gets to interact with non-direct contributions to the signal. Thus, while the 2D plot of Fig. 16 plotted the signal strength as a function of the coupling times, Fig. 14 and Fig. 17 are functions of the detector position.

Fig. 17 shows non-direct contributions for different detector and switching pa-

rameters, in particular, including the scenarios of Fig. 14. Some features which are due to secondary, tertiary and quaternary non-direct null geodesics are highlighted by labels. Their characteristics are somewhat different from the characteristics observed in Fig. 16, because now all contributions are integrated up over a long interaction time of Bob whereas previously, in Fig. 16, a short interaction time window of Bob was shifted over various switch-on times. In particular, we find that the secondary null geodesics now create a single ripple in the 3D plots of Fig. 17 rather than a double-peak as observed above. Also, the tertiary null geodesics create a step-like feature rather than a peak as above.

Let us first focus on the “outermost” distinct feature (i.e., the distinct feature at the largest radius for a fixed angle), which is a ripple, in the plots in Fig. 17. This ripple is a consequence of secondary null geodesics. The plots in Figs. 17c and 17d show how the ripple moves to smaller angular separation  $\gamma$  than in Figs. 17a and 17b. That is, this outermost ripple moves closer to Alice for larger switch-off times  $B_2$  of Bob. This is expected since increasing  $B_2$  means that the secondary null geodesics have more time to propagate around the black hole to reach Bob before he switches off his detector. Whereas the position of the ripple only depends on  $B_2$ , thus is identical for Figs. 17a and 17b, and Figs. 17c and 17d, the shape of the ripple also depends on the energy gaps of the detectors. This becomes clear by comparing Fig. 17a to Fig. 17b, and Fig. 17c to Fig. 17d, which only differ in Bob’s detector energy changing from being identical to Alice’s,  $\Omega_A = \Omega_B = 1/M$ , to being half of Alice’s,  $\Omega_B = 1/(2M)$ .

The ripple has the form we expect it to have based on Fig. 32a of Appendix F, which shows the signal contribution from a PV  $\left(\frac{1}{\sigma}\right)$ -distribution for the detector frequencies and sender switching times corresponding to the 3D plots of Fig. 17. Again in Fig. 32a, the PV  $\left(\frac{1}{\sigma}\right)$ -distribution is used to approximate the GF along secondary null geodesics up to an overall prefactor. Thus, it yields the qualitative behaviour of the contribution from secondary null geodesics to the non-direct contribution of Fig. 17.

In fact, Fig. 18, which is a contourplot of Fig. 17b, shows that a (local) peak appears

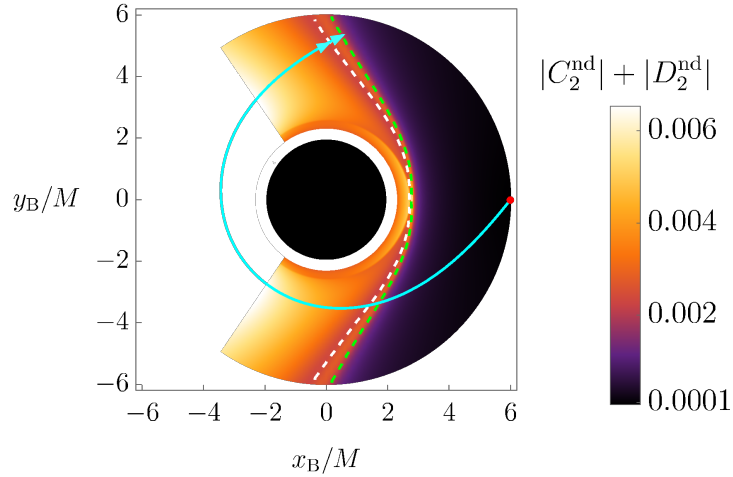


Figure 18 – Non-direct contribution  $|C_2^{\text{nd}}| + |D_2^{\text{nd}}|$  for  $A_1 = B_1 = 0$ ,  $A_2 = M$ ,  $\Omega_A = 1/M$ ,  $B_2 = 15M$  and  $\Omega_B = 1/(2M)$ . A red dot indicates Alice’s location. This is a contourplot version of Fig. 17b. The dashed lines indicate how far the secondary null rays emitted by Alice have propagated at the time when Bob switches off his detector: the green line, with smaller angular separation  $\gamma$ , shows the earliest secondary null rays from Alice, and the white line, with larger  $\gamma$ , shows the last secondary null rays from Alice.

between the arrival of the first and of the last secondary null geodesic. This matches the behaviour of the PV  $\left(\frac{1}{\sigma}\right)$ -signal observed for  $\Omega_A = 2\Omega_B = 1/M$  in Fig. 32a. In Fig. 18, the dashed green line (i.e., the dashed line corresponding to the smaller separation angles  $\gamma$  for a given radius) corresponds to points where the first secondary null geodesics from Alice (i.e., emitted at  $\tau_A = A_1 = 0$ ) arrive at Bob’s position exactly when Bob switches off the detector. The dashed white line (i.e., the dashed line corresponding to the larger angles  $\gamma$  for a given radius) corresponds to points where the last secondary null geodesic (i.e., emitted at  $\tau_A = A_2 = M$ ) arrives at Bob’s location when Bob switches off the detector. Therefore, for the points with a value of  $\gamma$  larger than that of a point on the larger-angle (white) dashed line at the same radius, i.e., further away from Alice, *all* secondary null geodesics arrive while Bob’s detector is switched on. Whereas for points with a value of  $\gamma$  smaller than that of a point on the smaller-angle (green) dashed line at the same radius, i.e., closer to Alice, *none* of the secondary null rays arrive before Bob’s switch-off. In-between the two dashed lines, i.e., where Bob switches the detector off roughly when Alice’s “middle” secondary null geodesic reaches him, lies the crest of the ripple and the magnitude of the non-direct contribution achieves a local maximum.

The appearance of the distinct ripple at the position that we just discussed, is a

consequence of the coupling parameters that we have chosen for the numerical evaluation of the full non-direct contribution in Fig. 17. The analytical solutions of Appendix F, which approximate the GF near divergences, show that when Alice emits longer signals, the signal strength from secondary null geodesics depends on Bob’s total coupling duration in an oscillatory fashion up to about the time when Alice’s last secondary null geodesic arrives at Bob, as seen in Fig. 32c. In particular, the maximal magnitude of signal strength does not increase just because the duration of Alice’s signal is increased. However, if Bob tunes his detector resonant, i.e.,  $\Omega_B = \nu\Omega_A$ , then the signal contribution from the secondary null geodesics increases roughly linearly with the duration of the signal.

In Figs. 17b and 17d we can also see the effect of *tertiary* light rays on the non-direct contribution. These rays are the main cause of the second outermost distinct feature in the plots, which is labelled “tertiary” in Fig. 17b. This feature is not quite a ripple, like the outermost feature was, but it is more steplike, at least for certain angles away from  $\gamma = 0$ . The tertiary feature is also more localized than the secondary one, because the GF has a  $-\delta(\sigma)$ -singularity for tertiary null geodesics. Hence, this singularity does not contribute to the integral in  $C_2^{\text{nd}}$  if Bob is located on one side of the steplike feature in Fig. 17b, but it does contribute to  $C_2^{\text{nd}}$  if Bob is located on the other side. Perhaps less intuitive is the fact that the contribution from the tertiary lightrays can decrease the magnitude of the non-direct contribution. This occurs when the sign of the tertiary contribution to the signal is opposite to the earlier contributions, as illustrated in Fig. 19.

Fig. 19 compares the integrand of expression (4.45) for  $C_2^{\text{nd}}$ , as well as the GF in that integrand, for two different locations of Bob: Fig. 19a corresponds to a location of Bob where all tertiary null geodesics arrive only after Bob has switched off the detector, i.e., a location above the step-like feature in Fig. 17b. On the other hand, Fig. 19b corresponds to a location where all tertiary null geodesics arrive while Bob is still coupled to the field.

The main features of the integrand are due to the  $\text{PV}(\frac{1}{\sigma})$ -singularity of the GF around secondary null geodesics, which appears in both figures. In addition to that, the peak at the right end of Fig. 19b is due to the  $-\delta(\sigma)$ -singularity from tertiary null

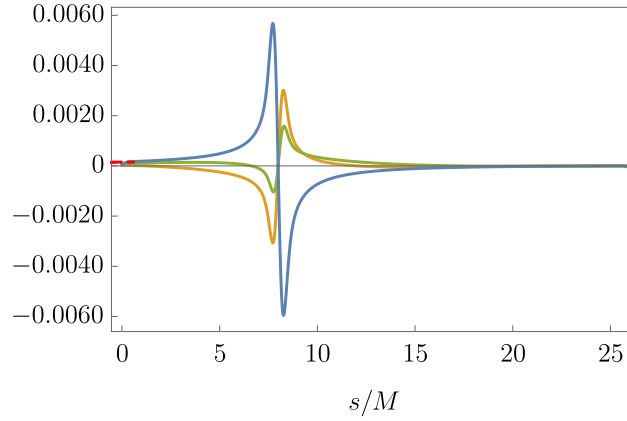
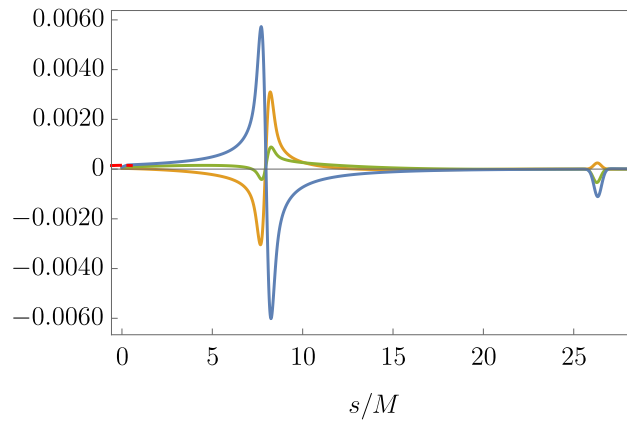
(a)  $r_A \approx 2.583M$ (b)  $r_A \approx 2.479M$ 

Figure 19 – Comparison of the integrand in  $C_2^{\text{nd}}$  in Eq. (4.44) for two different positions of Bob in the scenario of Fig. 17b: The top/bottom plots correspond to positions of Bob located at the top/bottom of the steplike feature due to tertiary light rays in Fig. 17b. Both positions have angular separation  $\gamma = 69\pi/100$  from Alice, but with different radial coordinates. The orange and green curves correspond to, respectively, the real and imaginary parts of the integrand (times  $M$ ) in Eq. (4.44). The solid blue and dashed red curves correspond to the GF  $M^2{}_0G_{\text{ret}}/4\pi$  (which is a factor in that integrand) in, respectively, the DP and QL regions (extended to slightly negative values of  $w/M$  for ease of visualization). The horizontal axes contain the integration variable  $w$  in Eq. (4.44) divided by  $M$ . (Recall that the switching parameters are  $A_1 = B_1 = 0$ ,  $A_2 = M$ ,  $B_2 = 15M$ ,  $\Omega_A = 1/M$  and  $\Omega_B = 1/(2M)$ .)

geodesics. Whereas the exact expression for the integrand is singular at these places, the figure only plots the numerical approximation to the GF of Sec. 4.2.2. This is why the singularities in the exact integrand appear smeared in these plots.

The full integration of the integrand plotted in Fig. 19a results in a real (imaginary) part of  $C_2^{\text{nd}}$  which is negative (positive). However, the extra contribution due to the tertiary light rays in Fig. 19b is negative (positive) for the real (imaginary) part. Thus, the contribution from the tertiary rays reduces the real and imaginary parts of  $C_2^{\text{nd}}$  and so also its absolute value. Hence, for the parameters at hand, the effect of the signal

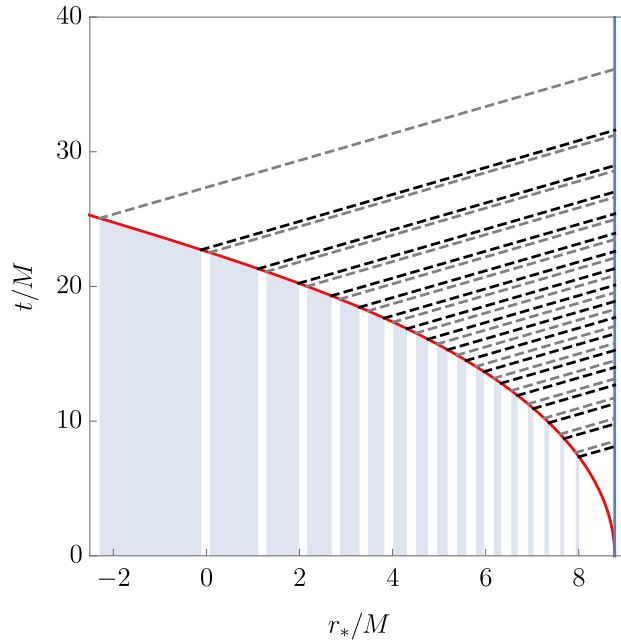


Figure 20 – Scenario where Alice follows a radially-infalling timelike geodesic starting from rest at  $r = 6M$ , and Bob is static at  $r = 6M$  (which corresponds to  $r_* = 6M + 2M \ln 4$ ). Alice’s worldline  $t = t(r_*(r_A))$  is given by the red line, Bob’s  $t = t(r_*(r_B))$  by the blue vertical line. The shaded regions indicate various coupling intervals during which Alice couples her detector to the field. The black-dashed lines represent the first radially-outgoing null geodesics emanating from Alice for each interval, the grey-dashed lines represent the last ones. All intervals last for the same amount of Alice’s proper time  $\Delta\tau_A = M/4$ . Time windows starting later on Alice’s worldline, i.e., closer to the horizon, extend over larger intervals of coordinate time (as well as of tortoise radial coordinate  $r_*$ ).

propagating along the tertiary null geodesics is to reduce the non-direct contribution to the signal strength.

Additionally, Fig. 17d even displays a feature due to quaternary lightrays, which is labelled “quaternary”. This feature is, similarly to the secondary effect, like a ripple, as one would expect from the fact that the singularity of the GF is of similar type (i.e.,  $PV\left(\frac{1}{\sigma}\right)$ ) at secondary and quaternary light-crossings. We have checked that this feature is indeed due to quaternary rays by an analysis of the integrand similar to that described above for the feature due to tertiary rays.

#### 4.2.5 Signaling between static and radial-infalling observers

In this scenario, the sender, Alice, follows a radial-infalling geodesic towards the black hole whereas the receiver, Bob, continues to be static.

In particular, as Alice starts falling from rest at  $r_A = 6M$ , she switches on her

detector at different positions, but with the same duration of her proper time:  $\Delta\tau_A = M/4$ . Accordingly, Bob whose position remains fixed at  $r_B = 6M$ , switches on (off) his detector immediately after the first (last) null ray emitted by Alice reaches his position (see Fig. 20). This setting allows us to inspect how the signal strength changes as Alice falls into the black hole. We then use Eq. (4.37) (with its equivalent expression for  $D_2^d$ ) to calculate the direct contribution  $C_2^d$  and  $D_2^d$ . The integral in Eq. (4.37) reduces significantly since  $U = \Delta^{1/2} = 1$  along radial null geodesics as discussed in Sec. 2.1.2. For the non-direct contribution we use Eq. (4.19) where we exclude the direct term from  ${}_0G_{\text{ret}}(x, x')$ , i.e., we use  ${}_0G_{\text{ret}}^{\text{nd}}(x, x')$  instead of  ${}_0G_{\text{ret}}(x, x')$ .

In Fig. 21 we plot the total signal strength  $|C_2| + |D_2|$  for a scenario where Alice and Bob have identical detectors, i.e.,  $\Omega_A = \Omega_B = \Omega$  with  $\Omega \in [0, 10/M]$  in the top 3D plot and  $\Omega = 1/M, 5/M, 10/M$  in the bottom 2D plot. Due to numeric limitations, for large  $\Omega$  we were not able to calculate properly the signal strength when Alice falls beyond  $r \approx 2.5M$ . To be precise, as Alice approaches the horizon, the integrand we have to evaluate to obtain  $C_2$  and  $D_2$  became highly oscillatory due to the time dilation, this resulted in an inaccurate signal strength when Alice's position goes below  $r \approx 2.5M$ . Different from the previous scenario where the non-direct contribution is always subdominant compared to the direct contribution, in this case, the non-direct term increases as Alice approaches the event horizon. When she falls below  $r_A \approx 2.3M$ , the non-direct contribution now becomes the dominant term in the signal strength. To understand this change in the behavior, we compare the magnitudes of the direct and non-direct contributions. For  $C_2$  this comparison is shown in Fig. 22<sup>4</sup>. In the figure we can see that the direct part is dominant over the non-direct up until a certain point (around  $r_A \approx 2.3M$  in this case) where the non-direct overcomes the direct part. The decrease in the direct contribution is not particularly unexpected since it is still inverse-proportional to the distance (see Appendix D for further analysis) between Alice and Bob. On the other hand, even though the increase in the non-direct contribution is not new (see Fig. 17), the increment in the magnitude eventually becomes larger than the direct contribution. This behaviour seems

<sup>4</sup>The contributions to  $D_2$  behave similarly.

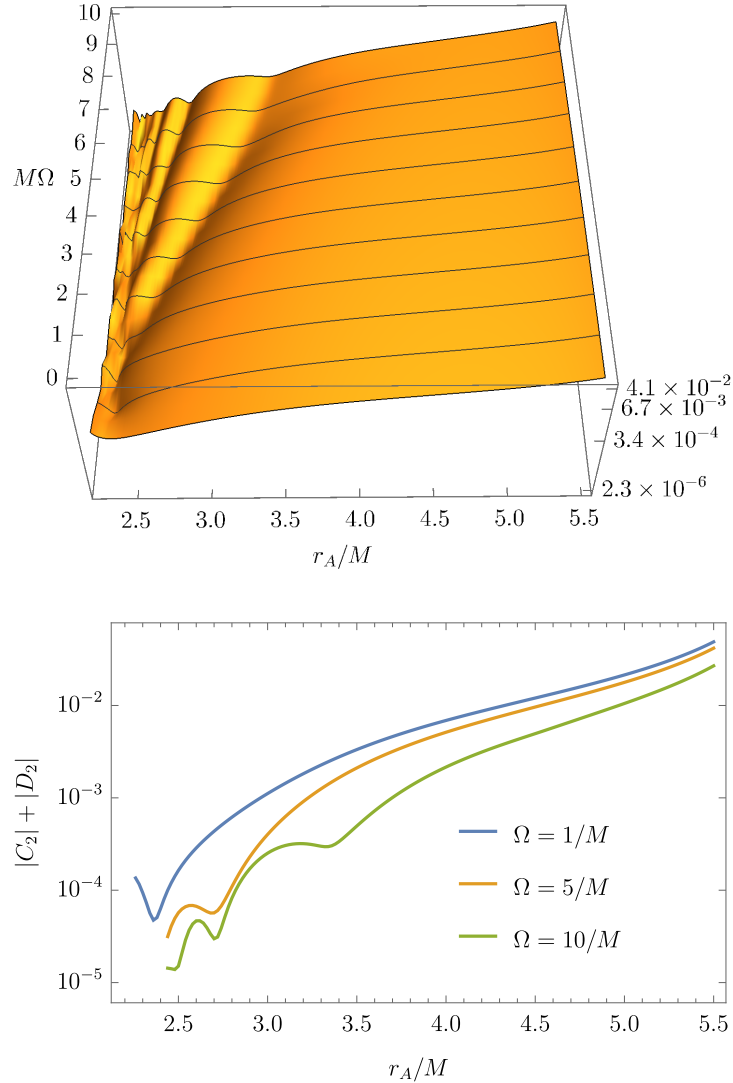


Figure 21 – Plots of  $|C_2| + |D_2|$  in the radial-infall scenario as a function of the radial coordinate  $r_A$  (when Alice switches on her detector) and detectors' frequency  $\Omega = \Omega_A = \Omega_B$ . Independently of the value of  $r_A$ , Alice switches off her detector after a fixed amount  $\Delta\tau_A = M/4$  of her proper time. Top: 3D plot (the red line corresponds to the case where  $\Omega = 1/M$ ). Bottom: 2D plot as a function of  $r_A$  for a sample of values of  $\Omega$  (so these curves are just cross-sections of the 3D plot at the top).

to be related with the four-fold singularity structure of  ${}_0G_{\text{ret}}$  [53]. While Alice approaches the black hole and switches on her detector for a constant interval of time  $\Delta\tau_A = M/4$ , from Bob's perspective, she switches on her detector for longer time intervals due to the time dilation. This effect causes the contribution from  ${}_0G_{\text{ret}}^{\text{nd}}$  to  $C_2^{\text{nd}}$  (and  $D_2^{\text{nd}}$ ) in Eq. (4.45) to be more significant. In its turn, the singularity structure of  ${}_0G_{\text{ret}}$  around secondary null rays (of type  $PV\left(\frac{1}{\sigma}\right)$ ) shows a monotonic increase in  ${}_0G_{\text{ret}}^{\text{nd}}$  prior arrival of secondary null rays. Thus this increase also leads to an increase in  $C_2^{\text{nd}}$  (and  $D_2^{\text{nd}}$ ) as seen in Fig. 21.



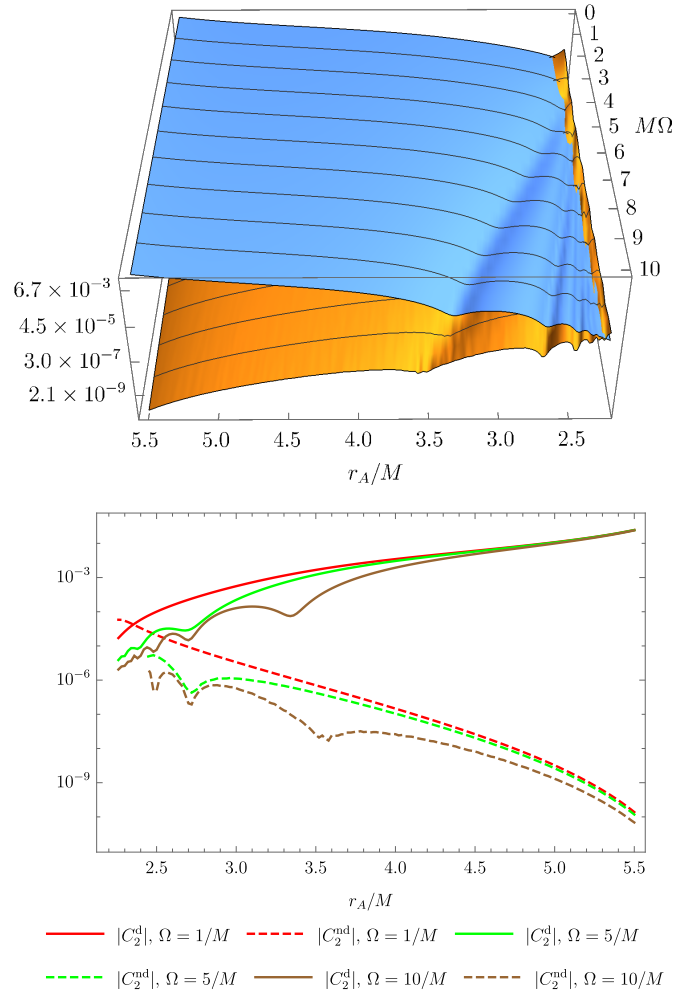


Figure 22 – Plots of direct  $|C_2^d|$  and non-direct  $|C_2^{nd}|$  contributions to  $C_2$  in the radial-infall scenario as functions of  $r_A$  (when Alice switches on her detector) and detectors' frequency  $\Omega$ . Top: 3D plot where the blue and orange surfaces respectively correspond to  $|C_2^d|$  and  $|C_2^{nd}|$ . Bottom: 2D plot as a function of  $r_A$  for a sample of values of  $\Omega$  (so these curves are just cross-sections of the 3D plot at the top).

All these results were widely discussed and included in [19]. In the Appendix C of Ref. [19] we included a prescription for the CID scheme we introduced in Sec. 2.2.1.

## 5 The Teukolsky Green function

In Chapter 2 we illustrated how the RWE describes field perturbations of Schwarzschild spacetime. After calculating the spin-2 retarded GF of the RWE, we could reconstruct the metric perturbation using  ${}_2G_{\text{ret}}$  together with the source of the perturbation. As discussed in Sec. 1.8.3, the RWE describes the odd-parity sector of gravitational perturbations. For the even-parity sector, we should also solve the Zerilli equation (see Sec. 1.8.4). As highlighted in Chapter 1, in contrast to the Regge-Wheeler formalism, the Teukolsky formalism extends beyond perturbations of Schwarzschild black holes to include Kerr black holes. The computation of the Teukolsky Green function in Schwarzschild spacetime serves as a foundational step towards establishing a more comprehensive framework for describing field perturbations of Kerr spacetime via the Teukolsky formalism.

For self-force calculations, the gauge choice is a key step we should have in mind. Regularising the metric perturbation in the Lorenz gauge is easy to perform but solving the field equation for the metric perturbation becomes difficult. In contrast, the Regge-Wheeler and radiation gauges have easily solvable field equations, but regularising the metric perturbation is challenging (as noted in Chapter 2), the regularisation process is not straightforward. In this chapter we mainly focus on solving the Teukolsky equation (TE), a key component for reconstructing the metric perturbation in the radiation gauge. We also explore a regularisation process similarly to the one shown in Chapter 2 for  ${}_sG_{\text{ret}}$ .

In Schwarzschild spacetime, a perturbation of spin  $s$  can be described via a field  ${}_s\Psi = {}_s\Psi(t, r, \theta, \phi)$  (see Sec. 1.8.5). This field satisfies the well-known Teukolsky equation given in Eq. (1.93). Particularly, we are interested in solving Eq. (1.93) via a Green function method, i.e., we aim to solve

$$\left[ \square + \frac{2s}{r^2} \left( \frac{3M - r}{f} \frac{\partial}{\partial t} + (r - M) \frac{\partial}{\partial r} + i \frac{\cos \theta}{\sin^2 \theta} \frac{\partial}{\partial \phi} + \frac{1 - s \cot^2 \theta}{2} \right) \right] {}_sG_{\text{ret}}^T(x, x') = -4\pi \delta_4(x, x'), \quad (5.1)$$

where  ${}_sG_{\text{ret}}^T$  is the retarded Green function of the TE. Calculating the self-force through

${}_sG_{\text{ret}}^T$  (except  $s = 0$ ) is an approach that has not been explored yet. Determining  ${}_sG_{\text{ret}}^T$  could provide an alternative approach for studying perturbations of Schwarzschild spacetime. We thus start by exploring the Hadamard form of  ${}_sG_{\text{ret}}^T$ , this allows us to easily identify its direct and non-direct parts.

## 5.1 Hadamard construction of ${}_sG_{\text{ret}}^T$

Within a normal neighbourhood of  $x'$ , the Hadamard form for  ${}_sG_{\text{ret}}^T(x, x')$  can be written as [33]

$${}_sG_{\text{ret}}^T = U^T(x, x')\delta_+(\sigma) - V_s^T(x, x')\theta_+(-\sigma), \quad (5.2)$$

where  $U^T(x, x')$  and  $V_s^T(x, x')$  are two smooth biscalars,  $\delta_+(\sigma) = \theta_+(x, x')\delta(\sigma)$  and  $\theta_+(-\sigma) = \theta_+(x, x')\theta(-\sigma)$ . Before applying any differential operator on Eq. (5.2), we define an asymptotic expression for  ${}_sG_{\text{ret}}^T$  (as suggested in [5] for the scalar case)

$${}_sG_{\text{ret}}^{T,\epsilon} \equiv U^T\delta_+(\sigma + \epsilon) - V_s^T\theta_+(-\sigma - \epsilon). \quad (5.3)$$

This approach to Eq. (5.2) does allow us to put it back into Eq. (5.1) to obtain the differential equations  $U^T$  and  $V_s^T$  satisfy. Before going further, for simplicity we introduce the quantities

$$A^\mu \equiv \frac{2s}{r^2} \left[ \left( -r + \frac{M}{f} \right) \delta_t^\mu + (r - M)\delta_r^\mu + i \frac{\cos\theta}{\sin^2\theta} \delta_\phi^\mu \right], \quad (5.4)$$

$$B \equiv \frac{s}{r^2} (1 - s \cot^2\theta), \quad (5.5)$$

so that the TE can be written as

$$(\square + A^\mu \partial_\mu + B) {}_sG_{\text{ret}}^T = -4\pi \delta_4(x, x'). \quad (5.6)$$

We now insert  ${}_sG_{\text{ret}}^{T,\epsilon}$  in the above equation. By considering the identities (see [5])

$$\sigma \delta_+(\sigma + \epsilon) = -\epsilon \delta_+(\sigma + \epsilon), \quad (5.7)$$

and

$$\sigma \frac{d^n}{d\sigma^n} \delta_+(\sigma + \epsilon) = -n \frac{d^{n-1}}{d\sigma^{n-1}} \delta_+(\sigma + \epsilon) - \epsilon \frac{d^n}{d\sigma^n} \delta_+(\sigma + \epsilon), \quad (5.8)$$

for  $n > 0$ , we find that

$$\begin{aligned}
(\square + A^\mu \partial_\mu + B)_s G_{\text{ret}}^{T,\epsilon} &= -2U^T \epsilon \delta'_+(\sigma + \epsilon) \\
&+ \delta_+(\sigma + \epsilon) \left\{ (\square + A^\mu \partial_\mu + B) U^T + (2\sigma^\mu \partial_\mu + \sigma^\mu{}_\mu + \sigma_\mu A^\mu - 2) V_s^T \right\} \\
&+ \delta'_+(\sigma + \epsilon) \left( 2\sigma^\mu \partial_\mu U^T - 4U^T + \sigma^\mu{}_\mu U^T + \sigma_\mu A^\mu U^T - \epsilon V_s^T \right) \\
&+ \theta_+(-\sigma - \epsilon) \left( \square V_s^T + A^\mu \partial_\mu V_s^T + B V_s^T \right), \tag{5.9}
\end{aligned}$$

where the primes indicates differentiation with respect to  $\sigma$ . The limit  $\epsilon \rightarrow 0^+$  yields

$$\begin{aligned}
(\square + A^\mu \partial_\mu + B)_s G_{\text{ret}}^T &= -4\pi U^T \delta_4(x, x') + \\
&+ \delta_+(\sigma) \left\{ (\square + A^\mu \partial_\mu + B) U^T + (2\sigma^\mu \partial_\mu + \sigma^\mu{}_\mu + \sigma_\mu A^\mu - 2) V_s^T \right\} \\
&+ \delta'_+(\sigma) \left( 2\sigma^\mu \partial_\mu U^T - 4U^T + \sigma^\mu{}_\mu U^T + \sigma_\mu A^\mu U^T \right) \\
&+ \theta_+(-\sigma) \left( \square V_s^T + A^\mu \partial_\mu V_s^T + B V_s^T \right), \tag{5.10}
\end{aligned}$$

where we have used  $\lim_{\epsilon \rightarrow 0^+} \epsilon \delta'_+(\sigma + \epsilon) = 2\pi \delta_4(x, x')$  [5]. When comparing Eq. (5.10) to Eq. (5.6), we immediately find that  $U^T$  has to satisfy the coincidence limit

$$[U^T(x, x')] = U^T(x, x') \Big|_{x=x'} = 1. \tag{5.11}$$

From the term involving  $\delta_+(\sigma)$ , we obtain the constraint for  $V_s^T$  on the light cone, i.e, for  $V_s^T \Big|_{\sigma=0} = \hat{V}_s^T$  we have that

$$\sigma^\mu \partial_\mu \hat{V}_s^T + \frac{1}{2} (\sigma^\mu{}_\mu + \sigma_\mu A^\mu - 2) \hat{V}_s^T = \frac{1}{2} \left( \square U^T + A^\mu \partial_\mu U^T + B U^T \right) \Big|_{\sigma=0}. \tag{5.12}$$

The initial condition for the above transport equation is obtained by evaluating it at coincidence and imposing regularity. This reads

$$[\hat{V}_s^T] = \frac{1}{2} [\square U^T] + \frac{1}{2} A^\mu [\partial_\mu U^T] + \frac{1}{2} B. \tag{5.13}$$

From the terms involving  $\delta(\sigma)$  and  $\theta(-\sigma)$ , we obtain two independent differential equations for  $U^T$  and  $V_s^T$ ,

$$(2\sigma^\mu \partial_\mu + \sigma^\mu{}_\mu - 4 + \sigma_\mu A^\mu) U^T = 0, \tag{5.14}$$

$$(\square + A^\mu \partial_\mu + B) V_s^T = 0, \tag{5.15}$$

where, as expected, when  $s = 0$  (i.e.,  $A^\mu = 0$  and  $B = 0$ ), we recover the equations for  $U$  and  $V_0$  for the Regge-Wheeler  ${}_0G_{\text{ret}}$ . In fact, with this relation between  $U^T$  and  $U$  we may go a step further to simplify Eq. (5.14). Let

$$U^T = e^\alpha U, \quad (5.16)$$

where  $\alpha = \alpha(x, x')$  is a smooth biscalar. When substituting this expression for  $U^T$ , we find that  $\alpha$  satisfies the transport equation

$$2\sigma^\mu \partial_\mu \alpha + \sigma_\mu A^\mu = 0, \quad (5.17)$$

with the initial condition  $[\alpha] = 0$ , which results from  $[U^T] = [e^\alpha][U] = 1$ . Given an affine parameter  $\lambda$ , a direct integration of Eq. (5.17) reads

$$\alpha(x_1, x_2) = -\frac{1}{2} \int_{\lambda_1}^{\lambda_2} u_\mu A^\mu d\lambda, \quad (5.18)$$

where  $\sigma^\mu(x_1, x_2) = (\lambda_2 - \lambda_1)u^\mu$ ,  $x_1 = x(\lambda_1)$  and  $x_2 = x(\lambda_2)$ . Unfortunately, this expression for  $\alpha(x_1, x_2)$  cannot be integrated for arbitrary geodesics to obtain a closed form. Instead, we can integrate Eq. (5.18) along specific geodesics (or integrate it numerically). In particular, for a timelike circular geodesic with  $r = r'$  (i.e.,  $u^\mu = \sqrt{\frac{r}{r-3M}}(1, 0, 0, \sqrt{\frac{M}{r^3}})$ ), we find that  $\alpha(x, x') = s\sqrt{\frac{r-3M}{r^3 f(r)}}(t - t')$  and for radial null geodesics (with  $u^\mu$  given in Eq. (2.15)),  $\alpha(x, x') = \frac{s(\epsilon+3)}{4} \ln\left(\frac{r'}{r}\right) + \frac{s(\epsilon-1)}{4} \ln\left(\frac{r'-2M}{r-2M}\right)$ .

For  $V_s^T$ , when we compare Eqs. (5.12)–(5.13) and (5.15) with the equations for  $V_s$  in (2.3), it becomes apparent that  $V_s^T$  satisfies a characteristic initial value problem as well. Thus, the methods we detailed in Chapter 2 for calculating  $V_s$  could be adapted for  $V_s^T$ . Unfortunately, this adaptation is not straightforward. For instance, the Hadamard-WKB method introduced in [60] (and generalised to arbitrary spin  $s$  in Sec. 2.1.3) for obtaining a small-coordinate expansion for  $V_s$  does not apply since Eq. (5.15) lacks spherical symmetry. A numerical approach could be more suitable. Given the Hadamard expansion

$$V_s^T(x, x') = \sum_k s\nu_k^T(x, x')\sigma^k(x, x'), \quad (5.19)$$

we can solve numerically the transport equations satisfied by the  ${}_s\nu_k^T$  coefficients. However, in order for this numerical approach to work, the first coefficient  ${}_s\nu_0^T$  requires  $[V_s^T]$  (a solution to Eq. (5.13)) as initial condition to solve its transport equation. The expansion of bitensors near coincidence [5] could be a good starting point for obtaining  $[\square U^T]$  and  $[\partial_\mu U^T]$  and providing the required initial condition for  ${}_s\nu_0^T$ . Nonetheless, the expansion in Eq. (5.19) converges very slowly, e.g., see Fig. 10 for PH spacetime. Thus, instead of calculating  $V_s^T$ , we will focus on calculating  ${}_sG_{\text{ret}}^T$ .

## 5.2 Mode decomposition for ${}_sG_{\text{ret}}^T$

In order to calculate  ${}_sG_{\text{ret}}^T$ , once again, we perform a mode decomposition for  ${}_sG_{\text{ret}}^T$  [40], i.e.,

$${}_sG_{\text{ret}}^T = (r'^2 f(r'))^s \sum_{\ell=|s|}^{\infty} \sum_{m=-\ell}^{\ell} {}_sG_{\ell}^T(r, r', \Delta t) {}_sY_{\ell m}(\theta, \phi) {}_sY_{\ell m}^*(\theta', \phi'), \quad (5.20)$$

where

$${}_sG_{\ell}^T(r, r') = \frac{1}{2\pi} \int_{-\infty}^{\infty} {}_s\tilde{G}_{\omega\ell}^T(r, r') e^{-i\omega\Delta t} d\omega, \quad (5.21)$$

and the Fourier modes  ${}_s\tilde{G}_{\omega\ell}^T$  are a solution to Eq. (1.101) with source

$$-4\pi (r'^2 f(r'))^{-s} r^{-2} \delta(r - r'),$$

i.e., it is a Green function of Eq. (1.101). The approach we follow to calculate  ${}_s\tilde{G}_{\omega\ell}^T$  is via factorized Green functions (as in the Regge-Wheeler case). Let  ${}_s\tilde{R}_{\omega\ell}^{\text{in}}$  and  ${}_s\tilde{R}_{\omega\ell}^{\text{up}}$  be homogeneous solutions to Eq. (1.101) with asymptotic conditions

$${}_s\tilde{R}_{\omega\ell}^{\text{in}} \sim \begin{cases} {}_s\tilde{R}_{\omega\ell}^{\text{in,tra}} (r^2 f)^{-s} e^{-i\omega r_*}, & r_* \rightarrow -\infty, \\ {}_s\tilde{R}_{\omega\ell}^{\text{in,inc}} r^{-1} e^{-i\omega r_*} + {}_s\tilde{R}_{\omega\ell}^{\text{in,ref}} r^{-1-2s} e^{i\omega r_*}, & r_* \rightarrow \infty \end{cases} \quad (5.22)$$

and

$${}_s\tilde{R}_{\omega\ell}^{\text{up}} \sim \begin{cases} {}_s\tilde{R}_{\omega\ell}^{\text{up,inc}} e^{i\omega r_*} + {}_s\tilde{R}_{\omega\ell}^{\text{up,ref}} (r^2 f)^{-s} e^{-i\omega r_*}, & r_* \rightarrow -\infty, \\ {}_s\tilde{R}_{\omega\ell}^{\text{up,tra}} r^{-1-2s} e^{i\omega r_*}, & r_* \rightarrow \infty \end{cases}, \quad (5.23)$$

where  ${}_s\tilde{R}_{\omega\ell}^{\text{in,inc/ref/tra}}$  and  ${}_s\tilde{R}_{\omega\ell}^{\text{up,inc/ref/tra}}$  are, respectively, the incidence, reflection and transmission coefficients. We choose these boundary conditions in a way that  ${}_s\tilde{G}_{\omega\ell}^T$  are the

Fourier modes of  ${}_sG_{\text{ret}}^T$ . Additionally, we normalize these solutions in a way that their transmission coefficients  ${}_s\tilde{R}_{\omega\ell}^{\text{in,tra}}$  and  ${}_s\tilde{R}_{\omega\ell}^{\text{up,tra}}$  are equal to one.

In this way, given the solutions  ${}_s\tilde{R}_{\omega\ell}^{\text{in}}$  and  ${}_s\tilde{R}_{\omega\ell}^{\text{up}}$ , we construct the Green function

$${}_s\tilde{G}_{\omega\ell}^T(r, r') = -\frac{{}_s\tilde{R}_{\omega\ell}^{\text{in}}(r_<){}_s\tilde{R}_{\omega\ell}^{\text{up}}(r_>)}{W^T({}_s\tilde{R}_{\omega\ell}^{\text{in}}, {}_s\tilde{R}_{\omega\ell}^{\text{up}})}, \quad (5.24)$$

where  $r_> = \max(r, r')$ ,  $r_< = \min(r, r')$  and

$$W^T({}_s\tilde{R}_{\omega\ell}^{\text{in}}, {}_s\tilde{R}_{\omega\ell}^{\text{up}}) = (r^2 f)^{s+1} \left( {}_s\tilde{R}_{\omega\ell}^{\text{in}} \frac{d}{dr} {}_s\tilde{R}_{\omega\ell}^{\text{up}} - {}_s\tilde{R}_{\omega\ell}^{\text{up}} \frac{d}{dr} {}_s\tilde{R}_{\omega\ell}^{\text{in}} \right) = 2i\omega {}_s\tilde{R}_{\omega\ell}^{\text{in,inc}}. \quad (5.25)$$

In order to calculate  ${}_s\tilde{R}_{\omega\ell}^{\text{in}}$  and  ${}_s\tilde{R}_{\omega\ell}^{\text{up}}$ , we follow two methods. The first method is based on a numerical scheme implemented in the BHPT. The second method relies on the Chandrasekhar transformation detailed in Sec. 1.8.5. By comparing the asymptotic conditions for  ${}_s\tilde{X}_{\omega\ell}^{\text{in}}$  and  ${}_s\tilde{X}_{\omega\ell}^{\text{up}}$  with (5.22) and (5.23), it is natural to apply (1.104) on  ${}_s\tilde{X}_{\omega\ell}^{\text{in}}$  and  ${}_s\tilde{X}_{\omega\ell}^{\text{up}}$  and obtain two Teukolsky solutions with similar asymptotic conditions given in Eqs. (5.22)–(5.23). Moreover, it is possible to reduce higher order derivatives in  ${}_{-2}\tilde{\mathcal{C}}(r, \omega)$  by using the fact that  ${}_2\tilde{X}_{\omega\ell}^{\text{in}}$  and  ${}_2\tilde{X}_{\omega\ell}^{\text{up}}$  satisfy the homogeneous radial RWE, this reads

$$\begin{aligned} {}_{-2}\tilde{\mathcal{C}}_{\text{R}}(r, \omega){}_2\tilde{X}_{\omega\ell}^{\text{in}} &= -2rf(3M - r(1 + i\omega r)) \frac{d}{dr} {}_2\tilde{X}_{\omega\ell}^{\text{in}} + \\ &\quad \left[ l(l+1)rf + \frac{12M^2}{r} - 6M(1 + i\omega r) + 2ir^2\omega(1 + i\omega r) \right] {}_2\tilde{X}_{\omega\ell}^{\text{in}}, \end{aligned} \quad (5.26)$$

and

$$\begin{aligned} {}_{-2}\tilde{\mathcal{C}}_{\text{R}}(r, \omega){}_2\tilde{X}_{\omega\ell}^{\text{up}} &= -2rf(3M - r(1 + i\omega r)) \frac{d}{dr} {}_2\tilde{X}_{\omega\ell}^{\text{up}} + \\ &\quad \left[ l(l+1)rf + \frac{12M^2}{r} - 6M(1 + i\omega r) + 2ir^2\omega(1 + i\omega r) \right] {}_2\tilde{X}_{\omega\ell}^{\text{up}}, \end{aligned} \quad (5.27)$$

where the ‘R’ subindex indicates that high order derivatives in the operator have been reduced using Eq. (1.69). From the above expressions, we note that solutions to the radial TE with  $s = -2$  are constructed from solutions to the radial RWE with  $s = +2$ .

As Nakano and Sasaki showed in [44], this operation of reducing high order derivatives of  ${}_2\tilde{X}_{\omega\ell}^{\text{in}}$  and  ${}_2\tilde{X}_{\omega\ell}^{\text{up}}$  has a more fundamental implication than simplifying the calculation of high order radial derivatives. The non-direct part of  ${}_sG_{\text{ret}}^T$  contains a Heaviside

distribution  $\theta(-\sigma)$  which induces quasi-direct terms (see Sec. 2.2.3) when applying differential operators on it<sup>1</sup>. When one reduces the second order derivative in  ${}_{-2}\tilde{\mathcal{C}}$  (using the homogeneous radial RWE), the quasi-direct terms are partially removed<sup>2</sup> [44]. However, the first-order derivative in  ${}_{-2}\tilde{\mathcal{C}}_{\text{R}}$  may still lead to additional quasi-direct terms. As explained in Sec. 2.2.3, we address these additional quasi-direct terms by using an averaging procedure to remove direction-dependent terms from  ${}_{-2}\tilde{\mathcal{C}}_{\text{R}}(r, \omega) {}_2\tilde{X}_{\omega\ell}^{\text{in}}$  and  ${}_{-2}\tilde{\mathcal{C}}_{\text{R}}(r, \omega) {}_2\tilde{X}_{\omega\ell}^{\text{up}}$ .

In this way, we introduce the following homogeneous solutions to the radial Teukolsky equation

$$\begin{aligned} {}_{-2}\tilde{\mathcal{R}}_{\omega\ell}^{\text{in}} &= {}_{-2}\tilde{\mathcal{C}}_{\text{R}}(r, \omega) {}_2\tilde{X}_{\omega\ell}^{\text{in}}, \\ {}_{-2}\tilde{\mathcal{R}}_{\omega\ell}^{\text{up}} &= {}_{-2}\tilde{\mathcal{C}}_{\text{R}}(r, \omega) {}_2\tilde{X}_{\omega\ell}^{\text{up}}. \end{aligned} \quad (5.28)$$

Now we can rewrite Eq. (5.24) in the following way [40]

$$\begin{aligned} {}_{-2}\tilde{G}_{\omega\ell}^T(r, r') &= - \frac{{}_{-2}\tilde{\mathcal{R}}_{\omega\ell}^{\text{in}}(r_{<}) {}_{-2}\tilde{\mathcal{R}}_{\omega\ell}^{\text{up}}(r_{>})}{{}_{-2}\tilde{\mathcal{R}}_{\omega\ell}^{\text{in,tra}} {}_{-2}\tilde{\mathcal{R}}_{\omega\ell}^{\text{up,tra}} W^T} \\ &= - \frac{W}{{}_{-2}\tilde{\mathcal{R}}_{\omega\ell}^{\text{in,tra}} {}_{-2}\tilde{\mathcal{R}}_{\omega\ell}^{\text{up,tra}} W^T} {}_{-2}\tilde{\mathcal{C}}_{\text{R}}(r_{<}, \omega) {}_{-2}\tilde{\mathcal{C}}_{\text{R}}(r_{>}, \omega) \frac{{}_2\tilde{X}_{\omega\ell}^{\text{in}}(r_{<}) {}_2\tilde{X}_{\omega\ell}^{\text{up}}(r_{>})}{W} \\ &= - \frac{W}{{}_{-2}\tilde{\mathcal{R}}_{\omega\ell}^{\text{in,tra}} {}_{-2}\tilde{\mathcal{R}}_{\omega\ell}^{\text{up,tra}} W^T} {}_{-2}\tilde{\mathcal{C}}_{\text{R}}(r_{<}, \omega) {}_{-2}\tilde{\mathcal{C}}_{\text{R}}(r_{>}, \omega) {}_2\tilde{G}_{\omega\ell}, \end{aligned} \quad (5.29)$$

where  $W$  is the Wronskian given in Eq. (2.62),  ${}_{-2}\tilde{\mathcal{R}}_{\omega\ell}^{\text{in,tra}}$  and  ${}_{-2}\tilde{\mathcal{R}}_{\omega\ell}^{\text{up,tra}}$  are, respectively, the transmission coefficients<sup>3</sup> of  ${}_{-2}\tilde{\mathcal{R}}_{\omega\ell}^{\text{in}}$  and  ${}_{-2}\tilde{\mathcal{R}}_{\omega\ell}^{\text{up}}$ . We follow [40] to calculate these coefficients and the Wronskian ratio  $W/W^T$ . More specifically, we first take the asymptotics in Eq. (2.59) and add the next leading orders, i.e.,

$${}_2\tilde{X}_{\omega\ell}^{\text{in}} \sim \begin{cases} (1 + \alpha_+ \Delta_S + \beta_+ \Delta_S^2) e^{-i\omega r_*}, & r_* \rightarrow -\infty, \\ {}_2\tilde{X}_{\omega\ell}^{\text{in,inc}} \left(1 + \frac{\alpha_\infty}{r} + \frac{\beta_\infty}{r^2}\right) e^{-i\omega r_*} + {}_2\tilde{X}_{\omega\ell}^{\text{in,ref}} e^{i\omega r_*}, & r_* \rightarrow \infty, \end{cases} \quad (5.30)$$

where the solution  ${}_2\tilde{X}_{\omega\ell}^{\text{in}}$  was normalised with  ${}_2\tilde{X}_{\omega\ell}^{\text{in,tra}} = 1$  (see Sec. 2.2.2),  $\Delta_S = r(r-2M)$ , and the coefficients  $\alpha_+$ ,  $\beta_+$ ,  $\alpha_\infty$  and  $\beta_\infty$  are determined by demanding that (5.30) satisfies

<sup>1</sup>Differentiating the Heaviside distribution  $\theta(-\sigma)$  once leads to  $\delta(\sigma)$ , a distribution that shares the same behaviour we find in the direct part of  ${}_sG_{\text{ret}}^T$ .

<sup>2</sup>This was shown (to 1PN (post-Newtonian) approximation) in Appendix C of [44]. The authors in [44] claim this to be true to any NP order.

<sup>3</sup>The inclusion of these coefficients is related to the fact that the operator  ${}_{-2}\tilde{\mathcal{C}}_{\text{R}}$  does not necessarily return a Teukolsky solution normalized with a transmission coefficient equal to one.



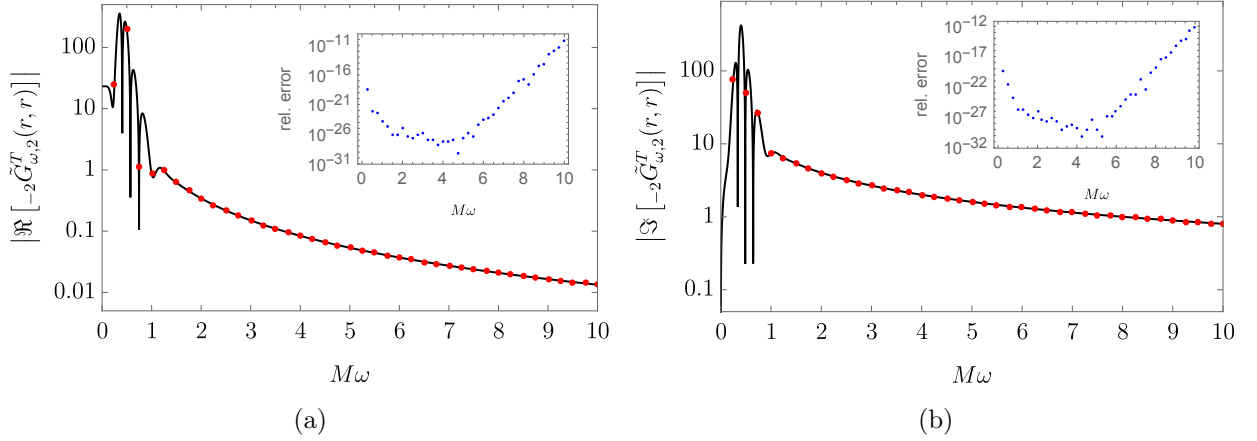


Figure 23 – Absolute values of the real (left) and imaginary (right) parts of  ${}_{-2}\tilde{G}_{\omega,2}^T$ . In this case  $r = r' = 6M$ . The black solid line is obtained by applying the Chandrasekhar transformation on  ${}_2\tilde{G}_{\omega,2}$  (see Eq. (5.29)) whereas the red dots are obtained using the numerical method available in the BHPT.

the radial RWE. This reads [40]

$$\alpha_+ = \frac{i(\ell(\ell+1) - 3)}{4M^2(4M\omega + i)},$$

$$\beta_+ = \frac{-12 - \ell^2(\ell+1)^2 + \ell(\ell+1)(2 - 16iM\omega) + 4(2\ell(\ell+1) + 20iM\omega - 3) - 20iM\omega}{64M^4(2M\omega + i)(4M\omega + i)},$$

$$\alpha_\infty = -\frac{i\ell(\ell+1)}{2\omega},$$

$$\beta_\infty = \frac{\ell(\ell+1)(2 - \ell(\ell+1)) + 12iM\omega}{8\omega^2},$$

and

$${}_{-2}\tilde{\mathcal{R}}_{\omega\ell}^{\text{in,tra}} = \frac{2(\alpha_+ + 2M^2\beta_+)}{M}, \quad (5.31)$$

$${}_{-2}\tilde{\mathcal{R}}_{\omega\ell}^{\text{up,tra}} = -4\omega^2, \quad (5.32)$$

$$\frac{W}{W^T} = \frac{M\beta_\infty}{\alpha_+ + 2M^2\beta_+}. \quad (5.33)$$

Before going further, we should remark the following. Once we integrate  ${}_{-2}\tilde{G}_{\omega\ell}^T(r, r')$  over  $\omega$  and perform the sum over  $\ell$  and  $m$ , we eventually require to take the coincidence limit  $x \rightarrow x'$ . When calculating  ${}_{-2}\tilde{G}_{\omega\ell}^T(r, r')$  via Eq. (5.29), this limit may depend on whether it is taken from  $r$  smaller or larger than  $r'$ . However, similar to  ${}_2\tilde{G}_{\omega\ell}(r', r')$ , the Fourier modes  ${}_{-2}\tilde{G}_{\omega\ell}^T(r', r')$  should not depend on the direction. As we shall see in the next section, this is indeed the case.

In Fig. 23 the black curve is  ${}_{-2}\tilde{G}_{\omega,2}^T$  obtained via Eq. (5.29). As detailed in Sec. 2.2.2, we apply the Jaffé series to calculate  ${}_2\tilde{X}_{\omega\ell}^{\text{in}}$  and numerically integrate the radial RWE to calculate  ${}_2\tilde{X}_{\omega\ell}^{\text{up}}$ , we then insert these results (together with their radial derivatives) in Eq. (5.29). The red dots in Fig. 23 correspond to values of  ${}_{-2}\tilde{G}_{\omega,2}^T$  obtained directly via Eq. (5.24) using the numerical method implemented in the BHPT<sup>4</sup>. As can be seen in the figure, as  $M\omega$  increases, the relative difference increases. We found out that computing  ${}_s\tilde{R}_{\omega\ell}^{\text{in}}$  and  ${}_s\tilde{R}_{\omega\ell}^{\text{up}}$  using the BHPT is much slower compared to the approach we follow, i.e., applying the Chandrasekhar operator on  ${}_2\tilde{X}_{\omega\ell}^{\text{in}}$  and  ${}_2\tilde{X}_{\omega\ell}^{\text{up}}$  in order to construct  ${}_{-2}\tilde{G}_{\omega\ell}^T$ . The reason for this is related to the method used to calculate the boundary conditions for  ${}_{-2}\tilde{R}_{\omega\ell}^{\text{in}}$  and  ${}_{-2}\tilde{R}_{\omega\ell}^{\text{up}}$ . In the Regge-Wheeler case, the boundary condition for  ${}_2\tilde{X}_{\omega\ell}^{\text{up}}$  (or  ${}_2\tilde{X}_{\omega\ell}^{\text{in}}$ ) is not as time expensive as for  ${}_s\tilde{R}_{\omega\ell}^{\text{in}}$  and  ${}_s\tilde{R}_{\omega\ell}^{\text{up}}$ . Internally, the BHPT calculates the boundary conditions for  ${}_{-2}\tilde{R}_{\omega\ell}^{\text{up}}$  and  ${}_{-2}\tilde{R}_{\omega\ell}^{\text{in}}$  using the embedded MST method. In the  $M\omega \gtrsim 5$  region, the MST method implemented in the BHPT becomes less accurate and requires a higher level of working precision to maintain consistent accuracy across all values of  $\omega$ . This is the main reason why calculating  ${}_{-2}\tilde{R}_{\omega\ell}^{\text{in}}$  and  ${}_{-2}\tilde{R}_{\omega\ell}^{\text{up}}$  takes more time than  ${}_2\tilde{X}_{\omega\ell}^{\text{up}}$ .

### 5.2.1 Convergence of the Fourier integral of ${}_{-2}\tilde{G}_{\omega\ell}^T$

Similarly to  ${}_2G_\ell$ , we can show that the  $\ell$ -modes of  ${}_{-2}G_\ell^T$

$${}_{-2}G_\ell^T(r, r'; \Delta t) = \frac{1}{2\pi} \int_{-\infty}^{\infty} {}_{-2}\tilde{G}_{\omega\ell}^T(r, r') e^{-i\omega\Delta t} d\omega \quad (5.34)$$

vanish for  $\Delta t < 0$ . From the Hadamard form for  ${}_{-2}G_{\text{ret}}^T$ , we ignore the case  $\Delta t = 0$  since the  $\theta_+(x, x')$  distribution already indicates that the Fourier integral of  ${}_{-2}\tilde{G}_{\omega\ell}^T$  will not converge for this particular value.

When applying  ${}_{-2}\tilde{\mathcal{C}}_R(r, \omega)$  on  ${}_2\tilde{X}_{\omega\ell}^{\text{in}}$  or  ${}_2\tilde{X}_{\omega\ell}^{\text{up}}$ , the form of these solutions and the terms involving  $\omega$  in  ${}_{-2}\tilde{\mathcal{C}}_R(r, \omega)$  may cause the Fourier integral of (5.29) to diverge. The exponential term involving  $\Delta t$  in the Fourier integral does not affect the decay in the large- $\omega$  regime. In fact, its oscillatory nature does help the integral to converge. From

<sup>4</sup>The BHPT provides the code to calculate the corresponding In and Up solutions for the TE. From those solutions, the calculation of  ${}_s\tilde{G}_{\omega\ell}^T = {}_s\tilde{G}_{\omega\ell}^T(r, r')$  is straightforward.

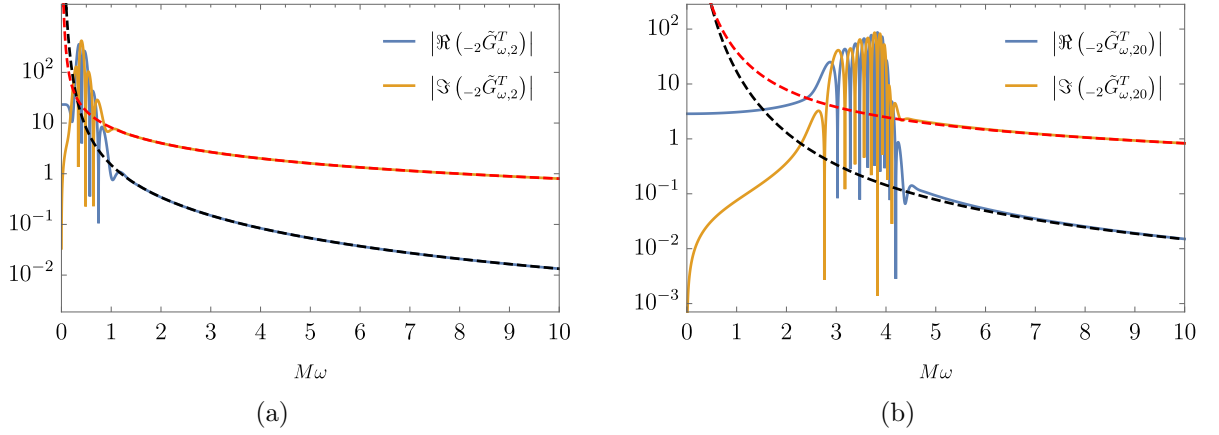


Figure 24 – Fourier modes  ${}_{-2}\tilde{G}_{\omega\ell}^T$ , for  $\ell = 2$  (left) and  $\ell = 20$  (right), alongside their corresponding large- $\omega$  asymptotic expansions (dashed curves) from (5.36).

Eqs. (5.31)–(5.33) we find that the factor

$$\frac{W}{{}_{-2}\tilde{\mathcal{R}}_{\omega\ell}^{\text{in,tra}} {}_{-2}\tilde{\mathcal{R}}_{\omega\ell}^{\text{up,tra}} W^T} = \frac{1}{(\ell - 1)\ell(\ell + 1)(\ell + 2) - 12iM\omega} \quad (5.35)$$

is order  $\omega^{-1}$  in the large- $\omega$  regime. Thus, we should check that

$${}_{-2}\tilde{\mathcal{C}}_{\text{R}}(r, \omega) {}_{-2}\tilde{\mathcal{C}}_{\text{R}}(r', \omega) \frac{{}_2\tilde{X}_{\omega\ell}^{\text{in}}(r_{<}) {}_2\tilde{X}_{\omega\ell}^{\text{up}}(r_{>})}{W}$$

is, at least, order  $\omega^0$  in this regime. In order to verify this, we make use of the asymptotic expansion for  ${}_2\tilde{X}_{\omega\ell}^{\text{in}}$  and  ${}_2\tilde{X}_{\omega\ell}^{\text{up}}$  given in Sec. 2.2.3. Inserting Eqs. (2.82)–(2.83) back into Eq. (5.29), the leading order for  ${}_{-2}\tilde{G}_{\omega\ell}^T(r, r')$ , after taking the limit  $r \rightarrow r'$ , takes the form

$${}_{-2}\tilde{G}_{\omega\ell}^T(r', r') = \frac{if(r')^2 r'^2}{2\omega} + \frac{f(r')^2 r'^2 (\ell - 1)\ell(\ell + 1)(\ell + 2)}{24M\omega^2} + \mathcal{O}\left[\left(\frac{1}{M\omega}\right)^3\right]. \quad (5.36)$$

This result does indeed prove the convergence of the Fourier integral of  ${}_{-2}\tilde{G}_{\omega\ell}^T(r, r')$ .

In Fig. 24 we plot the first two leading orders in Eq. (5.36) together with  ${}_{-2}\tilde{G}_{\omega\ell}^T$  (obtained using (5.29)) for  $\ell = 2$  (left plot) and for  $\ell = 20$  (right plot). As expected, the leading order agrees with  $\Im({}_{-2}\tilde{G}_{\omega\ell}^T)$  and the next-to-leading order with  $\Re({}_{-2}\tilde{G}_{\omega\ell}^T)$  in the large- $\omega$  regime. From the  $\ell = 20$  case, we are able to differentiate three regimes (more distinguishable as  $\ell$  increases): A non-oscillatory region that grows as  $\ell$  increases; A region oscillatory in the frequency; And the asymptotic region. In particular, the square root of the coefficient in front of  ${}_s\tilde{R}_{\omega\ell}$  in Eq. (1.101) (after multiplying the equation by a factor

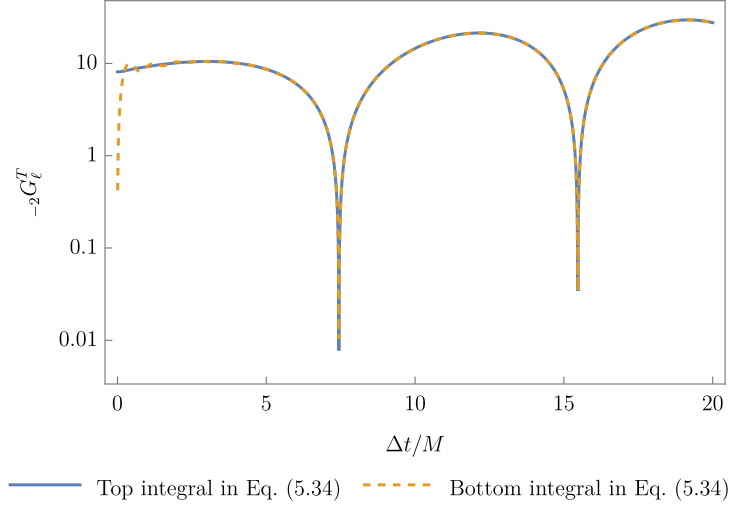


Figure 25 – Teukolsky  $\ell$ -mode  ${}_{-2}G_{\ell}^T$  (for  $r = r' = 6M$  and  $\ell = 2$ ) calculated using the two integrals appearing in Eq. (5.38). Due to the different numerical tweaks we introduced during the Fourier integral, we observe a discrepancy in the results depending on which integral we use in Eq. (5.38).

of  $\frac{f(r)}{r^2}$ ) allows us to estimate the value of the frequency  $\omega_{\text{osc}}$ . This yields

$$\omega_{\text{osc}} \approx \left[ \frac{f(r)}{r^2} (\ell - s)(\ell + s + 1) \right]^{1/2}. \quad (5.37)$$

This oscillatory feature inherits from the similar behaviour found in  ${}_s\tilde{G}_{\omega\ell}$  but in this case it begins at  $\omega_{\text{osc}}^{RW} \approx \sqrt{4\mathcal{Q}_s}$  where  $\mathcal{Q}_s$  is given in Eq. (2.36).

Now that we know the Fourier integral of the Fourier modes in Eq. (5.29) converges for  $\Delta t > 0$ , we calculate  ${}_{-2}G_{\ell}^T(r, r', \Delta t)$  according to

$$\begin{aligned} {}_{-2}G_{\ell}^T(r, r', \Delta t) &= \frac{2}{\pi} \theta(\Delta t) \int_0^{\infty} \Re \left[ {}_{-2}\tilde{G}_{\omega\ell}^T(r, r') \right] \cos(\omega\Delta t) d\omega \\ &= \frac{2}{\pi} \theta(\Delta t) \int_0^{\infty} \Im \left[ {}_{-2}\tilde{G}_{\omega\ell}^T(r, r') \right] \sin(\omega\Delta t) d\omega, \end{aligned} \quad (5.38)$$

where, similarly to  ${}_sG_{\ell}$ , we have used the properties

$${}_{-2}G_{\ell}^T(r, r'; -\Delta t) = 0, \quad \forall \Delta t > 0, \quad (5.39)$$

$${}_{-2}\tilde{G}_{-\omega\ell}^{T*}(r, r') = {}_{-2}\tilde{G}_{\omega\ell}^T(r, r'). \quad (5.40)$$

In practice, the upper limit in the integrals of Eq. (5.38) has to be capped to certain value  $\omega_{\text{max}}$ , in our case we took  $\omega_{\text{max}} = 10/M$ . Since the large- $\omega$  region is responsible for the behaviour of  ${}_{-2}G_{\ell}^T(r, r', \Delta t)$  at early times, this cap will result in a less accurate value

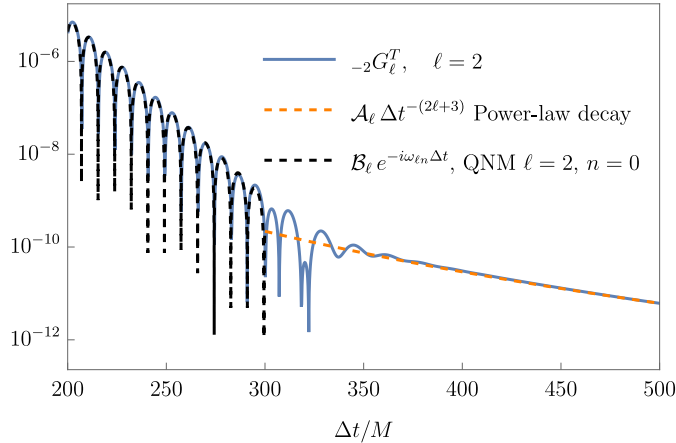


Figure 26 – Comparison of  ${}_{-2}G_2^T(r, r, t - t')$  (with  $r = 6M$ ) calculated according to (5.34) (blue), the quasi-normal mode  $\ell = 2$ ,  $n = 0$  estimated using [7] (black-dashed) and the late time decay  $\Delta t^{-(2\ell+3)}$  (orange-dashed).

of  ${}_{-2}G_\ell^T(r, r', \Delta t)$  for  $\Delta t$  small. On top of that, as suggested in [115], we introduce the smoothing factor  $\frac{1}{2}(1 - \text{Erf}[2(\omega - \frac{8}{10}\omega_{\text{max}})])$  in the integrand, this makes the numerical integration converge faster without significantly influencing the values of  ${}_{-2}G_\ell^T$  away from  $\Delta t = 0$ . In Fig. 25 we plot the two integrals in Eq. (5.38) after capping the upper limit and including the smoothing factor. We observe that the effect of introducing the cap and the smoothing factor has a more significant impact in the bottom integral than in the top integral. We then prefer to use the top integral in Eq. (5.38) for further calculations.

We next investigate the late time behaviour for  ${}_{-2}G_\ell^T$ . In Refs. [40, 116] we find an analysis for field perturbations in the frequency domain for small  $\omega$ . In fact, the analysis in the frequency domain provided in [40] found the expected power-law decay (for the radiative multipoles) previously obtained by Price [117, 118]. More specifically, the leading order term turns out to be  $\propto \Delta t^{-(2\ell+3)}$ . On the other hand, the quasi-normal modes<sup>5</sup> of  ${}_sG_{\text{ret}}^T$  also give an insight into its exponential decay  $\propto e^{-i\omega_{\ell n}\Delta t}$  (where  $\omega_{\ell n} \in \mathbb{C}$  is the quasi-normal frequency with angular momentum  $\ell$  and overtone  $n$ ) prior to the power-law decay.

In Fig. 26 we plot  ${}_{-2}G_\ell^T(r, r', \Delta t)$  for  $\ell = 2$ ,  $r = r' = 6M$  and  $\Delta t \in [200M, 500M]$ . Within this region, we are able to observe the two expected decays in  ${}_{-2}G_\ell^T$ . In the

<sup>5</sup>In this context we refer to quasi-normal modes to the set of frequencies containing all the poles of the radial Green function ( ${}_s\tilde{G}_{\omega\ell}^T$  or  ${}_s\tilde{G}_{\omega\ell}$ ).

exponential decay region, the black-dashed curve corresponds to  $\Re(\mathcal{B}_2 e^{-i\omega_{2,0}\Delta t})$  where  $\omega_{2,0} = (0.3736716844 - i0.8896231569 \times 10^{-1})M^{-1}$  is the quasi-normal frequency [7] for  $\ell = 2$  and overtone  $n = 0$ <sup>6</sup>. We estimated  $\mathcal{B}_2$  by imposing  $\Re(\mathcal{B}_2 e^{-i\omega_{2,0}\Delta t}) = {}_{-2}G_\ell^T(r', r', \Delta t)$  for two different values of  $\Delta t \in [200M, 280M]$  and  $r = r' = 6M$ . When moving away from the exponential decay, i.e., for  $\Delta t \gtrsim 400M$  in Fig. 26, we observe the expected  $\mathcal{A}_\ell \Delta t^{-7}$  power-law decay [40]. The factor  $\mathcal{A}_\ell$  is estimated in a way that  $\mathcal{A}_\ell (500M)^{-7} = {}_{-2}G_\ell^T(r', r', 500M)$ . This late time analysis provides an easy and simple way to verify the main behaviour of  ${}_{-2}G_\ell^T$  in this regime. We do not go further to develop a more rigorous approach for obtaining  $\mathcal{A}_\ell$  and  $\mathcal{B}_\ell$ , our main objective in this Chapter is to calculate  ${}_{-2}G_{\text{ret}}^T$  within the range  $\Delta t \in [0, 100M]$ .

## 5.2.2 Full Teukolsky Green function

Once the  $\ell$ -modes  ${}_{-2}G_\ell^T$  are calculated, the retarded Green function ( ${}_sG_{\text{ret}}^T$ ) of Eq. (5.1) may be calculated via Eq. (5.20) for the  $s = -2$  case. Similarly to the Regge-Wheeler case, we truncate the sum over  $\ell$  in Eq. (5.20). Once again, truncating the mode sum leads to high- $\ell$  oscillations in  ${}_{-2}G_{\text{ret}}^T$  which are smoothed out when we introduce the smoothing factor  $\exp[-\ell^2/(2\ell_{\text{cut}}^2)]$  with  $\ell_{\text{cut}}$  being a cutoff value for  $\ell$  [56].

In Fig. 27 we show  ${}_{-2}G_{\text{ret}}^T$  for two different scenarios. In the first scenario (Fig. 27a)  $x$  and  $x'$  are evaluated on a static worldline with  $r = r' = 6M$  and zero angular separation. In the second scenario (Fig. 27b) we have  $x$  and  $x'$  on a circular geodesic with  $r = r' = 6M$ . The mode sum was capped at  $\ell = 100$  for both scenarios and the smoothing factor in the  $\ell$ -sum had  $\ell_{\text{cut}} = 8$  and  $\ell_{\text{cut}} = 12$  for the static and circular case, respectively. Unlike the  $\ell$ -sum for  ${}_sG_{\text{ret}}$ , for  ${}_{-2}G_{\text{ret}}^T$  we chose a much lower value for  $\ell_{\text{cut}}$  because the oscillations coming from the high- $\ell$  modes are more marked than in the Regge-Wheeler case.

When comparing the results for  ${}_{-2}G_{\text{ret}}^T$  in Fig. 27 with  ${}_0G_{\text{ret}}$  and  ${}_2G_{\text{ret}}$ , we observe that the singularity structure [53] is the same as in Fig. 4 for the static case and Fig. 7 for the circular case, respectively. This structure is more marked in the static case compared

<sup>6</sup>The authors in [7] provided supplementary data which can be found at <https://pages.jh.edu/eberti2/ringdown/>.

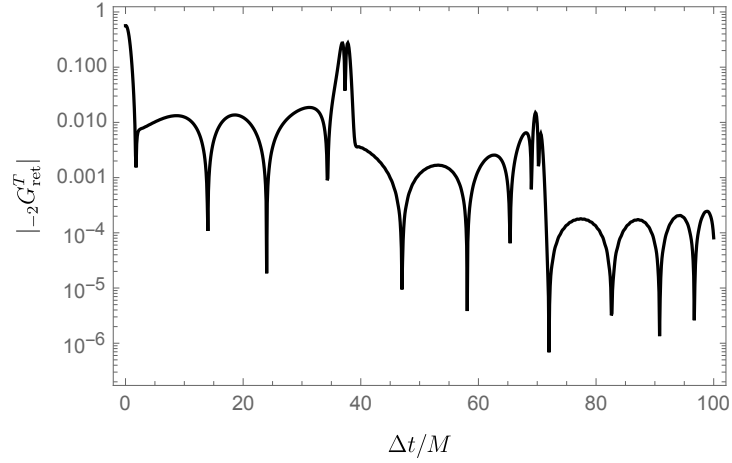
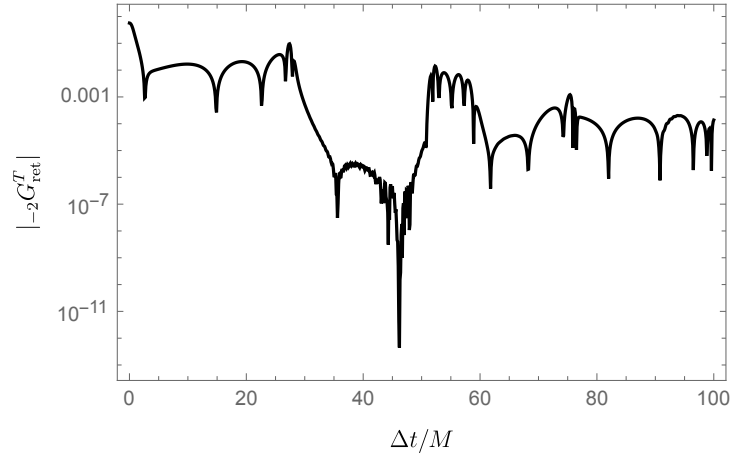
(a)  ${}_{-2}G_{\text{ret}}^T$  for  $x$  and  $x'$  on a static worldline with  $r = r' = 6M$ .(b)  ${}_{-2}G_{\text{ret}}^T$  for  $x$  and  $x'$  on a circular geodesic with  $r = r' = 6M$ .

Figure 27 – Full retarded Teukolsky Green function ( ${}_{-2}G_{\text{ret}}^T$ ) for two different scenarios, the  $\ell$ -sum was capped at  $\ell = 100$  and we used  $\ell_{\text{cut}} = 8$  for the static case and  $\ell_{\text{cut}} = 12$  for the circular case.

to the circular case. In particular, we observe that for the circular case in Fig. 27b, there are still spurious oscillations around  $\Delta t \approx 45M$ . We were not able to reduce further these oscillations without affecting the (already smoothed out) singularities in  ${}_{-2}G_{\text{ret}}^T$ . We thus require to examine other parameters like the cap in the mode sum or the Fourier integral for additional improvement. For instance, including more  $\ell$ -modes in the mode sum should increase the value of  $\ell_{\text{cut}}$  in the smoothing factor, reducing the high- $\ell$  oscillations. The alternative we are currently working on is increasing the precision in the data of  ${}_s\tilde{X}_{\omega\ell}^{\text{in}}$  and  ${}_s\tilde{X}_{\omega\ell}^{\text{up}}$ , this should increase the accuracy of the Fourier integral and, consequently, provide more accurate  $\ell$ -modes. Additionally, we could also improve the smoothing factor we introduced in the Fourier integral. However, the impact of the smoothing factor is only significant near coincidence.

### 5.2.3 Chandrasekhar operator in the time domain and regularisation

In the time domain, constructing  ${}_{-2}G_\ell^T$  from  ${}_{-2}G_\ell$  is not a straightforward procedure. Although we can construct the equivalent operator to (1.104) in the time domain (which we denote by  ${}_{-2}\mathcal{C}(r, \Delta t)$ ) by simply changing  $\omega \rightarrow i\frac{\partial}{\partial t}$  in it, we cannot follow this technique for the prefactor in Eq. (5.29). The appropriate procedure to handle this prefactor and obtain its time domain counterpart is through the convolution operator, i.e., in the time domain, we can write

$$\begin{aligned} {}_{-2}G_\ell^T &= - \left[ \frac{1}{2\pi} \int_{-\infty}^{\infty} \frac{W e^{-i\omega\Delta t}}{{}_{-2}\tilde{R}_\ell^{\text{in,tra}} \cdot {}_{-2}\tilde{R}_{\omega\ell}^{\text{up,tra}} W_T} d\omega \right] * {}_{-2}\mathcal{C}(r, \Delta t) {}_{-2}\mathcal{C}(r', \Delta t) {}_2G_\ell(r, r', \Delta t) \\ &= \left( \frac{\pi}{6M} e^{-\frac{(\ell-1)\ell(\ell+1)(\ell+2)\Delta t}{12M}} \theta(\Delta t) \right) * {}_{-2}\mathcal{C}(r, \Delta t) {}_{-2}\mathcal{C}(r', \Delta t) {}_2G_\ell(r, r', \Delta t), \end{aligned} \quad (5.41)$$

where the  $*$  represents the convolution operation (with respect to  $\Delta t$ ),  ${}_2G_\ell(r, r', \Delta t)$  are the  $\ell$ -modes of  ${}_2G_{\text{ret}}$ , and  ${}_{-2}\mathcal{C}(r, t)$  is the radial part of the Chandrasekhar operator in the time domain [40]

$${}_{-2}\mathcal{C}(r, \Delta t) = (rf)^2 \left( \frac{\partial}{\partial r} - \frac{1}{f} \frac{\partial}{\partial \Delta t} \right)^2 r. \quad (5.42)$$

Moreover, instead of using (1.104), we may go a step further and use (5.26) (or Eq. (5.27)) and write

$${}_{-2}\tilde{G}_{\omega\ell}^T = \left( \frac{\pi}{6M} e^{-\frac{(\ell-1)\ell(\ell+1)(\ell+2)\Delta t}{12M}} \theta(\Delta t) \right) * {}_{-2}\mathcal{C}_R(r, \Delta t) {}_{-2}\mathcal{C}_R(r', \Delta t) {}_2G_\ell(r, r', \Delta t), \quad (5.43)$$

where  ${}_{-2}\mathcal{C}_R$  is obtained by changing  $\omega \rightarrow i\frac{\partial}{\partial t}$  in  ${}_{-2}\tilde{\mathcal{C}}_R$ , i.e.,

$$\begin{aligned} {}_{-2}\mathcal{C}_R(r, t) &= f(r) (r\ell(\ell+1) - 6M) + 2r(r - 3M) \left( f(r) \frac{\partial}{\partial r} - \frac{\partial}{\partial t} \right) \\ &\quad - 2r^3 \left( f(r) \frac{\partial^2}{\partial t \partial r} - \frac{\partial^2}{\partial t^2} \right). \end{aligned} \quad (5.44)$$

In order to compare  ${}_{-2}G_\ell^T$  calculated via Fourier integral of Eq. (5.29) and more directly via Eq. (5.43), we need to calculate  ${}_2G_\ell$  and its corresponding radial and time derivatives directly in the time domain. In order to obtain these derivatives, we require another approach for computing  ${}_2G_\ell$  directly in the time domain. The Hadamard-WKB method provided in [60] for calculating  $V_0$  as a small coordinate expansion (which we adapted to work with general spin in Sec. 2.1) can be used to obtain the  $\ell$ -modes of  ${}_sG_{\text{ret}}$



instead of  $V_s$ . In fact, the procedure for obtaining  $V_0$  in [60] relies on first calculating  ${}_0G_\ell$  and then regularising it during the mode sum. More specifically, using the expressions given in Eqs. (2.7)–(2.14) of Ref. [60], we find that for  $r > r'$ , the  $\ell$ -modes  ${}_0G_\ell^E$  of the Euclidean Green function are given by<sup>7</sup>

$${}_0G_\ell^E(r, r'; -i\tau) = r^2 \int_0^\infty B(r, r') \cos(\hat{\omega}\tau) d\hat{\omega}, \quad r > r', \quad (5.45)$$

where  $\tau = it$  is the Euclidean time,  $\hat{\omega} = -i\omega$ , and  $B(r, r')$  is the Euclidean Fourier mode of  ${}_0G_\ell^E$ . The function  $B(r, r')$  is calculated by expanding it in powers of  $r - r'$

$$B(r, r') = \beta(r) + \alpha(r)(r' - r) + \dots, \quad (5.46)$$

and using a Hadamard-WKB method to obtain the  $\beta(r)$  and  $\alpha(r)$  coefficients (see [60]).

As proposed in Sec. 2.1.3, Eq. (5.45) can be generalised to  ${}_sG_\ell(r, r'; \Delta t)$  by adding the  $-s^2M/r^3$  term in Eq. (2.10) of Ref. [60]. In the  $r < r'$  case, we can perform the same procedure used for calculating  $B(r, r')$ . However, the symmetries of  ${}_2G_{\text{ret}}$  shows that for  $r < r'$  this calculation leads to the same function  $B(r, r')$  but with its arguments swapped.

In this way, for spin-2 we can write

$${}_2G_\ell^E(r, r'; -i\tau) = \int_0^\infty \left[ r^2 B_2(r, r') \theta(r - r') + r'^2 B_2(r', r) \theta(r' - r) \right] \cos(\hat{\omega}\tau) d\hat{\omega}, \quad (5.47)$$

where

$$B_2(r, r') = \beta_2(r) + \alpha_2(r)(r' - r) + \dots,$$

with  $\beta_2(r)$  and  $\alpha_2(r)$  coefficients to be determined similarly to  $\beta(r)$  and  $\alpha(r)$ . In this way,  $B_2(r, r')$  is the counterpart of  $B(r, r')$  for spin-2. The result of the integral in the right hand side of Eq. (5.47) is then expressed as a small coordinate expansion similar to Eq. (2.28). In our region of interest, which is within a normal neighborhood, a small coordinate expansion yields sufficient accuracy for comparison purposes.

The  $\ell$ -modes  ${}_sG_\ell$  of the retarded Green function can be obtained from the  $\ell$ -modes  ${}_sG_\ell^E$  of the Euclidean Green function by setting  $\tau = it$ . By modifying the supplementary

<sup>7</sup>Note that we already transformed the Euclidean time  $\tau$  to Schwarzschild time  $t$  and introduced a  $r^2$  factor to match the mode decomposition in Eq. (2.7) of Ref. [60] with Eq. (2.29).

code provided in [60], originally intended for calculating  $V_0$ , we successfully derived  ${}_sG_\ell$  as a small coordinate expansion. This involved incorporating the term  $-\frac{M}{r^3}s^2$  (note that this term generalises the code to arbitrary  $s$ ) into the potential outlined in Eq. (10) of [60]. Prior to conducting the mode-sum, we found that the first leading terms of  ${}_2G_\ell$  are

$${}_2G_\ell = \mathcal{G}_L(r, r'; \Delta t) \theta(r - r') + \mathcal{G}_L(r', r; \Delta t) \theta(r' - r), \quad (5.48)$$

$$\begin{aligned} \mathcal{G}_L(r, r'; \Delta t) = & \frac{1}{2} - \frac{r - r'}{2r} + \frac{(4L^2 + 15)r - 56M}{32r^3 f(r)} (r - r')^2 + \frac{f(r)(r - 4L^2r + 24M)}{32r^3} \Delta t^2 \\ & + \frac{144M^2 - (12L^2 + 55)Mr + 4L^2r^2 f(r) + 2(2L^2 - 1)r^2}{32r^5} (r - r') \Delta t^2 \\ & + \mathcal{O}(\Delta x^4), \end{aligned} \quad (5.49)$$

where  $L = \ell + \frac{1}{2}$  and  $\Delta x = x - x'$  with  $x = (t, r)$ .

The small coordinate expansion in Eq. (5.48) for  ${}_2G_\ell$  is the expression we insert into Eq. (5.41). As discussed in Sec. 2.2.3, taking radial derivatives of  ${}_2\tilde{G}_{\omega\ell}$  induces undesired quasi-direct terms. It turns out that, when calculating radial derivatives of  ${}_2G_\ell$  using Eq. (5.48), we encounter a similar situation. More precisely, if we differentiate Eq. (5.48) with respect to  $r$  (similar results arise for  $r'$ ) and take the limit  $r \rightarrow r'$ , we find that the result depends on how the limit  $r \rightarrow r'$  is taken, i.e.,

$$\lim_{r \rightarrow r'^+} \frac{\partial}{\partial r} {}_2G_\ell = -\frac{1}{2r'} + \frac{336M^2 - 11(4L^2 + 11)Mr' + 4(4L^2 - 1)r'^2}{32r'^5} \Delta t^2 + \mathcal{O}(\Delta t^3), \quad (5.50)$$

$$\lim_{r \rightarrow r'^-} \frac{\partial}{\partial r} {}_2G_\ell = \frac{1}{2r'} - \frac{144M^2 - 5(4L^2 + 11)Mr' + 2(4L^2 - 1)r'^2}{32r'^5} \Delta t^2 + \mathcal{O}(\Delta t^3). \quad (5.51)$$

Although the radial derivative of  ${}_2G_\ell$  is expected to have a discontinuity, when constructing  ${}_2G_\ell^T$  from  ${}_2G_\ell$  and evaluating it at  $r = r'$ , we should remove any discontinuity coming from the radial derivatives of  ${}_sG_\ell$ . This is because  ${}_2G_\ell^T(r, r'; \Delta t)$  must be continuous at  $r = r'$ , i.e.,

$$\lim_{r \rightarrow r'^+} {}_2G_\ell^T(r, r'; \Delta t) = \lim_{r \rightarrow r'^-} {}_2G_\ell^T(r, r'; \Delta t).$$

In order to achieve this continuity for  ${}_2G_\ell^T$ , we take the average of the two limits given in Eqs. (5.50)–(5.51).

We now go a step further and propose

$$\begin{aligned} {}_{-2}G_{\ell}^{T,\text{nd}} &\equiv \left( \frac{\pi}{6M} e^{-\frac{(\ell-1)\ell(\ell+1)(\ell+2)\Delta t}{12M}} \theta(\Delta t) \right) * {}_{-2}\mathcal{C}_{\text{R}}(r, \Delta t) {}_{-2}\mathcal{C}_{\text{R}}(r', \Delta t) {}_2G_{\ell}^{\text{nd}} \\ &= \left( \frac{\pi}{6M} e^{-\frac{(\ell-1)\ell(\ell+1)(\ell+2)\Delta t}{12M}} \theta(\Delta t) \right) * {}_{-2}\mathcal{C}_{\text{R}}(r, \Delta t) {}_{-2}\mathcal{C}_{\text{R}}(r', \Delta t) ({}_2G_{\ell} - G_{\ell}^{\text{dir}}), \end{aligned} \quad (5.52)$$

to be the  $\ell$ -modes of the non-direct part of  ${}_{-2}G_{\text{ret}}^T$ , i.e., we identify

$${}_{-2}G_{\text{ret}}^{T,\text{nd}} \equiv (r'^2 f(r'))^{-2} \sum_{\ell=2}^{\infty} \sum_{m=-\ell}^{\ell} {}_{-2}G_{\ell}^{T,\text{nd}} {}_{-2}Y_{\ell m}(\theta, \phi) {}_{-2}Y_{\ell m}^*(\theta', \phi') \quad (5.53)$$

as the non-direct part of  ${}_{-2}G_{\text{ret}}^T$ . This approach for obtaining the non-direct part of  ${}_{-2}G_{\text{ret}}^T$  from  ${}_2G_{\ell}^{\text{nd}} = {}_2G_{\ell} - G_{\ell}^{\text{dir}}$  was first proposed by Nakano and Sasaki in the frequency domain [44]. While the initial concept presented in [44] was developed only to one post-Newtonian order, we would expect Eq. (5.52) to be the time domain counterpart of Eq. (4.1) in [44]. If this is not the case, any additional term that is not part of  ${}_{-2}G_{\ell}^{T,\text{nd}}$  should be properly addressed. For instance, a similar discontinuity appearing in (5.50)–(5.51) arises in the frequency domain and it is handled with an averaging procedure as well (see Sec. 2.2.3).

The next observation is connected to the Heaviside distribution embedded in the non-direct part of  ${}_2G_{\text{ret}}$ . This distribution leads to a Dirac-delta distribution that should not be part of  ${}_sG_{\text{ret}}^{T,\text{nd}}$ . In the frequency domain, Nakano and Sasaki addressed this problem by substituting the Chandrasekhar operator  ${}_{-2}\tilde{\mathcal{C}}$ , a second order differential operator, with the first order differential operator  ${}_{-2}\tilde{\mathcal{C}}_{\text{R}}$  (see Appendix C of Ref. [44]). In the time domain, this does not seem to be the case since the operator  ${}_{-2}\mathcal{C}_{\text{R}}$  (the time domain counterpart of  ${}_{-2}\tilde{\mathcal{C}}_{\text{R}}$ ) in Eq. (5.52) involves up to fourth order derivatives with respect to  $\Delta t$ . Despite the possibility for these high-order derivatives to introduce Dirac-delta distributions, these terms become finite after the convolution operation in Eq. (5.52).

In Fig. 28 we plot the result of applying  ${}_{-2}\mathcal{C}_{\text{R}}(r, \Delta t) {}_{-2}\mathcal{C}_{\text{R}}(r', \Delta t)$  on the small coordinate expansion of  $G_{\ell}^{\text{dir}}$  (see [6]) and  ${}_2G_{\ell}$ , for  $\ell = 2$  (top) and  $\ell = 25$  (bottom). In both cases we set  $r = r' = 6M$ . For the  ${}_{-2}\mathcal{C}_{\text{R}}(r, \Delta t) {}_{-2}\mathcal{C}_{\text{R}}(r', \Delta t) G_{\ell}^{\text{dir}}$  case (blue curve), we observe a divergence at  $\Delta t = t_{\mathcal{N}} \approx 20.726713M$  (or  $\eta = \eta(r', r', \Delta t) = \pi$ ) coming from differentiating the  $\sqrt{\frac{\sin \eta}{\eta}}$  factor in Eq. (2.13). Considering that, in order to obtain  ${}_{-2}G_{\ell}^{T,\text{nd}}$  we require to perform the convolution in Eq. (5.52), the divergence at  $\Delta t = t_{\mathcal{N}}$  will not let the convolution integral converge.

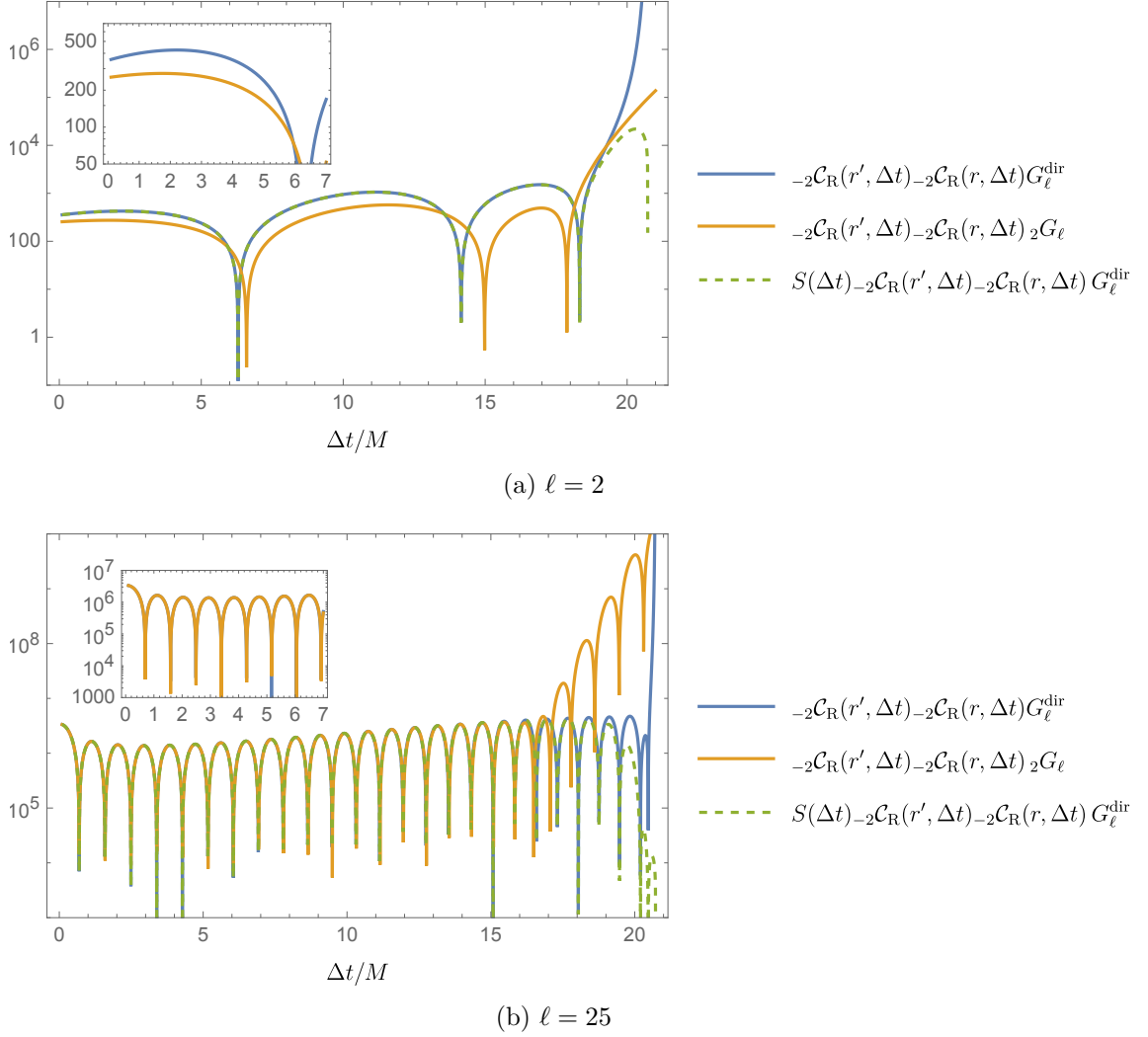


Figure 28 – Comparison between  $-{}_2\mathcal{C}_R(r, \Delta t) - {}_2\mathcal{C}_R(r', \Delta t) {}_2G_\ell$ ,  $-{}_2\mathcal{C}_R(r, \Delta t) - {}_2\mathcal{C}_R(r', \Delta t) G_\ell^{\text{dir}}$  and  $S(\Delta t) - {}_2\mathcal{C}_R(r, \Delta t) - {}_2\mathcal{C}_R(r', \Delta t) G_\ell^{\text{dir}}$  for  $\ell = 2$  (top) and  $\ell = 25$  (bottom).

From (5.44) and Eq. (5.52), the factor  $\sqrt{\frac{\sin \eta}{\eta}}$  has to be differentiated four times and it leads to a divergence of type  $(\pi - \eta)^{-7/2}$  in the right hand side of Eq. (5.52). In order to remove this divergence and be able to perform the convolution in Eq. (5.52), we could introduce a smoothing factor which goes to zero at  $\eta = \pi$  faster than  $(\pi - \eta)^{7/2}$ . For instance, the smoothing function

$$S(\Delta t) = \begin{cases} \tanh^4(t_{\mathcal{N}} - \Delta t) \tanh^4(\Delta t - t_{\mathcal{N}}), & |\eta| \leq \pi, \\ 0, & |\eta| > \pi, \end{cases} \quad (5.54)$$

has the required properties at  $\eta = \pi$ . The green-dashed curve in Fig. 28 corresponds to  $-{}_2\mathcal{C}_R(r, \Delta t) - {}_2\mathcal{C}_R(r', \Delta t) G_\ell^{\text{dir}}$  smoothed out by this function. We observe that for  $\ell = 2$  and at early times, there is a notable difference between the results from  $G_\ell^{\text{dir}}$  (blue curve) and  ${}_2G_\ell$  (orange curve). On the other hand, we found out that this difference reduces as

$\ell$  increases (see the  $\ell = 25$  case in Fig. 28). In order to understand the implications of including a smoothing function in  ${}_{-2}\mathcal{C}_R(r, \Delta t){}_{-2}\mathcal{C}_R(r', \Delta t)G_\ell^{\text{dir}}$ , let us substitute  ${}_{-2}G_\ell^{T, \text{nd}}$  in Eq. (5.53) with

$$\left( \frac{\pi}{6M} e^{-\frac{(\ell-1)\ell(\ell+1)(\ell+2)\Delta t}{12M}} \theta(\Delta t) \right) * \left( S(\Delta t) {}_{-2}\mathcal{C}_R(r, \Delta t){}_{-2}\mathcal{C}_R(r', \Delta t)G_\ell^{\text{dir}} \right) \quad (5.55)$$

and perform the corresponding  $\ell$ -sum. In the ideal scenario where we are able to conduct this  $\ell$ -sum exactly, there is no need to introduce the smoothing factor  $S(\Delta t)$ . As illustrated in Eq. (2.12), the  $\ell$ -modes of the direct part of  ${}_sG_{\text{ret}}$  extend beyond  $\Delta t = 0$ , yet these contributions ultimately cancel out. We anticipate a similar cancellation phenomenon during the  $\ell$ -sum of (5.55), subsequently mitigating the impact of  $S(\Delta t)$  in the final result.

We encountered difficulty in obtaining a complete calculation for  ${}_{-2}G_\ell^{T, \text{nd}}$  due to the inadequacy of the small coordinate expansion for  $G_\ell^{\text{dir}}$  and  ${}_sG_\ell$  to facilitate the convolution operation in Eq. (5.52). We made additional analyses (e.g., asymptotic expansions for large  $\ell$ ) on the left hand side of Eq. (5.52) in order to determine whether the  $\ell$ -sum of  ${}_{-2}G_\ell^{T, \text{nd}}$  resulted in any divergences at coincidence. Unfortunately, these analyses did not yield conclusive results.

We intend to continue analysing this approach for the Chandrasekhar operator in the time domain. Our ongoing results are incomplete and require further development. For instance, we could analytically carry out the convolution operation in Eq. (5.52) given a sufficient accurate expansion for  ${}_{-2}\mathcal{C}_R(r, \Delta t){}_{-2}\mathcal{C}_R(r', \Delta t){}_2G_\ell$  (and  ${}_{-2}\mathcal{C}_R(r, \Delta t){}_{-2}\mathcal{C}_R(r', \Delta t)G_\ell^{\text{dir}}$ ). Additionally, we could improve  ${}_sG_\ell$  by providing a large- $\omega$  asymptotic expansion for  ${}_s\tilde{G}_{\omega\ell}$  instead of introducing a smoothing function in the Fourier integral.

## 6 Conclusions

Understanding gravitational waves became crucial after LIGO's first detection of gravitational waves [1] since it marked the birth of gravitational wave astronomy. Describing the motion of two massive compact objects is not an easy task. It requires a combination of numerical and analytical techniques to solve the equation of motion for such binary systems. In the case of EMRI's, we model the system as a small compact object moving on a background spacetime generated by the supermassive black hole. Therefore, our problem reduces to solving the equations of motion for a compact object. The particle's own field acts as a self-force deviating its motion from a geodesic one. In this work, as we have detailed, applications of the Green function extend beyond EMRIs alone. We demonstrated that the scalar retarded Green function plays a crucial role in quantum communication. Calculating Green functions in curved spacetime poses a considerable challenge, to yield the results presented in this work, we developed various techniques and methods to calculate both the Regge-Wheeler Green function and the Teukolsky Green function.

In Chapter 1 we started by introducing the theory of general relativity and the non-geodesic motion of a scalar charge and a point particle in curved spacetime. We provided a brief review of how to construct the self-force and perform a self-consistent evolution in these two cases. We also discussed the fundamentals of Green functions in curved spacetime and showed how to regularise them. Later on, we focused on describing gravitational perturbations of Schwarzschild spacetime using two different formalisms. Firstly, we used the Regge-Wheeler formalism to derive the spin-2 Regge-Wheeler equation (which can be generalised to also describe scalar and electromagnetic perturbations). Solutions to the spin-2 Regge-Wheeler equation allow us to calculate the odd-parity sector of the metric perturbation, while the even-parity sector is described by the Zerilli equation. Secondly, we explored the Teukolsky formalism, where field perturbations are described by a spin- $s$  field. Teukolsky showed that scalar, electromagnetic, and gravitational perturbations of

Kerr spacetime can be obtained by solving a master equation (the Teukolsky equation) for a spin- $s$  master field. Since Kerr spacetime reduces to Schwarzschild when the angular momentum is zero, we can also describe field perturbations of Schwarzschild spacetime with the Teukolsky formalism. Once we calculate the master field, we are able to partially reconstruct the physical field perturbation.

In Chapter 2 we calculated the retarded Green function  ${}_sG_{\text{ret}}$  for the Regge-Wheeler equation in the scalar ( $s = 0$ ) and gravitational ( $s = 2$ ) cases. The methods we developed rely on mixed (numerical and analytic) methods for calculating  ${}_sG_{\text{ret}}$ . In the time domain, the  $\ell$ -modes of  ${}_sG_{\text{ret}}$  satisfy a characteristic initial value problem. By establishing characteristic initial data (CID) on the light cone, we developed a higher order CID scheme than the ones found in [64, 63] that works for arbitrary spin  $s$ . We truncated the mode sum in Eq. (2.29) and introduced a smoothing factor to smear the high- $\ell$  oscillations. Consequently, a Gaussian distribution centered at coincidence arises and it narrows approaching to  $\delta(\sigma)$  as more modes are included in the sum. The method of matched expansions [31] is an effective procedure for removing this Gaussian distribution near coincidence. We calculated the Hadamard tail  $V_s$  (in the QL region, using a small distance expansion) and matched it with  ${}_sG_{\text{ret}}$  (previously calculated via CID). The result of this matching process returns the non-direct part of  ${}_sG_{\text{ret}}$  (denoted by  ${}_sG_{\text{ret}}^{\text{nd}}$ ) for any pair of points  $x$  and  $x'$  within the region limited by the domain of the CID scheme. Later on, we followed a relatively new prescription (introduced in [6]) for calculating  ${}_sG_{\text{ret}}^{\text{nd}}$ . This method consists of subtracting  $G_\ell^{\text{dir}}$  (the  $\ell$ -modes of the direct part of  ${}_sG_{\text{ret}}$ ) from  ${}_sG_\ell$ . While this procedure successfully eliminated the Gaussian distribution in  ${}_sG_{\text{ret}}$ , it produced inaccurate results for small values of  $\Delta t$ . This inaccuracy was directly connected to the numerical approach we used to compute  $\Delta_{2\text{d}}^{1/2}$ , a fundamental piece in  $G_\ell^{\text{dir}}$ . In [6] the authors provided a non-numerical prescription for calculating  $\Delta_{2\text{d}}^{1/2}$  which returned better results near  $\Delta t = 0$ . We then moved to this approach to compute  $\Delta_{2\text{d}}^{1/2}$  and improved our previous results. As seen in [6], in the scalar case ( $s = 0$ ), his approach yields the same result as that obtained through matched expansions. However, in the gravitational case ( $s = 2$ ), the value of  $[V_s] = -4Ms^2/r^3 \neq 0$  and  ${}_sG_{\text{ret}}^{\text{nd}} = -V_s\theta(-\sigma)\theta(\Delta t)$  lead to a discrep-

ancy near  $\Delta t = 0$  since the non-direct part is obtained via a truncated mode sum. More precisely, the Heaviside distributions in  ${}_sG_{\text{ret}}^{\text{nd}}$  are smoothed out due to the truncation of the mode sum. Nonetheless, as more modes are included in the sum, the result for  ${}_sG_{\text{ret}}^{\text{nd}}$  tends to  $V_s$  as expected.

In the frequency domain, we obtained  ${}_s\tilde{G}_{\omega\ell}$  via Eq. (2.61). For  ${}_s\tilde{X}_{\omega\ell}^{\text{in}}$  we used the Jaffé series [70] and for  ${}_s\tilde{X}_{\omega\ell}^{\text{in}}$  we numerically integrated the Regge-Wheeler equation. Additionally, we also calculated their radial derivatives. To accelerate the convergence of the Fourier integral of  ${}_s\tilde{G}_{\omega\ell}$ , we incorporated a smoothing factor into the numerical integration. However, this method comes at a cost: the resulting  ${}_sG_\ell$  is less accurate for small values of  $\Delta t$ . Fortunately, this is not a significant concern, as we have also truncated the mode sum<sup>1</sup>. Therefore, the loss of accuracy in  ${}_sG_\ell$  for small  $\Delta t$  values does not represent a problem.

In the last part of Chapter 2, we explored an alternative for calculating  $G_\ell^{\text{dir}}$  via a Fourier integral. For Schwarzschild spacetime, the authors in [72] were able to obtain Fourier modes of  $G_\ell^{\text{dir}}$  from the Fourier modes of the singular part of the Feynman Green function [73]. We compared the partial results in [73] with  ${}_s\tilde{G}_{\omega\ell}$  but we required further analysis to establish a regularisation procedure (in the Frequency domain) as prescribed in [44].

In Chapter 3 we moved away from  ${}_sG_{\text{ret}}$  and focus on the Hadamard tail. Our objective was to look for a new alternative to calculate  $V_s$ . The small distance expansion for  $V_s$  used in Chapter 2 only allowed us to calculate  $V_s$  in a quasi-local region which, in some cases, may not even overlap with the results from the distant past region. Thus, in Chapter 3 we calculated the Hadamard tail (denoted by  $V$ ) in Plebański-Hacyan (PH) spacetime using initial data on the light cone. As a toy model for black holes, this spacetime is a good starting point before moving to Schwarzschild spacetime. The Hadamard expansion for  $V$  (previously given in [55]) allowed us to establish the characteristic initial data required to solve the wave equation in PH spacetime. Therefore, we came up with a

---

<sup>1</sup>This truncation has the effect of transforming the  $\delta(\sigma)$  singularity at coincidence into a Gaussian distribution.



more general CID scheme than the one previously described in Chapter 2 for  ${}_s g_\ell$ . The symmetries of PH spacetime reduced the four-dimensional PDE for  $V$  into a two-dimensional one where the independent variables are  $\eta$  and  $\gamma$ , the proper time in  $\mathbb{M}_2$  and the angular separation between  $x$  and  $x'$  (which is also a geodesic distance in  $\mathbb{S}^2$ ), respectively.

In contrast to the PDE for  ${}_s g_\ell$ , the wave equation for  $V$  contains first order derivatives and, additionally, at  $\gamma = 0$  there is a coordinate singularity. As a result, we encounter two issues; the first order derivatives led to a reduction in the order of the CID scheme from an expected fourth order to a third order; for the fourth order CID scheme, the coordinate singularity required an additional analysis (along  $\gamma = 0$ ) that resulted in providing extra data on the light cone. The Hadamard expansion for  $V$  was used in order to obtain this extra data. We then obtained a third and fourth order CID schemes for  $V$  instead of the fourth and sixth order scheme we had for  ${}_s g_\ell$ . We presented results for  $V$  using both third and fourth order CID schemes for any pair of spacetime points where  $V$  is defined and for different values of the coupling constant  $\xi$ . Once  $V$  is determined, one may go further and calculate the scalar self-force in PH spacetime.

Next, we moved to Schwarzschild spacetime and attempted to develop a scheme for  $V_s$  using the CID scheme for  $V$  as a starting point. In [76] the authors provide a (numerical) method to calculate  $V_s$  on the light cone, i.e., this is the CID we require to formulate the characteristic initial value problem for  $V_s$ . Unfortunately, some additional difficulties appeared. More specifically, the four-dimensional wave equation was only reduced to a three-dimensional one and the two-dimensional grid we had for  $V$  became a three-dimensional mesh for  $V_s$ . The symmetry of this mesh makes it difficult to establish a standard grid of equally spaced points. Therefore, we could not fully provide a consistent CID scheme for  $V_s$  due to these difficulties. Unfortunately, evolving differential equations from such non-standard mesh is a relatively unexplored area. Due to this, we could not fully provide a consistent CID scheme for  $V_s$  due to these technical difficulties.

In Chapter 4 we explored an application for  ${}_0 G_{\text{ret}}$  in quantum quantum communication in curved spacetime. After successfully calculating  ${}_s G_{\text{ret}}$  (together with its

Hadamard biscalars  $U$  and  $V_s$ ), in Chapter 4 we used  ${}_0G_{\text{ret}}$  and produced new results in quantum communication near a Schwarzschild black hole. More specifically, we explored the implications of spacetime curvature on the quantum communication via a quantum scalar field. Given two observers (modeled by a Unruh-DeWitt particle detector) Alice and Bob and quantum scalar field  $\hat{\phi}$ , it turned out that the leading order signal strength  $|C_2| + |D_2|$  (the capacity for the channel to successfully transmit a bit of information) is solely determined by the scalar retarded Green function  ${}_0G_{\text{ret}}$ . For the case of static observers, we calculated  $|C_2| + |D_2|$  for Alice's position fixed at  $r_A = 6M$  and Bob's position spatially fixed at varying radii  $r_B \in [2.26M, 6M]$  and angular separation (with respect to Alice)  $\gamma \in [0, \frac{3}{4}\pi]$ . The CID results together with  $V_0$  were used to construct  ${}_sG_{\text{ret}}^{\text{nd}}(r_A, r_B; t_B - t_A)$  and be able to cover Bob's positions. As Bob couples to the field and collect null rays to receive Alice's message, besides direct null rays, he could be able to collect secondary or tertiary null rays depending on the time he keeps his detector coupled to the field. We observed that collecting non-direct null rays interferes with the signal strength. Depending on Bob's position this interference may enhance or diminish the signal strength. Another scenario of interest consisted of Alice falling into the black hole following a radial infalling geodesic. In this scenario the time dilation played an important role since Bob now coupled to the field for longer periods of time. The closer Alice was to the black hole, the more significant was the contribution to the signal strength from the non-direct part of  ${}_0G_{\text{ret}}^{\text{nd}}$ . When comparing the signal strength results to their counterparts in flat spacetime, we observed that the influence of non-direct null rays could either amplify or attenuate the ability of observers to communicate effectively. In certain scenarios, there exists a possibility for two observers to face communication challenges, as non-direct null rays may interfere destructively, preventing successful communication.

In Chapter 5 we focus on solving the Teukolsky equation via Green function methods. A brief discussion about the Hadamard form of the retarded Teukolsky Green function (namely  ${}_{-2}G_{\text{ret}}^T$ ) showed that calculating the biscalars  $U^T$  and  $V_s^T$  in Eq. (5.2) are more challenging than in the Regge-Wheeler case. For instance, calculating  $V_s^T$  using a small distance expansion is not trivial due to the lack of spherical symmetry of the Teukolsky

equation. On the other hand, the biscalar  $U^T$  may be obtainable from  $U$  via  $U^T = e^\alpha U$  but, unfortunately, the transport equation for  $\alpha$  cannot be solved analytically for arbitrary geodesics. We thus focused on calculating the retarded Green function  ${}_{-2}G_{\text{ret}}^T$  of the Teukolsky equation via mode decomposition and for the  $s = -2$  case. We calculated the  $\ell$ -modes of  ${}_sG_{\text{ret}}^T$  via Fourier integral. Instead of solving the radial Teukolsky equation, the Chandrasekhar transformation allowed us to obtain the Fourier modes of the  $\ell$ -modes of  ${}_sG_{\text{ret}}^T$  directly from homogeneous solutions to the radial Regge-Wheeler equation (i.e.,  ${}_2\tilde{X}_{\omega\ell}^{\text{in}}$  and  ${}_2\tilde{X}_{\omega\ell}^{\text{up}}$ ). Using the same techniques described in Chapter 2 for performing the Fourier integral and mode sum, we were able to successfully construct the full Teukolsky Green function (see Fig. 27) with a couple considerations. For  ${}_{-2}G_{\text{ret}}^T$ , the value of  $\ell_{\text{cut}}$  in the mode sum was lower than in the mode sum of  ${}_sG_{\text{ret}}$ . Although this low value removed the high- $\ell$  oscillations in the mode sum, it significantly smoothed out the singularities in  ${}_{-2}G_{\text{ret}}^T$  connected to the non-direct null rays. Increasing  $\ell_{\text{cut}}$  could enhance the singularities in  ${}_{-2}G_{\text{ret}}^T$  but, it is necessary to also include more  $\ell$ -modes to maintain the high- $\ell$  oscillations low. Since we did not considered any regularisation process yet, in Fig. 27 we observe a Gaussian distribution near coincidence (similarly to  ${}_sG_{\text{ret}}$ ). In order to remove this distribution, we proposed a regularisation procedure in the time domain. This procedure consists of applying the Chandrasekhar transformation (in the time domain) on  ${}_sG_\ell - G_\ell^{\text{dir}}$ . As we developed this procedure we encountered several issues arising from the fact that  ${}_sG_\ell - G_\ell^{\text{dir}}$  contains Heaviside distributions. We followed the suggestions provided by Nakano and Sasaki [44] to partially address these issues. Unfortunately, we were not able to fully complete this procedure since the approximations used for  ${}_sG_\ell$  and  $G_\ell^{\text{dir}}$  were very limited for understanding the distributions arising from applying the Chandrasekhar transformation in the time domain. The partial results shown in Fig. 28 seem promising and we are looking forward to address the questions related to Eq. (5.52).

Once we are able to calculate the non-direct part of  ${}_{-2}G_{\text{ret}}^T$ , the next objective would be to establish a scheme for constructing the metric perturbation in a radiation gauge. This will eventually require calculating the Weyl-NP scalars and the Hertz potentials. We expect that having access to the non-direct part of  ${}_{-2}G_{\text{ret}}^T$  would simplify these steps.

# Bibliography

- [1] Abbott, B. P. *et al.* Observation of gravitational waves from a binary black hole merger. *Phys. Rev. Lett.* **116**, 061102 (2016). URL <https://link.aps.org/doi/10.1103/PhysRevLett.116.061102>. Cited 4 times on pages 4, 5, 18, and 153.
- [2] Danzmann, K. & the LISA study team. Lisa: laser interferometer space antenna for gravitational wave measurements. *Classical and Quantum Gravity* **13**, A247 (1996). URL <http://stacks.iop.org/0264-9381/13/i=11A/a=033>. Cited 2 times on pages 4 and 5.
- [3] Poisson, E. Radiation reaction of point particles in curved spacetime. *Classical and Quantum Gravity* **21**, R153 (2004). URL <http://stacks.iop.org/0264-9381/21/i=16/a=R01>. Cited 3 times on pages 4, 5, and 18.
- [4] Barack, L. Gravitational self-force in extreme mass-ratio inspirals. *Classical and Quantum Gravity* **26**, 213001 (2009). URL <https://dx.doi.org/10.1088/0264-9381/26/21/213001>. Cited 3 times on pages 4, 5, and 19.
- [5] Poisson, E., Pound, A. & Vega, I. The motion of point particles in curved spacetime. *Living Reviews in Relativity* **14**, 7 (2011). URL <https://doi.org/10.12942/lrr-2011-7>. Cited 11 times on pages 4, 5, 19, 25, 26, 28, 29, 31, 134, 135, and 137.
- [6] Casals, M., Nolan, B. C., Ottewill, A. C. & Wardell, B. Regularized calculation of the retarded Green function in a Schwarzschild spacetime. *Phys. Rev. D* **100**, 104037 (2019). URL <https://link.aps.org/doi/10.1103/PhysRevD.100.104037>. Cited 9 times on pages 6, 49, 51, 52, 70, 73, 74, 150, and 154.
- [7] Berti, E., Cardoso, V. & Will, C. M. Gravitational-wave spectroscopy of massive black holes with the space interferometer lisa. *Phys. Rev. D* **73**, 064030 (2006). URL <https://link.aps.org/doi/10.1103/PhysRevD.73.064030>. Cited 3 times on pages 12, 144, and 145.

- [8] Warburton, N., Akcay, S., Barack, L., Gair, J. R. & Sago, N. Evolution of inspiral orbits around a schwarzschild black hole. *Phys. Rev. D* **85**, 061501 (2012). URL <https://link.aps.org/doi/10.1103/PhysRevD.85.061501>. Cited on page 19.
- [9] Diener, P., Vega, I., Wardell, B. & Detweiler, S. Self-consistent orbital evolution of a particle around a schwarzschild black hole. *Phys. Rev. Lett.* **108**, 191102 (2012). URL <https://link.aps.org/doi/10.1103/PhysRevLett.108.191102>. Cited on page 19.
- [10] Detweiler, S. Perspective on gravitational self-force analyses. *Classical and Quantum Gravity* **22**, S681 (2005). URL <https://dx.doi.org/10.1088/0264-9381/22/15/006>. Cited on page 19.
- [11] Pound, A. & Wardell, B. *Black Hole Perturbation Theory and Gravitational Self-Force*, 1–119 (Springer Singapore, Singapore, 2020). URL [https://doi.org/10.1007/978-981-15-4702-7\\_38-1](https://doi.org/10.1007/978-981-15-4702-7_38-1). Cited on page 19.
- [12] Quinn, T. C. Axiomatic approach to radiation reaction of scalar point particles in curved spacetime. *Phys. Rev. D* **62**, 064029 (2000). URL <https://link.aps.org/doi/10.1103/PhysRevD.62.064029>. Cited on page 19.
- [13] Burko, L. M. Self-force on a particle in orbit around a black hole. *Phys. Rev. Lett.* **84**, 4529–4532 (2000). URL <https://link.aps.org/doi/10.1103/PhysRevLett.84.4529>. Cited on page 19.
- [14] Barack, L. & Burko, L. M. Radiation-reaction force on a particle plunging into a black hole. *Phys. Rev. D* **62**, 084040 (2000). URL <https://link.aps.org/doi/10.1103/PhysRevD.62.084040>. Cited on page 19.
- [15] Detweiler, S., Messaritaki, E. & Whiting, B. F. Self-force of a scalar field for circular orbits about a schwarzschild black hole. *Phys. Rev. D* **67**, 104016 (2003). URL <https://link.aps.org/doi/10.1103/PhysRevD.67.104016>. Cited on page 19.
- [16] Diaz-Rivera, L. M., Messaritaki, E., Whiting, B. F. & Detweiler, S. Scalar field self-force effects on orbits about a schwarzschild black hole. *Phys. Rev. D* **70**, 124018

- (2004). URL <https://link.aps.org/doi/10.1103/PhysRevD.70.124018>. Cited on page 19.
- [17] Warburton, N. & Barack, L. Self-force on a scalar charge in kerr spacetime: Circular equatorial orbits. *Phys. Rev. D* **81**, 084039 (2010). URL <https://link.aps.org/doi/10.1103/PhysRevD.81.084039>. Cited on page 19.
- [18] Jonsson, R. H., Martín-Martínez, E. & Kempf, A. Information Transmission Without Energy Exchange. *Phys. Rev. Lett.* **114**, 110505 (2015). URL <http://link.aps.org/doi/10.1103/PhysRevLett.114.110505>. Cited 2 times on pages 19 and 112.
- [19] Jonsson, R. H., Aruquipa, D. Q., Casals, M., Kempf, A. & Martín-Martínez, E. Communication through quantum fields near a black hole. *arXiv preprint arXiv:2002.05482* (2020). Cited 6 times on pages 19, 21, 86, 103, 108, and 132.
- [20] Aruquipa, D. Q. & Casals, M. Hadamard tail from initial data on the light cone. *Phys. Rev. D* **107**, 084008 (2023). URL <https://link.aps.org/doi/10.1103/PhysRevD.107.084008>. Cited 3 times on pages 20, 80, and 102.
- [21] Aruquipa, D. Q., Mosna, R. A. & Pitelli, J. a. P. M. Analogue gravity and radial fluid flows: The case of ads and its deformations. *Phys. Rev. D* **97**, 104056 (2018). URL <https://link.aps.org/doi/10.1103/PhysRevD.97.104056>. Cited on page 21.
- [22] Einstein, A. Zur Allgemeinen Relativitätstheorie. *Sitzungsber. Preuss. Akad. Wiss. Berlin (Math. Phys. )* **1915**, 778–786 (1915). [Addendum: *Sitzungsber. Preuss. Akad. Wiss. Berlin (Math. Phys.)* 1915, 799–801 (1915)]. Cited on page 22.
- [23] Einstein, A. Erklärung der Perihelbewegung des Merkur aus der allgemeinen Relativitätstheorie. *Sitzungsberichte der Königlich Preussischen Akademie der Wissenschaften* 831–839 (1915). Cited on page 22.

- [24] Einstein, A. Die Feldgleichungen der Gravitation. *Sitzungsberichte der Königlich Preussischen Akademie der Wissenschaften* 844–847 (1915). Cited on page 22.
- [25] DeWitt, B. S. & Brehme, R. W. Radiation damping in a gravitational field. *Annals of Physics* **9**, 220 – 259 (1960). URL <http://www.sciencedirect.com/science/article/pii/0003491660900300>. Cited 3 times on pages 23, 77, and 82.
- [26] Gralla, S. E., Harte, A. I. & Wald, R. M. Rigorous derivation of electromagnetic self-force. *Phys. Rev. D* **80**, 024031 (2009). URL <https://link.aps.org/doi/10.1103/PhysRevD.80.024031>. Cited on page 23.
- [27] Pound, A. Self-consistent gravitational self-force. *Phys. Rev. D* **81**, 024023 (2010). URL <https://link.aps.org/doi/10.1103/PhysRevD.81.024023>. Cited on page 23.
- [28] Mino, Y., Sasaki, M. & Tanaka, T. Gravitational radiation reaction to a particle motion. *Phys. Rev. D* **55**, 3457–3476 (1997). URL <https://link.aps.org/doi/10.1103/PhysRevD.55.3457>. Cited on page 23.
- [29] Quinn, T. C. & Wald, R. M. Axiomatic approach to electromagnetic and gravitational radiation reaction of particles in curved spacetime. *Phys. Rev. D* **56**, 3381–3394 (1997). URL <https://link.aps.org/doi/10.1103/PhysRevD.56.3381>. Cited on page 23.
- [30] Quinn, T. C. Axiomatic approach to radiation reaction of scalar point particles in curved spacetime. *Phys. Rev. D* **62**, 064029 (2000). URL <https://link.aps.org/doi/10.1103/PhysRevD.62.064029>. Cited on page 23.
- [31] Anderson, W. G. & Wiseman, A. G. A matched expansion approach to practical self-force calculations. *Classical and Quantum Gravity* **22**, S783–S800 (2005). URL <https://doi.org/10.1088%2F0264-9381%2F22%2F15%2F010>. Cited 3 times on pages 30, 31, and 154.

- [32] Hadamard, J. *Lectures on Cauchy's Problem in Linear Partial Differential Equations* (Dover Publications, 2014). URL <https://books.google.com.br/books?id=9RNeBAAAQBAJ>. Cited on page 31.
- [33] Friedlander, F. *The Wave Equation on a Curved Space-Time*. Cambridge Monographs on Mathematical Physics (Cambridge University Press, 1975). URL <https://books.google.com.br/books?id=RDmpajLTw1oC>. Cited 4 times on pages 31, 51, 82, and 134.
- [34] Chandrasekhar, S. *The Mathematical Theory of Black Holes*. International series of monographs on physics (Clarendon Press, 1998). URL <https://books.google.com.br/books?id=LB0VcrzFfhsC>. Cited 3 times on pages 33, 43, and 44.
- [35] Carter, B. Global structure of the kerr family of gravitational fields. *Phys. Rev.* **174**, 1559–1571 (1968). URL <https://link.aps.org/doi/10.1103/PhysRev.174.1559>. Cited on page 34.
- [36] Regge, T. & Wheeler, J. A. Stability of a schwarzschild singularity. *Phys. Rev.* **108**, 1063–1069 (1957). URL <https://link.aps.org/doi/10.1103/PhysRev.108.1063>. Cited 7 times on pages 35, 36, 37, 38, 39, 40, and 41.
- [37] Vishveshwara, C. V. Stability of the schwarzschild metric. *Phys. Rev. D* **1**, 2870–2879 (1970). URL <https://link.aps.org/doi/10.1103/PhysRevD.1.2870>. Cited on page 35.
- [38] Zerilli, F. J. Gravitational field of a particle falling in a schwarzschild geometry analyzed in tensor harmonics. *Phys. Rev. D* **2**, 2141–2160 (1970). URL <https://link.aps.org/doi/10.1103/PhysRevD.2.2141>. Cited 3 times on pages 35, 40, and 41.
- [39] Eisenhart, L. *Riemannian Geometry*. Princeton Landmarks in Mathematics and Physics (Princeton University Press, 2016). URL <https://books.google.com.br/books?id=8h-TDAAAQBAJ>. Cited on page 35.



- [40] Casals, M. & Ottewill, A. High-order tail in schwarzschild spacetime. *Phys. Rev. D* **92**, 124055 (2015). URL <https://link.aps.org/doi/10.1103/PhysRevD.92.124055>. Cited 7 times on pages 39, 137, 139, 140, 144, 145, and 147.
- [41] Teukolsky, S. A. Perturbations of a Rotating Black Hole. I. Fundamental Equations for Gravitational, Electromagnetic, and Neutrino-Field Perturbations. *apj* **185**, 635–648 (1973). Cited 3 times on pages 41, 43, and 44.
- [42] Newman, E. & Penrose, R. An approach to gravitational radiation by a method of spin coefficients. *Journal of Mathematical Physics* **3**, 566–578 (1962). URL <https://doi.org/10.1063/1.1724257>. <https://doi.org/10.1063/1.1724257>. Cited on page 41.
- [43] Newman, E. & Penrose, R. An approach to gravitational radiation by a method of spin coefficients. *Journal of Mathematical Physics* **3**, 566–578 (1962). URL <https://doi.org/10.1063/1.1724257>. <https://doi.org/10.1063/1.1724257>. Cited on page 42.
- [44] Nakano, H. & Sasaki, M. The Gravitational Reaction Force on a Particle in the Schwarzschild Background. *Progress of Theoretical Physics* **105**, 197–218 (2001). URL <https://doi.org/10.1143/PTP.105.197>. <https://academic.oup.com/ptp/article-pdf/105/2/197/5198617/105-2-197.pdf>. Cited 10 times on pages 43, 46, 47, 69, 76, 138, 139, 150, 155, and 158.
- [45] Cohen, J. M. & Kegeles, L. S. Electromagnetic fields in curved spaces: A constructive procedure. *Phys. Rev. D* **10**, 1070–1084 (1974). URL <https://link.aps.org/doi/10.1103/PhysRevD.10.1070>. Cited on page 45.
- [46] Chrzanowski, P. L. Vector potential and metric perturbations of a rotating black hole. *Phys. Rev. D* **11**, 2042–2062 (1975). URL <https://link.aps.org/doi/10.1103/PhysRevD.11.2042>. Cited 2 times on pages 45 and 46.
- [47] Wald, R. M. Construction of solutions of gravitational, electromagnetic, or other perturbation equations from solutions of decoupled equations. *Phys. Rev. Lett.*

- 41, 203–206 (1978). URL <https://link.aps.org/doi/10.1103/PhysRevLett.41.203>. Cited 2 times on pages 45 and 46.
- [48] Kegeles, L. S. & Cohen, J. M. Constructive procedure for perturbations of space-times. *Phys. Rev. D* **19**, 1641–1664 (1979). URL <https://link.aps.org/doi/10.1103/PhysRevD.19.1641>. Cited on page 45.
- [49] Nakano, H., Sago, N. & Sasaki, M. Gauge problem in the gravitational self-force: First post-Newtonian force in the Regge-Wheeler gauge. *Phys. Rev. D* **68**, 124003 (2003). URL <https://link.aps.org/doi/10.1103/PhysRevD.68.124003>. Cited on page 48.
- [50] Thompson, J. E., Wardell, B. & Whiting, B. F. Gravitational self-force regularization in the Regge-Wheeler and easy gauges. *Phys. Rev. D* **99**, 124046 (2019). URL <https://link.aps.org/doi/10.1103/PhysRevD.99.124046>. Cited on page 48.
- [51] Dolan, S. R. & Ottewill, A. C. Wave Propagation and Quasinormal Mode Excitation on Schwarzschild Spacetime. *Phys. Rev.* **D84**, 104002 (2011). [1106.4318](https://doi.org/10.1103/PhysRevD.84.104002). Cited on page 49.
- [52] Zenginoğlu, A. i. e. i. f. & Galley, C. R. Caustic echoes from a schwarzschild black hole. *Phys. Rev. D* **86**, 064030 (2012). URL <https://link.aps.org/doi/10.1103/PhysRevD.86.064030>. Cited on page 49.
- [53] Casals, M. & Nolan, B. On the global hadamard form for the Green function in schwarzschild space-time (2020). [1606.03075](https://arxiv.org/abs/1606.03075). Cited 8 times on pages 49, 58, 95, 99, 113, 122, 131, and 145.
- [54] Harte, A. I. & Drivas, T. D. Caustics and wave propagation in curved space-times. *Phys. Rev. D* **85**, 124039 (2012). URL <https://link.aps.org/doi/10.1103/PhysRevD.85.124039>. Cited on page 49.
- [55] Casals, M. & Nolan, B. C. Kirchhoff integral approach to the calculation of Green’s functions beyond the normal neighborhood. *Phys. Rev. D* **86**, 024038 (2012). URL

- <https://link.aps.org/doi/10.1103/PhysRevD.86.024038>. Cited 10 times on pages 49, 52, 81, 82, 83, 84, 95, 97, 99, and 155.
- [56] Casals, M., Dolan, S., Ottewill, A. C. & Wardell, B. Self-force calculations with matched expansions and quasinormal mode sums. *Phys. Rev. D* **79**, 124043 (2009). URL <https://link.aps.org/doi/10.1103/PhysRevD.79.124043>. Cited 3 times on pages 49, 57, and 145.
- [57] Avramidi, I. G. Covariant methods for the calculation of the effective action in quantum field theory and investigation of higher-derivative quantum gravity. *arXiv preprint hep-th/9510140* (1995). Cited on page 51.
- [58] Ottewill, A. C. & Wardell, B. Transport equation approach to calculations of Hadamard Green functions and non-coincident DeWitt coefficients. *Phys. Rev. D* **84**, 104039 (2011). URL <https://link.aps.org/doi/10.1103/PhysRevD.84.104039>. Cited 2 times on pages 51 and 55.
- [59] Birrell, N. D. & Davies, P. C. W. *Quantum Fields in Curved Space*. Cambridge Monographs on Mathematical Physics (Cambridge University Press, 1982). Cited 2 times on pages 51 and 77.
- [60] Casals, M., Dolan, S., Ottewill, A. C. & Wardell, B. Padé approximants of the Green function in spherically symmetric spacetimes. *Phys. Rev. D* **79**, 124044 (2009). URL <https://link.aps.org/doi/10.1103/PhysRevD.79.124044>. Cited 7 times on pages 55, 70, 97, 136, 147, 148, and 149.
- [61] Anderson, P. R. & Hu, B. L. Radiation reaction in schwarzschild spacetime: Retarded Green's function via hadamard-wkb expansion. *Phys. Rev. D* **69**, 064039 (2004). URL <https://link.aps.org/doi/10.1103/PhysRevD.69.064039>. Cited on page 55.
- [62] Hadamard-wkb. <https://www.barrywardell.net/Research/Code/Hadamard-WKB>. Cited on page 55.

- [63] Mark, Z., Zimmerman, A., Du, S. M. & Chen, Y. A recipe for echoes from exotic compact objects. *Phys. Rev. D* **96**, 084002 (2017). URL <https://link.aps.org/doi/10.1103/PhysRevD.96.084002>. Cited 7 times on pages 57, 58, 86, 87, 89, 95, and 154.
- [64] Lousto, C. O. & Price, R. H. Understanding initial data for black hole collisions. *Phys. Rev. D* **56**, 6439–6457 (1997). URL <https://link.aps.org/doi/10.1103/PhysRevD.56.6439>. Cited 3 times on pages 58, 95, and 154.
- [65] O’Toole, C., Ottewill, A. & Wardell, B. Characteristic formulation of the Regge-Wheeler and Zerilli Green functions. *Phys. Rev. D* **103**, 124022 (2021). URL <https://link.aps.org/doi/10.1103/PhysRevD.103.124022>. Cited 6 times on pages 62, 63, 86, 87, 89, and 95.
- [66] Mano, S., Suzuki, H. & Takasugi, E. Analytic Solutions of the Teukolsky Equation and Their Low Frequency Expansions. *Progress of Theoretical Physics* **95**, 1079–1096 (1996). URL <https://doi.org/10.1143/PTP.95.1079>. <https://academic.oup.com/ptp/article-pdf/95/6/1079/5282662/95-6-1079.pdf>. Cited on page 64.
- [67] Mano, S., Suzuki, H. & Takasugi, E. Analytic Solutions of the Regge-Wheeler Equation and the Post-Minkowskian Expansion. *Progress of Theoretical Physics* **96**, 549–565 (1996). URL <https://doi.org/10.1143/PTP.96.549>. <https://academic.oup.com/ptp/article-pdf/96/3/549/5415226/96-3-549.pdf>. Cited on page 64.
- [68] Sasaki, M. & Tagoshi, H. Analytic black hole perturbation approach to gravitational radiation. *Living Reviews in Relativity* **6**, 6 (2003). URL <https://doi.org/10.12942/lrr-2003-6>. Cited on page 64.
- [69] Leaver, E. W. Solutions to a generalized spheroidal wave equation: Teukolsky’s equations in general relativity, and the two-center problem in molecular quantum mechanics. *Journal of Mathematical Physics* **27**, 1238–1265 (1986). URL <https://doi.org/10.1063/1.527130>. <https://doi.org/10.1063/1.527130>. Cited on page 65.

- [70] Jaffé, G. Zur theorie des wasserstoffmolekülions. *Zeitschrift für Physik* **87**, 535–544 (1934). URL <https://doi.org/10.1007/BF01333263>. Cited 2 times on pages 65 and 155.
- [71] Levi, A. & Ori, A. Mode-sum regularization of  $\langle\phi^2\rangle$  in the angular-splitting method. *Phys. Rev. D* **94**, 044054 (2016). URL <https://link.aps.org/doi/10.1103/PhysRevD.94.044054>. Cited on page 68.
- [72] Freitas, G. & Casals, M. A novel method for renormalization in quantum-field theory in curved spacetime. *International Journal of Modern Physics D* **27**, 1843001 (2018). URL <https://doi.org/10.1142/S0218271818430010>. <https://doi.org/10.1142/S0218271818430010>. Cited 3 times on pages 76, 77, and 155.
- [73] Casals, M. & Freitas, G. In preparation. Cited 3 times on pages 76, 77, and 155.
- [74] Plebański, J. F. & Hacyan, S. Some exceptional electrovac type d metrics with cosmological constant. *Journal of Mathematical Physics* **20**, 1004–1010 (1979). URL <https://doi.org/10.1063/1.524174>. <https://doi.org/10.1063/1.524174>. Cited on page 80.
- [75] Décanini, Y. & Folacci, A. Off-diagonal coefficients of the DeWitt-Schwinger and Hadamard representations of the Feynman propagator. *Phys. Rev.* **D73**, 044027 (2006). [gr-qc/0511115](https://arxiv.org/abs/gr-qc/0511115). Cited on page 82.
- [76] Ottewill, A. C. & Wardell, B. A Transport Equation Approach to Calculations of Hadamard Green functions and non-coincident DeWitt coefficients. *Phys.Rev.* **D84**, 104039 (2011). [0906.0005](https://arxiv.org/abs/0906.0005). Cited 3 times on pages 82, 102, and 156.
- [77] McDonough, J. M. *Lectures in Basic Computational Numerical Analysis* (University of Kentucky, 2007). Cited on page 97.
- [78] Wald, R. *General Relativity* (University of Chicago Press, 1984). URL <https://books.google.com.br/books?id=ibSdQgAACAAJ>. Cited on page 99.

- [79] Earman, J. The unruh effect for philosophers. *Stud. Hist. Philos. Sci. B* **42**, 81 – 97 (2011). URL <http://www.sciencedirect.com/science/article/pii/S1355219811000207>. Cited on page 103.
- [80] Fewster, C. J. & Verch, R. Quantum fields and local measurements (2018). 1810.06512. Cited on page 103.
- [81] Unruh, W. G. & Wald, R. M. What happens when an accelerating observer detects a rindler particle. *Phys. Rev. D* **29**, 1047–1056 (1984). Cited on page 103.
- [82] Gibbons, G. W. & Hawking, S. W. Cosmological event horizons, thermodynamics, and particle creation. *Phys. Rev. D* **15**, 2738–2751 (1977). URL <http://link.aps.org/doi/10.1103/PhysRevD.15.2738>. Cited on page 103.
- [83] Hodgkinson, L., Louko, J. & Ottewill, A. C. Static detectors and circular-geodesic detectors on the schwarzschild black hole. *Phys. Rev. D* **89**, 104002 (2014). URL <https://link.aps.org/doi/10.1103/PhysRevD.89.104002>. Cited on page 103.
- [84] Ng, K. K., Hodgkinson, L., Louko, J., Mann, R. B. & Martín-Martínez, E. Unruh-dewitt detector response along static and circular-geodesic trajectories for schwarzschild–anti-de sitter black holes. *Phys. Rev. D* **90**, 064003 (2014). URL <https://link.aps.org/doi/10.1103/PhysRevD.90.064003>. Cited on page 103.
- [85] Valentini, A. Non-local correlations in quantum electrodynamics. *Physics Letters A* **153**, 321 – 325 (1991). URL <http://www.sciencedirect.com/science/article/pii/0375960191909525>. Cited on page 103.
- [86] Reznik, B., Retzker, A. & Silman, J. Violating bell’s inequalities in vacuum. *Phys. Rev. A* **71**, 042104 (2005). URL <http://link.aps.org/abstract/PRA/v71/e042104>. Cited on page 103.
- [87] Pozas-Kerstjens, A. & Martín-Martínez, E. Harvesting correlations from the quantum vacuum. *Phys. Rev. D* **92**, 064042 (2015). URL <https://link.aps.org/doi/10.1103/PhysRevD.92.064042>. Cited on page 103.

- [88] Steeg, G. V. & Menicucci, N. C. Entangling power of an expanding universe. *Phys. Rev. D* **79**, 044027 (2009). URL <https://link.aps.org/doi/10.1103/PhysRevD.79.044027>. Cited on page 103.
- [89] Kukita, S. & Nambu, Y. Entanglement dynamics in de sitter spacetime. *Class. Quantum Grav.* **34**, 235010 (2017). Cited on page 103.
- [90] Henderson, L. J., Hennigar, R. A., Mann, R. B., Smith, A. R. H. & Zhang, J. Entangling detectors in anti-de Sitter space. *J. High Energy Phys.* **2019**, 178 (2019). URL [https://doi.org/10.1007/JHEP05\(2019\)178](https://doi.org/10.1007/JHEP05(2019)178). Cited on page 103.
- [91] Ng, K. K., Mann, R. B. & Martín-Martínez, E. Unruh-dewitt detectors and entanglement: The anti-de sitter space. *Phys. Rev. D* **98**, 125005 (2018). URL <https://link.aps.org/doi/10.1103/PhysRevD.98.125005>. Cited on page 103.
- [92] Henderson, L. J., Hennigar, R. A., Mann, R. B., Smith, A. R. H. & Zhang, J. Harvesting entanglement from the black hole vacuum. *Class. Quantum Gravity* **35**, 21LT02 (2018). Cited on page 103.
- [93] Unruh, W. G. Notes on black-hole evaporation. *Physical Review D* **14**, 870–892 (1976). URL <http://link.aps.org/doi/10.1103/PhysRevD.14.870>. Cited on page 104.
- [94] DeWitt, B. S. Quantum gravity: The new synthesis. In Hawking, S. & Israel, W. (eds.) *General Relativity : An Einstein Centenary Survey*, 680 (Cambridge University Press, Cambridge Eng; New York, 1979). Cited on page 104.
- [95] Martín-Martínez, E. & Rodriguez-Lopez, P. Relativistic quantum optics: The relativistic invariance of the light-matter interaction models. *Physical Review D* **97**, 105026 (2018). URL <https://link.aps.org/doi/10.1103/PhysRevD.97.105026>. Cited 2 times on pages 104 and 105.
- [96] Jonsson, R. H. Quantum signaling in relativistic motion and across acceleration horizons. *J. Phys. A: Math. Theor.* **50**, 355401 (2017). URL <http://stacks.iop>.

- [org/1751-8121/50/i=35/a=355401](https://doi.org/10.1088/1751-8121/50/i=35/a=355401). Cited 5 times on pages 105, 106, 108, 113, and 116.
- [97] Kay, B. S. & Wald, R. M. Theorems on the uniqueness and thermal properties of stationary, nonsingular, quasifree states on spacetimes with a bifurcate killing horizon. *Physics Reports* **207**, 49–136 (1991). URL <https://www.sciencedirect.com/science/article/pii/037015739190015E>. Cited on page 106.
- [98] Cliche, M. & Kempf, A. Relativistic quantum channel of communication through field quanta. *Phys. Rev. A* **81**, 012330 (2010). URL <http://link.aps.org/doi/10.1103/PhysRevA.81.012330>. Cited on page 106.
- [99] Jonsson, R. H., Martín-Martínez, E. & Kempf, A. Quantum signaling in cavity QED. *Physical Review A* **89**, 022330 (2014). URL <http://link.aps.org/doi/10.1103/PhysRevA.89.022330>. Cited 2 times on pages 106 and 107.
- [100] Landulfo, A. G. S. Nonperturbative approach to relativistic quantum communication channels. *Phys. Rev. D* **93**, 104019 (2016). URL <http://link.aps.org/doi/10.1103/PhysRevD.93.104019>. Cited on page 106.
- [101] Jonsson, R. H., Ried, K., Martín-Martínez, E. & Kempf, A. Transmitting qubits through relativistic fields. *J. Phys. A: Math. Theor.* **51** (2018). URL <http://iopscience.iop.org/10.1088/1751-8121/aae78a>. Cited on page 106.
- [102] Satz, A. Then again, how often does the Unruh-DeWitt detector click if we switch it carefully? *Class. Quantum Gravity* **24**, 1719–1731 (2007). Cited on page 108.
- [103] Louko, J. & Satz, A. Transition rate of the Unruh-DeWitt detector in curved spacetime. *Class. Quantum Gravity* **25**, 055012 (2008). Cited on page 108.
- [104] Hodgkinson, L. & Louko, J. How often does the Unruh-DeWitt detector click beyond four dimensions? *J. Math. Phys.* **53**, 082301 (2012). URL <http://arxiv.org/abs/1109.4377>. Cited on page 108.



- [105] Unruh, W. G. & Zurek, W. H. Reduction of a wave packet in quantum brownian motion. *Phys. Rev. D* **40**, 1071–1094 (1989). URL <https://link.aps.org/doi/10.1103/PhysRevD.40.1071>. Cited on page 109.
- [106] Hu, B. L. & Matacz, A. Quantum brownian motion in a bath of parametric oscillators: A model for system-field interactions. *Phys. Rev. D* **49**, 6612–6635 (1994). URL <https://link.aps.org/doi/10.1103/PhysRevD.49.6612>. Cited on page 109.
- [107] Massar, S. & Spindel, P. Einstein-podolsky-rosen correlations between two uniformly accelerated oscillators. *Phys. Rev. D* **74**, 085031 (2006). URL <https://link.aps.org/doi/10.1103/PhysRevD.74.085031>. Cited on page 109.
- [108] Lin, S.-Y. & Hu, B. L. Backreaction and the unruh effect: New insights from exact solutions of uniformly accelerated detectors. *Phys. Rev. D* **76**, 064008 (2007). URL <https://link.aps.org/doi/10.1103/PhysRevD.76.064008>. Cited on page 109.
- [109] Lin, S.-Y. & Hu, B. L. Entanglement creation between two causally disconnected objects. *Phys. Rev. D* **81**, 045019 (2010). URL <https://link.aps.org/doi/10.1103/PhysRevD.81.045019>. Cited on page 109.
- [110] Martín-Martínez, E., Fuentes, I. & Mann, R. B. Using berry’s phase to detect the unruh effect at lower accelerations. *Phys. Rev. Lett.* **107**, 131301 (2011). URL <https://link.aps.org/doi/10.1103/PhysRevLett.107.131301>. Cited on page 109.
- [111] Bruschi, D. E., Lee, A. R. & Fuentes, I. Time evolution techniques for detectors in relativistic quantum information. *J. Phys. A: Math. Theor.* **46**, 165303 (2013). Cited on page 109.
- [112] Brown, E. G., Martín-Martínez, E., Menicucci, N. C. & Mann, R. B. Detectors for probing relativistic quantum physics beyond perturbation theory. *Phys. Rev. D* **87**, 084062 (2013). URL <https://link.aps.org/doi/10.1103/PhysRevD.87.084062>. Cited on page 109.

- 
- [113] Martín-Martínez, E. Causality issues of particle detector models in qft and quantum optics. *Phys. Rev. D* **92**, 104019 (2015). URL <https://link.aps.org/doi/10.1103/PhysRevD.92.104019>. Cited 2 times on pages 110 and 111.
- [114] Jonsson, R. H. *Decoupling of Information Propagation from Energy Propagation*. PhD, University of Waterloo, Waterloo, Ontario (2016). URL <http://hdl.handle.net/10012/10770>. Cited 2 times on pages 113 and 116.
- [115] Buss, C. & Casals, M. Quantum correlator outside a schwarzschild black hole. *Physics Letters B* **776**, 168–173 (2018). URL <https://www.sciencedirect.com/science/article/pii/S0370269317309401>. Cited on page 144.
- [116] Hod, S. Late-time evolution of realistic rotating collapse and the no-hair theorem. *Phys. Rev. D* **58**, 104022 (1998). URL <https://link.aps.org/doi/10.1103/PhysRevD.58.104022>. Cited on page 144.
- [117] Price, R. H. Nonspherical perturbations of relativistic gravitational collapse. i. scalar and gravitational perturbations. *Phys. Rev. D* **5**, 2419–2438 (1972). URL <https://link.aps.org/doi/10.1103/PhysRevD.5.2419>. Cited on page 144.
- [118] Price, R. H. Nonspherical perturbations of relativistic gravitational collapse. ii. integer-spin, zero-rest-mass fields. *Phys. Rev. D* **5**, 2439–2454 (1972). URL <https://link.aps.org/doi/10.1103/PhysRevD.5.2439>. Cited on page 144.

# Appendix

# APPENDIX A – Asymptotic coefficients $a_n^{\text{in}}$ and $a_n^{\text{in}}$ for ${}_s\tilde{X}_{\omega\ell}^{\text{in}}$ and ${}_s\tilde{X}_{\omega\ell}^{\text{up}}$

In this appendix we calculate the asymptotic coefficients  $a_n^{\text{in}}$  and  $a_n^{\text{up}}$  in Eqs. (2.82)–(2.83) for  $n = 1, 2, 3, 4$ . Integrating Eqs. (2.84)–(2.85) yield

$$a_1^{\text{in}} = -\frac{i(M\hat{s} + \Lambda r)}{2r^2}, \quad (\text{A.1})$$

$$a_2^{\text{in}} = -\frac{\Lambda r(4M + (\Lambda - 2)r) + M\hat{s}(M\hat{s} + 8M + 2(\Lambda - 2)r)}{8r^4}, \quad (\text{A.2})$$

$$a_3^{\text{in}} = \frac{i}{240r^6} \left[ 5\Lambda r \left( 72M^2 + 15(\Lambda - 4)Mr + (\Lambda - 6)(\Lambda - 2)r^2 \right) \right. \\ \left. + M\hat{s} \left( 960M^2 + 12(19\Lambda - 70)Mr + M\hat{s}(5M\hat{s} + 160M + 3(5\Lambda - 28)r) \right. \right. \\ \left. \left. + 15(\Lambda - 6)(\Lambda - 2)r^2 \right) \right], \quad (\text{A.3})$$

$$a_4^{\text{in}} = \frac{1}{1920r^8} \left\{ 5\Lambda r \left[ 2880M^3 + 48(11\Lambda - 70)M^2r + 12(\Lambda(3\Lambda - 40) + 104)Mr^2 \right. \right. \\ \left. \left. + (\Lambda - 12)(\Lambda - 6)(\Lambda - 2)r^3 \right] \right. \\ \left. + M\hat{s} \left[ 46080M^3 + M\hat{s} \left( 8640M^2 + 136(7\Lambda - 60)Mr \right. \right. \right. \\ \left. \left. + M\hat{s} \left( 5M\hat{s} + 400M + 4(5\Lambda - 54)r \right) + 6(\Lambda(5\Lambda - 86) + 320)r^2 \right) \right. \right. \\ \left. \left. + 480(21\Lambda - 118)M^2r + 12(\Lambda(61\Lambda - 780) + 1880)Mr^2 \right. \right. \\ \left. \left. + 20(\Lambda - 12)(\Lambda - 6)(\Lambda - 2)r^3 \right] \right\}, \quad (\text{A.4})$$

and

$$a_1^{up} = -\frac{if(\hat{s}(2M+r) + 2\Lambda r)}{8Mr}, \quad (\text{A.5})$$

$$a_2^{up} = \frac{f}{128M^2r^3} \left[ \hat{s} \left( 64M^3 + 16\Lambda M^2r - r\hat{s}(2M+r)^2f - 4\Lambda r^3 \right) - 4\Lambda r \left( \Lambda r^2f - 8M^2 \right) \right], \quad (\text{A.6})$$

$$a_3^{up} = \frac{if}{15360M^3r^5} \left\{ 3840\Lambda M^3r(3M-r) + 30\hat{s} \left( 128M^4(8M-3r) + \Lambda r\hat{s}(r^2-4M^2)^2 \right) \right. \\ \left. - 4rf \left[ 5\Lambda^2r^2(60M^2+4Mr+r^2) + 6\Lambda r\hat{s}(152M^3+32M^2r+4Mr^2+r^3) \right] \right. \\ \left. + 2\hat{s}^2(320M^4+152M^3r+12M^2r^2+4Mr^3+r^4) \right. \\ \left. + 5r^2f^2 \left[ 12\Lambda^2r^2\hat{s}(2M+r) + \hat{s}^3(2M+r)^3 + 8\Lambda^3r^3 \right] \right\}, \quad (\text{A.7})$$

$$a_4^{up} = \frac{f}{491520M^4r^7} \left\{ \hat{s} \left[ 16 \left( 960M^3(-\Lambda r^2(-42M^2+5Mr+r^2))f \right. \right. \right. \\ \left. \left. - 8M^2(48M^2-35Mr+6r^2) \right) \right. \\ \left. + \Lambda^2r^4f^2(-1464M^3-484M^2r+10\Lambda r^2(2M+r)f-78Mr^2-17r^3) \right) \\ \left. + r\hat{s}f \left\{ 120 \left( \Lambda^2r^2(r^2-4M^2)^2 + 128M^4(36M^2+2Mr-3r^2) \right) \right. \right. \\ \left. + rf(-32\Lambda r(952M^4+592M^3r+114M^2r^2+26Mr^3+5r^4)) \right. \\ \left. - 32\hat{s}(200M^4+92M^3r+12M^2r^2+4Mr^3+r^4)(2M+r) \right. \\ \left. + 5r\hat{s}(2M+r)^3(2M\hat{s}+r\hat{s}+8\Lambda r)f \right\} \right] \\ \left. + 80\Lambda r \left[ -23040M^6 + 384(40-11\Lambda)M^5r - 288((\Lambda-10)\Lambda+8)M^4r^2 \right. \right. \\ \left. \left. - 8\Lambda((\Lambda-32)\Lambda+48)M^3r^3 + 12(\Lambda-4)\Lambda^2M^2r^4 - 6\Lambda^3Mr^5 + (\Lambda-2)\Lambda^2r^6 \right] \right\}. \quad (\text{A.8})$$

# APPENDIX B – Going beyond a fourth order CID scheme for calculating $V$ in PH spacetime

In this appendix we lay out the ground work for deriving a fifth –and potentially, sixth– order scheme, by following a similar prescription to that described in Secs. 3.2.2.1 and 3.2.2.2. For a fifth or sixth order CID scheme, it is necessary to include the next nontrivial order in Eqs. (3.27)–(3.29). The corresponding equations are given by:

$$\int_{SE\text{NW}} Q \frac{\partial V}{\partial v} dv du = 4h^2 Q_O \left( \frac{\partial V}{\partial v} \right)_O + \frac{2}{3} \left[ 2 \left( \frac{\partial Q}{\partial u} \frac{\partial^2 V}{\partial u \partial v} \right)_O + \left( \frac{\partial V}{\partial v} \right)_O \left( \frac{\partial^2 Q}{\partial u^2} + \frac{\partial^2 Q}{\partial v^2} \right)_O + 2 \left( \frac{\partial Q}{\partial v} \frac{\partial^2 Q}{\partial v^2} \right)_O + Q_O \left( \frac{\partial^3 V}{\partial u^2 \partial v} + \frac{\partial^3 V}{\partial v^3} \right)_O \right] h^4 + \mathcal{O}(h^6), \quad (\text{B.1})$$

$$\int_{SE\text{NW}} S \frac{\partial V}{\partial u} dv du = 4h^2 S_O \left( \frac{\partial V}{\partial u} \right)_O + \frac{2}{3} \left[ 2 \left( \frac{\partial S}{\partial v} \frac{\partial^2 V}{\partial u \partial v} \right)_O + \left( \frac{\partial V}{\partial u} \right)_O \left( \frac{\partial^2 S}{\partial u^2} + \frac{\partial^2 S}{\partial v^2} \right)_O + 2 \left( \frac{\partial S}{\partial u} \frac{\partial^2 V}{\partial u^2} \right)_O + S_O \left( \frac{\partial^3 V}{\partial u^3} + \frac{\partial^3 V}{\partial u \partial v^2} \right)_O \right] h^4 + \mathcal{O}(h^6), \quad (\text{B.2})$$

$$\int_{SE\text{NW}} V dv du = 4h^2 V_O + \frac{2}{3} \left( \frac{\partial^2 V}{\partial u^2} + \frac{\partial^2 V}{\partial v^2} \right)_O h^4 + \mathcal{O}(h^6), \quad (\text{B.3})$$

where, as usual, the subscript  $O$  on a quantity in brackets indicates that it is evaluated at the point  $O$ .

When replacing the expressions in Eq. (3.25) and Eqs. (B.1)–(B.3) back into Eq. (3.24) and isolate for  $V_N$ , we find

$$\begin{aligned} V_N = & V_E + V_W - V_S - \left[ Q_O \left( \frac{\partial V}{\partial v} \right)_O + S_O \left( \frac{\partial V}{\partial u} \right)_O + \zeta V_O \right] h^2 - \\ & \frac{1}{6} \left[ \zeta \left( \frac{\partial^2 V}{\partial u^2} + \frac{\partial^2 V}{\partial v^2} \right)_O + 2 \left( \frac{\partial Q}{\partial v} \right)_O \left( \frac{\partial^2 V}{\partial v^2} \right)_O + 2 \left( \frac{\partial S}{\partial u} \right)_O \left( \frac{\partial^2 V}{\partial u^2} \right)_O + \right. \\ & \left. \left( \frac{\partial V}{\partial v} \right)_O \left( \frac{\partial^2 Q}{\partial u^2} + \frac{\partial^2 Q}{\partial v^2} \right)_O + 2 \left( \frac{\partial^2 V}{\partial u \partial v} \right)_O \left( \frac{\partial Q}{\partial u} + \frac{\partial S}{\partial v} \right)_O + \left( \frac{\partial V}{\partial u} \right)_O \left( \frac{\partial^2 S}{\partial u^2} + \frac{\partial^2 S}{\partial v^2} \right)_O + \right. \\ & \left. S_O \left( \frac{\partial^3 V}{\partial u \partial v^2} + \frac{\partial^3 V}{\partial u^3} \right)_O + Q_O \left( \frac{\partial^3 V}{\partial u^2 \partial v} + \frac{\partial^3 V}{\partial v^3} \right)_O \right] h^4 + \mathcal{O}(h^6). \quad (\text{B.4}) \end{aligned}$$

The next step is to replace into Eq. (B.4) the expressions for the Taylor coefficients given in Eqs. (3.36)–(3.45) and then isolate for  $V_N$ . We do not display the resulting expression for  $V_N$  since it is very long and trivial to obtain. We note that, despite Eq. (B.4) being  $\mathcal{O}(h^6)$ , the expressions for the Taylor coefficients given in Eqs. (3.36)–(3.45) reduce the order of the resulting expression of  $V_N$  by one (i.e., to  $\mathcal{O}(h^5)$ ). Thus, we end up with a fifth order CID scheme. One could of course use Eq. (B.4) for a sixth order scheme merely by obtaining expansions for the Taylor coefficients appearing in it to one order higher than in Eqs. (3.36)–(3.45).

Finally, and similarly to the third and fourth order CID schemes in Secs. 3.2.2.1 and 3.2.2.2, the  $u_O = v_O$  (i.e.,  $\gamma_O = 0$ ) case should be handled separately. The coefficient of  $h^4$  in Eq. (B.4) involves derivatives of the functions  $Q$  and  $S$  evaluated at the point  $O$ . As a consequence, terms involving derivatives of  $\cot \frac{v-u}{2} = \cot \gamma$  should be evaluated appropriately as  $\gamma_O \rightarrow 0$ . This would eventually require calculating fourth order derivatives of  $V$  and, consequently, require additional explicit data (additional with respect to the lower schemes, e.g., second order derivatives of  $V$ ) on the light cone. In this paper we do not pursue this higher order scheme further and leave it here with the indication of how it could be completed.

# APPENDIX C – Derivation of time-mirror symmetry

This appendix gives the derivation of the time-mirror symmetry introduced and discussed in Sec. 4.1.4. Given a signaling scenario (with worldlines  $x_D(t)$ , switching functions  $\eta_D(t)$  for  $D = A, B$ , and signal terms  $C_2$  and  $D_2$ ), the time-mirrored scenario has worldlines  $x'_D(t) = x_D(-t)$  and switching functions  $\eta'_D(t) = \eta_D(-t)$ . We assume, without loss of generality, that the proper times of the detectors are given by  $\tau'_D(t) = -\tau_D(-t)$  for both detectors in the inverted scenario. The detector frequencies are the same in the original and the mirrored scenario. However, since A acts as the receiver in the mirrored scenario, their frequency  $\Omega_A$  enters with a positive sign in the imaginary exponent of the coefficient  $C'_2$  for the mirrored scenario, whereas it enters with a negative sign in the original coefficient  $C_2$ . Then, if the Green function of the spacetime obeys Eq. (4.34), we have that the coefficient for the mirrored scenario

$$\begin{aligned}
C'_2 &= \frac{-i}{4\pi} \int dt_1 \int^{t_1} dt_2 \frac{d\lambda'_A}{dt_1} \eta'_A(t_1) \frac{d\tau'_B}{dt_2} \eta'_B(t_2) e^{i(\Omega_A \tau'_A(t_1) - \Omega_B \tau'_B(t_2))} {}_0G_{\text{ret}}(t_1, \vec{x}'_A(t_1), t_2, \vec{x}'_B(t_2)) \\
&= \frac{-i}{4\pi} \int ds_2 \int^{s_2} ds_1 \frac{d\tau'_A(-s_1)}{ds_1} \eta'_A(-s_1) \frac{d\tau'_B(-s_2)}{ds_2} \eta'_B(-s_2) \times \\
&\quad e^{i(\Omega_A \tau'_A(-s_1) - \Omega_B \tau'_B(-s_2))} {}_0G_{\text{ret}}(-s_1, \vec{x}'_A(-s_1), -s_2, \vec{x}'_B(-s_2)) \\
&= \frac{-i}{4\pi} \int ds_2 \int^{s_2} ds_1 \frac{d\tau_A(s_1)}{ds_1} \eta_A(s_1) \frac{d\tau_B(s_2)}{ds_2} \eta_B(s_2) \\
&\quad e^{-i(\Omega_A \tau_A(s_1) - \Omega_B \tau_B(s_2))} {}_0G_{\text{ret}}(-s_1, \vec{x}_A(s_1), -s_2, \vec{x}_B(s_2)) \\
&= \frac{-i}{4\pi} \int ds_2 \int^{s_2} ds_1 \frac{d\tau_A(s_1)}{ds_1} \eta_A(s_1) \frac{d\tau_B(s_2)}{ds_2} \eta_B(s_2) \\
&\quad e^{-i(\Omega_A \tau_A(s_1) - \Omega_B \tau_B(s_2))} {}_0G_{\text{ret}}(s_2, \vec{x}_B(s_2), s_1, \vec{x}_A(s_1)) = C_2
\end{aligned} \tag{C.1}$$

is identical to the coefficient  $C_2$  for the original scenario. (And we introduced integration variables  $s_1 = -t_1$ ,  $s_2 = -t_2$ .) For the signal term  $D_2$ , we analogously find  $D'_2 = -D_2^*$ . This we can also deduce, from the general relation  $C_2(\Omega_A, \Omega_B) = -D_2(\Omega_A, -\Omega_B)$ , which



implies

$$\begin{aligned} D_2'(\Omega_B, \Omega_A) &= -C_2'(\Omega_B, -\Omega_A) = -C_2(-\Omega_A, \Omega_B) \\ &= D_2(-\Omega_A, -\Omega_B) \end{aligned} \tag{C.2}$$

and, indeed, in Eq. (4.14) we see that  $D_2(-\Omega_A, -\Omega_B) = -D_2(\Omega_A, \Omega_B)^*$ .

# APPENDIX D – Contribution to the leading order signal strength from $C_2^{\text{d}}$ and $D_2^{\text{d}}$

In order to further analyze the characteristics of the direct contribution, in the following we focus on a special case where the direct contribution can be solved analytically. This is the case where sender and receiver have identical angular variables, i.e., zero angular separation  $\gamma = 0$ , which we refer to as radially separated detectors. The radial null geodesic connecting Alice at radial coordinate  $r_A$  to Bob at  $r_B$  is of the form

$$t(\lambda) = \lambda \mp 2M \ln \frac{r_A \mp \lambda - 2M}{r_A - 2M}, \quad r(\lambda) = r_A \mp \lambda, \quad (\text{D.1})$$

where the negative sign applies if  $r_B < r_A$  and the positive sign applies if  $r_A < r_B$ . We choose the affine parameter so that  $r(\lambda = 0) = r_A$  and so that the geodesic reaches Bob at affine parameter value  $\lambda = |r_A - r_B|$ . Furthermore, the van Vleck determinant appearing in Eq. (4.40) is equal to 1 for radially separated detectors, because it is equal to 1 between points connected by a radial null geodesic (see Sec. 2.1.2). Altogether, for radially separated, static detectors, the direct contribution to  $C_2$  in Eq. (4.40) thus reads

$$C_2^{\text{d}} = \frac{-i}{2\pi} e^{i \frac{(\Omega_B - \nu \Omega_A)(A_1 + A_2)}{2\nu}} \frac{\sqrt{f(r_A)}}{r_A - r_B} \times \frac{1}{\Omega_B - \nu \Omega_A} \sin \left( \frac{(\Omega_B - \nu \Omega_A)(A_2 - A_1)}{2\nu} \right), \quad (\text{D.2})$$

where  $\nu = \sqrt{f(r_A)/f(r_B)}$  is the red-shift factor between Alice and Bob, as defined in Eq. (4.36). Fig. 29 shows the direct contribution  $|C_2^{\text{d}}| + |D_2^{\text{d}}|$  to the signal strength for identical detectors ( $\Omega_B = \Omega_A$ ) and for resonant detectors ( $\Omega_B = \Omega_A \nu$ ) with different radial separations.

The gravitational red-shift caused by the spacetime curvature, impacts on the value of  $C_2^{\text{d}}$  in two different ways. The first effect is that the red-shift impacts on the

resonance between the detectors. The second effect is that the proper time during which the receiver gets to interact with the direct contribution is affected by the red-shift.

If the detectors are off-resonant, i.e.,  $\Omega_A \nu \neq \Omega_B$ , there is a bound on the magnitude of  $C_2^d$  which is independent of the duration  $A_2 - A_1$  of Alice's signal. This is because of the last sine-factor in  $C_2^d$  above, which yields

$$|C_2^d| \leq \frac{\sqrt{f(r_A)}}{2\pi|r_A - r_B||\Omega_B - \nu\Omega_A|}. \quad (\text{D.3})$$

Analogously,  $|D_2^d|$  is then bounded by

$$|D_2^d| \leq \frac{\sqrt{f(r_A)}}{2\pi|r_A - r_B||\Omega_B + \nu\Omega_A|}. \quad (\text{D.4})$$

A linear growth of signal strength with the duration of the signal requires resonance, i.e., Bob needs to account for the red-shift and tune his detector to the frequency  $\Omega_B = \nu\Omega_A$ . In this case, the direct contribution to  $C_2$  simplifies to

$$C_2^d = \frac{-i\sqrt{f(r_A)}}{4\pi(r_A - r_B)} \frac{A_2 - A_1}{\nu} \quad (\text{D.5})$$

Hence, for resonant detectors the direct contribution grows linearly with the duration of the signal. It is interesting to note that the specific value of  $\Omega_A$  and  $\Omega_B$  has no impact on  $C_2^d$  as long as the detectors are resonant. Instead, we see that the determining factor for the magnitude of the direct contribution between resonant detectors is the duration of the signal as measured in terms of Bob's proper time, which is  $(A_2 - A_1)/\nu$ . Thus, a linear bound of the form  $|C_2| + |D_2| \leq C_{\mathbb{B}}(A_2 - A_1)/\nu$  (where  $C_{\mathbb{B}} < \infty$  is a constant) applies to this direct contribution here in the case of sharp switching functions. In particular, as Bob approaches the horizon (i.e.,  $r_B \rightarrow 2M$ ), the red-shift factor diverges (i.e.,  $\nu \rightarrow \infty$ ), and so the duration of the signal with respect to Bob's proper time goes to zero and  $C_2^d \rightarrow 0$ : Bob becomes increasingly transparent for *incoming* signals as Bob is placed increasing closer to the horizon.

An interesting question is how the signal strength between static observers in curved Schwarzschild spacetime compares to flat Minkowski spacetime as a function of the distance between sender and receiver. However, a priori, it is not clear which notion

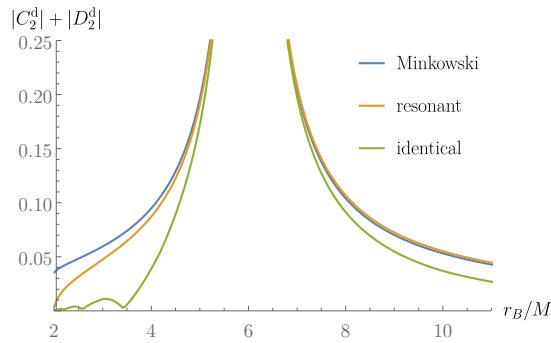


Figure 29 – Logarithmic plot comparing the direct signal strength  $|C_2^d| + |D_2^d|$  for radially separated static detectors in Schwarzschild and in Minkowski spacetime. In Schwarzschild spacetime Alice is located at  $r_A = 6M$ , her detector gap is  $\Omega_A = 10/M$  and she couples to the field for a proper time duration of  $A_2 - A_1 = 3M$ . Bob’s radial coordinate is  $r_B$ . He couples to the field in such a way that he receives all of Alice’s direct null geodesics. The resulting signal strengths in Schwarzschild spacetime are shown for Bob using an identical detector with  $\Omega_B = 10/M$  (green), and a resonant detector with  $\Omega_B = \nu\Omega_A$  (yellow). In Minkowski spacetime (blue), Alice and Bob use identical detectors ( $\Omega_A = \Omega_B = 10/M$ ) which are placed so that their static distance in Minkowski spacetime  $d(r_A, r_B)$  is the same as in the Schwarzschild scenario (see Eq. (D.6)).

of distance between the observers is appropriate for this comparison. Various notions could be thought of that coincide in Minkowski spacetime, but give different results in Schwarzschild spacetime, as we illustrate in the following.

A distance measure between static observers which we find to result in similar signal strengths in Schwarzschild and Minkowski distance, we will refer to as *static distance* (for the purpose of this subsection). It is most easily obtained by picking a slice of constant coordinate time, using Schwarzschild coordinates in Schwarzschild spacetime and standard coordinates in Minkowski spacetime. (The spatial coordinates of sender and receiver are independent of the choice of time slice, because sender and receiver are static.) The static distance is then given by the proper distance along the shortest (spacelike) geodesic connecting the sender to the receiver on the slice of constant time. For radially separated detectors in Schwarzschild spacetime, located at radial coordinates  $r_A$  and  $r_B$ , this static distance is

$$d(r_A, r_B) = \left| r_A \sqrt{f(r_A)} - r_B \sqrt{f(r_B)} + M \log \left( \frac{r_A \sqrt{f(r_A)} - M + r_A}{r_B \sqrt{f(r_B)} - M + r_B} \right) \right|, \quad (\text{D.6})$$

while in flat Minkowski spacetime it just corresponds to  $d(\vec{x}_A, \vec{x}_B) = |\vec{x}_A - \vec{x}_B|$ . In a

coordinate-independent fashion, the static distance can be defined as the proper distance along the shortest spacelike geodesic connecting the static sender and static receiver, orthogonal to the timelike Killing vector field of the static spacetime. Note that, as Bob approaches the horizon in Schwarzschild, the static distance approaches a finite limit

$$\lim_{r_B \rightarrow 2M} d(r_A, r_B) = \left| r_A \sqrt{f(r_A)} + M \log \left( \frac{r_A \sqrt{f(r_A)} - M + r_A}{M} \right) \right|. \quad (\text{D.7})$$

As seen in Fig. 29, resonant detectors in Schwarzschild spacetime achieve a direct signal strength which resembles the signal strength between detectors at equal static distance in Minkowski spacetime. (Where in Minkowski spacetime identical and thus resonant detectors are chosen, which generally maximizes the signal strength for long enough coupling times.) In fact, if  $r_B > r_A$  the signal strength in Schwarzschild spacetime is slightly larger than the signal strength in Minkowski spacetime. In the other direction, where Bob is closer to the horizon and  $r_B < r_A$ , we find the opposite: The signal strength in Schwarzschild spacetime is smaller; in particular, it drops down to zero as Bob approaches the horizon. The behaviour in both directions arises because, in Schwarzschild spacetime, Bob has, respectively, more or less proper time at hand to interact with Alice's signal, as explained above.

The use of the static distance for the comparison of signal strength between Schwarzschild and Minkowski spacetimes above may appear rather ad hoc. One could think of other ways to measure the distance between two given static detectors which, arguably, could even be more physical or operational.

For example, a very operational approach would be for Alice and Bob to measure the distance in terms of the proper time that they observe it takes for a signal to propagate along direct null geodesics from the sender to the receiver, and back again to the sender. From this perspective, we would compare a given scenario in Schwarzschild spacetime with scenarios in Minkowski spacetime that have the same signal return time. One caveat with this approach is that it is asymmetric. In curved spacetime Alice and Bob will measure the

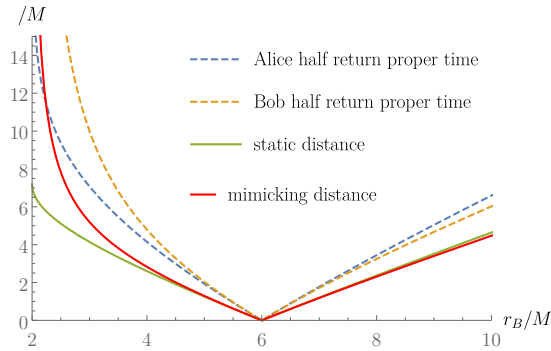


Figure 30 – The figure compares various measures of distance between two radially separated static observers, Alice (sender) at  $r_A = 6M$  and Bob at varying  $r_B$ , in Schwarzschild spacetime. The plot shows half of the signal return time for Alice (blue, dashed) and Bob (yellow, dashed), i.e., the time it takes for a signal to propagate from Alice to Bob measured in terms of the respective proper times of Alice and Bob, and the static distance (green, solid) in Eq. (D.6). The plot also shows the “mimicking distance” (red, solid), i.e., the distance in Minkowski spacetime at which two identical detectors ( $\Omega_B = \Omega_A$ ) achieve the same direct signal strength as the two detectors in Schwarzschild spacetime at  $r_A$  and  $r_B$  when they are resonantly-tuned ( $\Omega_B = \nu\Omega_A$ ). (The return times and the mimicking distance diverge, as  $r_B \rightarrow 2M$ , whereas the static distance remains finite, see (D.7).)

signal-return time in terms of their respective proper times and thus assess the distance between them differently.

In flat Minkowski spacetime all these notions coincide: Alice and Bob both measure the same signal return time, and the signal return time coincides with two times the static distance (due to  $c = 1$ ). Of course, all of these notions just correspond to the one natural notion of distance between two static observers in flat spacetime.

In curved spacetime, all of these notions of distance differ, as Fig. 30 illustrates for Schwarzschild spacetime. There, two static, radially separated observers are placed at radial coordinates  $r_A = 6M$  and  $r_B$ . The plot shows the static distance between them (green) as well as half of the signal-return time as measured in Alice’s proper time (dashed blue) and in Bob’s proper time (dashed yellow).

In addition, Fig. 30 plots a “mimicking distance” (red) which is the distance in Minkowski spacetime for which the direct signal strength between two identical detectors ( $\Omega_B = \Omega_A$ ) in Minkowski spacetime is the same as between the two radially separated detectors in Schwarzschild spacetime at  $r_A$  and  $r_B$  which are tuned into resonance ( $\Omega_B = \nu\Omega_A$ ). (Note that this distance is independent of Alice’s detector frequency  $\Omega_A$ .)

Fig. 30 motivates our previous use of the static distance to compare Schwarzschild and Minkowski spacetime because for small distances it resembles the mimicking distance more closely than the signal-return times. The differences between the different distance measures actually may open up for an interesting way of measuring spacetime curvature. Because, as noted above, in regions without spacetime curvature all four notions of distance would coincide, Alice and Bob may be able to detect and quantify spacetime curvature by measuring and comparing signal strength and signal-return times.

# APPENDIX E – Change of integration variable in tail contribution for static detectors

This appendix discusses how, for static detectors in a static spacetime, a change of integration variables in the double integrals of  $C_2$  and  $D_2$  makes it possible to separate the expression into a product of one integral containing the Green function and another integral involving the switching functions. The latter can often be performed analytically thus leaving only the first integral to be performed numerically.

Since the spatial coordinates of detectors at rest do not change, the value of the Green function in the integrand of  $C_2$  only depends on the coordinate time difference between Alice and Bob. Following the definitions at the beginning of Section 4.2.2, the coordinate time difference is

$$t(\tau_B) - t(\tau_A) = \frac{1}{v(r_A)} (\nu\tau_B - \tau_A) + \Delta t_{A \rightarrow B}. \quad (\text{E.1})$$

In a static spacetime, the retarded Green function only depends on the time coordinate difference between its arguments. We use this and define

$$w = \nu\tau_B - \tau_A \quad (\text{E.2})$$

such that

$${}_0G_{\text{ret}}(x_B(\tau_B), x_A(\tau_A)) = {}_0G_{\text{ret}}(t(\tau_B) - t(\tau_A), \vec{x}_B, \vec{x}_A) \quad (\text{E.3})$$

$$= {}_0G_{\text{ret}}(w/v(r_A) + \Delta t_{A \rightarrow B}, \vec{x}_B, \vec{x}_A). \quad (\text{E.4})$$

Next, we can change the integration variables in  $C_2$  in Eq. (4.19) from  $(\tau_A, \tau_B)$  to  $(s, \tau_B)$ . To this end, denote the support of the switching functions in terms of detector proper times as  $\text{supp } \eta_A(\tau_A) = [A_1, A_2]$  and  $\text{supp } \eta_B(\tau_B) = [B_1, B_2]$ . The integrand of the



double-integral in  $C_2$  then has support only in the region  $B_1 \leq \tau_B \leq B_2, A_1 \leq \tau_A \leq \min[A_2, \nu\tau_B]$ .

One can visualize the role of  $s$  in a 2D-plot of the integration region. We put  $\tau_A$  on the y-axis and  $\tau_B$  on the left axis. Then  $s$  is constant along straight lines cutting through the first quadrant of the coordinate system. Their angle depends on  $\nu$ , i.e., the redshift between Alice and Bob.  $s$  increases as one moves to the bottom right in the plot, i.e., for increasing  $\tau_B$ . Points in the integration region which lie on a line of constant  $s$  correspond to point pairs on the worldline of Alice and Bob which are separated by the same amount of coordinate time. This means they are mapped into each other by translations along the Killing field of coordinate time. E.g., there is the line of  $w = 0$  which has all points connected by a direct null geodesic on it. And there is the line of constant  $s$  which has all the points connected by a secondary null geodesic on it, and so on.

Under the change of integration variables from  $(\tau_B, \tau_A)$  to  $(\tau_B, w)$ , the integral thus transforms to

$$\int_{B_1}^{B_2} d\tau_B \int_{A_1}^{\min[A_2, \nu\tau_B]} d\tau_A = \int_{\max[\nu B_1 - A_2, 0]}^{\nu B_2 - A_1} dw \int_{\max[B_1, (w+A_1)/\nu]}^{\min[B_2, (w+A_2)/\nu]} d\tau_B, \quad (\text{E.5})$$

such that

$$C_2 = \frac{-i}{4\pi} \int_{\max[\nu B_1 - A_2, 0]}^{\nu B_2 - A_1} dw e^{i\Omega_A w} {}_0G_{\text{ret}}(w/v(r_A) + \Delta t_{A \rightarrow B}, \vec{x}_B, \vec{x}_A) \times \int_{\max[B_1, (w+A_1)/\nu]}^{\min[B_2, (w+A_2)/\nu]} d\tau_B \eta_B(\tau_B) \eta_A(\nu\tau_B - w) e^{i(\Omega_B - \nu\Omega_A)\tau_B} \quad (\text{E.6})$$

The inner integral over  $\tau_B$  is typically easy to solve analytically. In particular, sharp switching functions  $\eta_A(\tau_A) = \eta_{[A_1, A_2]}(\tau_A)$  and  $\eta_B(\tau_B) = \eta_{[B_1, B_2]}(\tau_B)$ , as defined in Eq. (4.17), yield

$$C_2 = \frac{-i}{4\pi} \int_{\max[\nu B_1 - A_2, 0]}^{\nu B_2 - A_1} dw e^{i\Omega_A w} {}_0G_{\text{ret}}(w/v(r_A) + \Delta t_{A \rightarrow B}, \vec{x}_B, \vec{x}_A) \times \int_{\max[B_1, (w+A_1)/\nu]}^{\min[B_2, (w+A_2)/\nu]} d\tau_B e^{i(\Omega_B - \nu\Omega_A)\tau_B} \quad (\text{E.7})$$

$$= \int_{\max[\nu B_1 - A_2, 0]}^{\nu B_2 - A_1} dw \frac{e^{i\Omega_A w} {}_0G_{\text{ret}}(w/v(r_A) + \Delta t_{A \rightarrow B}, \vec{x}_B, \vec{x}_A)}{4\pi(\Omega_B - \nu\Omega_A)} \times \left( e^{i(\Omega_B - \nu\Omega_A)\max[B_1, (w+A_1)/\nu]} - e^{i(\Omega_B - \nu\Omega_A)\min[B_2, (w+A_2)/\nu]} \right). \quad (\text{E.8})$$

# APPENDIX F – Signal contribution from principal value distribution

This appendix discusses what qualitative features of the signal strength are expected to arise from secondary light rays. Due to the singularity structure of the Green function in Schwarzschild spacetime, discussed in Sec. 4.2.2, the leading order behaviour of the Green function between points that are connected by secondary null geodesics corresponds to the product of a principal value  $\text{PV}\left(\frac{1}{\sigma}\right)$  distribution and a regular function. In order to understand the qualitative behaviour of the signal contribution from secondary null geodesics between stationary detectors, we essentially ignore that pre-factor function and thus replace the Green function in Eq. (E.6) by

$${}_0G_{\text{ret}}(w/v(\vec{x}_A) + \Delta t_{A \rightarrow B}, \vec{x}_B, \vec{x}_A) \rightarrow \frac{1}{L} \text{PV}\left(\frac{1}{w - w_2}\right), \quad (\text{F.1})$$

where  $L$  is some length scale. The value of  $w_2$  corresponds to the time it takes secondary null geodesics to propagate from Alice to Bob, in terms of the integration variable  $w$  in Eq. (E.6). Concretely, it mimicks the scenario where a secondary null geodesic emanating from Alice at her proper time  $\tau'_A$  arrives at Bob's location at his proper time

$$\tau'_B = \frac{w_2 + \tau'_A}{\nu}. \quad (\text{F.2})$$

(See Eq. (E.2) and discussion on p. 188 for the definition of  $w$ .)

Assuming sharp switching functions, just as in Appendix. E, we find that the expression for the contribution from the principal value distribution, which we obtain by inserting Eq. (F.1) into Eq. (E.7), is

$$C_2 = \frac{-i}{4\pi L} \int_{\max[\nu B_1 - A_2, 0]}^{\nu B_2 - A_1} dw e^{i\Omega_A w} \text{PV}\left(\frac{1}{w - w_2}\right) \underbrace{\int_{\max[B_1, (w+A_1)/\nu]}^{\min[B_2, (w+A_2)/\nu]} d\tau_B e^{i(\Omega_B - \nu\Omega_A)\tau_B}}_{=: f(w)}. \quad (\text{F.3})$$

(Remember Eq. (4.16), i.e.  $D_2(\Omega_A, \Omega_B) = -C_2(\Omega_A, -\Omega_B)$ .) The inner integral, which we denoted by  $f(w)$  is straightforward to evaluate, with the resonant case  $\Omega_B = \nu\Omega_A$  requiring a separate treatment.

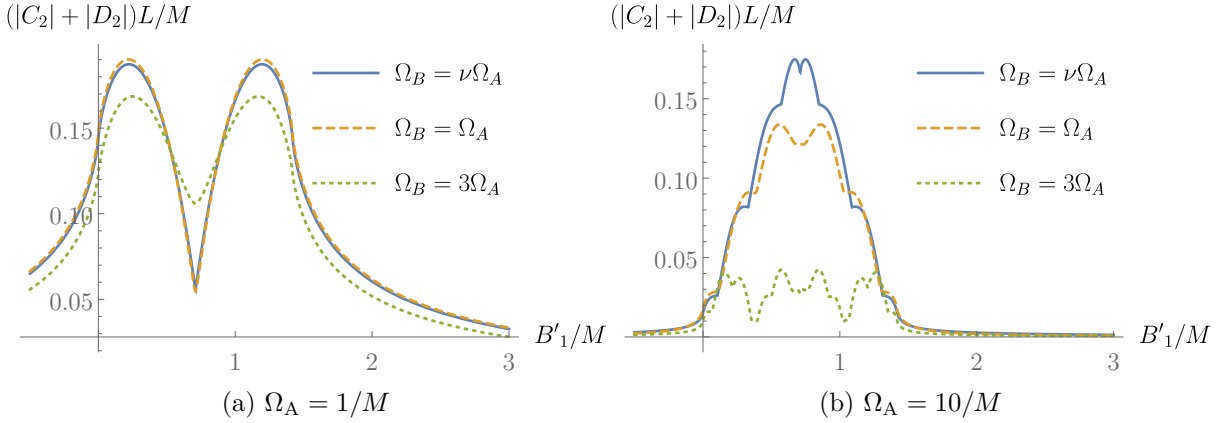


Figure 31 – Contribution to the leading order signal strength from a PV  $\left(\frac{1}{\sigma}\right)$ -distribution, as resulting from Eq. (F.4), with  $\nu = \sqrt{(1 - 2/6)/(1 - 2/3.01)} \approx 1.40954$ ,  $A_1 = 0$  and  $A_2 = M$ . The horizontal axes show  $B'_1 := B_1 - \frac{w_2 - A_2 + 2A_1}{\nu}$  which is the switch-on time  $B_1$  of Bob shifted so that, for  $B'_1 < 0$ , Alice and Bob are not connected by the singularity of the PV  $\left(\frac{1}{\sigma}\right)$ -distribution while coupling to the field. This corresponds to Bob switching off his detector before any secondary null geodesics emanating from Alice arrive at his location. The graphs are symmetric about the point  $B'_1 = \frac{A_2 - A_1}{\nu}$ . This corresponds to the switching-on and switching-off of sender and receiver being exactly connected by secondary null geodesics. The parameters in Fig. 31a match those in Fig. 16, thus the curve with equal frequencies ( $\Omega_A = \Omega_B$ ) here reproduces the features due to secondary null geodesics seen there.

The appearance of the PV  $\left(\frac{1}{w-w_2}\right)$ -distribution in Eq. (F.3) raises the question of whether  $C_2$  is well-defined and finite when  $w_2$  coincides with one of the boundaries of the  $w$ -integral. It turns out that the expression is well-defined. The reason being that, in this specific case that  $s_2$  coincides with either of the boundaries of the outer integral, the absolute value of the inner integral  $|f(w)| = \mathcal{O}(|w - w_2|)$  goes to zero linearly, thus rendering the value of  $C_2$  finite. Hence, even for sharp switching functions, the leading order signal contributions from secondary null geodesics are finite, just as they are for the primary direct null geodesics. (Note, that this also holds true when taking into account the regular pre-factor in the Green function which we are not taking into account in this appendix.)

We can reproduce the features of Fig. 16 which are due to secondary null geodesics. To this end, we let Alice couple to the field during the fixed proper time interval  $A_1 \leq \tau_A \leq A_2$ . Bob begins to couple at varying proper times  $\tau_B = B_1$ . However, he always switches off after a time corresponding to the red-shifted duration of Alice's signal, i.e.,  $B_2 - B_1 = (A_2 - A_1)/\nu$ . In particular, if  $B_1 = (A_1 + w_2)/\nu$ , both the switching-on and switching-off of both detectors are connected by secondary null geodesics. For non-resonant detectors

in this scenario, Eq. (F.3) has the solution

$$\begin{aligned}
C_2 &= \frac{-i}{4\pi L} \int_{\max[\nu B_1 - A_2, 0]}^{\nu B_1 + A_2 - 2A_1} dw e^{i\Omega_A w} \text{PV} \left( \frac{1}{w - w_2} \right) \int_{\max[B_1, (w+A_1)/\nu]}^{\min[B_1 + (A_2 - A_1)/\nu, (w+A_2)/\nu]} d\tau_B e^{i(\Omega_B - \nu\Omega_A)\tau_B} \\
&= \frac{-1}{4\pi L(\Omega_B - \nu\Omega_A)} \left[ R(\Omega_B/\nu, \nu B_1 - A_2, w_m, w_2) e^{i(\Omega_B - \nu\Omega_A)A_2/\nu} \right. \\
&\quad - R(\Omega_A, \nu B_1 - A_2, w_m, w_2) e^{i(\Omega_B - \nu\Omega_A)B_1} \\
&\quad + R(\Omega_A, w_m, \nu B_2 - A_1, w_2) e^{i(\Omega_B - \nu\Omega_A)B_2} \\
&\quad \left. - R(\Omega_B/\nu, w_m, \nu B_2 - A_1, w_2) e^{i(\Omega_B - \nu\Omega_A)A_1/\nu} \right], \tag{F.4}
\end{aligned}$$

with  $w_m := \nu B_1 - A_1 (= \nu B_2 - A_2)$  and, for resonant detectors, i.e.,  $\Omega_B = \nu\Omega_A$ , it has the solution

$$\begin{aligned}
C_2 &= -\frac{i}{2\pi L} \frac{(B_2 - B_1)(w_2 - \nu B_1 + A_2)}{\nu(B_2 - B_1) + A_2 - A_1} R(\Omega_A, \nu B_1 - A_2, w_m, w_2) \\
&\quad - \frac{i}{4\pi L} \left( (B_2 - B_1) - \frac{2(B_2 - B_1)(w_2 - \nu B_1 + A_1)}{\nu(B_2 - B_1) + A_2 - A_1} \right) R(\Omega_A, w_m, \nu B_2 - A_1, w_2) \\
&\quad + \frac{(B_2 - B_1)}{2L\Omega_A (\nu(B_2 - B_1) + A_2 - A_1)} \left( e^{i\Omega_A(\nu B_2 - A_1)} - 2e^{i\Omega_A w_m} + e^{i\Omega_A(\nu B_1 - A_2)} \right). \tag{F.5}
\end{aligned}$$

Here we defined, using  $\text{Ci}(w) = -\int_w^\infty du \cos(u)/u$  and  $\text{Si}(w) = \int_0^w du \sin(u)/u$ ,

$$\begin{aligned}
R(\omega, X, Y, w_2) &:= \text{PV} \left( \int_X^Y dw \frac{e^{i\omega w}}{w - w_2} \right) \\
&= e^{i\omega w_2} (\text{Ci}(|\omega(Y - w_2)|) - \text{Ci}(|\omega(X - w_2)|) + i \text{Si}(\omega(Y - w_2)) - i \text{Si}(\omega(X - w_2))). \tag{F.6}
\end{aligned}$$

While this function is singular as  $w_2 \rightarrow X$  or  $w_2 \rightarrow Y$ , all expressions for  $C_2$  are finite and well-defined. This is because they contain a combination of terms with  $R$ -functions of different arguments, such that the singularities between the different terms exactly cancel out.

Some contributions to the signal strength, resulting from different coupling durations and detector frequencies, are plotted in Fig. 31. As seen there, the signal strength is symmetric about the point where Alice's and Bob's switchings are exactly connected by secondary null geodesics. I.e., it is the point for which Bob switches on his detector when the secondary null geodesic emanating from Alice's switch-on arrives and he switches off when the secondary null geodesic from Alice's switch-off arrives. At this point the signal

strength has a local minimum. Overall, if the detectors are resonant or close to resonance, the resulting signal strength rises to its highest levels around this symmetry point. For resonant detectors this maximum scales roughly linearly with the duration of the signal. For non-resonant detectors the signal strength exhibits a mostly periodic behaviour without a distinct maximum in the region where the detectors are connected by some secondary null geodesics. Outside of this region, i.e., when Bob couples to the field strictly before or after any of Alice's secondary null geodesics arrive, the signal strength exhibits a decaying tail which results from the PV  $\left(\frac{1}{\sigma}\right)$  behaviour of the Green function. The tail appears independently of whether the detectors are resonant or not.

Similarly, we can also isolate the contribution from secondary null geodesics in the plots in Figs. 14 and 17. In these plots we have  $B_1 = A_1/\nu$ , i.e., Bob always switches on his detector when the first signal from Alice arrives. (Note that this signal is predominantly carried by the  $\delta(\sigma)$ -contribution from primary null geodesics, which we discard here.) Then we ask how the signal strength depends on  $B_2$ , i.e., the point in time at which Bob switches his detector off again. For reasons of simplicity, let us assume that Bob couples at least for a time such that  $B_2 \geq A_2/\nu$ . Then the contribution to the signal strength from the PV  $\left(\frac{1}{\sigma}\right)$ -distribution is, for general detector frequencies,

$$\begin{aligned} C_2 &= \frac{-i}{4\pi L} \int_{\max[\nu B_1 - A_2, 0]}^{\nu B_2 - A_1} dw e^{i\Omega_A w} \text{PV} \left( \frac{1}{w - w_2} \right) \int_{(w+A_1)/\nu}^{\min[B_2, (w+A_2)/\nu]} d\tau_B e^{i(\Omega_B - \nu\Omega_A)\tau_B} \\ &= \frac{-1}{4\pi L(\Omega_B - \nu\Omega_A)} \left[ e^{i(\Omega_B/\nu - \Omega_A)A_2} R(\Omega_B/\nu, 0, w_n, w_2) - e^{i(\Omega_B/\nu - \Omega_A)A_1} R(\Omega_B/\nu, 0, w_n, w_2) \right. \\ &\quad \left. + e^{i(\Omega_B - \nu\Omega_A)B_2} R(\Omega_A, w_n, \nu B_2 - A_1, w_2) - e^{i(\Omega_B/\nu - \Omega_A)A_1} R(\Omega_B/\nu, w_n, \nu B_2 - A_1, w_2) \right], \end{aligned} \quad (\text{F.7})$$

where  $w_n := \nu B_2 - A_2$ , and for resonant detectors, i.e.,  $\Omega_B = \nu\Omega_A$ , it is

$$\begin{aligned} C_2 &= \frac{-i}{4\pi L\nu} \left[ (A_2 - A_1) R(\Omega_A, 0, w_n, w_2) + (B_2 - A_1 - w_2) R(\Omega_A, w_n, \nu B_2 - A_1, w_2) \right. \\ &\quad \left. + i \left( e^{i\Omega_A(\nu B_2 - A_1)} - e^{i\Omega_A w_n} \right) \right]. \end{aligned} \quad (\text{F.8})$$

Fig. 32 plots the resulting signal strength in various scenarios. In particular, Fig. 32a reproduces the features discussed in Figs. 18 and 17. The plots show that the resulting signal strength changes significantly as a function of the switch-off time, if the switch-off

happens while secondary null geodesics arrive at Bob's position that emanated from Alice while she was coupled to the field. For non-resonant detectors the signal strength exhibits an oscillatory and periodic behaviour within this time interval. For resonant detectors, however, the signal strength grows roughly linearly in this region. After this region, where the switch-off time is such that all secondary null geodesics that emanate from Alice arrive at Bob while he is coupled to the field, the signal strength only shows an oscillatory behaviour for later switch-off times. The oscillations decay and asymptote to a final value as  $B_2 \rightarrow \infty$ . The limit value appears to be determined by the duration of the original signal emitted by Alice.

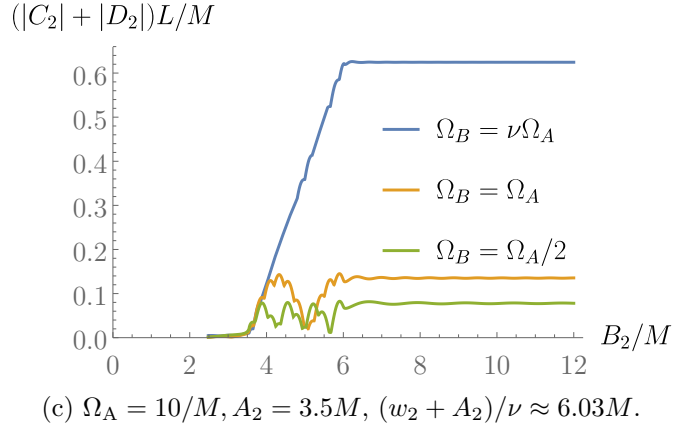
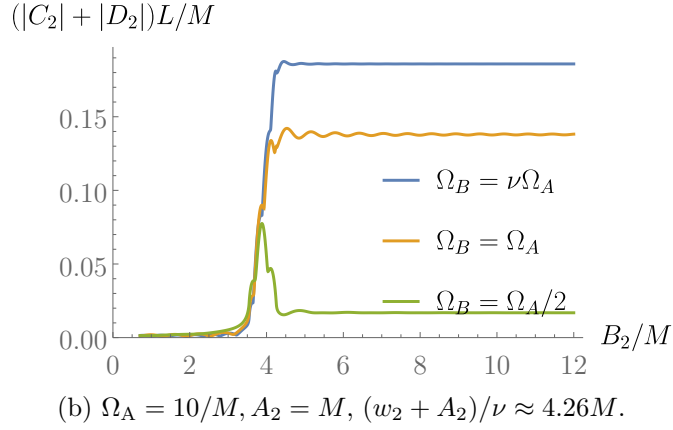
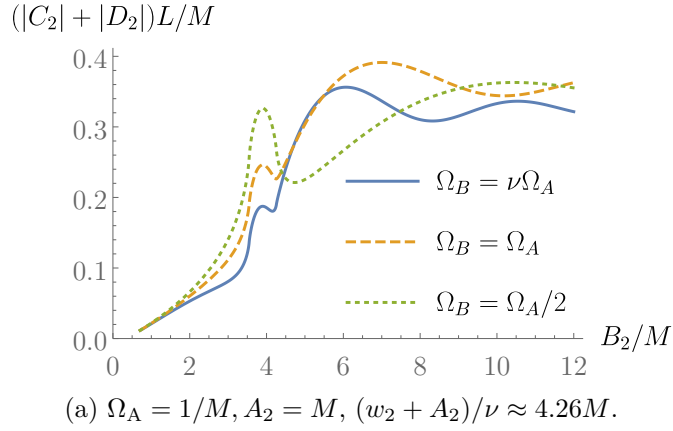


Figure 32 – Contribution to the leading order signal strength from PV  $(\frac{1}{\sigma})$ -distribution, as resulting from Eq. (F.7), with  $\nu = \sqrt{(1 - 2/6)/(1 - 2/3.01)} \approx 1.40954$ ,  $A_1 = 0$  and  $s_2 = 5M$ . (For this cumulative signal strength we always have  $B_1 = A_1/\nu = 0$ .) Alice’s first light ray, emanating at  $A_1 = 0$ , is connected by the PV  $(\frac{1}{\sigma})$ -singularity to the point on Bob’s worldline with proper time  $\tau_B = (w_2 + A_1)/\nu \approx 3.55M$ . Alice’s last light ray, emanating at her proper time  $A_2$ , is connected to Bob’s worldline at his proper time  $\tau_B = (w_2 + A_2)/\nu$  which is different for the two figures. The curve in Fig. 32a with  $\Omega_B = \Omega_A/2$  reproduces the features discussed in Figs. 18 and 17. In all three figures the oscillations in all curves decay as  $B_2 \rightarrow \infty$  and asymptote to constant values. (Note for non-colour print: The curve in Figs. 32b and 32c asymptote in the same order as they appear in the legend.)